

POLITECNICO DI TORINO

Master's Degree in Materials Engineering



Master's Degree Thesis

Sorption Thermal Energy Storage: a review of sorbent materials and the introduction of an innovative cost-effective cement based composite material

Supervisors

Prof. Matteo PAVESE

Dott. Luca LAVAGNA

Prof. Eliodoro CHIAVAZZO

Candidate

Maria Letizia AGHEMO

2020 July

Summary

The massive exploitation of renewable energy sources cannot overlook the development of storage systems, with the aim of compensate the discrepancy between surplus energy and energy demand peak times. In this field, sorption thermal energy storage (STES) is recently become of crucial interest. In particular, the process of charging and discharging consists of reversible reactions between a material with the ability of sorption (sorbent) and a fluid (sorbate). When combining the two elements heat is released, while their following separation requires heat from the environment. The lack of robust and low-cost sorbent materials, however, still represents a formidable technological barrier for long-term storage of thermal energy and, more generally, for adsorptive heat transformations. This work first aims to provide a wide general view of the existing sorbents-sorbate couples, consisting in four main classes: liquids, solids, chemicals and composite materials. In the latter, hygroscopic salts are introduced into a porous matrix. Several charts allow the reader to first compare materials and, more generally, classes, in terms of Energy Storage Density (ESD, MJ/m³), Energy Storage Capacity (ESC, kJ/kg) and temperature of desorption (charging temperature). In addition, new charts give access to the less-explored comparison of sorbents in terms of kWh/€, which is related to the Storage Capacity Cost (SCC). The latter is a crucial parameter when approaching the study of materials with economic and feasibility considerations, and in some cases, the ranking change of the material performances stands out. To refine the comparison between the main sorption materials in the field of STES, the model of a typical reactor is designed. The latter enables considering the required reactor volume and, consequently, the cost for the non-active material, the amount of fluids, the pressure losses of the sorbate going through the adsorbent. As next step, this work aims to introduce an innovative cost-effective cement-based composite sorbent material, in the horizon of existing sorbent materials. It is well

known that cement offer a tunable mesoporous porous structure, thus representing a good host for hygroscopic salts. Through a first optimization of the cement (Portland, 52.5) morphology, a water-to-cement ratio of 1,5 and an antisetling agent concentration of 1% wt are fixed, reaching 58% of porosity. With a dry-impregnation step, 36%wt of MgSO_4 has been introduced into the porous matrix. In addition, a novel in situ – approach for synthesizing cement-based composites is explored. Differently from the so-used impregnation method, when a salt solution enters the accessible pores of the matrix, salt is now introduced when mixing cement powder with water. As a result, hygroscopic salt molecules can be finely dispersed into the structure, thus allowing the increase in salt concentration and the decrease of the out of pores - salt deliquescence risk. In order to first understand if the synthesised composites yield a certain adsorption heat or not, a preliminary experimental analysis is carried out. It consists on pouring liquid water on the samples and recording the temperature raise of hydrated samples. An experimental energy density of 0.08 GJ/m^3 and 0.14 GJ/m^3 have been obtained for impregnated and in-situ cementitious sorbents respectively. To compare the energetic performances of the cementitious material with other sorbents, the standard EDS value can be derived from the experimental one by adding the enthalpic contribution of water vaporization (i.e. 41 kJ/mol). The experimental values are under the expectations, thus underlining a certain reactivity between our cement and MgSO_4 . The latter results in the decrease of the amount of available hygroscopic salt inside the porous matrix. In conclusion, cement is demonstrated to be used as super-porous material, Portland Cement 52.5 critically limits the energetic performances, since a large part of salt is not more available for the process of hydration. Future research works will investigate other types of cement, i.e. aluminous or magnesia cements, thus reducing the reactivity between the two phases. On the other side, other types of hygroscopic salts will be explored in the role of host into Portland Cement 52.5, thus looking for an almost inert loading phase.

Acknowledgements

Per lo svolgimento di questo lavoro ringrazio il professor Matteo Pavese e Luca, che hanno fatto fronte con me in modo originale agli imprevisti di quest'ultimo periodo, senza perdere il desiderio di insegnarmi ciò che sanno e di dare un reale contributo al mondo della ricerca scientifica. Un grazie speciale va poi a Betto e Puma, con cui ho condiviso questi mesi da tesisti, e a Elena ed Elena che hanno avuto a cuore il mio lavoro dall'inizio alla fine, anche da lontano. Questa tesi conclude cinque anni di università e la gratitudine è immensa. Sono grata per la compagnia dei miei amici del CLU, con cui mi sono goduta il poli e ho affrontato le giornate, una diversa dall'altra, scoprendo sempre più in tutte la bellezza di una vita donata. Ringrazio poi per aver avuto al mio fianco gli amici del liceo che con me hanno iniziato il poli e i miei fantastici compagni di corso, con cui anche in classe mi sono sempre sentita a casa. Tra loro, un grazie particolare è per aver incontrato Francesca e Maria che mi hanno voluto un bene immenso e hanno preparato con me ogni esame. Tra gli ultimi regali ricevuti, uno dei più belli è stato l'incontro con gli amici di Losanna, con cui ho vissuto sei mesi di grandi scoperte su di me e sul mondo. La presenza e il bene di tutti questi amici mi ha accompagnato negli anni, durante i quali ho scoperto una passione grande per lo studio di come è pensato bene il mondo. Per questo ringrazio di cuore tutti i professori che hanno speso il loro tempo e le loro energie con noi studenti e Anna e Matteo, che hanno fatto con me un pezzetto di strada nella scoperta del mondo della ricerca. Ringrazio per la pazienza della mia famiglia durante questi anni, sperando che un giorno Elena e Marco non si ricordino più di tutte le volte in cui ho fatto un po' la dissociata per studiare. Sono grata, infine, per la compagnia di Simo, che è il riferimento da cui parto nel desiderio di dare la mia vita per il mondo.

Table of Contents

List of Tables	VIII
List of Figures	X
1 Sorption thermal energy storage	1
1.1 Thermal energy storage systems	3
1.2 Sorption thermal energy storage	6
1.2.1 Open or closed systems	7
1.2.2 Selection criteria and evaluation parameters	10
1.2.3 Classification of sorbents	12
1.2.4 Comparison between sorbent materials	46
1.2.5 Cementitious composite materials for thermal energy storage applications	54
1.2.6 Conclusion	57
2 Model of a modular system for closed or open STES systems and working cycle optimization	59
2.1 Reference scenario	59
2.2 Selection of materials	61
2.3 Closed system	61
2.4 Open system	72
2.5 Optimization of the closed system working cycle	78
2.6 Conclusion	86
3 Fundamentals of cement-based materials	88
3.1 The manufacture of Portland cement	89
3.2 Hydration process of Portland cement	91
3.2.1 Cement composition and minerals	91
3.2.2 Chemical reactions involved in hydration	93
3.2.3 Mechanism of Portland cement hydration and heat of hydration	96
3.2.4 Heat of hydration	103

3.3	Setting of Portland cement	104
3.3.1	Mechanism of setting	105
3.3.2	Flash setting and false setting	106
3.4	Pore structure	108
3.4.1	Type of pores	108
3.4.2	Types of water	110
3.4.3	Bleeding of water in cement paste	110
4	Experimental section	114
4.1	Preparation and morphological characterization	114
4.1.1	Materials and methods of characterization	114
4.1.2	Results and discussion	121
4.2	Preliminary test analysis	138
4.2.1	Method	138
4.2.2	Results	140
4.2.3	Conclusion	144
A	Methods for evaluating the heat of adsorption	147
B	Thermal analysis	152
	Bibliography	155

List of Tables

1.1	Typical values of charging temperature and Energy Storage Capacity of the four categories of sorbent materials: solids, liquids, chemicals and composite materials.	13
1.2	Performances of liquid sorbent materials for STES systems.	15
1.3	Performances of the main solid sorbent materials for STES systems.	35
1.4	Commercial price of the main solid sorbent materials for STES systems	36
1.5	Performances of chemical sorbent materials for STES systems. . . .	39
1.6	Performances of composite sorbent materials for STES systems. . .	47
2.1	Thermal energy performances of the selected sorption materials. . .	61
2.2	Thermal energy performances of a closed STES system for different sorption materials.	67
2.3	Key parameters of two different climatic cycles: warm cycle, typical of areas as South Asia, North Africa and Central America, and cold cycle, typical of areas as South Russia, Europe and North America.	83
2.4	Characteristic values of the adsorption cycles, WC and CC, with different discharging temperatures.	83
3.1	Main components of Portland cement.	92
3.2	Chemical composition of Portland cement clinkers.	92
3.3	Main reactions of Portland cement hydration.	93
4.1	Oxides weight percentage of Portland cement 52.5	115
4.2	Dehydrated phases (above) and hydrated products (below) weight percentage of Portland cement 52.5	115
4.3	Lists of the prepared cement samples.	116
4.4	Composition of the <i>in situ</i> composite material.	118
4.5	Main properties of the prepared cement samples.	130
4.6	Composite samples after single or double impregnation.	131

4.7 Results of the preliminary thermal analysis of *impregnated* and *in-situ* cementitious composites. *Energy Density is calculated by considering an heat of hydration of 300J/g for MgSO₄ and 70J/g for pure cement, calculated from the experimental energy density of C1.5 **The Experimental Energy Density is a preliminary energetic parameter. To have the standard ESD value, the enthalpy of vaporization (41 kJ/mol) has to be added. 142

List of Figures

1.1	Pie chart representing the total heating and cooling demand as share of EU final energy consumption [1].	2
1.2	Graphic representation of the Solar Radiation (W/m^2) and the heat demand (kW): solar radiation does not match seasonal heat demand [3].	2
1.3	Above, schematic illustration of different storage systems: sensible heat storage (a), latent heat storage (b), sorption thermal energy storage (c). Below, stored specific heat versus temperature and the related thermodynamic equation for (a) sensible TES (water at $25\text{ }^\circ\text{C}$), (b) latent heat ($\text{C}_{20}\text{H}_{42}$ with melting temperature of $37\text{ }^\circ\text{C}$), and (c) thermochemical energy storage (sorbent material $\text{Na}_2\text{S}\cdot\text{H}_2\text{O}$, with heating rate of 1K min^{-1} [12]).	4
1.4	Energy storage capacities of PCMs (blue), sorption materials (green) and water (red line). Values of PCMs are taken from [13] while values of sorbent materials are taken from this work).	5
1.5	Number of publications from abstract and citation database “Scopus”.	5
1.6	Schematic representation of the mechanism of adsorption (left) and absorption (right) [16].	7
1.7	Schematic representation of closed systems.	9
1.8	Chart representing the working cycle of an adsorption heat storage: red lines represent the charging phase (desorption) while blue lines the discharging phase (adsorption) [19].	9
1.9	Schematic representation of open systems.	10
1.10	P(T) curve representing the seasonal solar energy storage cycle of $\text{LiBr}/\text{H}_2\text{O}$ [24].	14
1.11	Chart reporting the values of Energy Storage Density of the main liquid sorption materials.	16
1.12	Chart reporting the values of Energy Storage Capacity of the main liquid sorption materials.	17

1.13	Schematic representation of the mechanism of adsorption, with the formation of monolayer, multilayer and pore condensation [26]. . . .	18
1.14	Ideal representation of isotherm, isobar and isoster curves. [29] . . .	19
1.15	Schematic representation of different curves, depending on the morphology of the solid structure [29].	20
1.16	Schematic representation of the mechanism of water adsorption upon a surface of Silica [33].	22
1.17	Schematic representation of the mechanism of adsorption upon the surface of a Zeolite. Taking inspiration from [40].	25
1.18	Schematic representation of the mechanism of adsorption upon the surface of a Zeolite in the presence of cations. taking inspiration from [40].	25
1.19	Adsorption/desorption isotherms at 30 °C, 40 °C, 50 °C and 60 °C measured for the adsorbent materials: a-b) AlPO-18; c-d) FAPO-34; e-f)SAPO-34 [56].	28
1.20	Plot of the material degradation with regard to the number of cycles [57].	29
1.21	Schematic representation of the MOF's structure [59].	30
1.22	Water adsorption (solid symbols) and desorption (open symbols) isotherms of DUT-4 (a), ZIF-8(b), H-KUST-1(c), MIL100(Fe) (d), MIL101 (e) [60].	31
1.23	Chart reporting the values of Energy Storage Density of the main solid sorption materials.	33
1.24	Chart reporting the values of Energy Storage Capacity of the main solid sorption materials.	34
1.25	Schematic representation of the reaction of salt hydration and dehydration.	34
1.26	Curve of log(P) with respect to temperature, representing a common cycle of charging (right) and discharging (left) for a typical sorption thermal energy storage system with hydrated salts [83].	37
1.27	Chart reporting the values of Energy Storage Density of the main chemical sorption materials.	38
1.28	Chart reporting the values of Energy Storage Capacity of the main chemical sorption materials.	39
1.29	Schematic representation of the mechanism of adsorption and desorption for a “hygroscopic salt in porous host” material.	41
1.30	P(T) plot of thermochemical energy storage cycle using MgCl ₂ -zeolite composite sorbent [88].	42
1.31	Chart reporting the values of Energy Storage Density of the main composite sorption materials.	45

1.32	Chart reporting the values of Energy Storage Capacity of the main composite sorption materials.	46
1.33	Chart reporting the values of Energy Storage Density of the different sorption material categories with regards to the temperature of charging.	47
1.34	Chart reporting the values of Energy Storage Capacity of the different sorption material categories with regards to the temperature of charging.	48
1.35	Chart reporting the values kWh/€of the different sorption material categories with regards to the temperature of charging.	51
1.36	Chart reporting the values of Energy Storage Density of different solid sorption materials with regards to the temperature of charging.	52
1.37	Chart reporting the values of kWh/€of different solid sorption materials with regards to the temperature of charging.	53
1.38	Chart reporting the values of kWh/€of the different sorption material categories with regards to their Energy Storage Density.	54
1.39	Cementitious composite thermal energy storage cycles: (a) T of charging = 80 °C, (b) T of charging = 14 °C.	56
1.40	Chart reporting the values of kWh/€of the different sorption composite materials with regards to their Temperature of charging. A red dot marks the innovative cementitious sorbent	56
2.1	Nomenclature.	60
2.2	Schematic representation of a closed STES system.	63
2.3	Examples of closed systems from literature [114] [43] [115].	64
2.4	Schematic representation of the modular reactor model.	65
2.5	Chart reporting the value of Energy Storage Density of the sorbent material (blue dots) or of the closed STES system as a whole (green dots).	68
2.6	Graphic representation of the whole volume of a closed STES system with different sorption materials.	69
2.7	Graphic representation of the volume contribute of the different components of a closed STES reactor.	69
2.8	Graphic representation of the contribute in terms of price of the different components of a closed STES reactor.	71
2.9	Chart reporting the value of Energy storage Capacity per cost (kWh/kg) of the sorbent material (blue dots) or of the closed STES system as a whole (red dots).	71
2.10	Schematic representation of an open STES system [117] [118] [17].	73
2.11	Examples of closed systems from literature.	74

2.12	Chart reporting the value of Energy Storage Density of the sorbent material (blue dots), of the open STES system as a whole (red dots) and of the closed STES system as a whole (green dots).	75
2.13	graphic representation of the whole volume of an open (red) or closed (green) STES system.	76
2.14	Graphic representation of the price contribute of the different components of an open STES system.	77
2.15	Chart reporting the value of Energy Storage Capacity per cost (kWh/kg) of the sorbent material (blue dots), of the open STES system as a whole (red dots) and of the closed STES system as a whole (green dots).	78
2.16	Schematic representation of a ideal (closed) sorption TES cycle in a Clausius-Clapeyron chart.	79
2.17	Schematic representation of a ideal (closed) sorption TES cycle in a Coverage-Pressure chart.	80
2.18	Geographical chart representing the world average temperature [119].	82
2.19	Coverage-Pressure chart for WC and CC cycles with temperature desorption of 80 °C.	84
2.20	Coverage-Pressure chart for WC and CC cycles with temperature desorption of 140 °C.	85
3.1	Picture of Portland cement powder.	88
3.2	Schematic representation of the process of cement manufacturing [122].	89
3.3	SEM images of fracture surfaces on hardened Portland cement paste at very early hydration [141].	96
3.4	Plot of the progress of hydration with regard to the time of reaction of the main components of Portland cement [144].	97
3.5	Plot of the progress of formation of the main products of hydration with regard to the time of reaction [144].	98
3.6	Concentration versus time curves for solution filtered from cement paste, with $w/c = 2$ [146].	99
3.7	SE-SEM image of a hydration C_3S grain one hour before the peak. Note that C-S-H does not form a continuous layer around the grain, its surface is actually still in contact with the pore solution. This weakens the diffusion barrier hypothesis [151].	100
3.8	SEM image representing two types of C-S-H, the main product of Portland cement hydration. At left, <i>outer</i> is away from the cement particle surface, filling water-filled space and characterized by high porosity. At right, <i>inner</i> C-S-H is formed during later hydration and is characterized by lower porosity [155].	102

3.9	Images of two sizes of alite particles, hydrates separately, taken near the peak of reaction rate. a) original particle size is 38 micron, b) original particle size is 6 micron. It is possible to note that the thickness of the layer of products after hydration around small grains is much greater than that around large grains [160].	103
3.10	Plot of the hydration heat evolution of an ordinary Portland cement. 1: K_2SO_4 dissolution. 2: early stage reaction. 3: dormant period. 4: middle-stage reaction (C-S-H formation). 5: AFt formation. 6: AFt-AFm conversion [144].	104
3.11	On top, back scattered electron images of fresh cement paste by SEM based on the sample freezing method after 5 minutes, 60 minutes and 6 hours. Below, schematic representation of the mechanism of flocculation in the same moments [162].	106
3.12	SEM pictures of surface of cement particle hydrated at a) 0 s, b) 15, c) 120 min, d) 240 min, e) 480 min, f) 480 min at higher magnification. At 0s, the surfaces are bare. After 15 s and 120 min of hydration, the surfaces of the particles are still found to be bare, but new lumps and platelets have formed. After 240 min of hydration, a carpet is covering the cement particles and is seen to consist of needle-like protruding structures. The latter can be attributed to the formation of C-S-H [163].	107
3.13	Correlation between capillary porosity and degree of hydration (α) in pastes prepared at different w/c. In these calculations, α is provided as an input, and the corresponding capillary porosity is calculated based on the phase assemblages predicted by the Powers model. The solid vertical line indicates the average value of α of all pastes, prepared using the coarse cement at the main hydration peak [166].	109
3.14	Picture representing the effect of bleeding.	111
3.15	Schematic representation of mono-size particle sedimentation. For most of the time, cement paste can be compared with a suspension of mono-size particles, whose rate of settling depends on to inter-particle attraction [166].	112
3.16	Schematic representation of bleeding of cement, in absence (a) or presence (b) of bentonite. Bentonite is showed to absorb large quantities of water so that the slurry homogeneity is preserved and settling is hindered [171].	113
3.17	SEM image of mortar modified using 1% of methyl cellulose (MC). After wet storage, one can appreciate the presence of (a) bridges of MC film between ettringite crystals and (b) bridges of MC film between CH crystals [172].	113

4.1	Schematic representation of the method of preparation of the composite cement-MgSO ₄ sorbent material by <i>impregnation</i>	117
4.2	Schematic representation of the method of preparation of the composite cement-MgSO ₄ sorbent material <i>in situ</i>	118
4.3	TGA and DTG curves of the pure Portland cement 52.5 sample cured in oven at 85 °C for 24 hours.	123
4.4	TGA and DTG curves of the pure Portland cement 52.5 sample cured in oven at 85 °C for 24 hours (dot line) and pure Portland cement 52.5 sample cured for 28 days at room temperature in water (continuous line).	123
4.5	TGA and DTG curves of pure MgSO ₄	124
4.6	TGA and DTG curves of the cement+MgSO ₄ material.	126
4.7	Chart of comparison between ideal w/c and actual w/c.	127
4.8	Chart of actual w/c with regards to the concentration of antisetling agent introduced into a cement sample with w/c equals to 1 (blue dots) or 1,5 (black dots).	127
4.9	Chart representing the values of density of the pure cement samples, with respect to the ideal w/c (black dots) and actual w/c (blue dots); regarding the latter, empty dots represents cement samples with the anti-settling agent.	129
4.10	Chart representing the values of porosity of the pure cement samples, with respect to the ideal w/c (black dots) and actual w/c (blue dots); regarding the latter, empty dots represents cement samples with the anti-settling agent. The red line indicates the theoretical value of porosity.	129
4.11	Optical microscopy images of pure cement samples with different w/c values.	133
4.12	Optical microscopy image of a pure cement sample with w/c equals to 1: some spherical dots (red circles) are clearly detectable as pores, but some other dark spots (blue circles) are hard to recognise as big pores or the sum of small pores or even some light effects due to the surface roughness.	134
4.13	Stereomicroscopic images (left) and elaborated black-white images (right) of pure cement samples with w/c equals to 0.40, 0.56, 0.71 .	135
4.14	Stereomicroscopic images (left) and elaborated black-white images (right) of pure cement samples with w/c equals to 0.79, 0.86, 1.43 .	136
4.15	Stereomicroscopic image of a cementitious composite material after the impregnation step: small white dots confirm that the porous matrix is able to host the hygroscopic salt.	137

4.16	Stereomicroscopic image of an <i>in-situ</i> cementitious composite material:quite large dark shadows (orange circle) are supposed to correspond to gypsum precipitates while small circular shadows (blue circle) refers to pores.	137
4.17	Schematic representation of the preliminary thermal test set up. . .	139
4.18	Schematic representation of the preliminary thermal test set up along with its actual dimension in millimeters.	140
4.19	Plot reporting the water temperature evolution caused by the endothermic reaction of hydration of dried cement-MgSO ₄ composite material introduced into the water bath.	141
4.20	Plot reporting the TG analysis of Im1.5 ₁	143
4.21	Plot reporting the TG analysis of Mg(OH) ₂ [185].	144
A.1	Schematic view of TGA-DSC set-up (left) and typical result of de/rehydration of a 7 mg encapsulated CaCl ₂ sample subjected to 1.3kPa water vapour pressure (right)[97].	148
A.2	Clausius-Clapeyron diagram representing two different adsorption cycles for Li/Ca halogenides inside Multi-wall Carbon Nano-tubes [102].	149
A.3	Clausius-Clapeyron diagram representing two different adsorption cycles for Li/Ca halogenides inside Multi-wall Carbon Nano-tubes [102].	151
B.1	Plot reporting the water temperature evolution caused by the endothermic reaction of hydration of Im1.5-1 introduced into the water bath.	152
B.2	Plot reporting the water temperature evolution caused by the endothermic reaction of hydration of Im1.1-1 introduced into the water bath.	153
B.3	Plot reporting the water temperature evolution caused by the endothermic reaction of hydration of Im1.1-2 introduced into the water bath.	153
B.4	Plot reporting the water temperature evolution caused by the endothermic reaction of hydration of S1 introduced into the water bath.	154
B.5	Plot reporting the water temperature evolution caused by the endothermic reaction of hydration of S1.5 introduced into the water bath.	154

Chapter 1

Sorption thermal energy storage

The heating and cooling sector is vitally important for the transition to a low-carbon energy system. It is responsible for half of all consumed final energy in Europe and the majority of the demand is provided by fossil fuels. In detail, heating and cooling accounts for 68% of all EU gas imports. As reported in “Mapping and analyses of the current and future (2020 - 2030) heating/cooling fuel deployment (fossil/renewables)”, published by the European Commission Directorate-General For Energy [1], the heating and cooling energy is exploited for space heating (26%), water heating (5%), process heating (15%) and process cooling (2%), and to a lesser extent for cooking (2%) and space cooling (1%) 1.1. About 45% of energy for heating and cooling in the EU is used in the residential sector, 37% in industry and 18% in services [2]. With the aim of reaching Europe’s sustainability goals, a decisive reduction in the use of fossil fuels to provide heating and cooling energy is the most rapid way. A decisive reduction in the use of fossil fuels to provide heating and cooling services in Europe, including thermal energy systems, is the fastest way to reach Europe’s sustainability goals. However, the integration of renewable energy into cooling and heating systems asks to solve the problem of discrepancy between surplus energy and energy demand peak times during the year. Solar energy, indeed, is available in abundance during the summer months while most of the heating requirement is in the winter (Figure 1.2). It is clear that the massive exploitation of renewable energy sources cannot overlook the development

of storage systems, with the aim of compensate the discrepancy between demand and energy peak times.

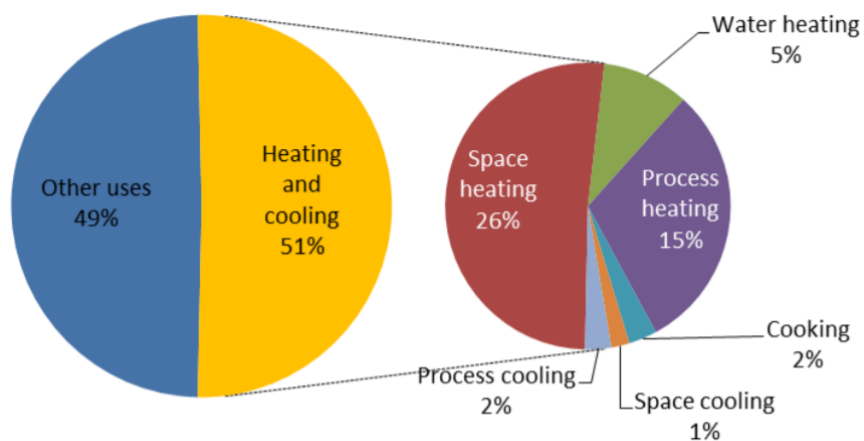


Figure 1.1: Pie chart representing the total heating and cooling demand as share of EU final energy consumption [1].

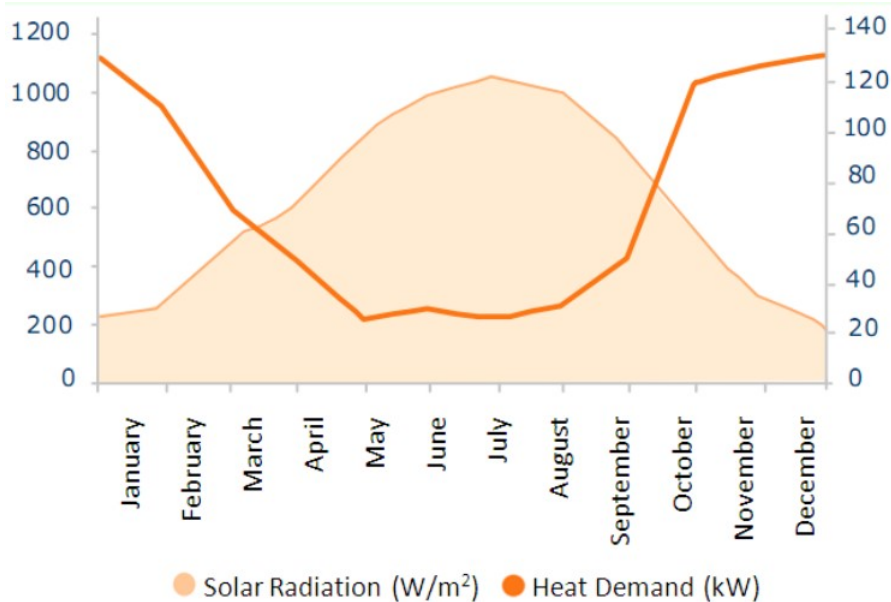


Figure 1.2: Graphic representation of the Solar Radiation (W/m²) and the heat demand (kW): solar radiation does not match seasonal heat demand [3].

1.1 Thermal energy storage systems

In thermal energy storage systems, the charging-discharging cycle of energy is related to the ability of materials to gain and release heat under certain conditions. According to the origin of the latter, it is possible to distinguish three types of systems: sensible heat storage (SHS), latent heat storage (LHS) and sorption thermal energy storage (STES) [4]. The working principle of each system is reported in Figure 1.3, while a comparison between performances is represented in Figure 1.4. In SHS systems, thermal energy is stored by heating or cooling a liquid or solid storage medium, with water being the most common option [5]. Hence, thermal energy is stored as a function of the temperature difference only and the amount of stored energy depends on the heat capacity of the material. The main advantages are the cost-effectiveness of the system and the wide temperature range of applications. However, sensible heat storage requires in general large volume, because of its low energy density. Moreover, due to the heat dissipation through the environment, these systems are not suitable for medium-long term period [6].

LHS systems utilize materials with the property of releasing or absorbing thermal energy through a phase change (commonly named Phase Change Materials), depending on the latent heat of the substance. PCMs includes organic materials (paraffin, ester, alcohol), inorganic materials (salt hydrate, metallic) and eutectics, combining two or more low melting materials with similar melting and freezing point [7]. The phase change can involve either a solid-liquid transition, a liquid-gas transition or a solid-solid transition, i.e. from one crystal structure to a different one. They have values of energy storage density in the range 100-250 kJ kg⁻¹, together with low working temperatures, in the range 20-40 °C [8] and [9]. In addition, PCMs benefit from the isothermal nature of heat discharging, since the phase transition develops at constant temperature. However, a complex design is required to avoid conditions of low thermal conductivity of the material and risks of supercooling or segregation, both affecting the energy storage efficiency of the system [10].

In sorption thermal energy storage systems (STES), the process of charging and discharging is based on reversible reactions between a material with the ability of sorption (sorbent) and a fluid (sorbate). When combining the two elements heat is released while their following separation requires heat from the environment.

STES systems present the high performances in terms of energy storage capacities, reaching values next to 4400 kJ kg^{-1} [11].

Hence, this technology appears promising in the attempt of improvement of the storage of thermal energy and it is recently become of crucial interest, as evidenced by the increase of publications (Figure 1.5, from abstract and citation database “Scopus”). However, some limitations as the slow reaction kinetic and relatively high working temperature ($50\text{-}190 \text{ }^\circ\text{C}$), as well as heat and mass transfer resistance within the material, cause this technology to be still in the laboratory research stage.

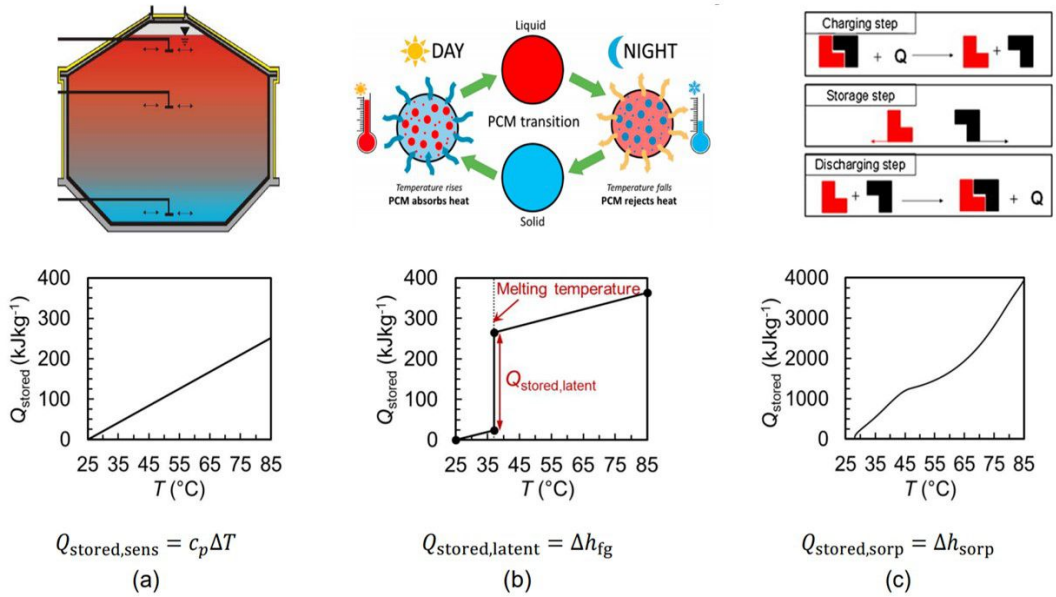


Figure 1.3: Above, schematic illustration of different storage systems: sensible heat storage (a), latent heat storage (b), sorption thermal energy storage (c). Below, stored specific heat versus temperature and the related thermodynamic equation for (a) sensible TES (water at $25 \text{ }^\circ\text{C}$), (b) latent heat ($\text{C}_{20}\text{H}_{42}$ with melting temperature of $37 \text{ }^\circ\text{C}$), and (c) thermochemical energy storage (sorbent material $\text{Na}_2\text{S-H}_2\text{O}$, with heating rate of 1K min^{-1} [12]).

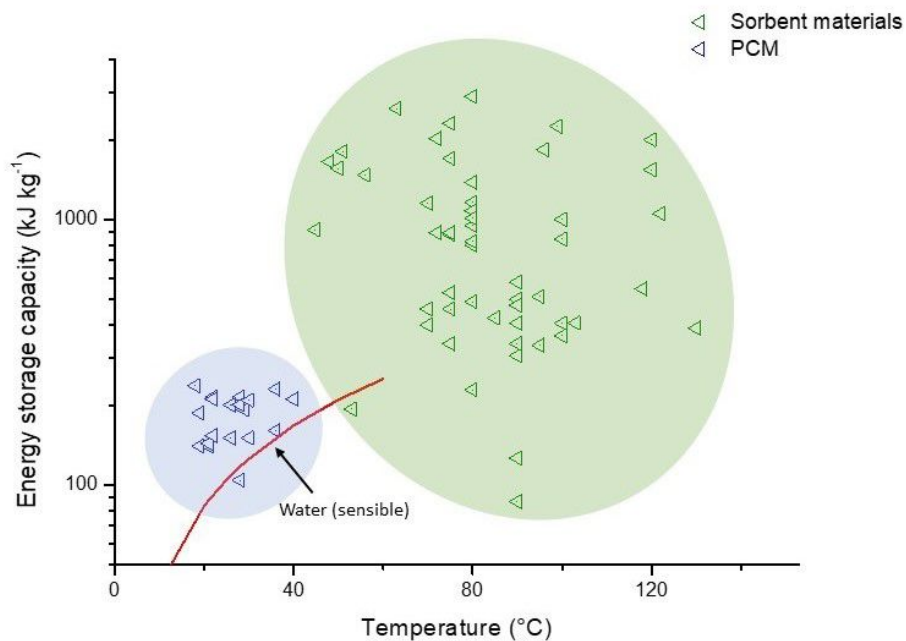


Figure 1.4: Energy storage capacities of PCMs (blue), sorption materials (green) and water (red line). Values of PCMs are taken from [13] while values of sorbent materials are taken from this work).

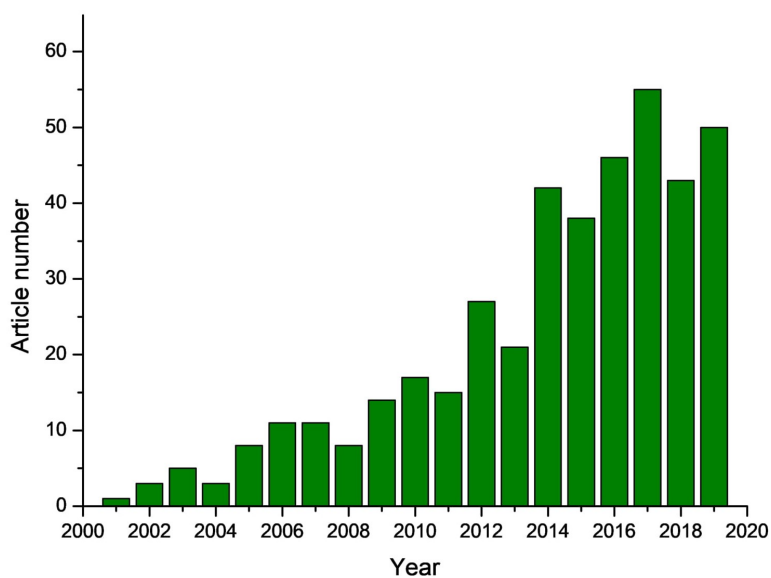


Figure 1.5: Number of publications from abstract and citation database “Scopus”.

The following section presents details about classification and characterizations of the most suitable materials for STES, trying to compare the main promising ones between each other. It must be noted that the state of the art on STES is constantly growing but a standard guide line for the properties and capacities of these systems lacks. As a result, to have a clear comparison between research works is a difficult task. Hence, it is important to have knowledge about the general behaviour and principle mechanism of sorption, such to be able to approach a research work in this scope.

1.2 Sorption thermal energy storage

The protagonist of this type of energy storage is a sorption couple. Under the influence of a certain amount of heat, a compound AB (sorbent + sorbate) is endothermically dissociated into A and B, which can be stored separately without any loss as long as the two reaction elements are kept separately. Hence, this technology is promising for long-term (seasonal) storage systems. Reversely, when A and B are put in contact, under some conditions, component AB is exothermically formed, releasing heat [14]. The mechanism can be represented as follow:



The term “sorption” refers to both adsorption and absorption. A schematic representation of the two mechanisms is reported in Figure 1.6. Adsorption is used when the surface of a solid has tendency to attract and retain molecules of other species (gas or liquid) with which such surfaces come in contact. Absorption is the phenomenon in which the substance is not only retained on the surface but passes through the surface, to become distributed throughout the body of a solid or a liquid [15]. Hence, adsorption is a surface phenomenon whereas absorption is a bulk phenomenon. In adsorption, the concentration of the adsorbed molecules is always found to be greater in the immediate vicinity of the surface than in the free phase while, on contrary, absorption involves bulk penetration of the molecules into the solid or liquid structure by diffusion.

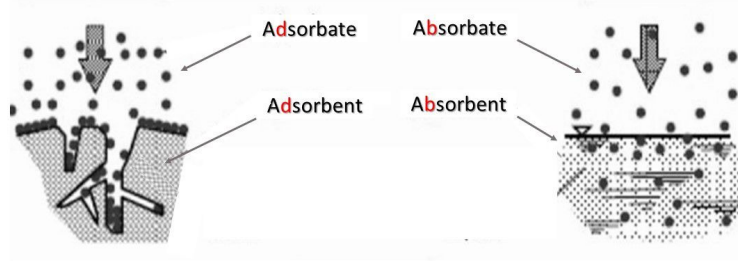


Figure 1.6: Schematic representation of the mechanism of adsorption (left) and absorption (right) [16].

1.2.1 Open or closed systems

A common application considered for the integration of a sorption heat storage system is a family passive-house, which has a space heating and domestic hot water demand, and solar thermal collectors on its roof able to provide the required desorption temperature [17]. Two kinds of systems are possible, closed or open. In closed systems (Figure 1.7), sorbent and sorbate are isolated from the environment. During charging process (desorption), heat from a high thermal source heats sorbent and thus that sorbate phase is desorbed. Q_{ch} is the amount of heat for complete desorption. The desorbed phase is condensed at temperature T_c and then pumped out of the container into a separate tank. The heat of condensation Q_c can be dissipated in the ambient or delivered to the load. When the charging process ends i.e. when the sorbent is completely dehydrated, condenser and reactor are not more connected. During the period of storage, the dry adsorbent and the sorbate are kept separately hence heat is preserved. In the discharging process, sorbate is evaporated (Q_{ev}) and the vapour fluxes into the sorbent material. Since the sorption is an exothermic reaction, heat is released (Q_{dis}). The process can be defined “closed” since the sorbate follows continuously evaporation-condensation cycles, without mass or heat transfer with the environment. Figure 1.8 represents the working cycle of an adsorption heat storage: the red lines represent the charging

phase (desorption) while the blue lines the discharging phase (adsorption). In open systems (Figure 1.9), water vapour (i.e. the sorbate) is directly captured from the environment and the released heat of sorption is directly used to heat air i.e. without the use of closed loops containing a heat transfer fluid. During charging, a hot and dry air flux enters the sorption couple, causing the desorption of the sorbent. Hence, exiting air is cooler and more humid than entering flux. On contrary, during discharging, the humid and cold air flux enters the sorbent material, resulting in the sorption and consequent release of heat. As a result, the temperature of air is increased and its degree of humidity is decreased. The performance of the sorbent material is strictly related to the value of the inlet relative humidity (RH) of air. Helaly et al. have observed the effect of RH on the system performance, thus underlining an increase of ESD with increasing RH% [18]. Both systems present some advantages and disadvantages. Open systems are relatively simple structures, less expensive and easy to maintain. However, since air directly fluxes from the sorbent to the environment, no hazardous materials can be recruited as sorbate. Moreover, the system changes the moisture conditions of the room, perturbing the thermal comfort. On the other side, closed systems can exploit different sorbates, since no heat or nor mass transfer with the environment are likely. In addition, heat of condensation could be recovered. On contrary, the system presents more structural complexity, since heat exchangers are required to provide or extract heat to the sorbent and the evaporator/condenser. As a result, both the cost and the volume of the system increase [4].

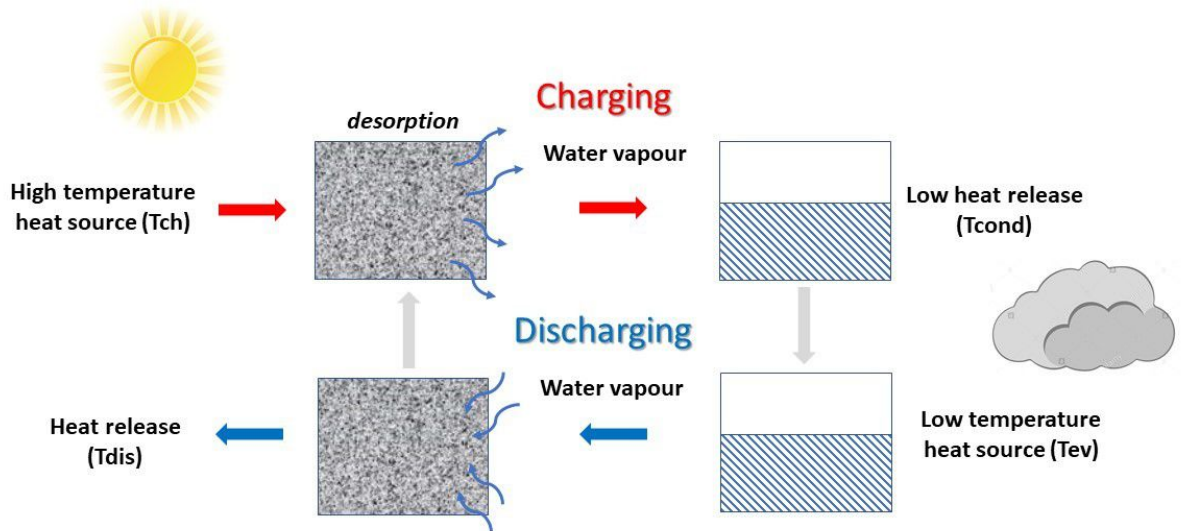


Figure 1.7: Schematic representation of closed systems.

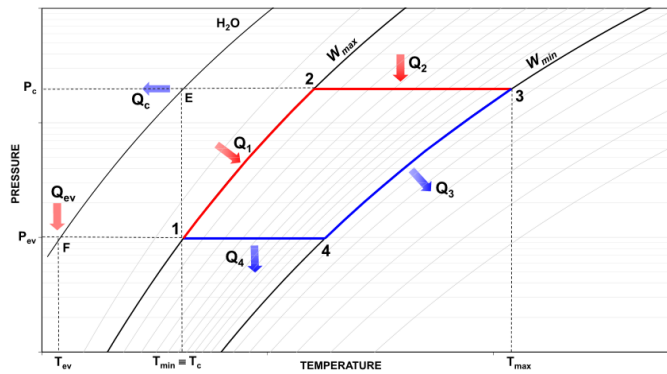


Figure 1.8: Chart representing the working cycle of an adsorption heat storage: red lines represent the charging phase (desorption) while blue lines the discharging phase (adsorption) [19].

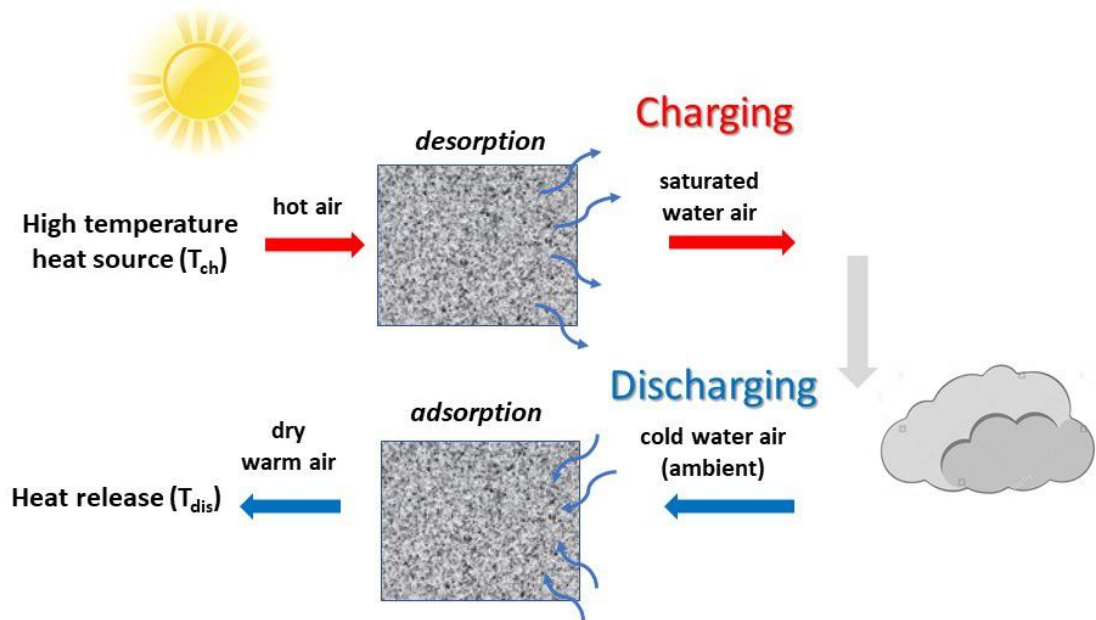


Figure 1.9: Schematic representation of open systems.

1.2.2 Selection criteria and evaluation parameters

Sorption materials are the basis for designing STES systems and their properties strictly define the potential of the system. The main criteria for the selection of materials and the parameters through which materials are evaluated are reported below.

High massive or volumetric energy storage

In the scope of thermal energy storage, the main requirement indicator for a system is the ability to storage energy as much as possible, which is commonly evaluated starting from the sorption equilibrium data for the given sorption couple. It can be referred either to the unit of mass of the sorbent (Energy Storage Capacity, ESC) or to the unit of volume of the sorbent (Energy Storage Density, ESD). Both

parameters can be used for the characterization of the sorption couple in laboratory, following the relation below:

$$\text{ESD} = \text{ESC} \cdot \rho$$

where ρ is the density of the sorbent. It must be noted that, by comparison, one material could have higher value of ESC but lower value of ESD than another one, depending on the density of both materials. However, which parameter will be considered in the selection of the material for thermal storage will depend on the application of the energetic system. Mass is important in terms of cost of the material and weight of the system. Volume, instead, plays a key role when the system has to be placed in a restricted place or if the cost of containing and maintaining working conditions is high. Not always, however, both parameters are declared, thus the comparison between materials is not always complete.

Low charging temperature (desorption)

During charging, heat source causes the dissociation of sorbent and sorbate, which will be stored separately until the stage of discharging. The amount of heat, i.e. the temperature required for charging, depends on the properties of the sorption couple. As can be deduced, the lower the temperature of charging, the lower the amount of energy that must be spent i.e. the higher is the efficiency of the solar collectors. Generally, solar collectors reach 150 °C, hence a charging temperature below that value is required [17].

Large thermal conductivity

In order to ensure the efficiency of the system, thermal conductivity of the material is an important parameter to evaluate. The sorbent, indeed, might be able to exchange heat with a heat transfer fluid. The requirement of proper heat conduction ability is still a challenge. First, in case of solid sorbents, the sorption ability of the material is generally favoured by maximising the porosity of the structure which in turn hinders the thermal conduction. Hence, it is necessary to find a compromise, ensuring a good thermal conductivity without being at the expense of other properties. Also hydrated salts, suitable candidates as sorbents, have intrinsically low thermal conductivity [20]. One possible solution provides the addition of conductive particles, which enhance the ability of thermal conduction

of the system.[21]. Such kind of measurements, however, are relatively rare and are scattered throughout the scientific and technological literature. Lele et al. summarized the working principle of the two main methods of evaluation of the thermal conductivity, differential scanning calorimetry and radial flow apparatus, called guarded hot cartridge [22].

Thermal and chemical stability

Minimum deterioration in performance or degradation of the working material with repeated cycling is always desirable. It ensures a performance of quality during application and a long life-time of the material, thus minimizing the impact of investment with years.

Low cost and high availability

Taking into account the availability and commercial price is mandatory when evaluating the feasibility and scalability of a system. Highly performant but also dramatically expensive materials do not offer a reliable solution for the low temperature - thermal energy storage.

1.2.3 Classification of sorbents

Yu et al. [23] proposed the classification of sorption materials for storage distinguishing between four different categories: liquid absorption, solid adsorption, chemical reaction and composite material. The typical parameters for each class are reported in Table 1.1. The following part is dedicated to the explanation of the main working principles of each category of sorbents while a comparison between their performances is proposed in Section 1.2.4.

Liquid absorption

In case of liquids, the mechanism of storage is based on absorption of a fluid (solvent) into a liquid (solute), thus forming a solution whose concentration changes during the whole cycle. In particular, the temperature of the solution changes with the concentration, where the vapour pressure of the sorbate is kept constant. A comprehensive analysis of liquid adsorption solution was made by Hui et al. [24], where the mechanism of sorption and several examples are pointed out.

Category	Temperature of charging [°C]	Energy Storage Density [MJ kg ⁻¹]
Liquid	40-150	190-4400
Solid	90-160	35-950
Salt	50-190	1500-2240
Composite	75-150	340-2800

Table 1.1: Typical values of charging temperature and Energy Storage Capacity of the four categories of sorbent materials: solids, liquids, chemicals and composite materials.

The working cycle in case of seasonal storage is close to what is described for a closed system and it is roughly the following. During summer, the solution with low mass fraction of absorbent (named poor solution) flows from the solution tank to the generator, where it is heated up by the collected solar energy. When heated, the sorbate is vaporized and transferred to the condenser, where it is condensed and releases its latent heat. The latter can be released or, sometimes, can be exploited to heat water. The sorbate, in the condensed form, is stored in the sorbate tank. The remaining solution, which is characterized by high mass fraction of absorbent after the desorption of the sorbate (named rich solution) flows back to the solution tank. For the period of storage, no mass or heat transfer are possible. During winter, the sorbate is evaporated and, following the solution thermodynamic equilibrium, is absorbed by the rich solution. During absorption, heat (Q_{abs}) is released to satisfy the energy requirement for house heating. The cycle ends by returning of the poor solution to the solution tank. Depending on the configuration of the system and the nature of the absorbate-absorbent, the liquid solution can reach the crystallization point. In Figure 1.10, the seasonal solar energy storage cycle of LiBr/H₂O is represented. If crystallization is avoided, P(T) follows the blue line and the main steps are the following:

- 1 → 2: poor solution is heated up by solar energy, keeping the absorbent concentration constant
- 2 → 3: the solution is heated and the absorbate is desorbed from the solution, following the solution thermodynamic equilibrium
- C: the desorbed absorbate condensed

- 3 → 5: during storage, the solution at state 3 is cooled down to state 5, at the temperature of ground i.e. where the storage tank is placed
- 5 → 6: the solution absorbs the vapour from the evaporator, the mass fraction of the solution decreases and its pressure increases until it is equal to the pressure of evaporation (point E)
- 6 → 7: heat is used to satisfy the heating energy requirements and the solution leaves the absorber after the absorption
- 7 → 1: the solution goes back to the solution storage tank

If crystallization is not avoided, P(T) follows also the additional orange path. The mass fraction of absorbent at 3' is higher than that at 3. During the storage, P(T) crosses the crystallization line at state 4 and crystals appear in the solution tank and growth until state 5. It must be pointed out that the presence of crystals requires higher complexity of the system. However, it allows the reduction of the volume of the material i.e. the cost of the system.

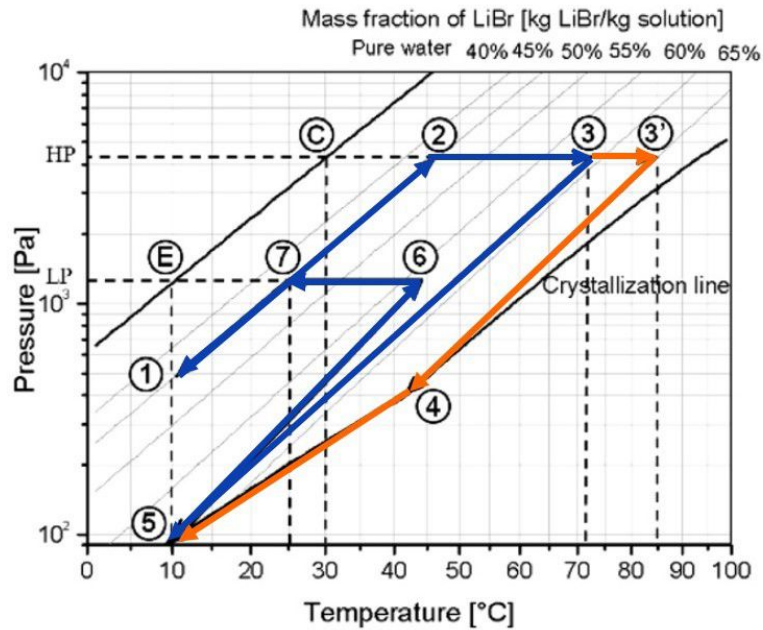


Figure 1.10: P(T) curve representing the seasonal solar energy storage cycle of LiBr/H₂O [24].

Generally, the heat transferred from state i to state j can be calculated by the energy balance following Equation 1.1, without considering the power delivered by the pumps between the tanks and the heat exchangers:

$$Q_i = m_j h_j + m_{vap,i} h_{vap,i} - m_i h_i \quad (1.1)$$

in which $h_{vap,i \rightarrow j}$ is the enthalpy of evaporation of absorbate that is evaporated from the solution [24]. The solar energy required for the dehydration is $Q_{1 \rightarrow 3}$ or $Q_{1 \rightarrow 3'}$; while the heat of absorption corresponds to $Q_{5 \rightarrow 7}$.

Some considerations can be done when choosing the proper absorbent-absorbate couple. First, it must present a large amount of Q_{abs} , thus offering high values of ESD or ESC. Moreover, as previously said, the temperature of desorption of the absorbate from the absorbent might be minimized, to maximize the efficiency of solar collectors. In this case, the temperature of collectors decreases with decreasing the temperature of condensation. On the other end, absorption might be happened at a high temperature and the temperature of absorption increases with increasing the temperature of evaporation. Since decreasing the temperature of condensation and increasing the temperature of evaporation are in contrast to each other, the choice of the sorption couple needs a compromise between the two. Moreover, security parameters (health, flammability, reactivity etc.) and low investment cost might be taken into account.

Examples of the main used liquids for STES are reported in Figure 1.11 (ESD vs T of charging) and Figure 1.12 (ESC vs T of charging); additional information are reported in Table 1.2.

Material	Price [€/tonn]	Tc [°C]	Td [°C]	Additional information	Water uptake [g/g]	ESD [MJ/m ³]	ESC [MJ/kg]	SCC [€/kWh]	Ref.
CaCl ₂ /H ₂ O	160	44,8	20-45	Tc=30 °C, Te=10 °C	0,398	429	0,91	0,6297	
Glycerin/H ₂ O		53		Pads=1.2 kPa, Pdes=5.6 kPa	0,9	180	0,193		
H ₂ O/NH ₃		155,5			0,9	352	1,32		
KOH/H ₂ O	1200	63			0,508	1125	2,618	1,6488	
LiBr/H ₂ O	5500	72			0,588	1125	2,02	9,7990	
LiCl/H ₂ O	2700	65,6			0,443	1440	4,39	2,2139	
NaOH/H ₂ O	400	50			0,335	554,4	1,56	0,9235	

Table 1.2: Performances of liquid sorbent materials for STES systems.

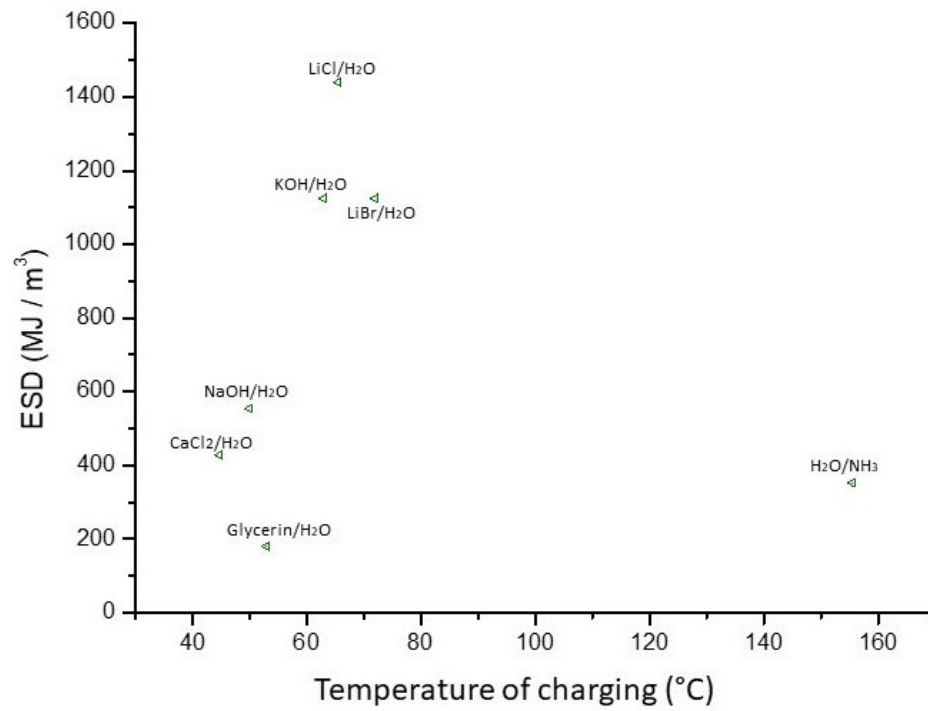


Figure 1.11: Chart reporting the values of Energy Storage Density of the main liquid sorption materials.

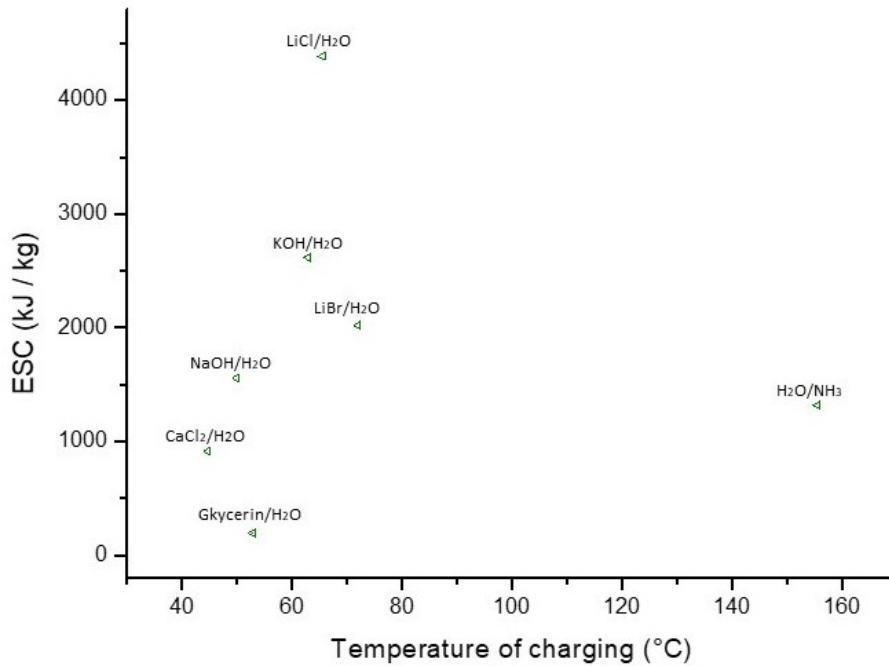


Figure 1.12: Chart reporting the values of Energy Storage Capacity of the main liquid sorption materials.

Solid adsorption

Solid systems are based on adsorption, i.e. the interaction between the surface of a solid (adsorbent) and the molecules of a fluid (adsorbate) (Figure 1.13).

The mechanism is driven by the unbalance of forces for surface atoms, which can't completely saturate their bonds. Depending on the nature of oncoming gaseous molecules and solid surface, two types of adsorption, physical or chemical, might be distinguished. *Physisorption* is performed by weak Van der Waals forces, generating relatively low heat of sorption (low than 80 kJ per mol of sorbate [25]). The phenomenon does not require any activation energy and it is generally easy to reverse by simply application of heat and/or vacuum. It can become irreversible in case of capillary condensation. When the adsorbent has a porous structure, indeed, pore spaces become filled with condensed liquid. Due to an increase of the number of Van der Waals interactions between vapour phase molecules inside the confined space of a capillary, condensation can occur below the saturation vapour pressure.

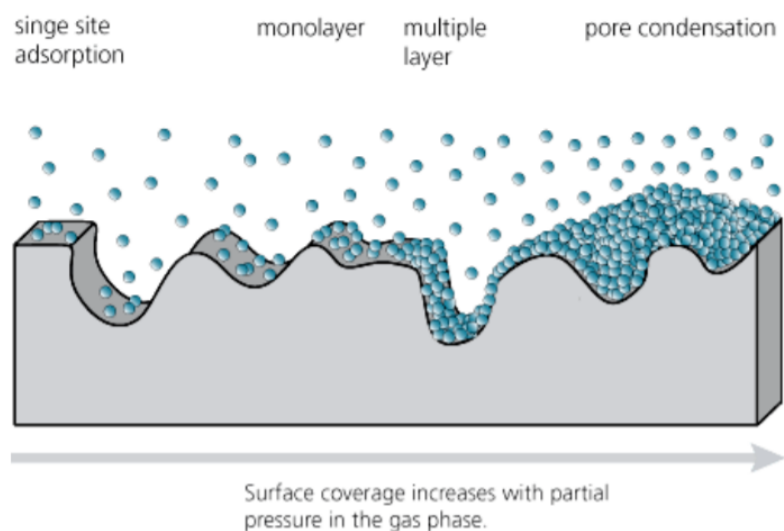


Figure 1.13: Schematic representation of the mechanism of adsorption, with the formation of monolayer, multilayer and pore condensation [26].

As a result, during desorption, lower values of pressure are required to remove the sorbate. In most cases, heat storage systems exploit physical sorption of porous solid materials. The capacity of the solid for fluid adsorption depends on its pore system geometry, and the chemical properties defining the fluid-solid interaction [27]. If chemical bonds (i.e. hydrogen bonds) are involved, the phenomenon is defined *chemisorption*. It is accompanied by much higher heat effect, which depends on the nature and strength of the chemical bond between the adsorbent and the adsorbate. The main factors determining the amount of the substance adsorbed on the surface of the adsorbent at equilibrium are temperature, pressure and the specific surface area (SSA) of the solid. About the latter, it is clear that the higher is the specific surface of the adsorbent, the higher number of molecules can be entrapped on it. In case of chemisorption, where the development of chemical bonds between adsorbent and adsorbate requires the direct contact of the two phases, only a single layer of gaseous molecules can be formed on the free solid surface hence the number of adsorbed molecules is directly proportional to SSA. In case of physisorption, instead, gaseous molecules can overlap to the others, forming a multilayer structure. The extension of SSA increases from non-porous materials

to microporous materials. It must be pointed out that microporous materials suffer the risk of size exclusion effect i.e. only small particles pass through the pore structure [28]. However, it has to be considered only in case of the competition of different sized molecules. On the other side, microporous structure might not perform capillary condensation (typical of mesopores), which cause an increase of the mass transfer resistance. The phenomenon of adsorption is usually represented by isotherm, isobar or isostere curves. Representative examples are reported in Figure 1.14.

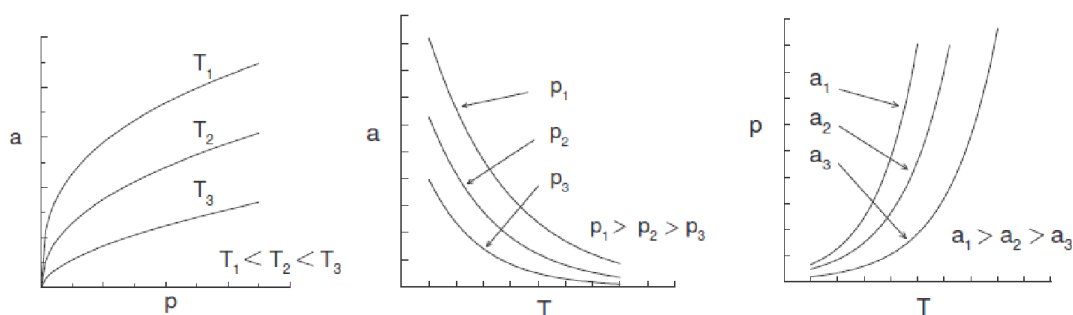


Figure 1.14: Ideal representation of isotherm, isobar and isostere curves. [29]

The study of adsorption of gas molecules on a porous solid surface is generally to be done using the so-called Brunauer–Emmett–Teller (BET) theory, which is also the basis for the analysis technique of measurement of SSA [30]. The theory suggests that one can plot the adsorbed gas quantity (for examples in terms of volume) with respect to its pressure. According to the morphology of the porous structure, five curves can be distinguished (Figure 1.15). Curve I is specific for the situation of formation of only a single layer of gas molecules, directly in contact with the surface. As is possible to see, the curve presents a very steep initial portion, approaching a limiting adsorption saturation loading at medium relative pressure (P/P_0). Adsorbents displaying this type of isotherm present high affinity with gaseous molecules hence the adsorption happens fast but it is limited by reaching the complete coverage of the solid surface. Therefore, the saturation value is controlled by the accessible pore volume. For curves II, III, IV and V, the adsorption phenomenon is not limited by monolayer formation i.e. multilayers of gaseous molecules form while increasing the pressure. In particular, curve II is typical for non-porous or macroporous materials, while curve III, which is

essentially the inverse of the type I, shows reversible adsorption, that results when the adsorbate-adsorbate interactions are stronger than the adsorbate-adsorbent ones. Curve IV, instead, describes capillary condensation, where the last part of the curve is related to the condensation in micropores (>20 Å diameter), before reaching the saturation pressure.

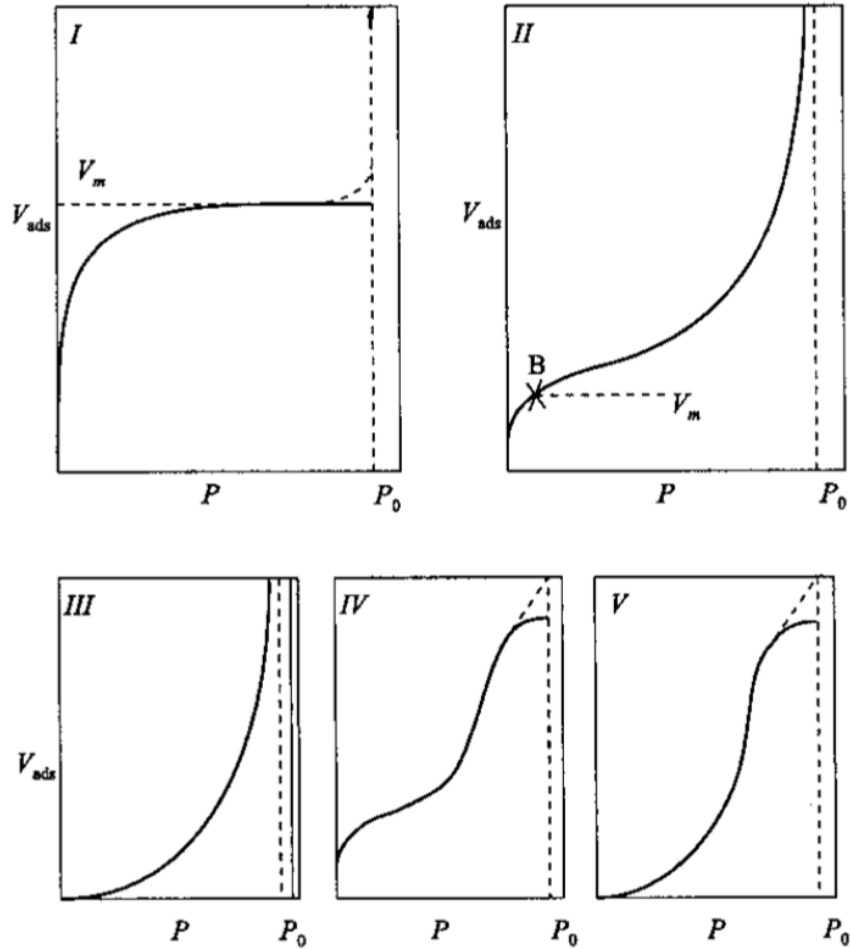


Figure 1.15: Schematic representation of different curves, depending on the morphology of the solid structure [29].

Since the characteristics of an ideal adsorbent strongly depend on the requirements of the process (i.e. temperature of charging or temperature of discharging), there is no “one size” adsorbent for heat transformation applications. Hence, there is a considerable research in the development and testing of novel adsorbents, trying to point out the relationship between adsorbent structure and sorption properties.

The most important figures of merit for a given adsorption material in view of heat transformation applications are the loading spread (i.e. the difference in sorbate uptake between charged and discharged state) and the heat of adsorption, usually expressed with regard to one mole of sorbate (kJ/mol). An additional consideration that must be done when screening different porous sorbents, regards the meaning of hydrophilic or hydrophobic behaviour. Usually, the adjective hydrophilic refers to a high affinity with water. However, in case of porous materials, the water adsorption loading is dictated by pore volume. As a result, the hydrophilicity of a solid adsorbent is determined on the basis of the selectivity of the material for water over other components in a mixture.

The most commonly employed solid materials in thermal storage are silica, zeolite, activated carbon, natural rock and novel porous solids as AlPO (Aluminophosphate), SAPO (silico-aluminophosphate) and MOF (metal organic framework). In the following, each class is briefly presented. It must be pointed out that this work does not pretend to report an exhaustive knowledge about each class of solid sorbents, since a huge number of studies have been carried out about each single material and several reviews have been done to summarize the current understanding in the scope. This part aims to describe the key mechanism of adsorption and the main advantages and limits of each class, without neglecting that its performance can vary between a range by modulating experimental parameters or structural aspects of the material. Thus, the reader will have a key of lecture for comparing different categories. Silica gel, a highly porous, non-crystalline form of silica, is suitable for low cost and low temperature – heat storage applications, thanks to the low temperature of regeneration from 50 °C to 90 °C [31]. Porous silica gel, indeed, consists of an incompletely dehydrated polymeric structure of colloidal silicic acid with the formula $\text{SiO}_2 \cdot n\text{H}_2\text{O}$. Its surface comprises mainly Si-OH and Si-O-Si groups [32]. Water molecules can be adsorbed on the silanol groups through hydrogen bonding or physically adsorbed by hydrogen bonding between water molecules to form H_2O clusters and eventual water condensation on top of these groups (Figure 1.16). Modelling of the interaction of water with the silica surface was proposed by Fang et al. [33]. According to the authors, at low temperatures (roughly below 160 °C) only physical desorption occurs. Desorption of H_2O bonded to -OH groups, instead, requires high temperatures, until 400 °C. Since the temperature of desorption in the adsorption-desorption cycle for thermal

storage might not exceeds 150 °C, chemical bonds are not involved. As a result, the amount of energy associated with the phenomenon of sorption is relatively low (it usually does not exceed 25 kWh/m³) and the energy storage density could not satisfy the energy demand. In addition, Chang et al. [34] investigated the effect of regeneration time and temperature on the moisture adsorption in packed silica gel beds, checking that the amount of adsorbent increased together with the degree of regeneration. They highlighted the advantage in using modified silica gel, with a microporous structure, instead of commercial silica gel, which generally presents a mesoporous structure, because of the low mass transfer resistance of the first one. As said before, indeed, a mesoporous structure is affected by capillary condensation, which cause hysteresis (i.e. kinetic slowing down) in adsorption-desorption.

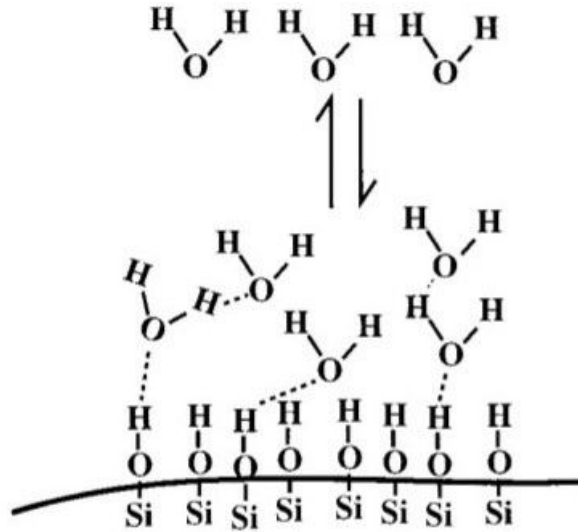


Figure 1.16: Schematic representation of the mechanism of water adsorption upon a surface of Silica [33].

Zeolites are crystalline hydrated aluminosilicates with small pores comparable with molecule in frameworks based on extensive three-dimensional networks of oxygen ions [35]. The ability of large energy sorption density and capacity is due to the higher strength of sorbent-sorbate bond which characterize the zeolite mechanism of adsorption. Besides the morphology of the porous structure (size, SSA and pore volume), the ability of adsorption is strictly related to the Si/Al

ratio. In particular, materials with low Al per unit cell are characterized as being hydrophobic. This is due to the low concentration of hydrophilic protons in the material and the weak interactions of the Si-O-Si with oxygen [36]. However, stronger hydrophilic behaviour do not always mean higher adsorption performances. In order to understand the fundamental relationship between adsorbent microstructure and water adsorption equilibrium, with particular regard to the Si/Al ratio, Henninger et al.[37] performed molecular simulation of water adsorption in various zeolites. By comparing Li-Y zeolites with Si/Al ratio of 2.5, 7 and 11, relative water uptakes (i.e. difference of water amount between adsorption and desorption stages) of 0.24 g/g, 0.34 g/g and 0.37g/g were found. Higher loading lift values with higher Si/Al ratios are due to the lower water loadings at the charging temperature, because of the lower hydrophilicity of the structures with less amount of Al. By analysing Zeolite Na-A, a decrease of water uptake at 150 °C from 0.229 to 0.09 is reported, when passing from Si/Al of 2.49 to 10.29. In addition, the authors found high differences between simulated and experimental data. This is probably due to post-synthetic treatments which seem to cause the partial destruction of the pore structure, as reported [38] [39]. The latter can cause the reduction of water adsorption capacity when compared to the simulation results, as the framework is free of crystal defects. The heat of adsorption increases when small cations (Na, Li..) are introduced into the zeolite structure. Jentys et al. [40] described the surface chemistry of water adsorbed on zeolite and a series of alkali-metal zeolite, exploiting transmission absorption IR spectroscopy for analysis. With traditional zeolite, the shape of the adsorption isotherm of water is of type “I”. This reflects the tendency of the material to have preferential water clustering (i.e. interactions between adsorptive molecules). Thus, interactions among water molecules are of higher strength than the interaction of a second water molecule with the adsorption site, resulting in physisorption mechanism (Figure 1.17). With alkali-metal-exchanged zirconia, instead, the situation is more complicated. At low pressure, the presence of alkali-metal cations prevents clustering of water molecules i.e. all water molecules are bound to the cations on the solid surface. The interaction of the second, third, or fourth water molecule with the alkali-metal cation is stronger than the interaction among the water molecules themselves hence chemisorption is favoured than physisorption (1.18). As a result, the ability of adsorption increased. Finally, at higher equilibrium pressures, a second shell of water starts to build up. Janchen et al. in

2003, investigated and confirmed the improvement of the storage properties by ion exchange with physico-chemical methods such as thermogravimetry, differential scanning calorimetry, microcalorimetry and isotherm measurements. Then, they pelleted and tested selected materials in a lab-scaled storage, founding 536 kJ/kg for Zeo-NaX and 630kJ/kg for Zeo-MgNaX [41]. It must be remembered, however, that large strength of sorbate-sorbent bonds causes high regeneration temperature. For Zeo-NaX and Zeo-MgNaX, a charging temperature of 180 °C was necessary. Hence, when modifying the chemical structure of a zeolite, a compromise of water sorption capacity and temperature of regeneration is mandatory. An energy storage with 7000 kg zeolite 13X was installed in a school building in Munich, Germany, by 1996 and connected to the district heating system and an energy density of 124 kWh/m³ was experimentally obtained [42]. Investigating chemical heat storage technologies for low-temperature applications through a laboratory test rig, the Institute for Thermodynamics and Thermal Engineering (ITW), University Stuttgart reported values of 450 MJ/m³ (643 kJ/kg) and 353 MJ/m³ (504 kJ/kg) for zeolite 4A when the temperature of charging is 180 °C or 150 °C respectively [43]. Recently (2020), Wu et al. tested the potential use of commercially available 13X zeolite, modified by ion-exchange with cerium compensating cations, in view of low-temperature storage of solar energy. Moreover, Monte Carlo simulations were used to determine the limit values of the amount adsorbed and differential heat of adsorption, which could be obtained experimentally if the zeolite samples were completely dried. In order to maintain the stability of the zeolite structure, a charging temperature of 80 °C was chosen. Good performances have been found. However, a loss of the energy storage capacity of 25 per cent and 36 per cent for zeolite and Ce-exchanged zeolite respectively (from 800 kJ/kg to 600 kJ/kg and from 1100 kJ/kg to 700 kJ/kg) was recorded, proving that zeolite needs higher charging temperature to completely desorb water [44].

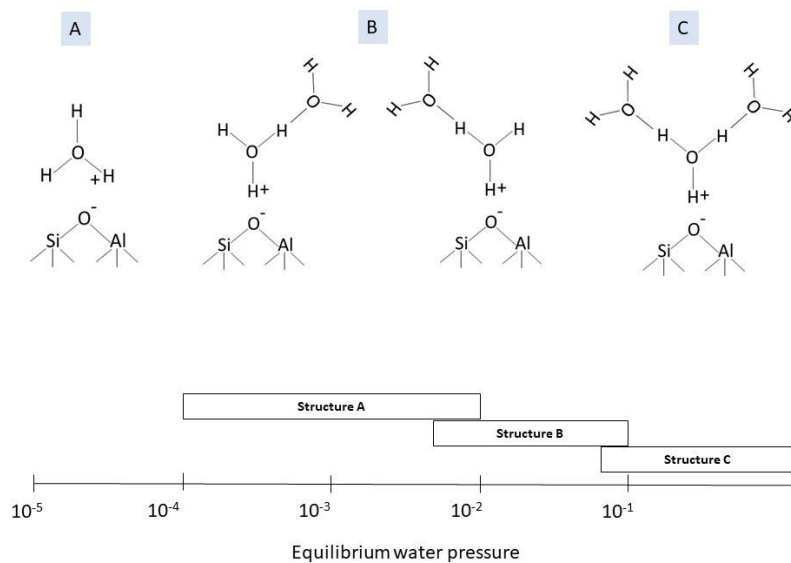


Figure 1.17: Schematic representation of the mechanism of adsorption upon the surface of a Zeolite. Taking inspiration from [40].

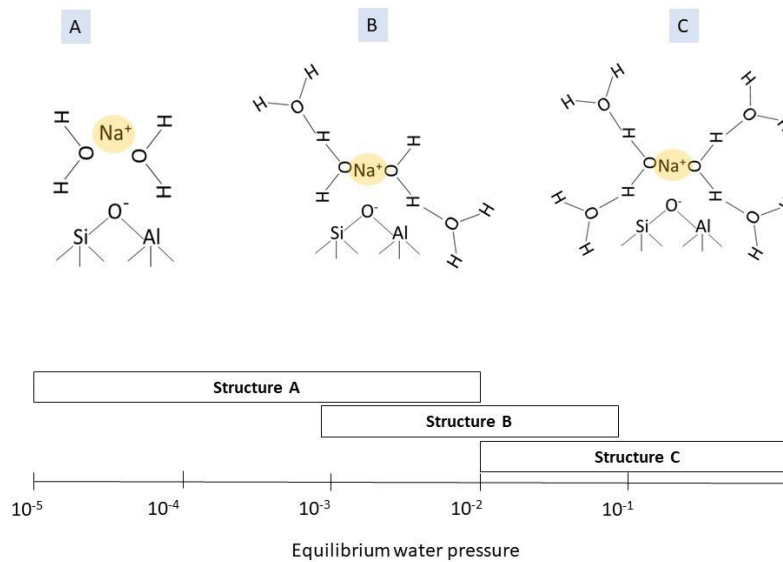


Figure 1.18: Schematic representation of the mechanism of adsorption upon the surface of a Zeolite in the presence of cations. taking inspiration from [40].

Aluminophosphates (AlPOs) are the isoelectronic analogues of silica-zeolites, reported for the first time by Wilson et al at Union Carbide Corporation in 1982 [45]. The basic building units are made of AlO_2^- and PO_2^+ , forming AlPO_4 . They are alternatively distributed, generating a neutral 3D-framework with well defined channels or cavities of the size of small molecules [46]. AlPO molecular sieves cover a wide range of different structure types, which are denoted with the number “n” following the acronym AlPO. In addition, most of the structures have been assigned a three-letter framework structure code by the International Zeolite Association’s Structure Commission. The code describes the structural landscape, that is independent on the chemical composition and several databases, such as [47], collect all possible structures. From AlPOs, it is possible to introduce new atomic elements into the structure. In particular, by substituting Si atoms for P atoms, SilicoAluminoPhosphates (SAPOs) are synthesized. Si atoms can replace P atoms at isolated tetrahedrally sites or may aggregate in large assemblies, forming Si-islands. the substitution introduces Bronsted acids (i.e. species capable of donating a proton) into the AlPO-based molecular sieves. Sparked by the potential use of AlPOs and SAPOs in heat transformation applications, a number of researchers have investigated the adsorption of water in these systems. These materials present S-shaped water adsorption isotherms and isobars, a feature that is attractive because a large loading of sorbate can be reached upon a moderate change in pressure and temperature. A sigmoidal course of an adsorption isotherm is generally caused by lateral attracting interactions between the adsorbed species. It is identical with type V of the IUPAC classification [48]. In particular, Henninger et al. [37] reported that, in comparison with traditional zeolites, AlPOs show a step-gradient of relative water uptake in a very narrow temperature range, with more advantages for thermal storage applications than the larger isobars of classical zeolites (Figure 1.20). The energy analysis made by Poulet et al. [49] showed that the stability of the hydrated structure of $\text{AlPO}_3\text{H}_2\text{O}$ is not created by the individual interaction of water molecules with the AlPO_4 channel but is ensured by the formation of a collective hydrogen-bond network. This explains why the system shows an abrupt transition between an empty and a full phase with 12 water molecules per unit cell. By comparative thermogravimetric and calorimetric studies, Ristić et al. highlighted the performance of different microporous aluminophosphates, correlating this with their structural features. In particular, they explore the role of the morphology

of pores, pointing out that regular elliptical cages ensure low relative pressures for water adsorption than elliptical, pear-shaped pores [50]. The presence of dopants in AlPOs, thus forming SAPO molecular sieves, seems to enhance the water sorption capacity because structural defects enable better interactions of polar water molecules with the surface. In particular, the gradual water uptake is governed by the presence of randomly distributed Si in the framework. Si^{4+} atoms usually replace P^{5+} in the aluminophosphate structure, leading to the formation of highly acidic bridging OH groups (Si-OH-Al), which are supposed to be the primary sites for adsorption [50]. Who stands the better sorption capacities between AlPOs and SAPOs, however, is an hard issue. Several works, indeed, pointed out the thermal instability of SAPO materials, which make them less attractive for STES systems, where a reasonable cyclability is appreciated. Ristic and coworkers reported significant hydrolysis of SAPO-34 in water, along with the formation of an amorphous phase after six months. In addition, they emphasised a transfer from the framework acidic -OH group to water, with the formation of H_3O^+ . In the end, SAPO-34 requires 140 °C of charging temperature, while AlPO molecular sieves can good perform with charging at 95 °C . On the other hand, Baver et al. have studied the stability of AlPO and SAPO molecular sieves by in-situ XRD measurements [51]. They found that the incorporation of silicon and hence the hydrophilicity of SAPO34 is crucial in terms of stability. In particular, high silicon content (e.g. SAPOs) causes fast irreversible structural degradation while low silicon content (e.g. AlPOs) determines complete reversible structural changes, ensuring the structural integrity. However, it must be pointed out that the thermal degradation of SAPO34 is well known and several studies have been done in the scope. In particular, Henninger et al. in 2010 experimentally demonstrated that water adsorption properties strongly depend on the sample preparation. In detail, SAPO34 synthesis with morpholine as template shows a certain degradation of the material after some cycles. As a result, SAPO34 has found to have a high load and good stability or a loss of 25 % over 6 cycles, as reported in Figure 1.20, depending on the method of preparation [52]. On the other side, older researches have demonstrated that SAPO34 is affected by a loss of crystallinity under water adsorption. Samples containing Si islands can restore their crystallinity after a prolonged exposure to humidity, whereas samples with isolated Si- lose their crystallinity irreversibly, because of the increased likelihood of the hydrolysis of

Si-O-Al linkages [53] [54]. Recently, Fischer et al. studied the interaction of different models of SAPO34 with water was studied using dispersion-corrected density-functional theory (DFT-D) calculations [55]. They confirmed that due to the positive influence of Si-islands on the stability of the material, synthesis routes or post-synthesis treatments that lead to the formation of Si-islands must be favoured when targeting SAPO34 for material adsorption. In the end they pointed out the negative influence of defects on the structure, confirming the crucial role of the SAPO atoms structure in the definition of its performance, in comparison with AIPO molecular sieves.

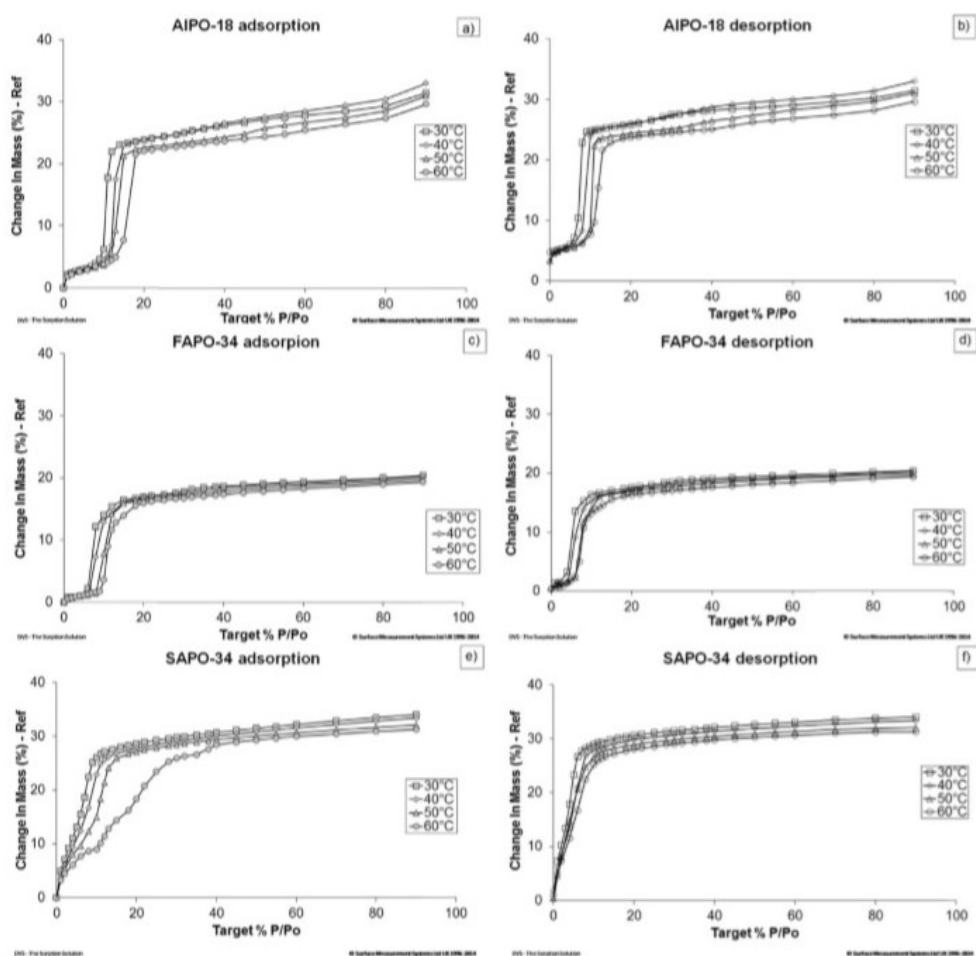


Figure 1.19: Adsorption/desorption isotherms at 30 °C, 40 °C, 50 °C and 60 °C measured for the adsorbent materials: a-b) AIPO-18; c-d) FAPO-34; e-f) SAPO-34 [56].

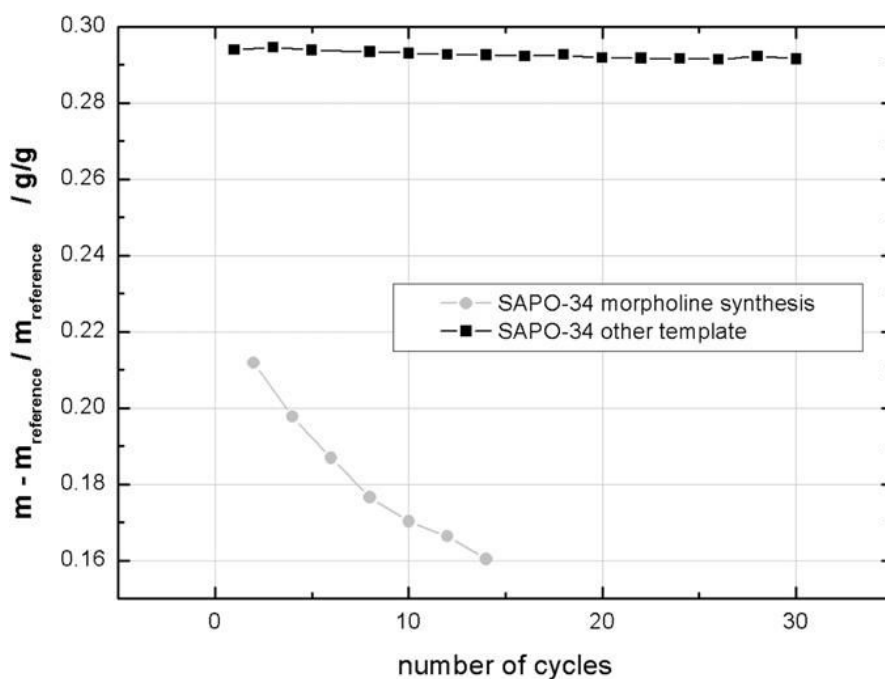


Figure 1.20: Plot of the material degradation with regard to the number of cycles [57].

Metal-organic frameworks (MOFs) are organic-inorganic hybrid crystalline porous materials that consist of a regular array of positively charged metal ions surrounded by organic 'linker' molecules. The metal ions (usually named inorganic Secondary Building Units, uSBU) form nodes that bind the arms of the linkers (usually named organic Secondary Building Units, oSBU) together to form a repeating, cage-like structure (1.22). Since different metal centres and ligands can be selected to produce MOFs as molecular building blocks, a high flexibility for modifying physical and chemical features is possible [58]. Thanks to this hollow structure, MOFs have an extraordinarily large internal surface area, large pore volume and changable pore size [59].

Different types of MOFs can be synthesized. According to the structure, the adsorption on metallic clusters which modifies the first coordination sphere of the metal ion (chemisorption) or layer/ cluster (reversible) adsorption occur. Since the combination of inorganic clusters and organic ligands is virtually infinite, so far about 20,000 different MOFs were synthesized. The good adsorption ability of MOFs is usually related to the presence of unsaturated metal centres, existing in

the structure, that has been formed after the removal of axial ligands from metal atoms. They are able to attract water molecules, offering extra-binding sites to the guests.

The majority of MOFs present type I isotherm, showing a good affinity with the adsorbate. However, is not surprising if they different curves, as they are also known to exhibit unusual hybrids of the isotherm types. Examples of different isotherm water adsorption curves, with relative considerations about the water physisorption properties of MOFs, are reported in Figure 1.22 [60].

Among all MOFs, widely studied materials for sorption thermal energy storage are MIL100(M^{3+}), where M^{3+} is typically Fe^{3+} , Al^{3+} or Cr^{3+} . They consist on a three-dimensional system of mesopores formed from octahedra of M^{3+} trimers, connected by oxygen atoms from the BTC ligand. They can present both micropores (<8 nm) or mesopores (<30 nm) [61]. The main advantage of MIL100(M^{3+}) is due to the presence of highly charged M^{3+} , which are used to assemble the structure. They cause a strong metal-ligand bond, that result in excellent stability. The water sensitivity of certain MOFs, indeed, has been well documented, and thermal cycling stability is widely considered to be a challenge.

Numerous works are dedicated to the analysis and review in the scope of stability [61] [62] [63], that are leaved to the reader interest.

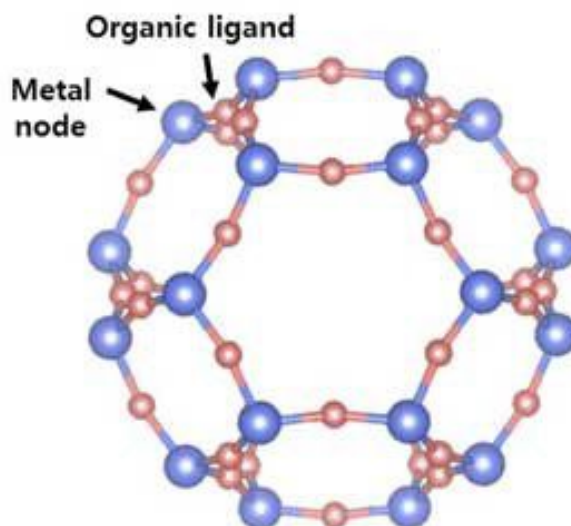


Figure 1.21: Schematic representation of the MOF's structure [59].

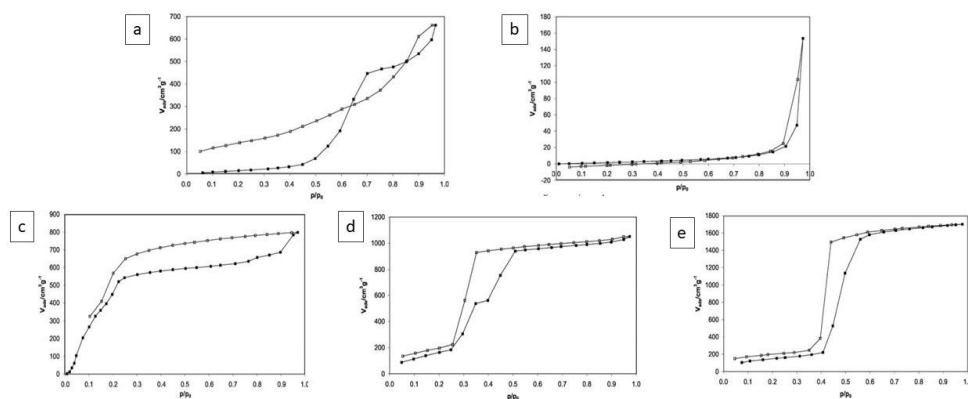


Figure 1.22: Water adsorption (solid symbols) and desorption (open symbols) isotherms of DUT-4 (a), ZIF-8(b), H-KUST-1(c), MIL100(Fe) (d), MIL101 (e) [60].

Besides the four classes of adsorbents detailed above, other materials can be considered for the purpose of adsorption of water vapour.

Among them, *Activated Alumina* (AA) is widely used as sorbent. Carruthers et al [64] proposed five mechanisms of water sorption:

- i) hydrogen bonding between water molecules and surface hydroxyl group
- ii) hydration of cations on surface
- iii) dissociative chemisorption, in case of alpha alumina
- iv) deep hydration of poorly ordered Al^{3+} , originally solvated and not fully coordinated in the ordered structure
- v) hydroxide or oxide-hydroxide formation in depth.

Since chemisorption is generally not involved when the material is used as protagonist of STES, relatively low regeneration temperature is required.

Clays, which are chemically inert, resistant to deterioration and are commercially available in large quantities, have been also investigated as adsorbents. The atomic structure of the clay minerals consists of two basic units, an octahedral sheet and a tetrahedral sheet. The octahedral sheet consists of closely packed oxygens and hydroxyls in which Al is arranged in octahedral coordination. The second unit is the silica tetrahedral layer in which the silicon atom is equidistant from four oxygens or possibly hydroxyls, forming a tetrahedron with Si in the centre. Montmorillonite,

whose belongs to the family of clays, consists of one alumina octa-hedral sheet sandwiched by two silica tetrahedron sheets [65]. The substitution of Fe^{2+} and Mg^{2+} atoms for Al^{3+} in the octahedral layer gives to the overall structure a net negative charge. As a consequence, exchangeable cations, such as Na^+ , K^+ , Ca^{2+} , or Mg^{2+} , are introduced in the interlayer space to compensate the negative charge [66]. When exposed to the water, montmorillonite clay can absorb large quantities of water, until 10 times of its volume. The adsorption energy of water is the driving force against the electrostatic attraction between the negative layers and the cations and the Van der Waals attraction between layers. Hydration-dehydration behaviour of bentonite, an absorbent aluminum silicate clay consisting mainly of montmorillonite, has been widely studied in view of STES [67] [68]. Salles et al. [69] reported that the driving force for hydration of the montmorillonite type clays is generally a function of the nature of the interlayer cation (Na^+ , Ca^{++}), its charge and its size. It must be pointed out, however, that the ability of bentonite of adsorbing large amounts of water could cause problems. Jabbari et al. reported that pure bentonite adsorbs more water than silica gel and alumina at $\text{RH} = 30\%$. According to the authors, this behaviour is most likely linked to the non-rigid structure of bentonite which can host huge quantities of water by swelling out. Even if this brings to higher quantity of heat during adsorption, the swelling is an undesirable phenomenon, which negatively impacts the system [70]. Olphen et al. investigated the adsorption-desorption behaviour of vermiculite clays [71]. The adsorption of water appears to take place in two distinct steps corresponding with the intercalation of the lattice with one and with two monomolecular layers of water. The observed hysteresis of the isotherm is probably due to a retardation of the adsorption process owing to the development of elastic stresses in the crystalline structure during the first penetration of water between the unit layers. However, since the heat of hydration of clays is relatively low while the volume of pores is large, bentonite and vermiculite are usually used as porous host for hygroscopic salts (see part “composites” below). Examples of the main used solid materials for STES are reported in Figure 1.23 (ESD vs Temperature of charging) and Figure 1.24 (ESC vs Temperature of charging). Additional information are reported in Table 1.3, while their commercial price is reported in Table 1.4. It must be noted that the reported values have been obtained for researches through isosteric or calorimetric methods (additional information about the two methods of analysis are reported in

Appendix A) or through open or closed systems. The choice of distinguishing the results with regards to the method of evaluation of the performance stems from the awareness of the energetic losses which affect the sorption cycle of a systems (pressure or thermal losses) , and the results of the second type of analysis, as a consequence. Therefore, the knowledge of through which method the material has been evaluated gives access to a more complete comparison between the adsorbents. Additional information and references are reported in Table 1.3, at the end of the report. For each adsorbent material, where not otherwise defined, water is the sorbate.

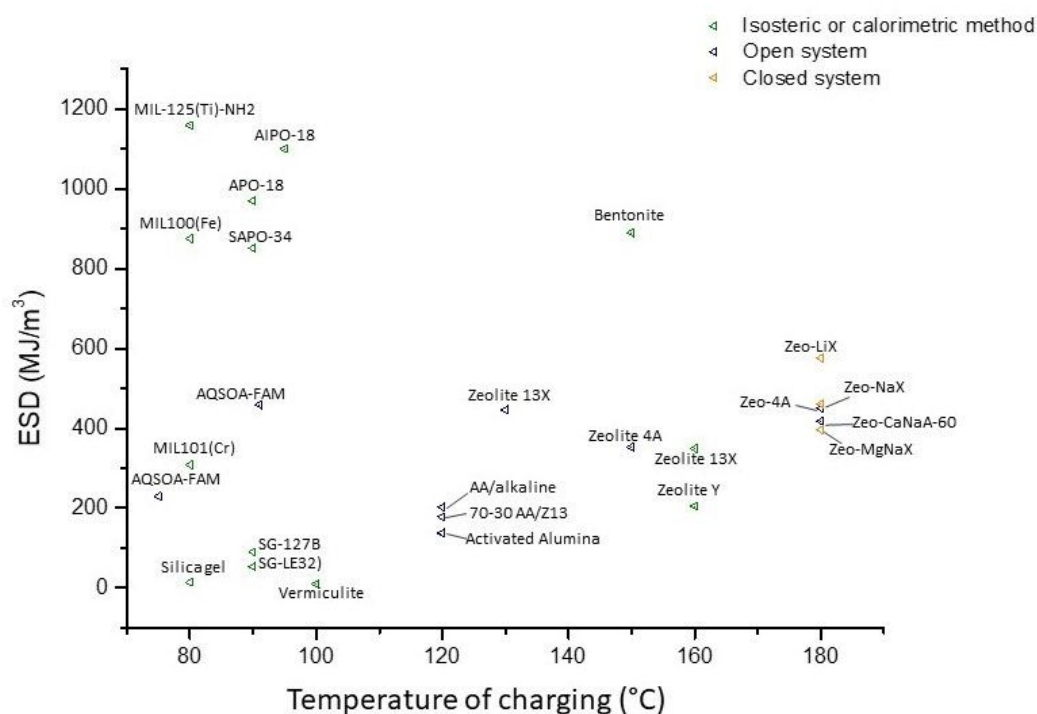


Figure 1.23: Chart reporting the values of Energy Storage Density of the main solid sorption materials.

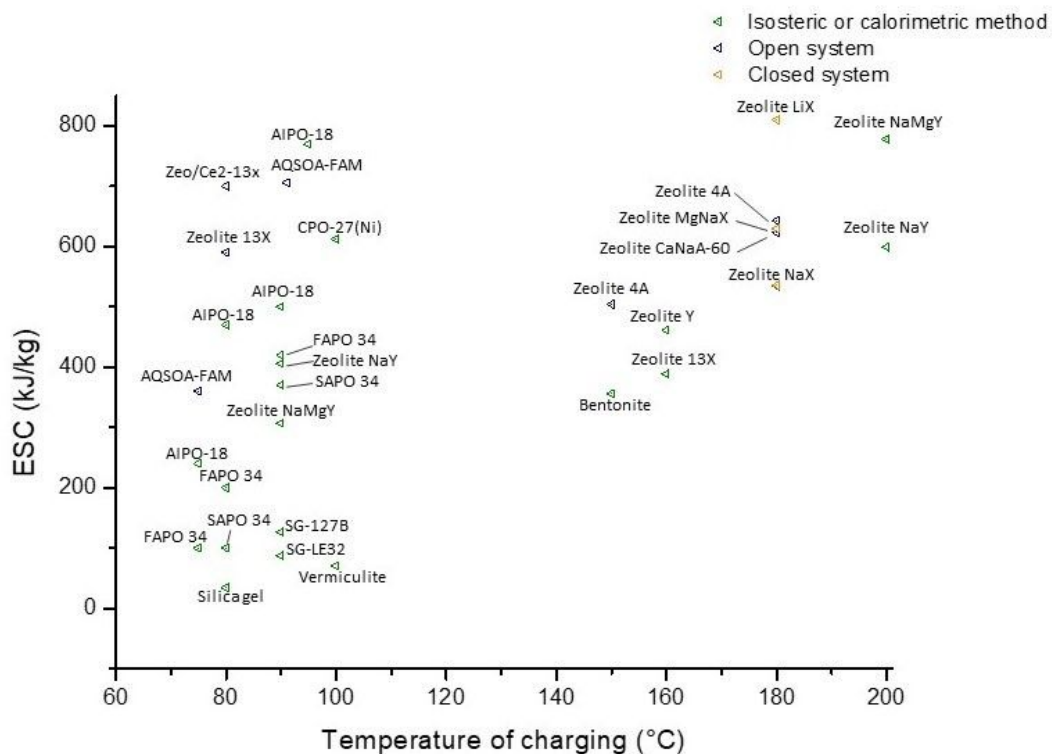


Figure 1.24: Chart reporting the values of Energy Storage Capacity of the main solid sorption materials.

Chemical reaction

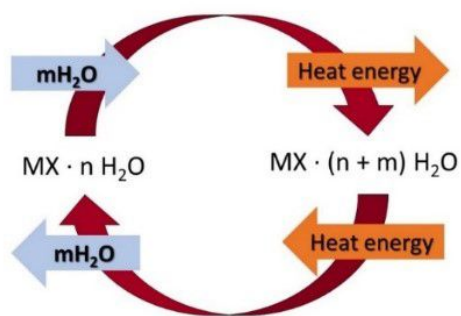
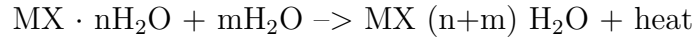


Figure 1.25: Schematic representation of the reaction of salt hydration and dehydration.

Material	Tc [°C]	Td [°C]	Additional information	Water uptake [g/g]	Method of analysis	ESD [MJ/m ³]	ESC [KJ/kg]	SCC [€/kWh]	Ref.
50/50 AA_Z13	120		RH=50%		Open system	137			[72]
70/30 AA_Z13	120		RH=50%		Open system	178			[72]
Activated Alumina	120		RH=50%		Open system	138			[72]
AA + alkaline	120		RH=50%		Open system	203			[72]
AIPO-18	90	35	Tc=30 °C, Te= 10 °C				500	719	[56]
AIPO-18	75	35	Tc=30 °C, Te= 10 °C		Isosteric		240	1499	[56]
AIPO-18	80	35	Tc=15 °C, Te= 5 °C		Isosteric		470	765	[56]
FAPO 34	80	35	Tc=30 °C, Te= 10 °C		Isosteric		200	1799	[56]
FAPO 34	75	35	Tc=30 °C, Te= 10 °C		Isosteric		100	3597	[56]
FAPO 34	90	35	Tc=30 °C, Te= 10 °C		Isosteric		420	856	[56]
SAPO34	80	35	Tc=30 °C, Te= 10 °C		Isosteric		100	3597	[56]
SAPO34	90	35	Tc=30 °C, Te= 10 °C		Isosteric		370	972	[56]
AIPO-18	95	40	Pads=1.2 kPa, Pdes=5.6 kPa		Isosteric		770	467	[57]
SAPO-34	95	40	Pads=1.2 kPa, Pdes=5.6 kPa		Calorimetric		637	565	[57]
AIPO 18	90	35	Pads=1.2 kPa, Pdes=5.6 kPa	0,305	Calorimetric	970			[23]
SAPO-18	95	40	Pads=1.2 kPa, Pdes=5.6 kPa	0,254	Calorimetric	1100			[23]
FAPO 34	90	35			Calorimetric	852			[23]
AQSOA FAM Z02	75	35	Tc=30 °C, Te= 11 °C		Open system	230	360		[73]
AQSOA FAM Z02	81	30	Tc=15 °C, Te= 6 °C		Open system	330	510		[73]
AQSOA FAM Z02	91	35	Tc=15 °C, Te= 10 °C		Open system	459	706		[73]
Bentonite	150	20			Calorimetric	890	356	1,67	[70]
MIL100(Fe)	80	30	Pdes=12.5 kPa		Calorimetric	875			[74]
MIL101(Cr)	80	30	Pdes=12.5 kPa		Calorimetric	309			[74]
MIL-125(Ti)-NH2	80	30	Pdes=12.5 kPa		Calorimetric	1159			[74]
MIL100(Fe)	95	40			Open system		4320	208	
Aluminium fumarate	95	40			Open system		3232	278	[75]
Silica gel (SG-127B)	90	40	Tc=40 °C, Te= 15 °C		Calorimetric	90	126	36	[75]
silica gel (SG-LE32)	90	40	Tc=40 °C, Te= 15 °C		Calorimetric	54	87	51,7	
Silica gel	80	35	Tc=10 °C, Te= 4 °C		Isosteric	14	34	132	
Vermiculite	100				Calorimetric	9,7	70	8,2	[76]
Zeolite 13X	130				Open system	446			[77]
Zeolite 4A	180	65		0,18	Open system	450	643	6,8	[78]
Zeolite 4A	150	65		0,14	Open system	353	504	8,7	[43]
Zeolite CaNaA-60	180		Tc=27 °C, Te= 1 °C	0,162	Open system	418	623		[43]
Zeolite LiX	180		Tc=27 °C, Te= 1 °C	0,244	Closed system	576	810	7,9	[41]
Zeolite MgNaX	180		Tc=27 °C, Te= 1 °C	0,212	Closed system	396	630	10,2	[41]
Zeolite NaX	180		Tc=27 °C, Te= 1 °C	0,192	Closed system	461	536	12,1	[41]
Zeolite 13X	80	23		0,175	Open system		590	9,5	[41]
Zeolite Ce2-13x	80	23		0,15	Open system		700		[44]
Zeolite NaMgY	200	40	Tc=10 °C, Te= 10 °C		Isosteric		778	13,4	[44]
Zeolite NaMgY	90	40	Tc=10 °C, Te= 10 °C	0,418	Isosteric		307	33,9	[79]
Zeolite NaY	90	40	Tc=10 °C, Te= 10 °C	0,335	Isosteric		406	25,7	[79]
Zeolite NaY	200	40	Tc=10 °C, Te= 10 °C		Isosteric		599	17,4	[79]
Zeolite Y	160	40	Tc=40 °C, Te= 5 °C		Calorimetric	205	461	8,3	[79]
MOF-801	100	30			Isosteric		2960		[80]
CPO-27(Ni)	100						612		[81]
MIL125-NH2	90	30	Tc=30 °C, Te= 10 °C	0,42	Calorimetric		1100		[82]

Table 1.3: Performances of the main solid sorbent materials for STES systems.

Chemical reactions for thermal energy storage applications mainly involve hydration/dehydration reactions of salt hydrates, according the following equation:



where MX represents the anhydrous salt (Figure 1.25). Hence, hydration is an exothermic reaction, with the development of heat. Donkers et al. have recently

Material	Price [€/kg]	Material	Price [€/kg]
Zeolite 4	1,2	Silica gel	1,2
Zeolite 13X	1,6	Expanded clay	0,2
Zeolite Y	1,1	Pumice	0,15
Zeolite NaX/LiX	1,8	AIPO	100
Zeolite NaY	2,9	SAPO	100
Bentonite	0,17	FAPO	100
Vermiculite	0,16	MWCNT	4,00
Activated Alumina	0,94	MOF	250

Table 1.4: Commercial price of the main solid sorbent materials for STES systems

performed a literature review, in order to collect and analyse the thermodynamic data of an utmost number of salt hydrates reactions (altogether 563 reactions), thus evaluating the theoretical possibilities and limitations of salt hydrates as thermochemical materials for seasonal energy storage [83]. The working conditions of the system are determined by the phase diagram of the thermochemical material. The phase diagram $P(T)$, indeed, indicates the conditions after which hydration-dehydration occurs. Examples of $P(T)$ during charging and discharging for a closed system are represented in Figure 1.26. During discharging, the initial material in the TCM reactor is MX_mH_2O and the temperature is T_{w1} , meaning that the vapour pressure is $P(\text{state } 2)$. Since the applied condition around the material is above the equilibrium line between $MX \cdot mH_2O$ and $MX \cdot nH_2O$. MX_nH_2O hydrates into $MX \cdot mH_2O$, and the temperature of the system increases, since the reaction is exothermic ($2 \rightarrow 3$). At temperature around T_h both phases, $MX \cdot mH_2O$ and $MX \cdot nH_2O$, can exist. Since the vapour pressure must remain constant, the temperature of the water vessel in the system has to be kept constant i.e. the evaporation heat of water must be overcompensated by heating water with the help of heat exchangers (3). During charging (desorption) a certain temperature T_d is applied to the material with a heat exchanger and the vapor pressure applied to the system by the material is equal to P_d (6). As long as this vapor pressure is higher than that of the water vessel, the material will dehydrate. Since the reaction of dehydration is endothermic, the temperature decreases until $T_{w2}(6 \rightarrow 7)$. Water in the gas phase will condensate in the water vessel, which must be cooled down in order no overcompensate the heat of condensation.

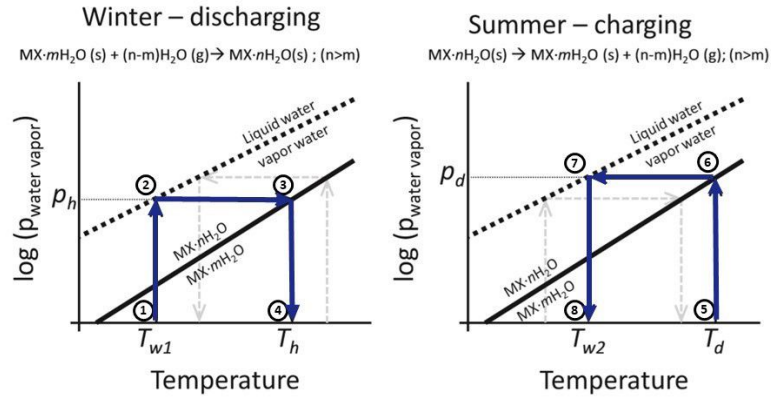


Figure 1.26: Curve of $\log(P)$ with respect to temperature, representing a common cycle of charging (right) and discharging (left) for a typical sorption thermal energy storage system with hydrated salts [83].

Several factors must be considered when selecting the proper thermochemical material. ESD and ESC might be as high as possible. However, the heat storage system performance only partially depends on the material storage capacity, since the choice of the system (open or closed) affects the effective storage performances. In addition to hydration and dehydration temperatures, which are key parameters for all sorbent materials, the volume variation during hydration, the temperature of melting, price and safety, chemical stability. Beside hydrated salts, NH_3 -salt couples are sometimes chosen as thermochemical storage materials [23]. As is possible to see from the graphs, they present high values of energy storage density. However, they can be used only in case of closed systems, since in open systems sorbate and sorbent are not separated from the environment. Closed systems require additional volume for the condenser-evaporator and for the sorbent-fluid storage, hence they not always meet the reduced-space demand. On the other side, higher additional costs due to the system apart from the active material are required for closed systems then for open ones. Hence, a comparison between hydrated salts and NH_3 -salt couples cannot be done without considering the specific requirements of the case. Examples of the main used solid materials for STES are reported in Figure 1.27 (ESD vs Temperature of charging) and Figure 1.28 (ESC vs Temperature of charging); additional information are reported in Table 1.5.

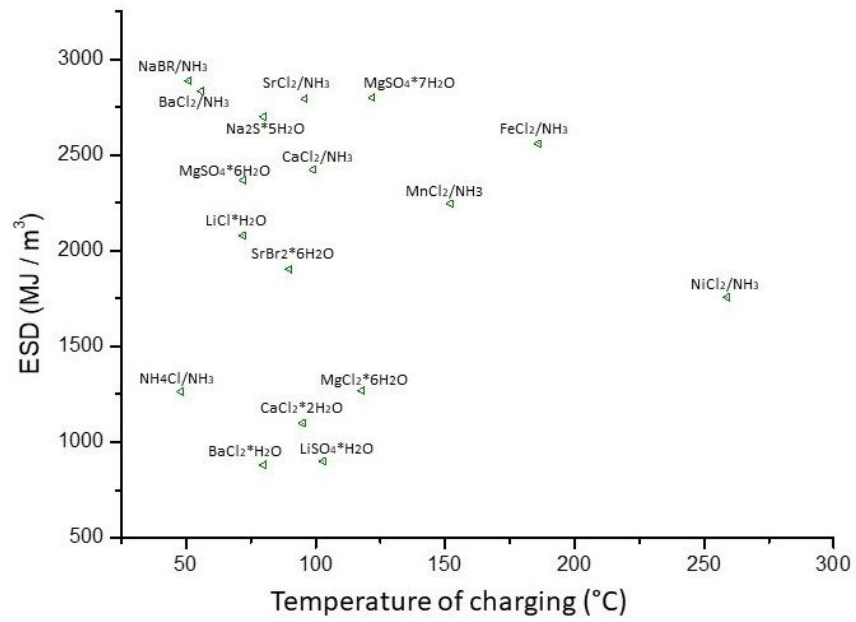


Figure 1.27: Chart reporting the values of Energy Storage Density of the main chemical sorption materials.

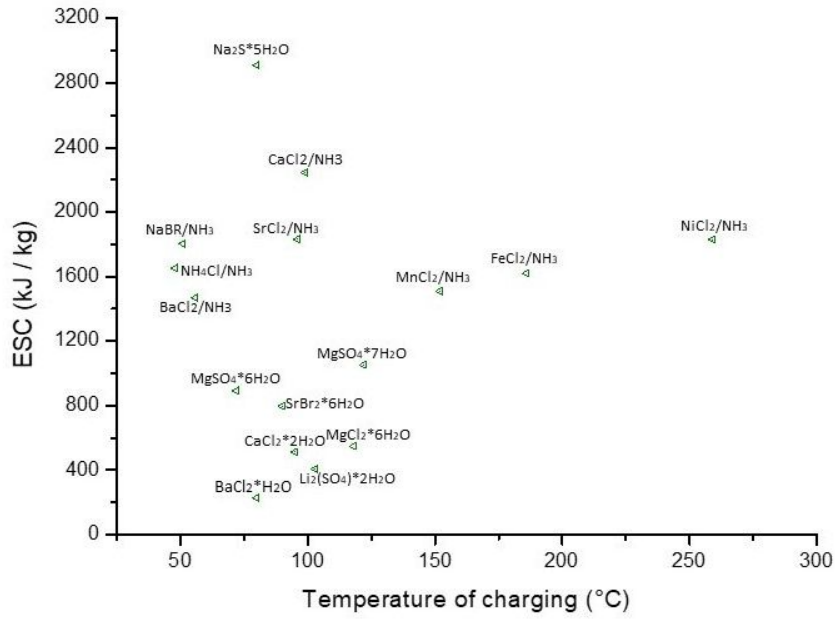


Figure 1.28: Chart reporting the values of Energy Storage Capacity of the main chemical sorption materials.

Material	Price [€/tonn]	Tc [°C]	Td [°C]	Additional information	ESD [MJ/m ³]	ESC [kJ/kg]	SCC [€/kWh]	Ref.
BaCl ₂ *H ₂ O/BaCl ₂	680	80			880	230	10,7	[83]
CaCl ₂ *2H ₂ O/CaCl ₂	160	95	95		1100	510	1,1	
Li ₂ SO ₄ *H ₂ O/LiSO ₄			103		900	410		
MgCl ₂ *6H ₂ O/MgCl ₂ *2H ₂ O	154	118	50		1270	550	1,0	
MgSO ₄ *6H ₂ O/MgSO ₄ *H ₂ O	77	72			2370	890	0,3	
MgSO ₄ *7H ₂ O/MgSO ₄	77	122			2800	1050	0,3	
Na ₂ S*5H ₂ O/Na ₂ S+0.5H ₂ O	348	80			2700	2910	0,4	
SrBr ₂ /6H ₂ O	2400	90			1904	800	10,8	
LiCl/H ₂ O		72			2080	1000		
BaCl ₂ /NH ₃	680	56		Pads=1.167	2833	1470	1,7	[84]
CaCl ₂ /NH ₃	160	99		Pads=1.167	2423	2240	0,3	
FeCl ₂ /NH ₃	845	186		Pads=1.167	2560	1620	1,9	
MnCl ₂ /NH ₃	1936	152		Pads=1.167	2246	1510	4,6	
NaBr/NH ₃	2011	51		Pads=1.167	2887	1800	4,0	
NH ₄ Cl/NH ₃	231	48		Pads=1.167	1264	1650	0,5	
NiCl ₂ /NH ₃	3500	259		Pads=1.167	1757	1830	6,9	
SrCl ₂ /NH ₃	920	96		Pads=1.167	2794	1830	1,8	

Table 1.5: Performances of chemical sorbent materials for STES systems.

Composites adsorption

As seen before, physical porous sorbents offer stable performances but low values of energy density and energy capacity. On the other side, chemical sorbents are characterized by higher storage capacities but the phenomenon of deliquescence, which affects grain stability, might limit their performances. Recently, several authors proposed a family of new working materials for solid sorption, consisting on “hygroscopic salts inside a porous matrix with open pores” [85]. In this case, the porous structure of the host matrix provides numerous gas diffusion paths hence the material performs vapour permeability enough to promote the hydration of salt. In addition, agglomeration of salts is hindered while deliquescence and solution absorption are promoted, since the salt solution can’t leak out from the solid material. As previously seen, the ability of salt adsorption of fluid phase depends on the chemical nature of the salt itself. However, several authors have pointed out that the performance of the sorbent-sorbate couple is not the result of a simple addition of the sorption by the bulk salt and the host material [86], [87]. It was observed that the salt sorption ability increases due to confinement into a microporous matrix, which also hinder the hysteresis behaviour of adsorption-desorption cycles. Hence, it seems that the space-confinement causes changes of the thermodynamic of the salt solution. However, in current literature, no satisfactory explanations have been found. Moreover, how porous host and salt behave when combined strictly depends on the nature of both components and the external working conditions. Hence, a deep research on it for each specific case is required. In Figure 1.40, the charging/discharging mechanism of the material is schematically represented and the main steps are described below.

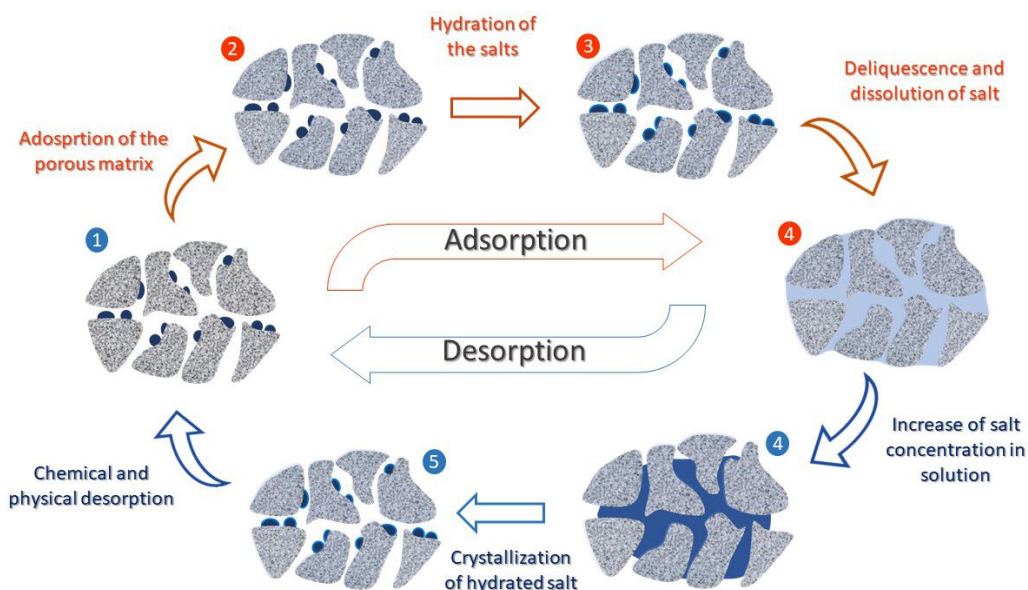


Figure 1.29: Schematic representation of the mechanism of adsorption and desorption for a “hygroscopic salt in porous host” material.

During discharging (adsorption):

- 1→2: the porous matrix adsorbs water (generally only through Van der Waals forces)
- 2→3: the anhydrous salt undergoes chemical sorption and salt hydrates are formed
- 3→4: deliquescence and dissolution of salt into pores occurs: adsorption of vapour continues and the salt concentration in solution decreases

During charging (desorption):

- 4→5: the dilute solution increases in concentration
- 5→6: crystallization of the saturated salt solution and efflorescence of crystals occur
- 6→1: chemical desorption and physical desorption take place, in sequence

The same mechanism is presented in Figure 1.31, where the sorbate pressure is reported with respect to the temperature.

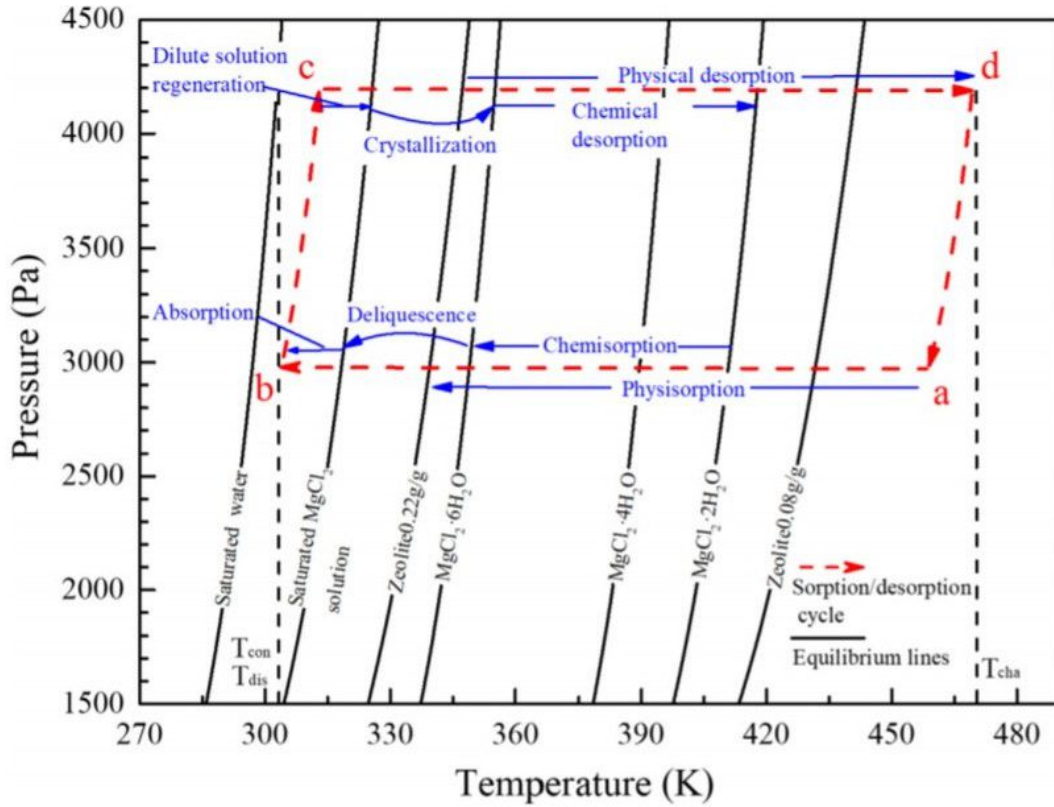


Figure 1.30: P(T) plot of thermochemical energy storage cycle using MgCl_2 -zeolite composite sorbent [88].

The higher sorption capacity is reached when deliquescence occurs, and the volume of the final formed solution is equal to the volume of pores. It is generally observed that the sorption ability of the system grows with the increase in the amount of salt (which gives the most relevant contribute to the heat release). However, too large salt content may result in oversaturation of the matrix in the hydration step. During adsorption, the aqueous salt solution overcomes in volume the available pore space and leakages out of the matrix. On the other hand, large amounts of salt can cause the retardation of the sorption dynamics due to the so-called “blocking effect”. Grekova and coworkers, for instance, reported a reduction of the pore volume of 30% when passing from vermiculite to vermiculite-LiCl composite [89]. Elsayed et al. pointed out how the water sorption curve of MIL-101/CaCl₂ changes due to the partial filling of pores by salt [90]. In general terms, the sorbate phase occupies almost whole pore space of the matrix, hence

the mass transfer barrier becomes stronger [91]. As result, the evaluation of the amount of salt is of key importance when introducing it in the porous host [92]. The most common method to synthesize the composite consists on the impregnation of the matrix with an aqueous solution [86]. First, the porous matrix is dried, such to remove all water adsorbed on its free surface. Then, the material is impregnated with a solution of the salt protagonist of the sorption process. At this stage two different methods, dry impregnation and wet impregnation, can be applied. The first one (dry) involves a volume of solution, V_s which is equal to that of the pore volume, V_p . While the liquid soaks quite fast into the porous matrix, salt ions could take more time hence the sample might be kept in the wetting state for several hours. In the second case (wet), V_s is higher than V_p . Hence, the matrix is dipped in water for several hours, after which the excess solution is removed through vacuum desiccator [86]. In both cases the encapsulated salt amount and distribution depends on the salt concentration into the solution, the eventual chemical interaction with the matrix and the drying scenario. In addition, in case of wet impregnation, during drying the salt can partially precipitate on the outside of the grains, forming large crystals. Hence, additional treatments during the synthesis of the composite has to be considered, in order to dissolve and remove such crystals. This has not been observed when involving dry impregnation [87], which is also preferred thanks to the low volume of solution required.

A secondary less explored but anyway promising method is defined “*in situ*”. It consists on the introduction of the selected salt directly while synthesizing the host material. It can be the case of silica gel, which is usually obtained starting from organic precursors. The salt hydrate can be slowly added in certain percentage in the siloxane matrix, under vigorous mixing until a homogeneous slurry is obtained. Finally, the foaming reaction must be performed in an oven under controlled temperature [93].

During discharging (adsorption), the sorbate uptake, which is usually expressed as m/m_0 , can be also described as the number of sorbate molecules per molecule of salt.

As previously said, low values of thermal conductivity can significantly limit the heat transfer rate in a STES, reducing the overall system performance. The key issue of energy storage materials – limited heat transfer performance is primarily due to the porous nature of the material, which is one of the main requirements

in choosing a suitable adsorbent host. It is well known, indeed, that the higher is the porosity, the lower is the thermal conduction of the material. On the other side, inorganic salts are known to be good thermal insulators. As a result, to overcome the low thermal conductivity of the sorption thermal energy storage systems, heat transfer enhancement techniques are often used, e.g. fins, metallic meshes. The latter, however, increase the total cost of the devices due to the use of extra parts and more complex design, decreasing the effective thermal energy storage density due to extra volume. Hence, optimizing the thermal conductivity without suffering the thermal energy performances is still under research. Lele et al. [94], for instance, reported that the effective thermal conductivity of a salt can be increased by two and around three times when impregnating porous matrices with the salt. This may probably be due to the reduction of the air volume inside the material, thus offering a better heat path. Another solution, which has been recently explored in literature, consists on the introduction of highly conductive elements inside the adsorbent, thus increasing the overall thermal conductivity. Shere et al. added multi-wall carbon nanotubes (1 per cent wt) in Zeolite 13x – MgCl₂ composite, improving the conductivity by 35 % [95]. Elsayed et al reported the enhancement of the thermal conductivity of MIL-101(Cr) by more than 2.5 times when using hydrophilic graphene oxide, both physically mixed or directly incorporated during the synthesis process of MIL-101(Cr). In the end, expanded graphite has been recently investigated as porous but also high thermally conductive host for salts hydrate [76]. The choice of carbonaceous materials as porous matrices do not allow to reach very high values of ESC and ESD but drastically increase the ability of heat conduction, allowing to avoid the use of heat exchanger fins. Since in some cases an incompatibility between the structures of graphite and a salt hydrate resulted in big salt aggregates, thus prejudicing high water adsorption performance. Salviati et al. have recently proposed to overcome these limitations by producing graphite composites encompassing a polyelectrolyte binder, PDAC (polydiallyldimethylammonium chloride), to enhance the compatibility between salt and matrix [96]

Examples of the main used composites materials for STES are reported in Figure 1.31 (ESD vs Temperature of charging) and Figure 1.32 (ESC vs Temperature of charging); additional information are reported in Table 1.6.

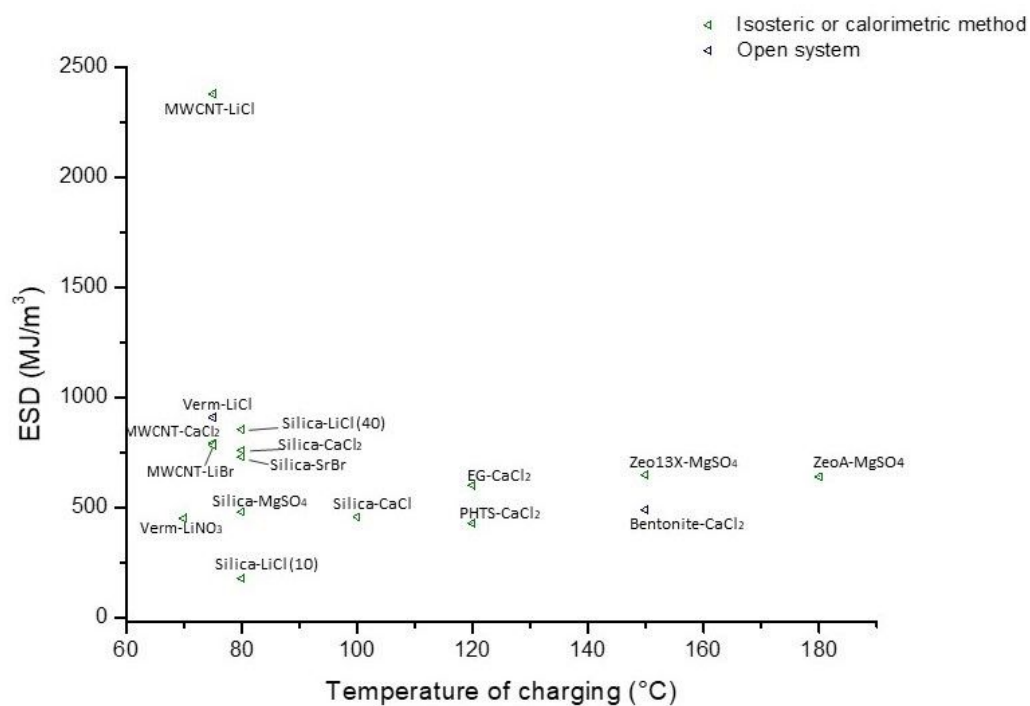


Figure 1.31: Chart reporting the values of Energy Storage Density of the main composite sorption materials.

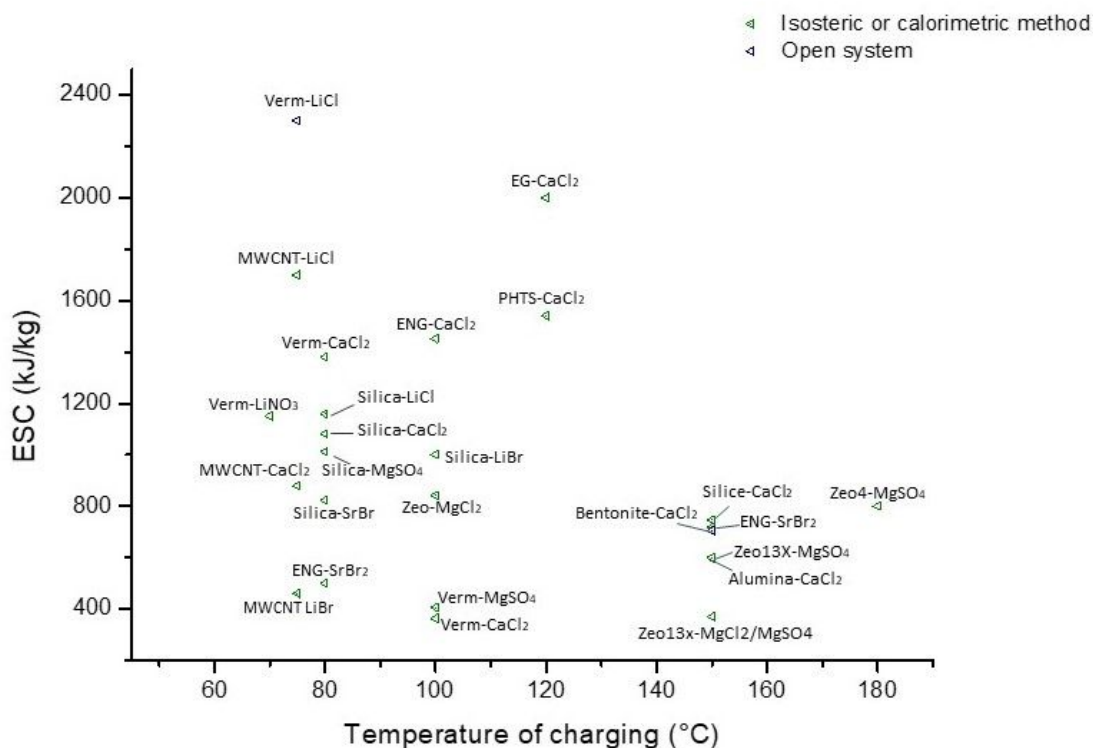


Figure 1.32: Chart reporting the values of Energy Storage Capacity of the main composite sorption materials.

1.2.4 Comparison between sorbent materials

Following, a comparison between performances of materials is done.

Figure 1.33 and 1.34 report ESD and ESC, relatively, with regards to the temperature of charging.

Sorption thermal energy storage

Sorption material	Price [€/tonn]	Tc [°C]	Td [°C]	Additional information	Water uptake [g/g]	Method	ESD [MJ/m ³]	ESC [kJ/kg]	SCC [€/kWh]	Ref.
Alumina + CaCl ₂ (14.4%)	828	150	20			Calorimetric		576	5.17	[70]
Bentonite + CaCl ₂ (15%)	123	150	20		0.2	Calorimetric		719	0.62	[70]
Bentonite + CaCl ₂ (40%)	163	150				Calorimetric	490	705	0.83	[43]
EG + CaCl ₂ (87%)		120				Calorimetric	600	2000		[97]
EG + CaCl ₂ (87%)		100				Calorimetric		1451		[98]
EG + SrBr ₂ (80%)		80				Calorimetric		500		[99]
EG + SrBr ₂ (80%)		150				Calorimetric		600		[99]
Expanded clay + SrBr ₂ (40%)	1080	110	20				313	711	5.46	[100]
MIL-100 (Fe) + CaCl ₂ (46%)	135070	80	30		0.57	Calorimetric	749	1206	403	[101]
MIL-101 (Cr) + CaCl ₂ (62%)	95100	80	30		0.75	Calorimetric	1116	1746	196	[101]
MWCNT CaCl ₂ (53%)	1965	75	15	Tc=15 °C, Te= 5 °C	0.18	Isosteric	477	530	13.3	[102]
MWCNT CaCl ₂ (53%)	1965	75	15	Tc=30 °C, Te= 10 °C	0.31	Isosteric	792	880	8.03	[102]
MWCNT LiCl (44%)	3311	75	35	Tc=15 °C, Te= 5 °C	0.57	Isosteric	2380	1700	7.01	[102]
MWCNT LiCl (44%)	3311	75	35	Tc=30 °C, Te= 10 °C	0.3	Isosteric	1246	890	13.4	[102]
MWCNT+LiBr (42%)	4795	75	35	Tc=15 °C, Te= 5 °C	0.31	Isosteric	782	460	37.5	[102]
MWCNT+LiBr (42%)	4795	75	35	Tc=30 °C, Te= 10 °C	0.23	Isosteric	578	340	50.7	[102]
PHTS + CaCl ₂ (10%)	1141	120	40	Tc=10 °C, Pdes=12.3 kPa	0.142	Isosteric	428	1541	2.66	[103]
Silica gel + LiBr (29%)	2458	100	40	Pads=11.4 kPa, Pdes=11.4 kPa	0.8	Isosteric		1000	8.84	[86]
Silica gel + LiCl (10%)	1395	80	35	Tc=10 °C, Te= 4 °C		Isosteric	176			[76]
Silica gel + LiCl (31%)	1700	100	40	Pads=11.4 kPa, Pdes=11.4 kPa	0.8	Isosteric		1000	6.11	[86]
Silica gel + LiCl (40%)	1830	80	35	Tc=10 °C, Te= 4 °C		Isosteric	854	1159	5.68	[76]
Silica gel + SrBr (58%)	1917	80	30			Calorimetric	730	825	8.36	[104]
Silica gel CaCl ₂ (43%)	781	80	30	Tc=10 °C, Pdes=12.5 kPa	0.77	Calorimetric	760	1081	2.60	[105]
Silice + CaCl ₂ (14%)	1097	150	20			Calorimetric		746	5.29	[70]
SiO ₂ + MgSO ₄ (58%)	570	80				Calorimetric	480	1012	2.02	[106]
Vermiculite + LiCl (59%)	1659	75	35			Open system	910	2300	2.59	
Vermiculite + LiNO ₃ (59%)	5877	70	28	Tc=35 °C, Te= 10 °C		Calorimetric	450	1150	18.4	[107]
Vermiculite CaCl ₂ (86%)	160	120				Calorimetric	1200	2000	0.29	[97]
Vermiculite SrBr (63%)	1571	100				Calorimetric	379	1656	3.41	[91]
Vermiculite+CaCl ₂	160	80	25	Pdes=12 kPa		Calorimetric	760	1380	0.42	[12]
Zeolite 13X + MgCl ₂ /MgSO ₄ (7.5%)	1343	150	30			Calorimetric		370	13.1	[108]
Zeolite 13X + MgSO ₄ (15%)	1338	150	25			Calorimetric	648	597	8.06	[109]
Zeolite 4A + MgSO ₄ (10%)	1106	180			0.23	Open system	640	800	4.95	[43]
ZeoliteNaX + MgCl ₂ (12.6%)	1593	100	30			Calorimetric		842	6.80	[110]

Table 1.6: Performances of composite sorbent materials for STES systems.

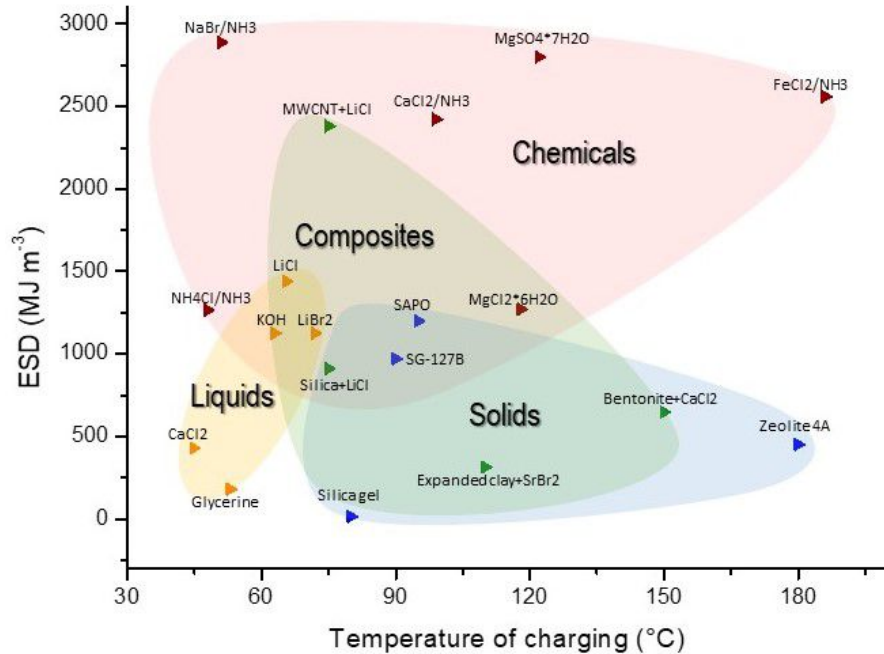


Figure 1.33: Chart reporting the values of Energy Storage Density of the different sorption material categories with regards to the temperature of charging.

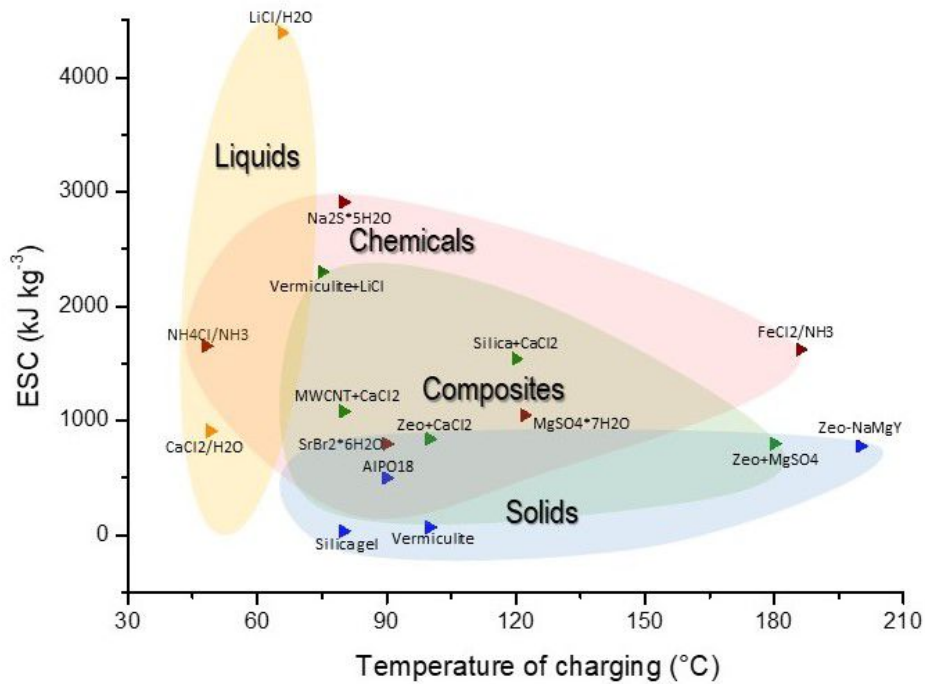


Figure 1.34: Chart reporting the values of Energy Storage Capacity of the different sorption material categories with regards to the temperature of charging.

As previously explained, the latter might be minimized thus reducing the amount of energy required to the solar collector. On the other side, the energy storage performance (ESD or ESC) might be maximised, in order to minimize the volume or mass required for providing the required energy. To point out, the plotted coloured contour for each class of materials takes into account all data reported in the previous tables. For the sake of clarity, only few names are reported on the charts.

Looking at both ESD and ESC values is of crucial interest. In some cases, mass is important in terms of cost of the material and weight of the system hence the material must present high ESC. On the other side, the system might be placed in a restricted place. In this case, the maximization of the storage energy density is more relevant than the storage energy capacity. Since the relation between ESC and ESD depends on the bulk density of the material itself, high values of ESC do not necessarily correspond to high values of ESD. From Figure 1.34, chemicals

appear as the best category of sorbent materials in terms of energy storage capacity (720-2900 MJ/m³), ranging from low to high temperatures of charging (80-190 °C). NaBr/NH₃ shows the best combination of high energy performance and low temperature of charging. However, it must be noted that it can be used only in case of closed systems, since in open ones the sorbate and the sorbent are not separated from the environment hence NH₃ cannot be involved in the sorption mechanism. On the other side, MgSO₄*7H₂O presents high values of ESC, with a charging temperature around 120 °C, hence it appears suitable for both closed and open systems, exploiting solar collectors. However, salts are affected by the problem of deliquescence, which affects grain stability and limits their performances after some cycles.

On contrary, solids (blue shadow) present lower values of energy storage density (10-1200 MJ/m³) and some of them require temperatures higher than 150 °C. The latter, as previously said, is considered as the limit for taking heat from the solar collectors. As a result, not all the solid adsorbents can be used for thermal energy storage systems coupled with solar collectors.

Composites (green shadow), which consist on the combination of solids and chemicals, represent a good compromise between the two categories, with reasonable energy storage performances when the temperature of desorption remains below 150 °C.

In the end, liquids can work at lower temperatures, if compared with the other categories of sorbents. It represents an advantage in terms of how much heat (i.e. thermal energy) is needed for charging. However, relative low values can be reached by liquids, without exceeding 1450 MJ/m³.

On the other side, it is reported that some of the salts, especially KOH and NaOH, are particularly harmful, especially for human tissues. In the same way, also ammonia can be irritating. From the corrosion point of view, all the salt-based solutions present a certain degree of corrosiveness against AISI 304 stainless steel. In this case, only glycerine and H₂O-NH₃ appear completely safe [111].

Nevertheless, liquids appear to be more promising when considering their energy storage capacity. Thanks to low densities, they offer higher values of ESC, if compared with the other categories, as well as the advantage of low temperatures of working. The other types of sorbents keep roughly their behaviours with respect to each other, with composites providing a good compromise between solids and

chemicals. An additional consideration can be done by looking at the class of solids. Generally speaking, it seems that the performances of the whole class gets worse when compared with the others in terms of ESC. While it covers a wide range of values when it comes to energy storage density, from 14 MJ/m³ for silica to 1200 MJ/m³ for SAPO-34, only a range of roughly less than 800 kJ/kg, from 70kJ/kg for vermiculite to 810 kJ/kg for Zeolite 4X, is found. One can expect highly porous solid adsorbents to be lightweight and large in volume, i.e. with low values of density, because of their morphology. Hence, passing from ESD to ESC, i.e. dividing the first value by the respective material density, is expected to be more convenient in terms of energy abilities. However, it must be noted that the higher performances are reached with zeotype materials. The latter do not due their ability mainly to the pore volume but to the presence of highly hydrophilic groups, this promoting the water adsorption. Hence, good performances do not necessarily go together with high porosity and low density-values.

Alongside this, a comparison between adsorbents in terms of Storage Capacity Cost (SCC) is of crucial interest. The latter is defined as:

$$SCC = \frac{Euro/ton}{ESC \cdot 1000} \cdot 3.6 \quad (1.2)$$

It is generally expressed in terms of €/kWh. A comparison between materials taking into account their commercial price is mandatory when evaluating the feasibility and scalability of a system. Highly performant but also dramatically expensive materials do not offer a reliable solution for the low temperature - thermal energy storage. For simplicity, Figure 1.35 reports €/kWh (i.e. SCC⁻¹) with respect to the temperature of charging, thus keeping the best case towards the top of the graph.

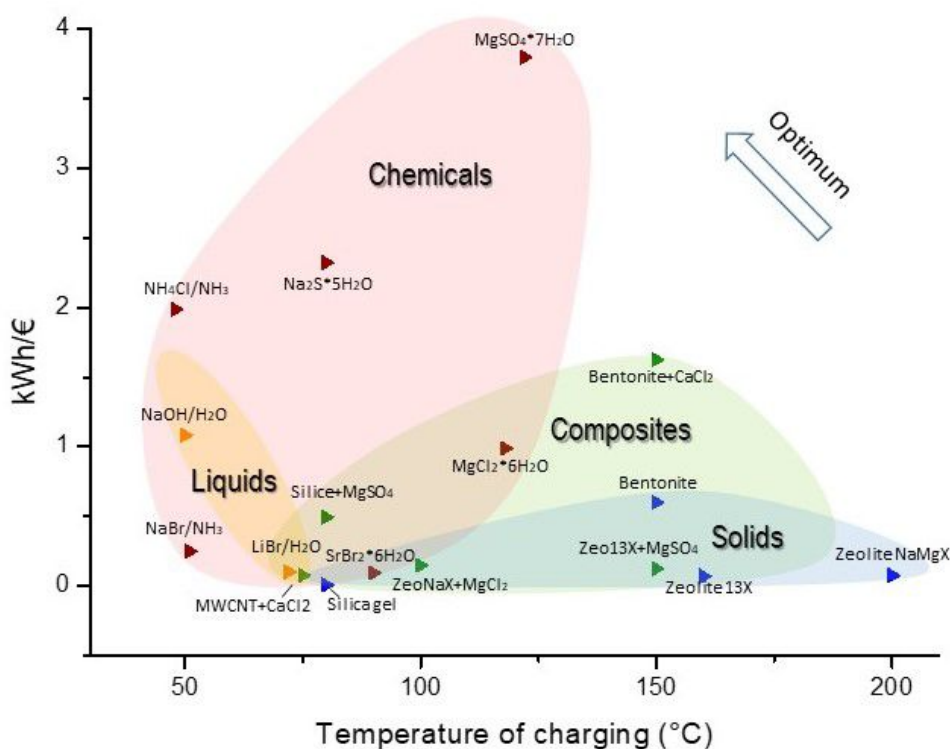


Figure 1.35: Chart reporting the values kWh/€ of the different sorption material categories with regards to the temperature of charging.

By comparing Figure 1.36 and Figure 1.37, a change stands out. Due to the high cost of the raw material, liquids do not seem to be convenient anymore. Despite their high capacity of energy storage, the same value normalized upon their price per ton, drastically drops. On the other side, some chemicals boast a relative low price, hence their performances outstand. Solid materials, in the end, inverse their trend. Details are pointed out by comparing Figure 1.36 and Figure 1.37. Zeolites present a market price of around 2500 €/tonn, higher than that of bentonite or vermiculite (around 160 €/tonn). As a result, zeolites overcome clay adsorptive materials with regards to the energy storage density but drop when considering also the price. On the other side, zeotype and MOF materials are commercially available for a price of about 100€/kg and 250€/kg, respectively, thus exceeding the price of zeolites and clays of two or three orders of magnitude. Despite their massive performances when tested in laboratory, they have not yet provided a

suitable and scalable solution for industrial STES systems. Several researches are needed to market these performant materials at feasible prices.

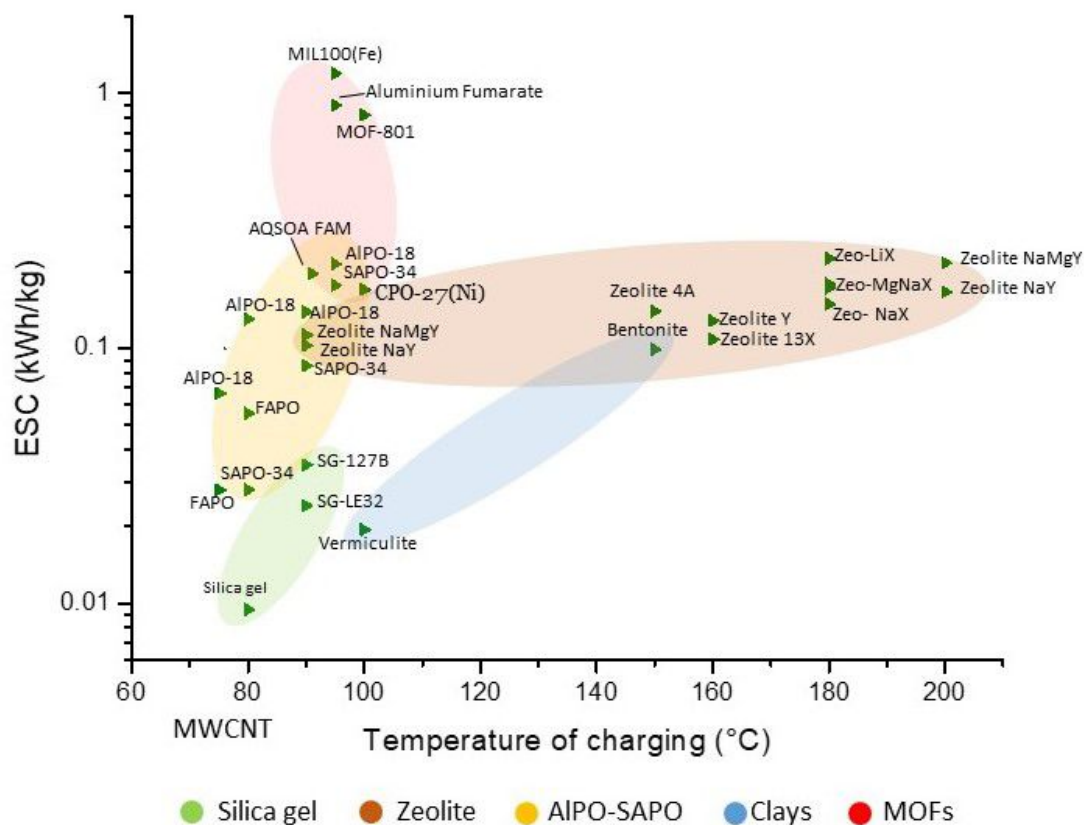


Figure 1.36: Chart reporting the values of Energy Storage Density of different solid sorption materials with regards to the temperature of charging.

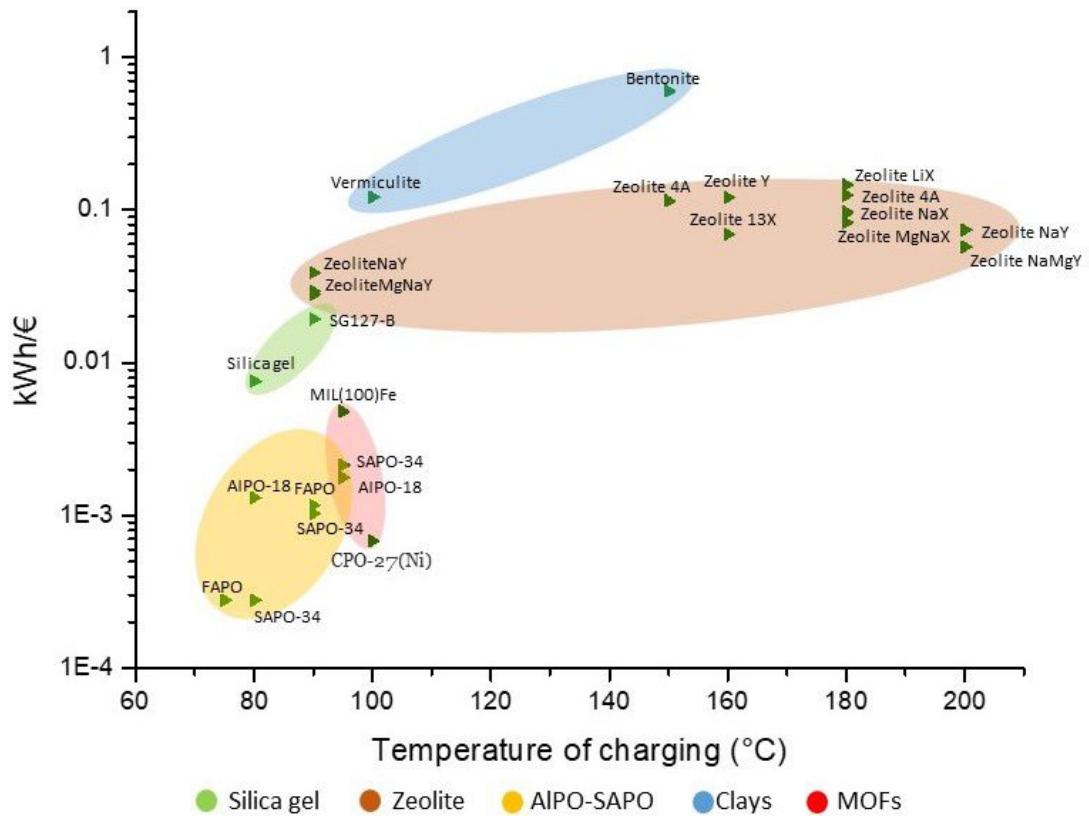


Figure 1.37: Chart reporting the values of kWh/€ of different solid sorption materials with regards to the temperature of charging.

In the end, a comparison in terms of energy density and storage capacity costs (SCC) appears as crucial so as to identify the best performing materials, taking into account the price of the system.

As said from the beginning, sorbents are desired to perform the ability to store high amounts of energy with minimum amount of mass. The lower the amount of active material needed for the storage, the lower is the total price for the latter, if considering that the price is defined for one ton of raw material. However, the cost of the reactor containing the sorbent, i.e. the cost and the amount of the supporting material (e.g. AISI316), cannot be ignored. The cost of the non-active material must be added up to the cost of the active material, thus defining the whole cost of the involved material. Moreover, high volume sizes of the reactor can cause relevant pressure losses, since they are affected by the path length of the

sorbate passing through the adsorbate bed. To minimize the size of the reactor, i.e. its cost and its inefficiency, sorbent materials with high energy storage density are preferred. In conclusion, materials with high SSC and high ESD give the best performances in term of energy storage abilities and cost of the system.

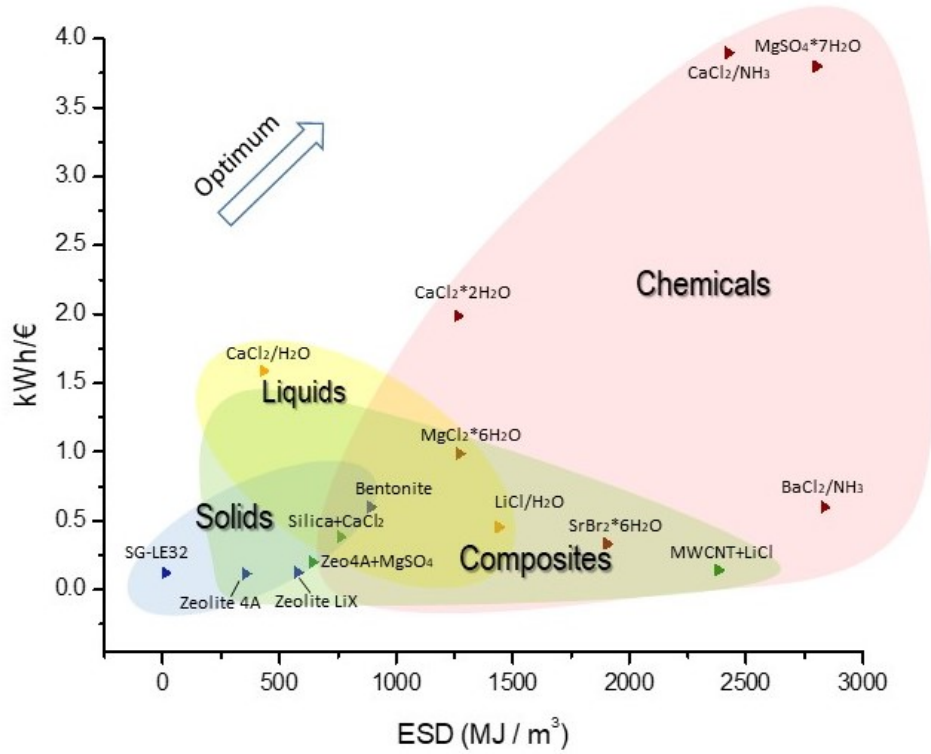


Figure 1.38: Chart reporting the values of kWh/€ of the different sorption material categories with regards to their Energy Storage Density.

1.2.5 Cementitious composite materials for thermal energy storage applications

In the horizon of the existing sorbent materials, an innovative cost-effective cement-based composite sorbent material can be introduced [112]. It is well known, indeed, that cement offer a tunable mesoporous porous structure, thus representing a good host for hygroscopic salts. In addition, it is definitely less expensive than

other common solid sorption materials. As an example, for pure cement powder, a maximum price of 155 e/ton is assumed, that is the highest European average factory gate price (UK, France), according to a EU report on the competitiveness of the European cement sector. The minimum price is assumed as 80 €/ton, that is the average value for other countries (Italy, Poland)[113] On contrary, the market price of a common Zeolite 13X is around 2500 €/ton.

A preliminary investigation of the sorption properties and thermal storage capacity of the innovative cementitious composite material has been performed by ([112]). In the work, $MgSO_4$ was introduced into the porous matrix and the calorimetric method was used to test the energetic performances of the composite. Figure 1.39 reports the thermodynamic storage cycles of the cementitious material, with a desorption temperature of 80 °C or 140 °C. For each cycle, the value of water adsorbed δx [g/g] is indicated, calculated graphically thanks to the operational constrain set. From the Polanyi-Dubinin model for sorption phenomena, a maximum water uptake value of 0,12 g/g was evaluated. The latter allowed to reach an Energy Storage Density of 0.28 GJ/m³. Thanks to its low price, an energy of 0.3 kWh/€ is obtained (Figure 1.39). The preliminary research results suggest to go on with the exploration of the energetic performances of the innovative cement composite. In detail, the porosity might be maximised, thus to increase the amount of salt that can be introduced into the pores of the cementitious matrix. In addition, the concept of cement-based composite materials directly obtained by mixing the cement paste with salt hydrates (in-situ approach) was investigated, thus exploiting the natural porosity formation in cement and a salt crystal precipitation within the pores.

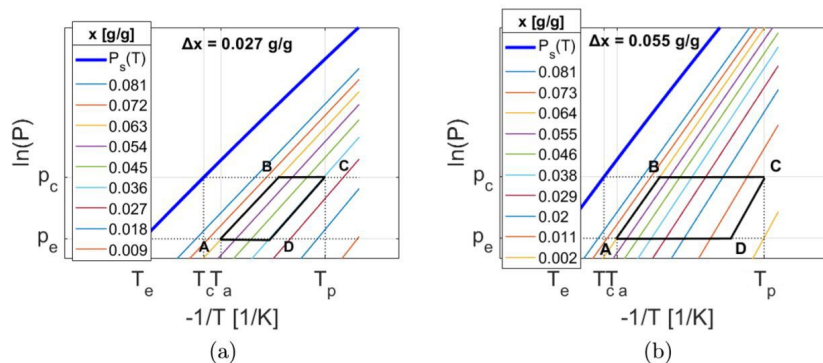


Figure 1.39: Cementitious composite thermal energy storage cycles: (a) T of charging = 80 °C, (b) T of charging = 14 °C.

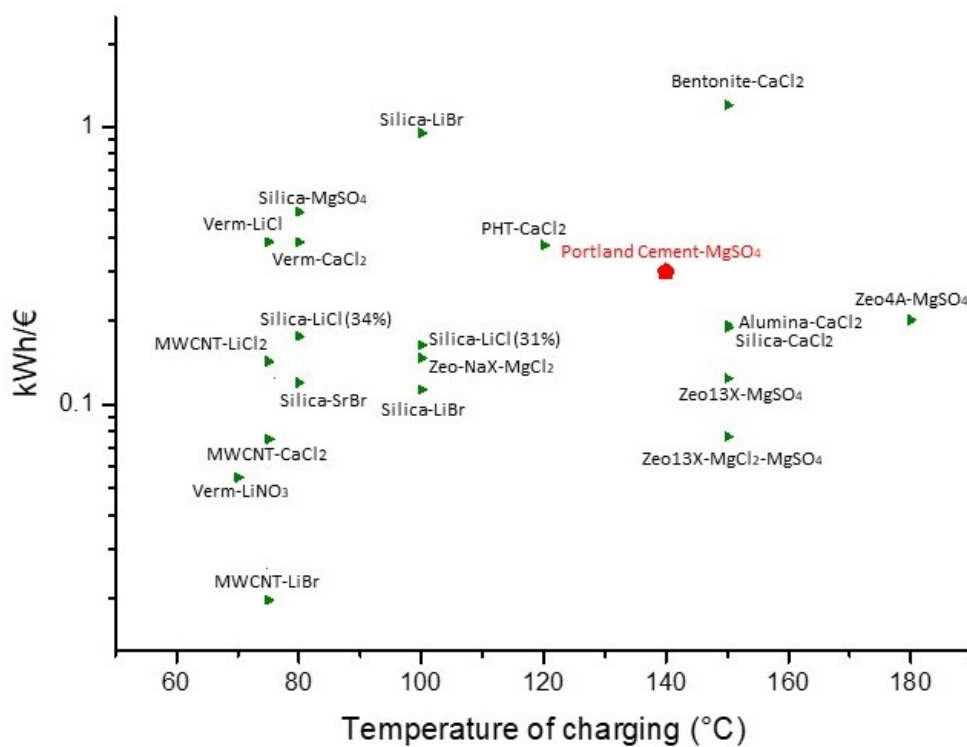


Figure 1.40: Chart reporting the values of kWh/€ of the different sorption composite materials with regards to their Temperature of charging. A red dot marks the innovative cementitious sorbent

1.2.6 Conclusion

Among all kinds of thermal energy storage systems, STES systems present the highest performances in terms of energy storage capacities. Hence, they appear promising in the attempt of improvement of the storage of renewable thermal energy, thus ensuring continuity of energy supply. A general review of the existing sorbent materials (solids, liquids, salts and composites), elucidating their mechanism of thermal energy storage and their main properties has been done. Several charts allow the reader to first compare materials and, more generally, classes, in terms of Energy Storage Density (ESD, MJ/m³), Energy Storage Capacity (ESC, kJ/kg), Storage Capacity Cost (SCC, €/kWh) and temperature of desorption (i.e. charging temperature). Liquids can work at relatively low charging temperatures, if compared with the other categories of sorbents. It represents an advantage in terms of how much heat (i.e. thermal energy) is needed for desorption. Relative low values of ESD can be reached by liquids, without exceeding 1450 MJ/m³. However, thanks to their low density, they offer high values of ESC, thus overcoming the other sorbent categories. By looking at SCC index, however, liquids do not seem to be convenient anymore. Despite their high capacity of energy storage, indeed, the high cost for the raw materials causes their energetic performances to fall drastically down. In addition, security parameters such as health, flammability, reactivity etc. play a crucial role in the choice of the exploitation of liquids as sorbent for thermal storage systems. Solid sorbents, instead, cover a wide range of values in terms of energetic performances, including the low storage capacity of silica gel and clays and the definitely higher storage capacity of MOFs, AlPOs and Zeolite. However, the latter group of solids is not affordable in terms of price for ton, if considering their industrial-scale application. As a result, when it comes to SCC, all solid sorbents performances flat to a low level, due to their low storage capacity or the high material price. On the other hand, chemicals appear as the best category of sorbent materials in terms of both ESC and ESD. It must be noted, however, that sorption couples involving NH₃ can be used for closed system only and all chemicals are affected by the problem of deliquescence. The latter affects grain stability and limits the material performances after some cycles. Composite sorbents, in which hygroscopic salts are introduced into a porous matrix, represent a good compromise between the two categories, with regards to the all energetic performance ratings. The possibility of choice of several porous matrices and

chemicals, combining them in different concentration and using a variety of ways, gives potential orders of magnitude increase in terms of energy storage capacity. Among all available composite materials, an innovative cementitious composite sorbent is preliminary investigated. When MgSO_4 is introduced inside a porous cement, through both matrix impregnation and in-situ ways, a values of 0.3 kWh/€ is reached. It overcomes that of of porous Zeolite, if the same hygroscopic salt is introduced. The good performances of the new cementitious composite are due to its great availability to host salts, together with its very low price. Hence, it appears promising in the attempt to find a real industrial-scale applicable sorbent material for thermal energy storage systems.

Chapter 2

Model of a modular system for closed or open STES systems and working cycle optimization

The previous charts give access to a primordial comparison between materials, taking into account SCC and ESD parameters for different sorption couples. However, the cost and the volume of the whole system are certainly higher. Non active – materials forming the reactor walls, the water tank and other additional components affect the whole results hence they must be taken into account to allow a more coherent comparison between adsorbents. In the following section, an estimation of the ideal systems performance in terms of ESD and SCC in a common reference scenario is provided. Different active materials are assumed and a comparison between their results is proposed. Among them, the innovative cementitious composite is analysed, thus exploiting its energetic prospectives.

2.1 Reference scenario

As common application, a family house space, heating having solar collector on its roof able to provide the required temperature of desorption, is considered.

The sorbent material stores energy during summer and releases it during winter, i.e. the material provides a seasonal storage thermal cycling. According to [17], where the integration of a sorption heat storage system in a family passive-house is investigated as well, the following reference scenario operating conditions are considered: $T_{\text{of charging}}=150\text{ }^{\circ}\text{C}$ $T_{\text{ambient}}=10\text{ }^{\circ}\text{C}$ $P_{\text{water,sat}}$ at $T_{\text{ambient}}=12.4\text{ mbar}$ The value of 12.4 mbar corresponds to the saturated water vapor pressure at $10\text{ }^{\circ}\text{C}$. In this scenario, a yearly energy demand of 10 GJ is assumed and the thermal storage will perform only one sorption/desorption cycle per year. For one year, 212 heating days are considered and, for simplicity, a constant power is required during those days. Thus, an energy amount of 47.2 MJ is daily required.

Nomenclature	
ESC_s : Storage Energy Capacity of the sorbent material	h : height of the material reservoir
ESD_s : Storage Energy Density of the sorbent material	ϵ : pellet bed porosity
ESD_s^I : Storage Energy Density of the bed of pellets	\dot{Q} : power of the heat exchanger per hour
ESC_{st} : Storage Energy Capacity of the system	A_{HX} : area of the reactor heat exchanger
ESD_{st} : Storage Energy Density of the system	V_{HX} : volume of the reactor heat exchanger
SCC_s : Storage Capacity Cost of the sorbent material	m_{Cu} : mass of copper for reactor heat exchanger
SCC_{st} : Storage Capacity Cost of the system	\dot{Q}_e : power of the bucket elevator
$m_{s,d}$: daily mass of the sorbent material	$V_{c/e}$: volume of the condenser/evaporator
$m_{s,y}$: yearly mass of the sorbent material	ρ_s : density of the sorbent material
$V_{s,d}$: daily volume of the sorbent material	ρ_{Cu} : density of copper
$V_{s,y}$: yearly volume of the sorbent material	$\rho_{AISI316}$: density of AISI 316
A_r : area of the reactor	$Price_s$: price of the sorbent material
$V_{r,sh}$: volume of the reactor shell	$Price_{ns}$: price of the non-sorbent material
$A_{m,r}$: area of the material reservoir	$Price_{HX}$: price of the heat exchanger material
$V_{m,r,sh}$: volume of the material reservoir shell	$Price_e$: price of the electrical vertical transport

Figure 2.1: Nomenclature.

2.2 Selection of materials

Four solid sorbent materials are selected and their main properties playing a key role for the analysis are reported in Table 2.1. Among them, zeolite NaY has been chosen as representative of the wide-explored class of zeolite materials, which appears as one the most performant solid adsorptive sorbent. Silica gel-LiCl and MIL100(Fe)-CaCl₂ have been chosen as sorbent composites, including in this way an example of both traditional and innovative porous sorbent materials. Silica gel is largely used for a variety of huge industrial scale applications. On the other hand, MIL100(Fe) has better performances but it is more expensive, hence it is produced on a smaller scale if compared to silica gel. In the end, cement-MgSO₄, whose performances has been tested in this work, is compared to the other existing materials, thus highlighting its advantages together with its limits.

Sorbent material		ZeoliteNaY [79]	MIL100(Fe)+CaCl ₂ [101]	Silica gel+LiCl [86]	Cement+MgSO ₄ [112]
T of adsorption	[°C]	40	30	30	30
ESC	[MJ/kg]	0,41	1,13	1,1	0,18
ESD	[MJ/m ³]	345	450	760	200
Water uptake	[kg/kg]	0,12	0,57	0,77	0,34
Price	[€/tonn]	2900	135000	780	110
SCC _s ⁻¹		0,039	0,005	0,385	0,460

Table 2.1: Thermal energy performances of the selected sorption materials.

2.3 Closed system

Figure 2.2 reports the scheme of a closed system, whose operation mode has been described in section 1.2. In this schematic representation, blue arrows represent the charging cycle. In particular, the lighter colour represents the thermo-fluid path, from the solar collector to the heat exchanger inside the reactor, while the darker one represents the water vapour moving from the adsorbent to the condenser, until the water tank where the fluid is stored. Red arrows, instead, represent the discharging cycle and again two shades of colour are discernible. The darker one represents the thermo-fluid path, whose aim is to transfer heat from the hydrated adsorbent material to the user, while the lighter one marks the path of water passing from the evaporator to the adsorbent material, where it is adsorbed. In

closed systems, the sorbent material is used in the form of pellets, whose size can be approximated to that of a sphere with few millimetres of diameter. However, since the sorption material has a very low heat conductivity, a heat exchanger is needed to provide the heat transfer into and out of the bed of pellets. While studying the adsorbent performances of LiCl, Zhao et al. designed the sorption reactor as formed by 25 identical sorption bed units, which are connected by manifold tubes in parallel (Figure 2.3, A [114]). In this case, sorbents covered the top of the coil uniformly and each heat exchanger layer could accommodate 0.47 kg sorbent. Also Fink and co-workers proposed a bed reactor consisting of a finned heat exchanger with a packed bed of Zeolite 5A spheres (2.3,B [43]). A crucial point when designing the reactor is the shape of the heat exchanger, which needs to be projected in such way that all the material of the fixed bed is reached and a sufficient power can be extracted. On the other side, the material amount, i.e. its cost, should be as low as possible. A model for the heat exchanger thus meeting these requirements is proposed by Koll et al. [115] (2.3,C). Recently, the idea of involving for each charging/discharging cycle the amount of sorbent material needed for the daily energy demand only is taking place. If the whole active material is packed in a single reactor, the large thermal mass has to heat it up at once, which makes the performance less controllable while the heat losses become larger. Thus, to reduce the reaction zone and by taking inspiration from [116], the design of a modular reactor, schematically represented in Figure 2.4, is proposed as model for the performance analysis of different sorbents. This model relies on the separation of the material reservoir, i.e. where the amount of active material answering to the yearly energy demand is stored, from the reactor, where the active material for a daily discharging cycle is placed. When complete adsorption is achieved at the end of the day, the material is removed from the reactor and the latter is refilled from the top with new charged material. A mechanical bucket elevator provides the relocation of the discharged material from the reactor to the material reservoir.

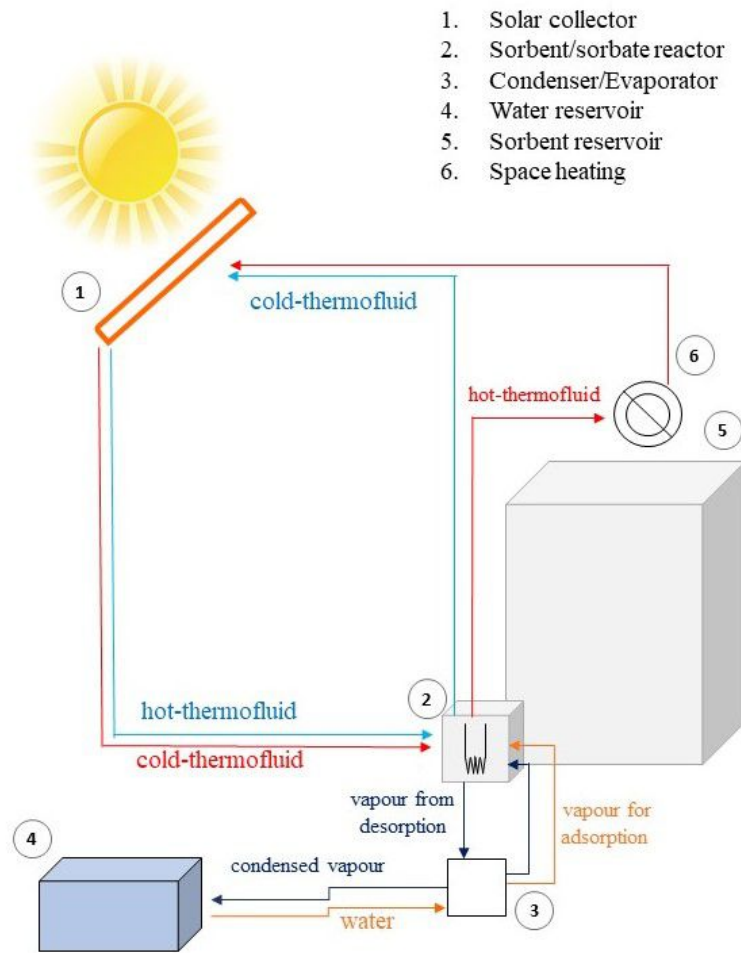


Figure 2.2: Schematic representation of a closed STES system.

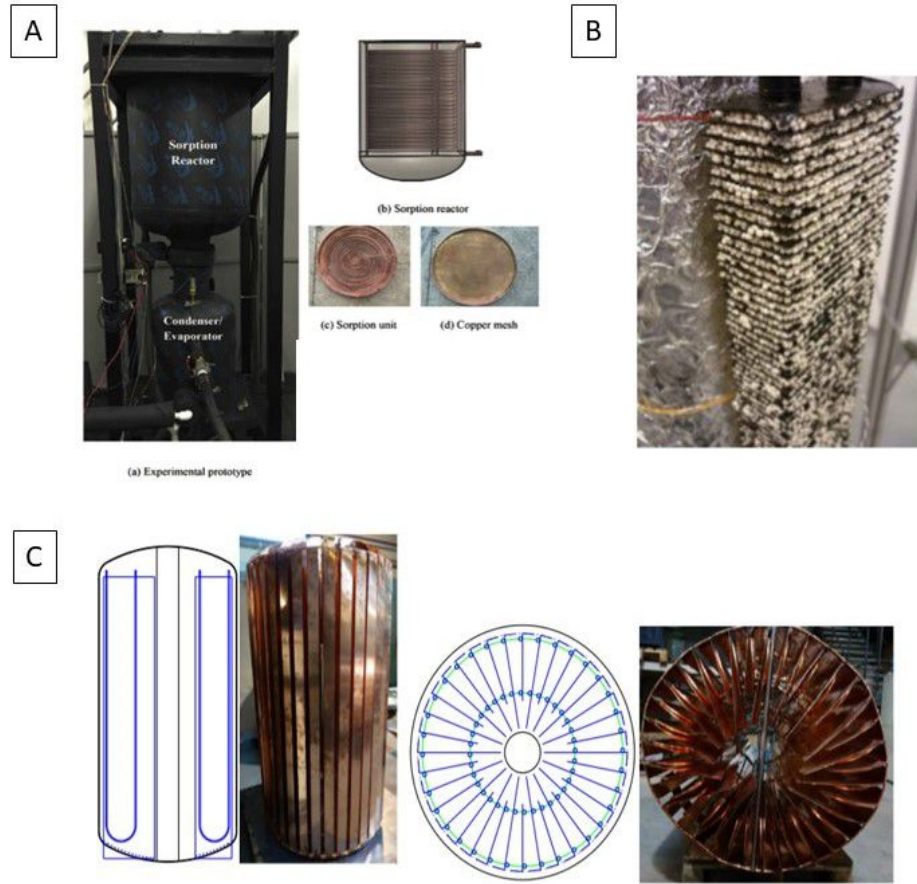


Figure 2.3: Examples of closed systems from literature [114] [43] [115].

First, it is possible to evaluate the daily and yearly mass of adsorbent material that is needed to provide 47.2 MJ and 10 GJ respectively :

$$m_{sd} = \frac{47,2MJ}{ESC_s} \quad (2.1)$$

$$m_{sy} = \frac{10GJ}{ESC_s} \quad (2.2)$$

At the same time, the volume of the daily and yearly amount of material can be evaluated by considering the energy storage density of the sorbent pellets. In this case, however, the energy storage density of the active material, ESD_s , must be multiply for a bed porosity factor, ϵ , thus obtaining the energy storage density

of the bed of pellets, ESD_s^I . In this case, a porosity factor of 0.4 is considered. As a result, the volumes of active material involved in the system for daily and yearly energy production are:

$$V_{sd} = \frac{47,2MJ}{ESD_s^I} \quad (2.3)$$

$$V_{sy} = \frac{10GJ}{ESD_s^I} \quad (2.4)$$

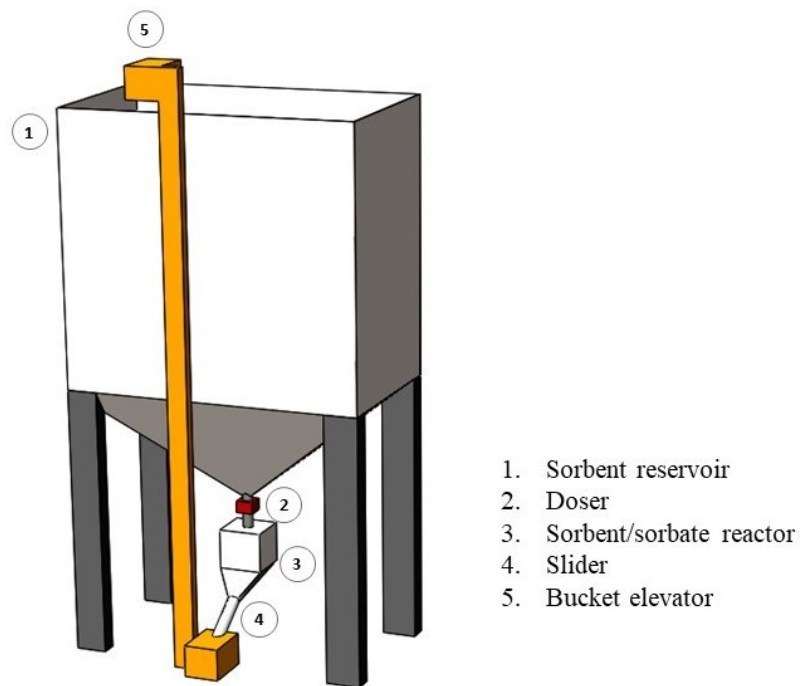


Figure 2.4: Schematic representation of the modular reactor model.

The volume of the heat exchanger inside the sorbent reactor can be calculated, by knowing the surface area and the thickness of the exchanger copper coil. The first one is arbitrary fixed at 10 millimetres. The surface area, A_{HX} , can be calculated if considering the power of the heat exchanger, Q . Since it is assumed

the heat exchanger to be able to provide the required daily energy, Q is equal to the daily energy demand divided by the number of hours in the day (i.e. 546 W)

$$A_{\text{HX}} = \frac{Q}{U \cdot \Delta T} \quad (2.5)$$

where U is the heat exchange coefficient, in $\text{W}/\text{m}^2\text{K}$. For a copper coil of 1 millimetre in thickness, which is used as heat exchanger between air and water, U corresponds to 118,1 $\text{W}/\text{m}^2\text{K}$. T is the temperature difference between outlet and inlet fluid. The first one is considered to be equal to the temperature of discharging of the adsorbent material. The temperature of the inlet fluid, instead, is considered to be preheated, if necessary, until reaching an ambient temperature of 25 °C. By knowing the volume of the sorbent material and the volume of the heat exchanger inside the reactor, the amount of non-active material involved in forming the shell of the reactor ($V_{\text{r,sh}}$) and the sorbent reservoir ($V_{\text{sr,sh}}$) can be found. For simplicity, the reactor can be approximated as a cube, whose side can be found from the volume of the daily sorbent material. The sorbent material reservoir, instead, is considered to be a parallelepiped with a rectangular base, as represented in Figure 2.4. This geometry allows to have a shorter side, thus reducing the path of the discharged material when it is carried from the bottom of the reactor to the starting point of the elevator. In order to make the following calculations, a short side of 1 meter is fixed for the material reservoir while the two other sides are defined to be equal to each other. In the same way, the thickness of the reactor and reservoir walls is arbitrary fixed at 20 millimetres. Both containers are made of AISI316, whose properties ensure a good mechanical resistance together with a certain corrosion resistance that is necessary in the presence of salt solutions. In terms of volume, another key element that has to be considered is the water tank, that is characteristic of closed STES systems only. Since it must supply the amount of fluid needed for one year, indeed, its volume cannot be neglected and is evaluated by knowing the adsorbent specific water uptake:

$$V_{\text{w}} = \left[\frac{\chi \cdot m_{\text{yd}}}{\rho_{\text{w}}} \right] \quad (2.6)$$

In the same way, the volume of the condensator/evaporator ($V_{\text{c/e}}$) can be evaluated, by considering $m_{\text{s,d}}$. Since the yearly amount of active material is drastically higher than the daily one, the volume of the condensator/evaporator is

definitely lower than that of the water tank, as well as the volume of the reactor if compared to the volume of the material reservoir. In the end, the electrical power for the vertical transport of the discharged material can be evaluated estimating a yield of the elevator of about 0,85.

$$Q_e = m \cdot g \cdot h \cdot \eta \quad (2.7)$$

As a final step, the prices of the active material, the whole non-active material (AISI316 and copper) and the electrical energy required for the transport are evaluated. The sum of them gives the cost of the whole system for one year of operation. In particular, the price of the non-active material is multiplied for a factor 0,1, thus considering that the system goes for at least ten years. Several works of research, indeed, attest the good cyclability of many sorbent materials. As a result, the price of the non-active material is spread over ten years. It is known that such estimation of cost does not include every aspect of the system. Such an example, the insulating material that is needed to reduce the thermal losses through the stainless-steel walls is neglected, as well as the thermodynamic efficiency. However, it is a good first estimation of what happen when considering the system as a whole. The main results of the analysis are represented in Table 2.2.

Sorbent material		Zeolite NaY	MIL100(Fe)+CaCl ₂	Silica gel+LiCl	Cement+MgSO ₄
$m_{s,d}$	[kg]	116	39	44	260
$m_{s,y}$	[kg]	2451	5250	9216	55290
V_{system}	[m ³]	57	27	29	90
Q_e	[Wh]	969	231	364	1405
Price _{system}	[€]	76300	1122500	9700	14070
ESD _{st}	[MJ/m ³]	175	363	339	111
ESC _{st}	[MJ/kg]	0,51	0,99	1,01	0,32
SCC _{st} ⁻¹	kWh/€	0,036	0,002	0,286	0,196

Table 2.2: Thermal energy performances of a closed STES system for different sorption materials.

A change in the Energy Storage Density, from that of the sorbent material to that of the system as a whole, is represented in Figure 2.5. In each case the value of ESD falls down, since the volume of the entire system is significantly higher than that of the sorbent material only. However, there is no prospect of a turnaround in

terms of performances, i.e. MIL100(Fe)-CaCl₂ is still in top position, followed by Silica gel-LiCl, Zeolite NaY and cement-MgSO₄ as the less performing material. In more details, the volume of the whole system for all materials is reported in Figure 2.6. Only 27 m³ of volume are expecting when using MIL100(Fe)-CaCl₂, thanks to the high energy storage density of the sorbent material (2380 MJ/m³). On contrary, much more space is required when using Cement-MgSO₄ or Zeolite NaY. From Figure 2.7, where the volume of all components contributing to that of the entire system is reported, one can notice that the volume of the condenser/evaporator and that of the reactor, where the daily amount of active material is placed, give a negligible contribute with respect to the volume of both the active material reservoir and water reservoir. The latter two components are leaders in determining the volume of the system and even if their relative contribute change a bit when considering one sorbent material or another, the active material reservoir is always the largest component of the system. This explains the notable difference between a system involving MIL100(Fe)-CaCl₂ with regards to a system involving Cement-MgSO₄, since the volume of the material reservoir strictly depend on the energy storage density of the sorbent material.

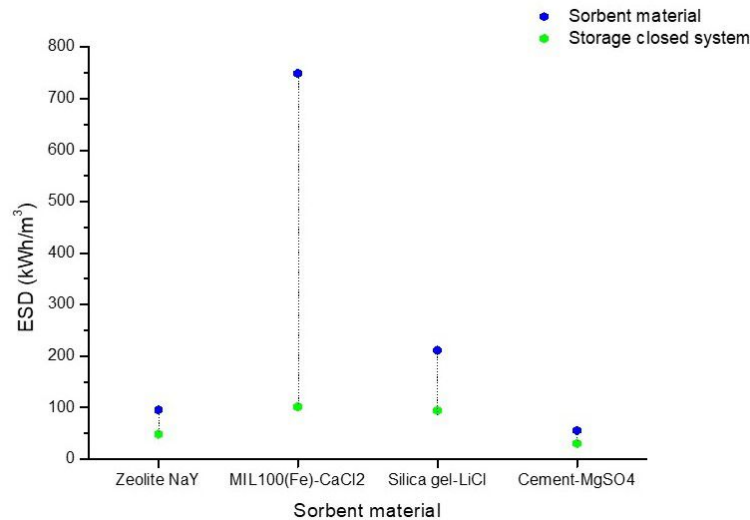


Figure 2.5: Chart reporting the value of Energy Storage Density of the sorbent material (blue dots) or of the closed STES system as a whole (green dots).

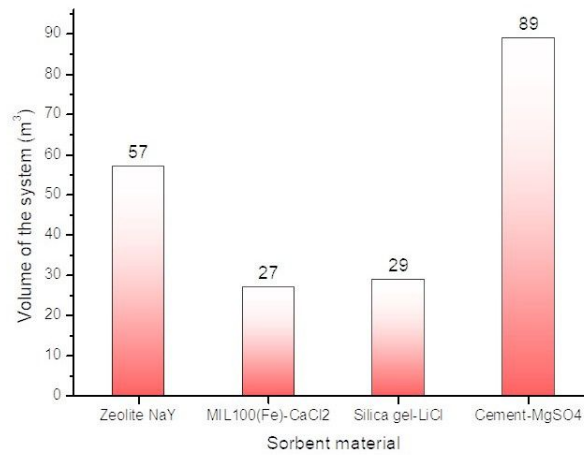


Figure 2.6: Graphic representation of the whole volume of a closed STES system with different sorption materials.

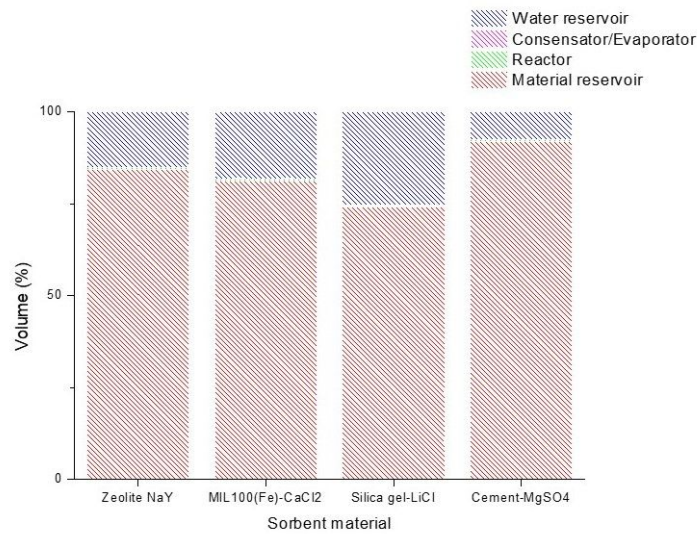


Figure 2.7: Graphic representation of the volume contribute of the different components of a closed STES reactor.

Beside the volume of the system, which plays a key role if the system has to be taken in a restricted place, the cost of the system, with regard to the type of sorbent material, is analysed. Figure 2.8 reports the relative contribute of the non-active material, the sorbent material and the electrical power for the vertical

transport of the discharged material, in terms of euros. The latter component appears to be irrelevant with regards to the cost of the entire system. However, it has been evaluated and results has been reported as confirming the feasibility of a modular system requiring a mechanical elevator for the transport of the material, which cost does not affect the system. As is possible to see, for Zeolite NaY, MIL100(Fe)-CaCl₂ and Silica gel-LiCl the cost of the active material is the more relevant, with regards to the whole system. When using Zeolite NaY the cost of the active material contributes for more than 90 % alone, while in case of Silica gel-LiCl as a sorbent, the cost of the latter covers around 75% of the whole cost. In the end, the very high price for MIL100(Fe)-CaCl₂ makes the cost for the non-active material almost irrelevant. An inverse trend is reported for Cement-MgSO₄, where the most relevant contribute to the cost of the energy storage system comes from the non-active material. The cementitious material, itself, features a very low price, estimated at 110 € for ton of material. The price of the active material defines the SCC (€/kWh) of the material which, as said, is of crucial importance evaluating the feasibility and scalability of a system. Highly performant but also dramatically expensive materials do not offer a reliable solution for the low temperature-thermal energy storage. In Figure 2.9 , the performances of the selected sorbent materials in terms of kWh/€ with regard to the cost of the active material alone and the cost of the whole system is reported. As might be expected, the cementitious material alone offers the best results (0,196 kWh/€) while MIL100(Fe)-CaCl₂ and Zeoline-NaY fall dramatically down. A more surprising result comes out when considering the performance of the system as a whole. Even when adding the price of the non-active material, (which, as previously seen, is definitely not negligible), the cementitious material continues offering good values of kWh/€. By looking at Figure 2.8, one might expect that the contribution of the non-active material cost may cause an inversion of the ranking trend, bringing cement-MgSO₄ near to the bottom. Against expectations, it does not remain anymore convenient with respect to the Silica gel-LiCl, because of the higher amount of non-active material (i.e. cost of the whole system) in case of the cementitious composite. Regarding the choice of using Zeolite NaY and MIL100(Fe)+CaCl₂, instead, energetic performances in terms of kWh/€ remain out of competition, because of the high price of the active material.

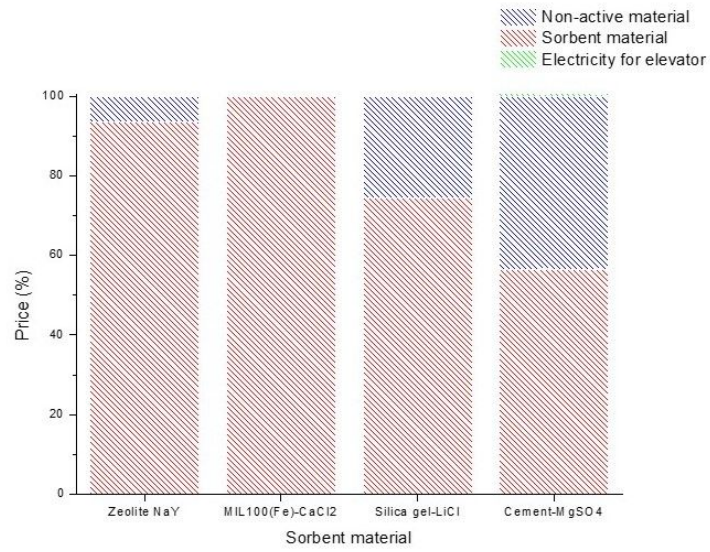


Figure 2.8: Graphic representation of the contribute in terms of price of the different components of a closed STES reactor.

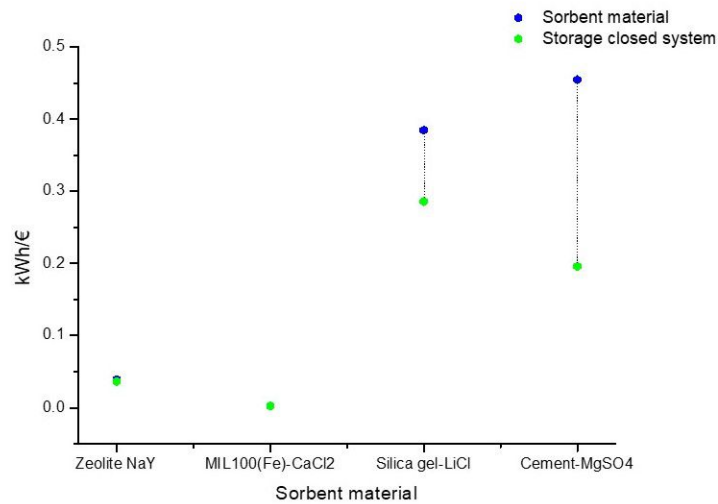


Figure 2.9: Chart reporting the value of Energy storage Capacity per cost (kWh/kg) of the sorbent material (blue dots) or of the closed STES system as a whole (red dots).

2.4 Open system

Figure 2.11 schematically represent a common STES open system, whose operation mode is described in Section 2.1. Similarly to what explained for the case of closed systems, blue arrows refer to the charging (desorption) cycle, while red arrows mark the discharging (adsorption) cycle. Again, two shades of colour can be distinguished for both cycles. In the blue cycle, lighter arrows refer to the thermo-fluid going from the solar collector to the fluid-to-air heat exchanger, where air is heat up. The latter, that is marked with the darker blue arrow, comes from the environment and enters the reactor, to induce the desorption of the sorbate. On the other hand, the darker red arrow represents the ambient humid air entering first an air-to-air reactor, to be pre-heated, and then the reactor, for the adsorption of the active material. In the end, dry hot air exits the reactor and it is available for the user. Because of the low temperatures during winter, in some cases the presence of a borehole is required, thus to increase the humidity percentage of the entering air. However, for simplicity, this component is not included in the scheme of the reactor. Otherwise, to include the borehole, the reader can refer to [117]. The open system type benefits from more structural simplicity, since it does not require a condenser-evaporator, with the associated water reservoir. The reactor when adsorption/desorption take place consists again in bed of sorbent pellets, whit a size similar to those of spheres with few millimetres in diameter. In this case, an air-to-fluid heat exchanger is not present inside the reactor. Humid air from the environment, indeed, crosses the pellets, gain heat and then directly enter the heating house space. However, also in the case of the open system typology, a modular reactor design is proposed. In this case, a reduction of the reactive zone allows to shorten the air path, thus minimizing the pressure losses across the bed of pellets. Recently, several authors proposed a segmentation configuration, i.e. the active material is divided in sequential segments and only one of them at a time is run. Both Gaeini et al. [117] and Weber et al. [118] chose a square prism cuboid reactor shape, dividing it in several quadrants (Figure 2.11, A and B). To investigate the integration of an open STES system for space heating, also Scapino et al. proposed a cuboid reactor, dividing the active material into 212 smaller cuboid [17] (Figure 2.11, C). However, the daily reactor – material reservoir design is found to be cheaper in terms of the amount of non-active material, since no

structural material is needed to separate the sorbent pellets 212 times. Moreover, an elaborated flow management is required to ensure the sequential access to each segment. For simplicity of configuration and since no evident advantages in using a unique large reactor are clearly left, the same design proposed for closed systems (Figure 2.4) is explored to make a comparison in terms of energetic performances between the selected materials.

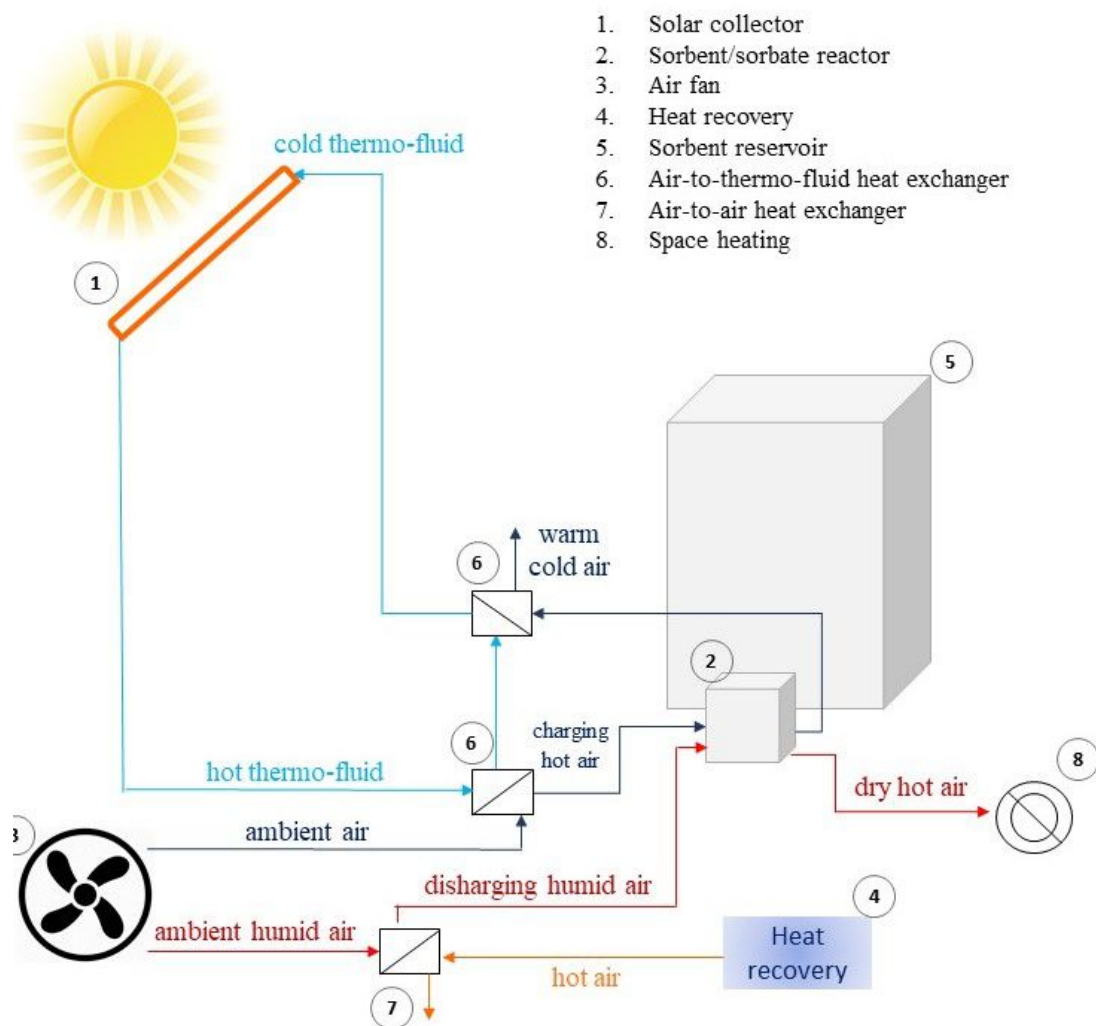


Figure 2.10: Schematic representation of an open STES system [117] [118] [17].

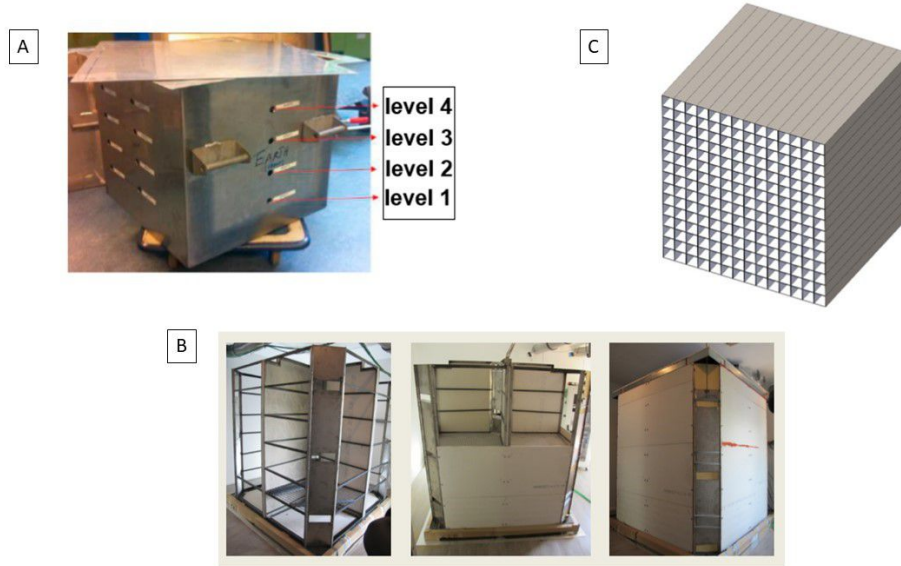


Figure 2.11: Examples of closed systems from literature.

As in the case of the closed system model, volumes and masses of the involved (active and non-active) materials can be evaluated. For details, readers can refer to the previous section. The heat transfer medium in an open system is humid air. The daily amount of heated air is estimated depending on \dot{Q} , the maximum achievable temperature from the sorption heat storage system and the temperature of the inlet air. The latter is taken from the environment. However, because of the low ambient temperature during winter, air can be preheated thanks to the presence of a heat recovery unit, which is supposed to recover air with temperature above 29 °C. If arbitrary considering a heat exchanger efficiency of 0,85, and assuming an environment temperature of 10 °C, a temperature of 27 °C of humid air entering the sorbent reactor can be supposed.

$$\dot{m}_{air} = \frac{\dot{Q}}{c_{p,air} \cdot (T_2 - T_1)} \quad (2.8)$$

Knowing \dot{m}_{air} , it is possible to evaluate the electrical power needed for air fans.

$$P_{fan} = \frac{\dot{m}_{air}}{\rho_{air}} \cdot \Delta p_l \quad (2.9)$$

The pressure losses, p_l , are evaluated according to the Ergun equation:

$$\Delta p_l = L \cdot \left(\frac{150 \cdot \mu_{air} \cdot (1 - \varepsilon)^2 \cdot \nu_{air}}{\varepsilon^3 \cdot D_p^2} + \frac{1,75 \cdot \rho_{air} \cdot (1 - \varepsilon)}{\varepsilon^3 \cdot D_p} \cdot \nu_{air}^2 \right) \quad (2.10)$$

In Figure 2.12 , a comparison between the Energy Storage Density of the sorbent material (blue dots), of the closed system (red dots) and of the open system (green dots) is made. As is possible to see, the closed system shows high energetic performances. Because of the low air-to-sorbent heat exchange efficiency when crossing the bed of pellets, indeed, a significant amount of active material is required. As a result, the volume of the system as a whole is larger in case of open systems with regards to that of the closed one (Figure 2.13), even if the closed system counts also the not negligible volume of the water reservoir. As expected, the material ranking with regard to the open system volume follows the same trend as the closed one.

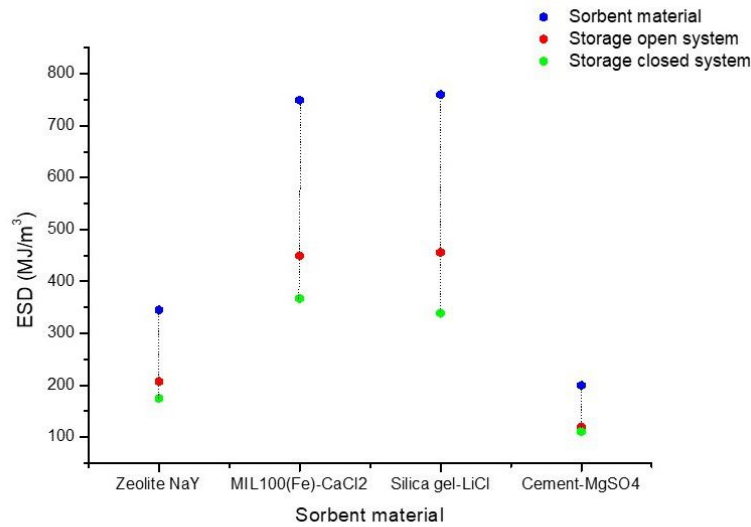


Figure 2.12: Chart reporting the value of Energy Storage Density of the sorbent material (blue dots), of the open STES system as a whole (red dots) and of the closed STES system as a whole (green dots).

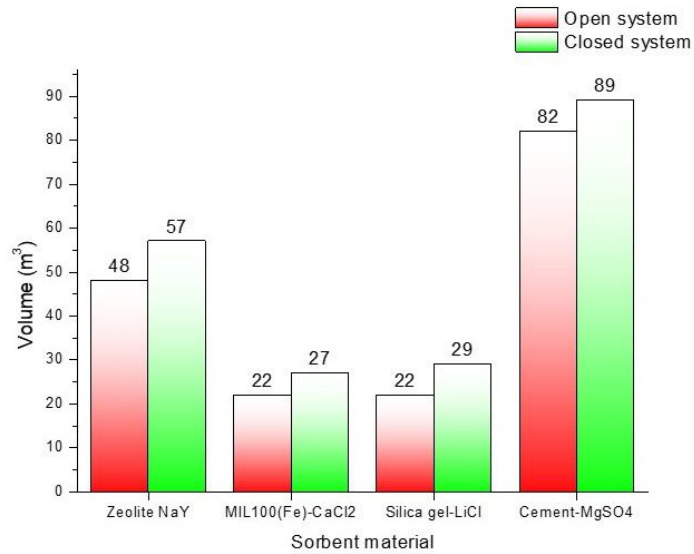


Figure 2.13: graphic representation of the whole volume of an open (red) or closed (green) STES system.

The relative economic contribute of four components composing the open system is compared in Figure 2.14. Now the active material plays the primary role, since the amount required to guarantee the yearly thermal energy is considerable. Moreover, the absence of a water reservoir, which is of key importance in the closed configuration, allows to reduce the amount of the involved non-active material. As previously pointed out, the yearly cost associated to the elevator carrying the discharged material from the reactor to the reservoir is negligible. In the end, the electrical power associated to the fan operation has a discrete contribute, with regards to the selected material. In particular, it is interesting to note that it makes about 20% of the whole system cost when using Silica gel-LiCl. In case of Zeolite NaY or cement-MgSO₄, it is overcome by the material cost. In the end it does not contribute anymore if MIL100(Fe)+CaCl₂ is chosen as sorbent. The analysis allows to point out a relevant aspect, usually little stressed, which is the temperature of discharging of the sorbent material. In case of open systems, the discharging temperature directly influences the air mass flow entering the bed of pellets. The higher the temperature of discharging, the lower is the mass of air required to answer the daily energy demand, i.e. the lower is the needed fan electrical power. It

must be remembered that low temperatures of desorption usually cause a decrease in the water uptake, since vapour condensation inside the porous structure is less spontaneous. Hence, this energetic consideration suggests to take it into account when evaluating the thermal energy storage abilities of different sorbents.

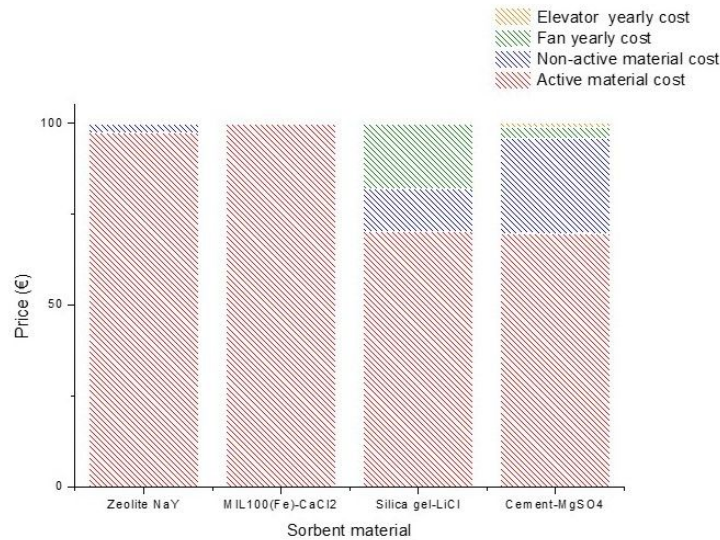


Figure 2.14: Graphic representation of the price contribute of the different components of an open STES system.

In the end, Figure 2.15 offers a comparison between systems and material alone, in terms of kWh/€. As is possible to see when choosing Zeolite NaY, MIL100(Fe)-CaCl₂ and Silica gel-LiCl, open and closed systems show a very similar performances, with the first one having slightly lower values. Cement-MgSO₄, instead, surprisingly inverts the trend, thus appearing drastically better if involved in a open system instead of a closed one. The reason of that comes from the fact that, as previously noted, the active material itself is particularly cheap and a more relevant cost is associated to the non-active material. Since open systems requires large amount of sorbent material but in the same time does not include relevant amount of non-active-material components, they result to be economically convenient if compared to closed systems, when cementitious materials are involved. On contrary, the open system configuration penalizes those materials having even good performances but at the same time a high price.

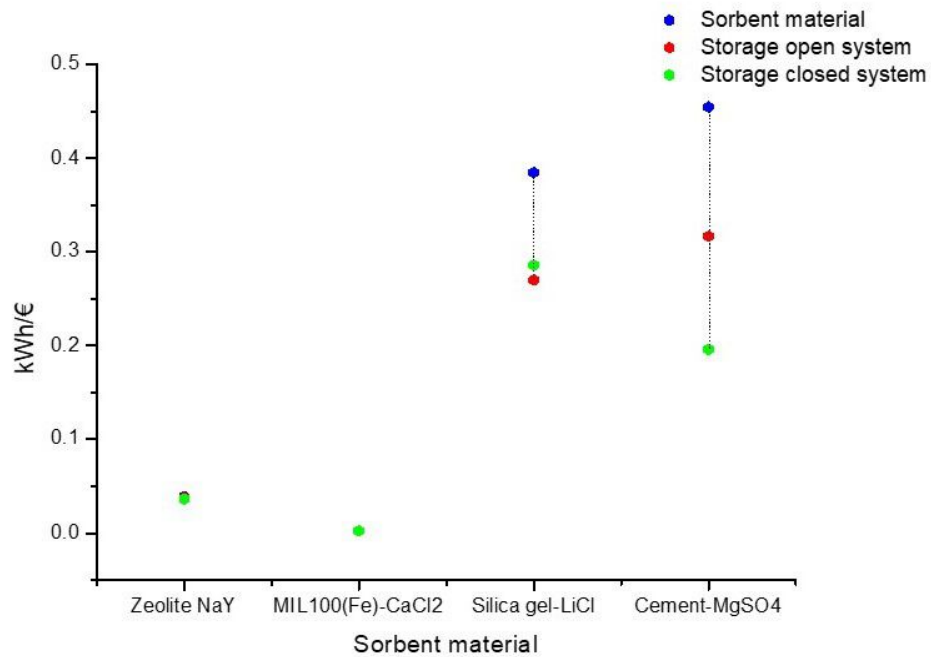


Figure 2.15: Chart reporting the value of Energy Storage Capacity per cost (kWh/kg) of the sorbent material (blue dots), of the open STES system as a whole (red dots) and of the closed STES system as a whole (green dots).

2.5 Optimization of the closed system working cycle

As evidenced in the previous section, several active material parameters, such as its discharging temperature, both ESC and ESD together with water uptake and material price must be considered thus to have a more precise idea about the energetic performances of a STES system. However, one step further in the attempt to investigate the system's energetic potential is required. It is related to the adsorption-desorption cycle working conditions, which directly affect the behaviour of the sorbent material.

The adsorption-desorption working cycle can be represented on a Clausius-Clapeyron chart i.e. a graphical representation of the pressure logarithm, $\ln(p)$ as a function

of the reciprocal temperature, $1/T$. (an example is on Figure 2.16). In particular, points A and C do not depend on the sorbent, being only dependent on the operating condition. In particular, A and C change with respect to the evaporation and condensation temperatures (i.e. their relative values of saturation pressure) respectively. On contrary, points B and D change with the chosen material as the isosteric slope and their spacing will change by changing the sorbent-sorbate pair.// The same working cycle can be represented in the Coverage-Pressure chart (Figure 2.17). In the latter, again, A and C are variable, depending on the working conditions. In the chart, the red line refers to the Coverage-Pressure line at the temperature of adsorption (discharging) while the blue one refers to the Coverage-Pressure line at the temperature of desorption (charging).

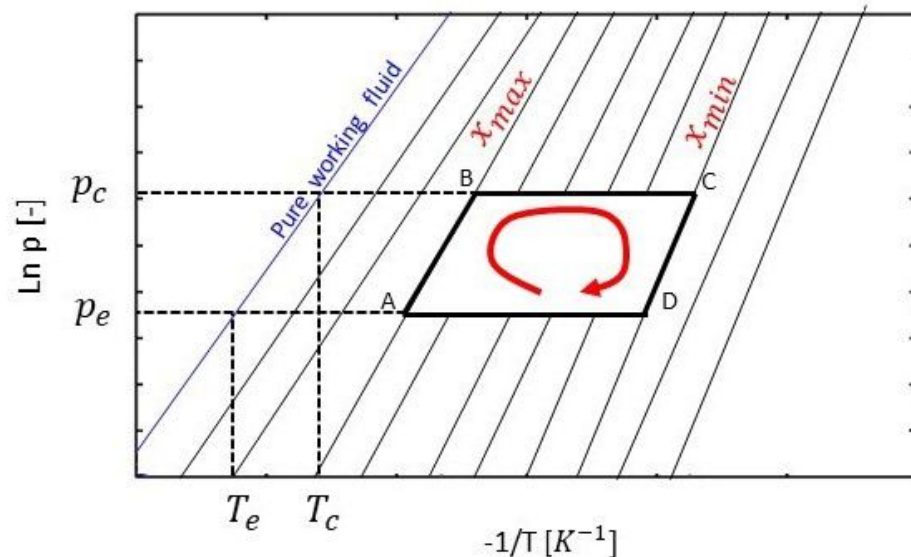


Figure 2.16: Schematic representation of an ideal (closed) sorption TES cycle in a Clausius-Clapeyron chart.

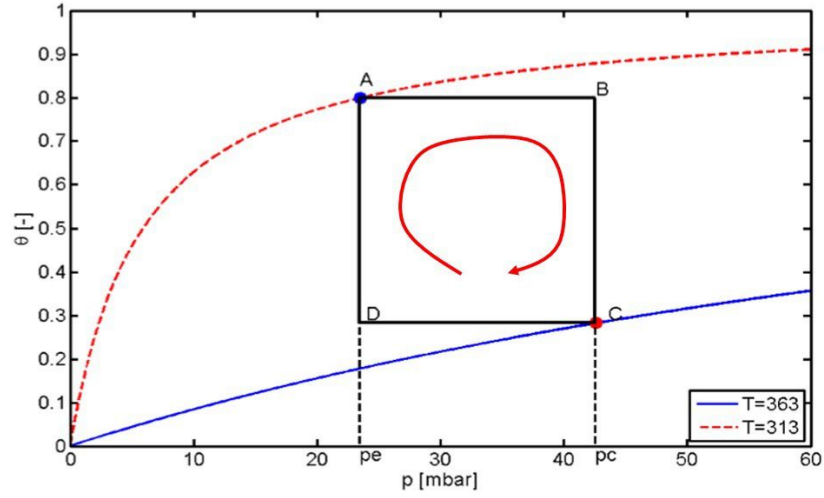


Figure 2.17: Schematic representation of an ideal (closed) sorption TES cycle in a Coverage-Pressure chart.

In a typical thermal storage application, the aim is to maximize the total heat that can be extracted during desorption (i.e. along the $A \rightarrow D$ segment). As previously said, the total adsorption heat (kJ/kg) can be calculated as follow:

$$Q_a = \frac{E_0 \cdot \Delta\theta}{PM_{H_2O}}$$

where E_0 is the isosteric heat of adsorption (kJ / mol of water), is the water uptake along the whole cycle and PM_{H_2O} is the water molecular weight (kg/mol).

The isosteric heat is typical of each adsorbent, depending on its physical and chemical behaviour. The water uptake, defined from the difference between the adsorbed water amount in the charging mode (i.e. after desorption) and the adsorbed water amount after discharging (i.e. after adsorption), depends instead on both material and working conditions. The material adsorption behaviour, indeed, determines the shape of the isotherms and, as a consequence, the height of the rectangular closed area. Many sorption materials exploited in STES systems show a type I isotherm. It is also the case of the cementitious material considered in this work. As previously said, the curve type I is specific for the situation of formation of a single layer of gas molecules, directly in contact with the surface.

The curve presents a very steep initial portion, approaching a limiting adsorption saturation loading at medium relative pressure (P/P_0). In view of maximizing the water uptake, the initial segment slope of the low temperature - isotherm might be as more pronounced as possible, making a sharp step. The saturation value is controlled by the accessible pore volume of the sorbent material. On the other hand, the working conditions fix both start-point (C) and end-point (A), defining the shape, i.e. the side lengths, of the rectangular cycle. As a result, while the shape of the isotherms is intrinsically defined by choosing the sorbent material, a certain degree of freedom while maximizing the water uptake is ensured by the cycle working conditions.

Hence, the sorption cycle can be optimized (i.e. the adsorption heat can be maximized) by choosing the working conditions for which the water uptake reach the maximum value. The working conditions strictly depend on where the sorption thermal energy system is located, i.e. which type of climate characterizes the considered area. During a cycle, indeed, the ambient air can be used as a heat source for evaporation and heat sink for condensation, since it is always available. As a result, by varying the local climate where the system is used, the temperature of condensation and the temperature of evaporation will change. By taking inspiration from [102], two different cycles, named WC and CC, are taken into account (Table 2.3).

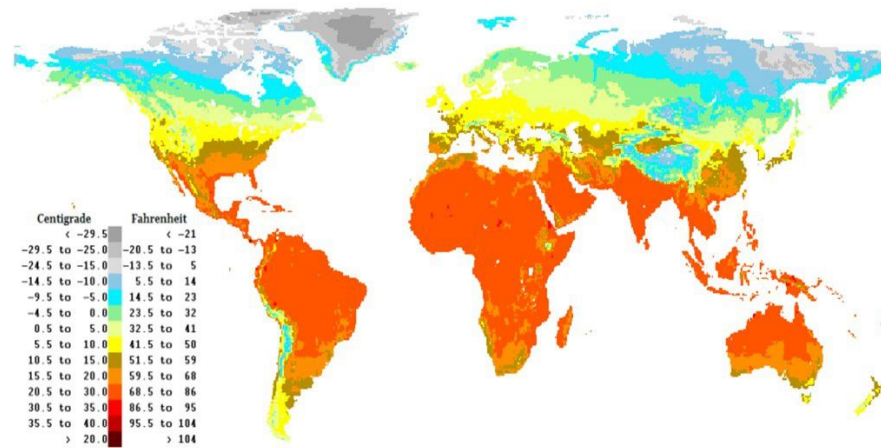


Figure 2.18: Geographical chart representing the world average temperature [119].

In areas with quite warm climate, such as South Asia, North Africa and Central America, the most feasible cycle is WC. The average temperature in January is about 10 °C, hence, the evaporation temperature equals 5 °C, which is somewhat lower than the temperature of the ambient air. The condensation temperature, instead, is fixed at 15 °C, which exceeds the outside air temperature. In regions with moderately cold climate (i.e. South Russia, Europe and central part of North America, the ambient temperature in winter reaches values below 0 °C, hence it appears too low to drive the evaporation. In comparison to air, the ground temperature in winter is higher and more stable. Hence, the heat needed to drive the evaporation can be extracted from the earth. By considering that the ground temperature equals approximately the average annual temperature, T_{ev} can be fixed at 10 °C while T_c is around 30 °C, which is around the average temperature in Summer. In the end, two discharging temperatures, 80 °C and 140 °C, can be considered for both cycles, according to the solar collector capacity.

Cycle	T charging	T discharging	T evaporation	T condensation
WC	80 / 140 °C	30 °C	10 °C	30 °C
CC	80 / 140 °C	30 °C	5 °C	15 °C

Table 2.3: Key parameters of two different climatic cycles: warm cycle, typical of areas as South Asia, North Africa and Central America, and cold cycle, typical of areas as South Russia, Europe and North America.

The water uptake of the whole ideal (closed system) WC and CC cycles for the cementitious material can be compared by looking at the isotherms reported on a Coverage-Pressure chart. In particular, in Figure 2.19 the reported cycles consider T_{dis} as to be 80 °C, while in Figure 2.20 T_{dis} equals 140 °C. In the first case, the adsorption heat is higher for CC ($\delta \theta = 0.025$) than for WC ($\delta \theta = 0.021$). In both cases, the water uptake is definitely lower than in case of T_{dis} equals to 140 °C. As is visible, indeed, the 140 °C-isotherm shows a very small step before assuming a plateau behaviour. As a result, the difference in height between the two isotherms (i.e. the amount of sorbate involved during the cycle) is more pronounced. Thanks to the well pronounced plateau-behaviour, the water uptake becomes more independent from the working conditions than the previous case. To conclude, with high-efficient solar collectors (i.e. able to provide a material heating up to 140 °C), the cementitious material shows good performances for both warm and cold climates. With low desorption – temperature, instead, this type of sorption material works well in warm-climate ambient. The Storage Capacity Cost increases by +19%, passing from WC to CC (Tab. 2.4).

Cycle	T discharging	Water uptake	ESC [KJ/kg]	SCC [€/kWh]
WC	80 °C	0,021	56	5,4
	140 °C	0,042	112	2,7
CC	80 °C	0,025	67	4,5
	140 °C	0,041	109	2,8

Table 2.4: Characteristic values of the adsorption cycles, WC and CC, with different discharging temperatures.

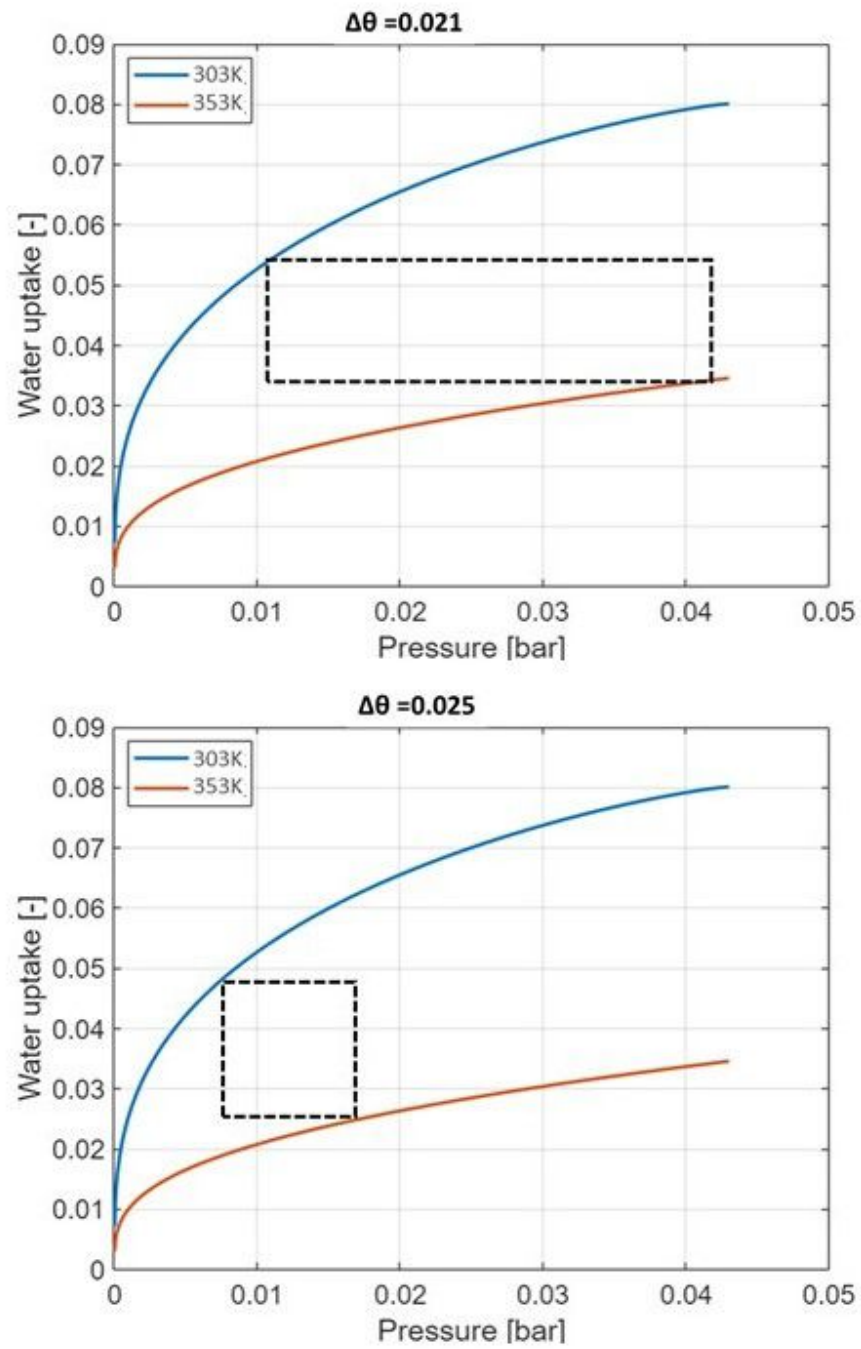


Figure 2.19: Coverage-Pressure chart for WC and CC cycles with temperature desorption of 80 °C.

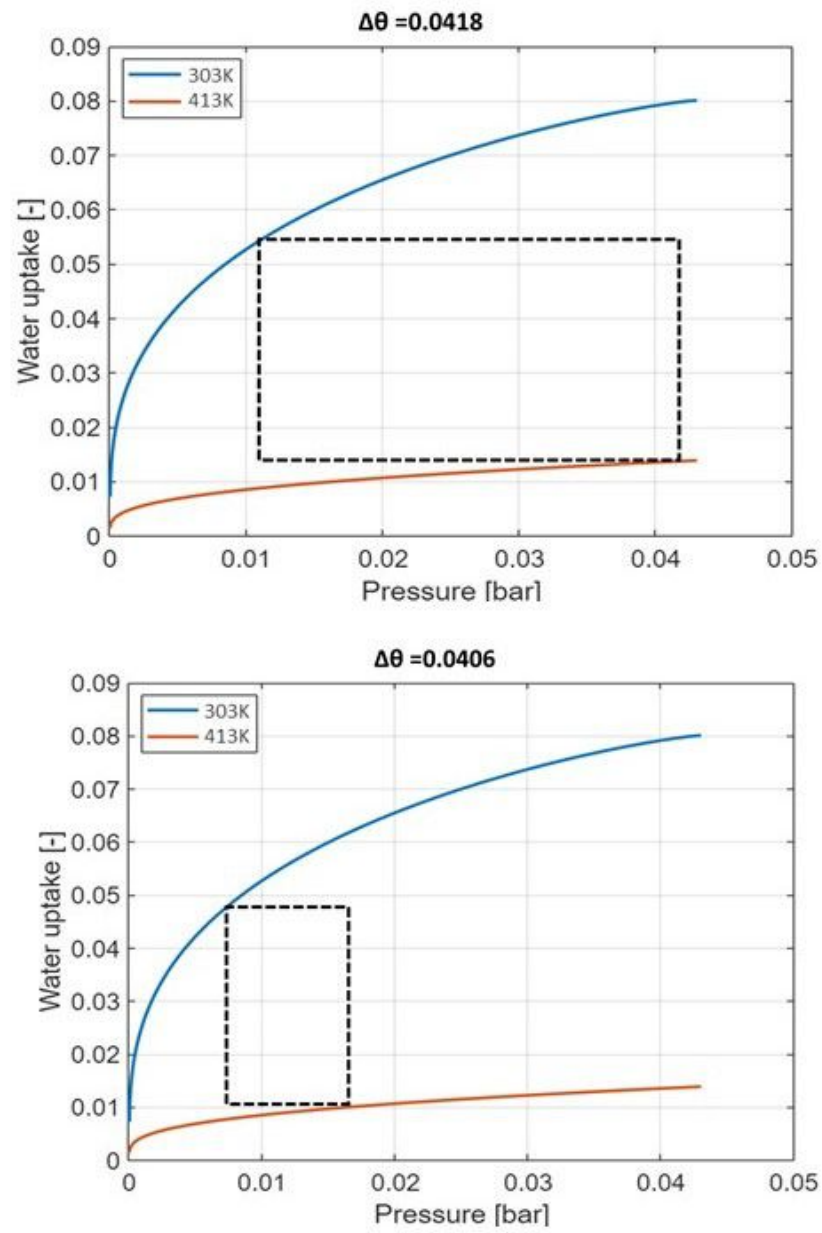


Figure 2.20: Coverage-Pressure chart for WC and CC cycles with temperature desorption of 140 °C.

2.6 Conclusion

In this section, an estimation of the ideal systems performance in terms of ESD and SCC. In particular, the novel cementitious material has been investigated in comparison with solid sorbent Zeolite NaY, and composites sorbents MIL100(Fe)-CaCl₂ and SiO₂-LiCl. As reference scenario, a family house space heating having solar collector able to provide the required temperature of desorption, is considered and a yearly energy demand of 10 GJ is assumed. Several energetic considerations have been allowed to evaluate both closed and open system features, such as the volume, the total price, ESD, ESC, and SCC. They have been compared to each other and to the active material alone. In the definition of the system's performances, the ESD value of the sorbent material plays a key role. It affects, indeed, the volume of the material reservoir and the reactor. The latter influences in the end the cost of the non-active material and the SCC of the system. The ESC of the sorbent material, indeed, defines the total amount of material required for the yearly thermal energy storage. As a result, the higher ESC, the higher is the yearly active material price, which directly affects the price of the system as a whole.

As expected, the Energy Storage Density of all systems falls down with respect to the active material, independently of the active material type. When considering the system as a whole, indeed, both the mass and the volume increase hence the specific energy values (with respect to the weight or the volume) decrease.

An interest comparison is done in terms of kWh/€. Because of the very high cost of Zeolite NaY and MIL100(Fe)-CaCl₂, normalizing the energy performance of both active material or system brings roughly to the same result. Silica gel-LiCl, instead, is more cost affordable even if less performant in terms of energy storage. Hence, it remains industrial-scale applicable. Cement-MgSO₄, instead, has the advantage to be decisively cheaper than the other active materials. It shows better performances when adopted in an open system. The latter, indeed, requires large amount of sorbent material but in the same time does not include relevant amount of non-active-material components, they result to be economically convenient if compared to closed systems. As previously said, this study does not pretend to be exhaustive however it comes from the awareness that a comparison between active materials only is simplistic and do not allow economic and feasibility considerations.

In the end, it has be highlighted that the real energetic performances of a sorbent material in closed systems also depend on the adsorption-desorption working conditions. In detail, it is possible to evaluate the sorbate uptake from the Coverage-Pressure charts. The latter reports both charging and discharging isotherms, whose shape depends on the material itself. Defining T_e and T_c (i.e. the working conditions) the sorbate uptake is evaluated and the heat of adsorption can be calculated.

Chapter 3

Fundamentals of cement-based materials



Figure 3.1: Picture of Portland cement powder.

Cements may be defined as adhesive substances capable of uniting fragments of solid matter to a compact whole [120]. They consist of grey powder that can be mixed with water and sand to make mortar or with water, sand, and small stones to make concrete [121]. When mixed, indeed, the cement paste hardens and develops binding property as consequence of numerous exothermic hydration

reactions, i.e. it behaves as hydraulic binder. Cement based materials have been used since many decades and the most widely used type of cement is Ordinary Portland Cement.

3.1 The manufacture of Portland cement

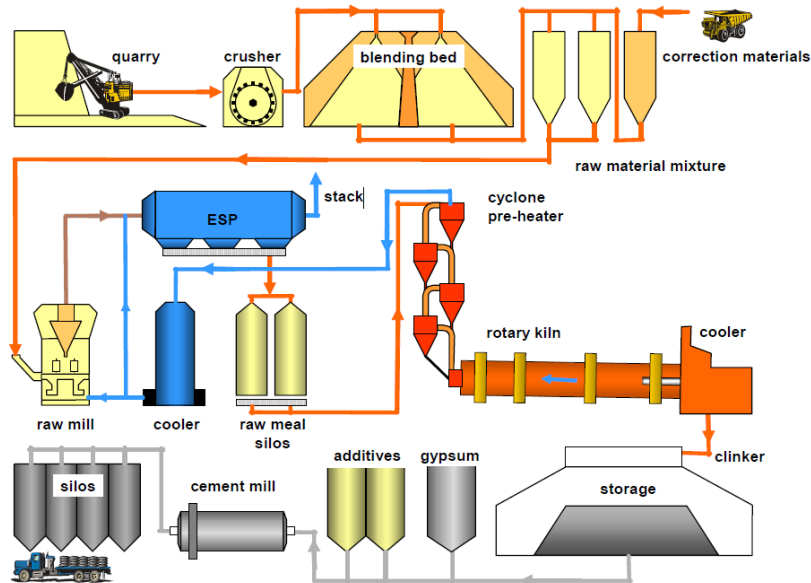


Figure 3.2: Schematic representation of the process of cement manufacturing [122].

Portland cement is a fine powder, grey or white in colour, consisting of a mixture of hydraulic cement materials which comprises primarily calcium silicates, aluminates and aluminoferrites. More than 30 raw materials are known to be used in the manufacture of Portland cement, and can be divided into four distinct categories: calcareous, siliceous, argillaceous, and ferriferous. These materials are chemically combined through processes of pyrolysis and subjected to subsequent mechanical processing operations to form the final product. The cement manufacture involves four different stages: quarrying, raw material preparation, clinkering and cement preparation [123]. Figure 3.2 schematically represents the production line of the cement. Thus process starts with the extraction of the raw material. The latter consists of rock mixture of about 80% of limestone (which is mainly composed

of calcium carbonate mineral, CaCO_3 [124] and 20% clay or shale, a source of silica, alumina and Fe_2O_3). After the extraction, raw materials are pre-crushed in a quarry usually located in the vicinity of the cement works. Quarrying is followed by the raw material preparation, which includes a variety of blending and sizing operations to provide a feed with appropriate chemical and physical properties. The raw material processing steps differ to each other with regard to which process, dry or wet, is used. In case of dry process, indeed, clay and limestone are crushed separately and then fed together into a mill. In the wet process, instead, clay is mixed to a paste in a washmill i.e. a tank in which the clay is grinded in the presence of water and crushed lime is added in the end. In both cases, laboratory analyses are required to ensure, and eventually adjust, the correct amount of all elements. The finely ground material is dried, heated inside a kiln and then cooled down again. This set of steps, to which one refers as clinkering, constitutes the main characteristic of Portland manufacture processing. It transforms the raw mix into clinkers, which are grey, glass-hard, spherically shaped nodules that range from 5 to 25 mm in diameter [125]. The reaction processes occurring within the kiln, heated by injecting pulverised coal dust into the discharge where it spontaneously ignites due to the very high temperatures, are not clearly understood. This is due to the wide variations in the chemistry of the raw mixture, the conditions of processing operations and the difficulties of extracting hot materials from the process for investigation before they cool. However, the chemical reactions and physical processes can be viewed as follow[124]:

- Evaporation of not combined-water from raw materials (20°C- 100°C);
- Dehydration (100°C - 430°C) : formation of oxides of silicon, aluminum, and iron;
- Calcination (800°C – 1100°C): formation of CaO, according the following reaction: $\text{CaCO}_3 \rightarrow \text{CaO} + \text{CO}_2$
- Exothermic reactions (1100°C – 1300°C): formation of secondary silicate phases: $2\text{CaO} + \text{SiO}_2 \rightarrow 2\text{CaO} \cdot \text{SiO}_2$
- Sintering and reaction within the melt (1300 - 1450 °C): formation of ternary silicates and tetracalcium aluminoferrates:



- Cooling and crystallisation of the various mineral phases

To obtain the final product, the clinker is mixed with gypsum and ground. Grinding is a high-cost operation consuming approximately 60% of the total electrical energy which is involved in a typical cement plant. The electrical energy consumed in the conventional cement making process is in the order of 110 kWh/tonne. Of that, about 30% is used for raw materials preparation while about 40% is invest for the final grinding. Finished cement is pumped pneumatically to storage silos from which it is drawn for packing in paper bags or for dispatch in bulk containers [126].

3.2 Hydration process of Portland cement

Hydration refers to a reaction of an anhydrous compound with water, yielding a hydrated compound. In cement chemistry, hence, hydration consists of the reaction of non-hydrated cement with water, having chemical and mechanical changes as consequences. Even if a partial hydration may take place in humid air, the complete hydration is reached by mixing the cement powder with a sufficient amount of water [127]. When cement is mixed with water, a number of chemical reactions starts to take place, causing the transformation from a plastic workable paste to a hard-solid material. The hydration of Portland cement is rather complex, since it is the result of the reaction of the main cement components with water. As a consequence, the clinker composition directly affects the transformation of the whole material.

3.2.1 Cement composition and minerals

The chemical composition of cement clinker is usually expressed as weight percentage of oxides. The most important oxides in Portland cement clinkers are CaO, SiO₂, Al₂O₃ and Fe₂O₃. The oxides occur in the cement clinker structure in forms of different clinker minerals. (21) . For simplicity, if we assume that the clinker contains mainly thus four main oxides, they can be simply represented by the

Bogue formulae. According to the latter, CaO, Al₂O₃, Fe₂O₃, and SiO₂ are denoted as C, A, F, and S, respectively [128]. However, there can be many other minor components, since natural clay also contains Na, K, Mg and other ions. Table 3.1 reports the composition of components, which is expressed as weight percentage. In Table 3.2 instead, the approximate composition of the cement clinker is described [129].

Compound	Formula	Notation	Weight (%)
Celite Tricalcium Aluminate	Ca ₃ Al ₂ O ₆ [3CaOAl ₂ O ₃]	C ₃ A	10
Brownmillerite Tetracalcium Aluminoferrite	Ca ₄ Al ₂ Fe ₂ O ₁₀ [4CaOAl ₂ O ₃ Fe ₂ O ₃]	C ₄ AF	8
Belite Dicalcium Silicate	Ca ₂ SiO ₄ [2CaOSiO ₂]	C ₂ S	20
Alite Tricalcium Silicate	Ca ₃ SiO ₅ [3CaOSiO ₂]	C ₃ S	55
Sodium oxide	Na ₂ O	N	<2
Potassium oxide	K ₂ O	K	
Gypsum Calcium Sulphate Dihydrated	CaSO ₄ ·2H ₂ O [CaOSO ₃ ·2H ₂ O]	CSH ₂	5

Table 3.1: Main components of Portland cement.

Component weight (%)	SiO ₂	Al ₂ O ₃	Fe ₂ O ₃	CaO	MgO	SO ₃
	21.9	6.9	3.9	63.0	2.5	1.7

Table 3.2: Chemical composition of Portland cement clinkers.

3.2.2 Chemical reactions involved in hydration

The hydration of Portland cement consists on a series of individual chemical reactions between water and the main components of cement powder. They take place both in parallel and successively.

Generally speaking, the progress of hydration is mainly affected by the phase composition, the fineness of the cement (i.e. specific surface and particle size distribution), the amount of mixing water with regard to the amount of cement (the so-called water-to-cement ratio, w/c), the temperature of curing and eventually the presence of chemical admixtures [130]. Due to the complexity of the cement composition, it is convenient to briefly discuss the hydration of the individual minerals. The main reactions are reported in Table 3.3 while Figure 3.3 reports the principle hydrated products.

		Main reactions of hydration			
(Eq 1)	2C ₃ S Alite	+ 6H ₂ O		→ C ₃ S ₂ 3H ₂ O C-S-H	+ 3Ca(OH) ₂ Portlandite
(Eq 2)	2C ₂ S Belite	+ 4H ₂ O		→ C ₃ S ₂ 3H ₂ O C-S-H	+ 3Ca(OH) ₂ Portlandite
(Eq 3)	2C ₃ A Aluminate	+ 21H		→ C ₄ AH ₁₃	+ C ₂ AH ₈
(Eq 4)	C ₃ A Aluminate	+ 3CSH ₂ Gypsum	+ 26H	→ C ₆ AS ₃ H ₃₂ Ettringite (AFt)	
(Eq 5)	2C ₃ A Aluminate	+ C ₆ AS ₃ H ₃₂ Ettringite (AFt)	+ 4H	→ 3C ₄ ASH ₁₂ AFm	
(Eq 6)	3C ₄ AF Brownmillerite	+ 12CSH ₂ Gypsum	+ 110H	→ 2[C ₆ (A,F)SH ₃₂] Ettringite (AFt)	+ 2(A,F)H ₃
(Eq 7)	3C ₄ AF Brownmillerite	+ 2[C ₆ (A,F)SH ₃₂] Ettringite (AFt)		→ 6[C ₄ (A,F)SH ₁₂] AFm	+ 2(A,F)H ₃

Table 3.3: Main reactions of Portland cement hydration.

C₃S

The main component of the Portland cement is tricalcium silicate (C₃S). It, indeed, controls in large extent the cement strength and hardening [131]. During the hydration of the component (Table 3.3, Eq. 1), four stages may be distinguished. First,

the so-called pre-induction period, lasting few minutes: immediately after coming in contact with water, there is a rapid hydration of C_3S . When C_3S comes into contact with water, indeed, a fast dissolution of ions from the surface takes place: O^{2-} ions enter the liquid phase as OH^- while SiO_4^{2-} ions enter as just dissociated $H_nSiO_{4(4-n)}$. As a result, the positive charge of Ca^{2+} entering the liquid phase is balanced by the negative charges of OH^- and silicate ions. Since the dissolution rate of C_3S is faster than the diffusion rate of ions from the surface, the liquid phase quickly becomes oversaturated with respect to calcium-silicate hydrate and a first layer of C-S-H products start to precipitate near the surface. This first step of reaction causes a relatively high heat of hydration. Successively, the rate of hydration slows down and then increases, with the second main heat evolution peak. Finally, the rate of hydration drops again in what is called deceleration period [132]. Several theories have been proposed to explain the not so obvious reasons for the decrease and following increase of the hydration rate. The deeply understanding of the kinetic of hydration, however, is out of the aim of this work and it is left to the reader's interest [133].

C-S-H constitutes the principal binding phase and its general chemical formula is $CaO \cdot SiO_2 \cdot H_2O_y$. The secondary product, CH, is formed since the CaO/SiO_2 molar ratio in the calcium hydrate phase is lower than that of tricalcium silicate i.e. 3:1.

C_2S

The second protagonist of the reaction of hydration is C_2S (Table 3.3, Eq. 2). In this case, as before, it is possible to distinguish different stages of reactions. An extended induction period, with a very low rate of hydration, is followed by a second stage of gradual increase of the hydration rate, since it slows down again in the third period of the hydration [134].

C_3A The third component involved in the reaction of hydration is the tricalcium aluminate, the most reactive phase in cement. Its role in (very) early hydration is of key importance and concerns both mechanical properties as well as rheological performances. The nature of the products that can be obtained through the hydration of C_3A depends on the presence or absence of calcium sulfate.

When no calcium sulfate is present, the first hydration product of C_3A is a gel-like material growing on the surface of the cement component. With time, this material

transforms into hexagonal crystals corresponding to the phases C_2AH_8 and C_4AH_{13} (or C_4AH_{19}) (Table 3.3, Eq. 3). These products finally convert into cubic C_3AH_6 . C_2AH_8 and C_4AH_{19} , indeed, are metastable hydration products while the latter is the only calcium aluminate hydrate that is stable at ambient temperature [135]. The rapid precipitation of hexagonal platelets cause the rapid setting, called “flash set”. The higher the temperature of hydration, the higher is the rate of conversion to the most stable hydration product. Moreover, when the temperature is above 80°C , C_3AH_6 forms directly from the hydration of C_3A . C_2AH_8 and C_4AH_{19} belong to the group of AFm. The latter is a shorthand for a family of mono-hydrated calcium aluminate phases structurally related to hydrocalumite. A representative formula is $[\text{Ca}_2(\text{Al,Fe})(\text{OH})_6] \cdot \text{X} \cdot x\text{H}_2\text{O}$, where X equals an exchangeable singly charged or half of a doubly charged anion. To avoid the rapid setting of the paste, keeping a longer period of workability, calcium sulfate is added to and ground together with the clinker. In the presence of calcium sulfate, indeed, ettringite is the main product of hydration, with composition $C_6AS_3H_{32}$ (3.3, Eq. 4). It belongs to the group of AFt, the family of three-hydrated calcium aluminate phases with the general formula $[\text{Ca}_3(\text{Al,Fe})(\text{OH})_6 \cdot 12\text{H}_2\text{O}] \cdot \text{X} \cdot x\text{H}_2\text{O}$. [136] Ettringite is stable as long as sulfates are still available in the system. Once calcium sulfate is consumed, ettringite reacts with the remaining C_3A to form AFm (Table 3.3, Eq. 5). As ettringite is gradually consumed, hexagonal calcium aluminate hydrate, C_4AH_1 , also starts to form. It may be present in the form of a solid solution with C_4ASH_{12} or as separate crystals [137].

C_4AF

The last element who participates to hydration is calcium aluminoferrite (C_4AF). It is also known as brownmillerite and it is the only variable phase with unfixed composition in ordinary Portland cement. Brownmillerite represents a large family of solid solution $\text{Ca}_2(\text{Al}_y\text{Fe}_{(2-y)})\text{O}_5$, where the values of y are in the range of 0 to about 1.33. As before, the hydration of the cementitious element is influenced by the presence (or the absence) of calcium sulfate. When in contact with water, if calcium sulfate is not involved, metastable C(A,F)H hydrates (hydroxy-AFm) are rapidly formed on the surface of the unhydrated grains and eventually transform into a stable phase $C_3(\text{A,F})H_6$. It is generally observed that the Al/Fe ratio of the original C_4AF is lower than that of the products of the reaction with water [138].

The decrease of Al/Fe of the hydrated products can be explained by the formation of an amorphous iron-rich gel or iron hydroxide, as a secondary product of reaction [139].

In the presence of calcium silicate, instead, the hydration products of C_4AF are similar to those of C_3A (Table 3.3, Eq. 6). The rates of reaction of the two components, however, differ to each other. C_4AF , indeed, reacts much slower than C_3A in the presence of gypsum, i.e. the latter retards the hydration of C_4AF more efficiently than it does C_3A . Generally speaking, the rate of hydration of C_4AF depends on the composition of the ferrite phase: the higher the amount of Fe, the lower the rate of hydration [140]. In presence of calcium sulfate, an AFt phase is the main product of reaction: In a subsequent reaction step the AFt phase converts to AFm, by the reaction of excess C_4AF with the sulfo-aluminate phase (3.3, Eq. 7).

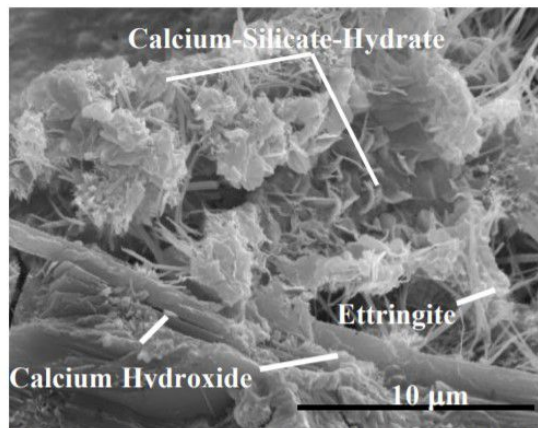


Figure 3.3: SEM images of fracture surfaces on hardened Portland cement paste at very early hydration [141].

3.2.3 Mechanism of Portland cement hydration and heat of hydration

The kinetic of hydration has been extensively under study, since it determines the development of the microstructure hence the evolution of the cement properties, both fresh and hardened. Since the cement-water reaction involves dissolution of the anhydrous phases together with the precipitation of the hydration products, its progress with time depends on the kinetic of dissolution [142], the rate of nucleation

and crystal growth of the hydrates [134],[143]. Hydration kinetic of an ordinary Portland cement is reported in Figure 3.4 and Figure 3.5. It is well accepted that the hydration of the cement paste can be divided into four steps: pre-induction period, induction (dormant) period, acceleration period, post – acceleration period. Each step is briefly described below.

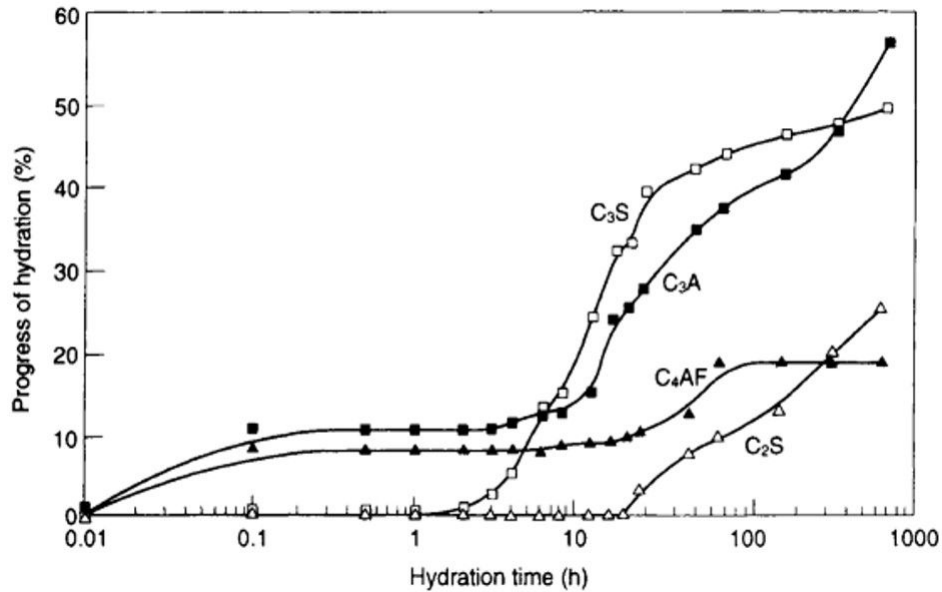


Figure 3.4: Plot of the progress of hydration with regard to the time of reaction of the main components of Portland cement [144].

Pre-induction period (few minutes)

Soon after cement and water enter in contact, ionic species fastly dissolve into the liquid promoting the formation of hydrates. In particular, alkali sulfates dissolve, releasing free K^+ , Na^+ , SO_4^- while calcium sulfate dissolves until saturation, releasing Ca^{2+} and SO_4^- . Meredith et al. [145] have used the so-called Environmental Scanning Electron Microscopy (ESEM) to observe the formation of a coating formed over the grain surfaces immediately upon contact. Sharma et al. have investigated the same reaction period exploiting FESEM. Both authors, and several other researches, recognized this primary product to be C-S-H in its early morphological form. The C-S-H layer is seen to thicken and extend to cover most of the grain surface by the end of the first period, until the exhaustion of easily available surface reactants. The reaction of C_3S with water proceeds, as previously discussed, via the

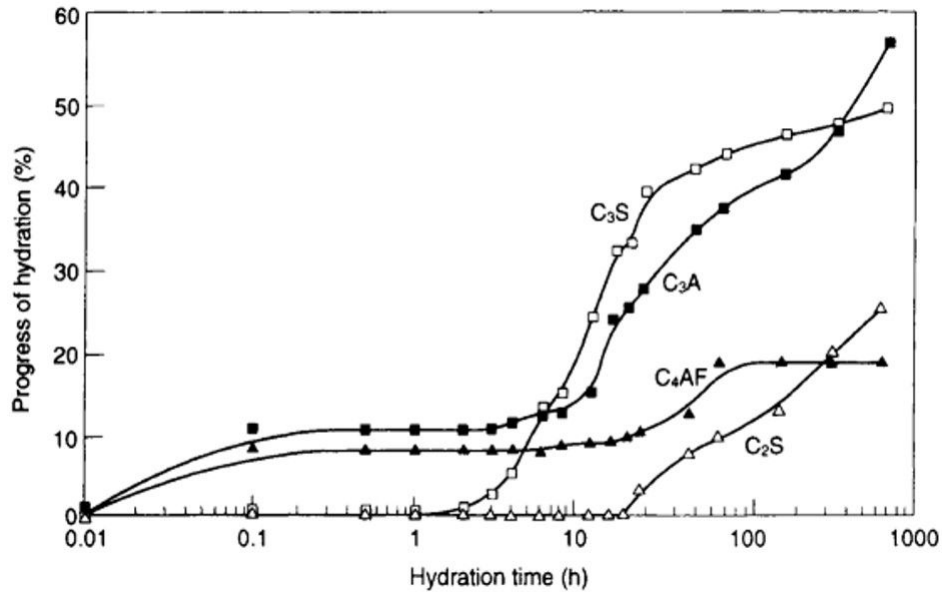


Figure 3.5: Plot of the progress of formation of the main products of hydration with regard to the time of reaction [144].

approximate route of Table 3.3, Eq.1 . Thomas et al. [146] have studied the solution chemistry of Portland cement, with particular attention to the concentrations of calcium and silicon in the aqueous phase during early stages of hydration (Figure 3.6). Since the CaO-SiO_2 ratio of the product is lower than that of C_3S , the concentration of Ca^{2+} and OH^- in the liquid phase increases during this first step of hydration. At the same time, according to Table 3.3, Eq.4, the addition of water in cement leads clinker mineral and gypsum to dissolve quickly, generating ions such as Ca^{2+} , OH^- , Al_2O_3 , SO_4^{2-} , which formed a supersaturated solution for ettringite. These ions diffuse together by concentration difference, and leads to the formation of ettringite through steps in liquid phase. In particular, according to Jiahui et al.[147] $[\text{Al}(\text{OH})_6]^{3-}$ octahedral formation is the slowest reaction, which controlled the AFt formation. Moreover, the kinetic rate of reaction depends on the concentration of aqueous ions. Among the ions forming ettringite, AlO_2^- is the lowest, so it is the main factor influencing the ettringite formation . Only a small amount of C_2S hydrates during this first step. Even if shows broad similarities to that of C_3S , the slower rate of hydration of belite is probably due to its different crystalline structure and the higher thermodynamic stability of C_2S . Moreover,

C_2S presents a high density whereas the presence of holes in the structure of C_3S makes it easily attacked by water [148].

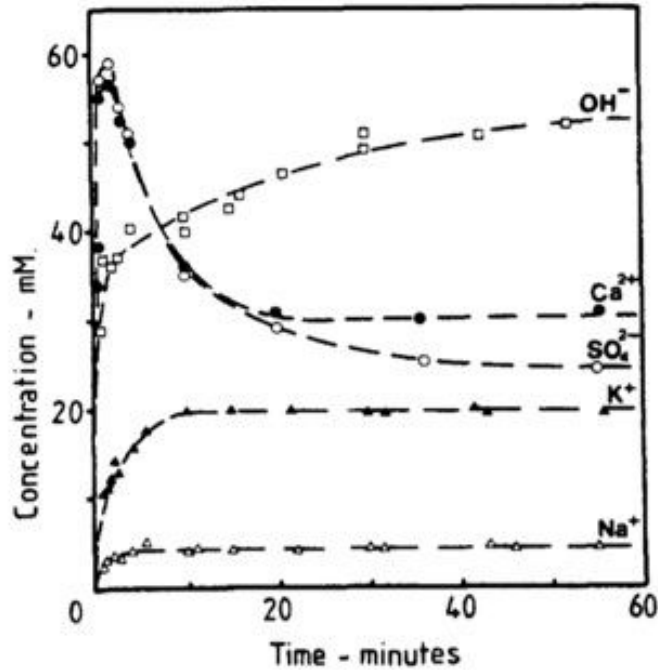


Figure 3.6: Concentration versus time curves for solution filtered from cement paste, with $w/c = 2$ [146].

Induction period (few hours)

After the short but fast hydration of the cement, the overall hydration rate slows down for few hours. Two main theories, the theory of the protective membrane and the theory of dissolution, have been proposed to give reasons of the sharp slowdown after few minutes, reconciling the apparent low reactivity with the high C_3S solubility calculated from its enthalpy of formation. Both of the two present some pros and cons, as recently highlighted by Scrivener et al. [149]. According to the theory of the protective membrane, a decrease of the rate of hydration is caused by the formation of a layer of metastable C-S-H. It covers the reacting surface of cement particles, preventing fast dissolution of C_3S [150]. As discussed before, several studies have provided evidence that C-S-H form rapidly just after entering in contact with water. However, what must be called into question is the formation of a low-permeable layer of hydrates, with enough density and coverage to dramatically slow down the rate of diffusion of ions from the anhydrous grains.

Figure 3.7 reports a SE-SEM image of a hydration C_3S grain during the induction period [151]. It is possible to appreciate that C-S-H does not form a continuous layer around the grains hence its surface is actually still in contact with the pore solution. According to the authors, this observation weakens the protective membrane guess as responsible for the decrease of the rate of hydration.

The second hypothesis suggests that the rate slowdown is due to the decrease of the kinetic of dissolution of C-S-H and alite while the system is moving towards equilibrium. Several researches have been done on it and some of them are summarized in [152]. However, as comment by the authors, the dissolution of C_3S has nearly always simplistically accounted for in all models addressing cement hydration kinetics, mostly because the dissolution step is studied in isolation i.e. independently from the other mechanisms which characterize the hydration of the cement paste. In the latter case, indeed, dissolution happens together with precipitation of hydrates, which presence on the reacting surface might interfere with the process of dissolution of the cement paste components. As a result, the hypothesis of the dissolution theory as cause for the induction period remains valid but research must go on in clearly highlighting how the kinetic of dissolution is responsible for the period of induction.

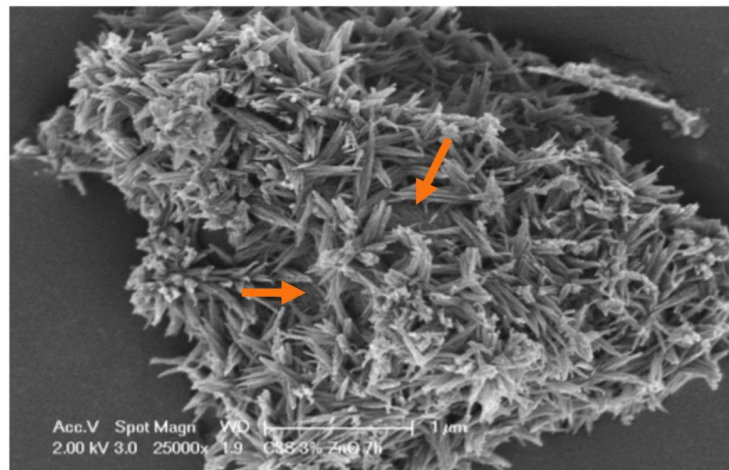


Figure 3.7: SE-SEM image of a hydration C_3S grain one hour before the peak. Note that C-S-H does not form a continuous layer around the grain, its surface is actually still in contact with the pore solution. This weakens the diffusion barrier hypothesis [151].

Acceleration period (3-12 hours)

In the third period the progress of hydration accelerates one more time, controlled by the nucleation and growth of the resultant hydration products. The rate of C₃S hydration accelerates, forming what is said to be “outer” C-S-H. It differs from the so-called “inner” C-S-H, that starts to form at the end of this third period. Tennis et al., [153] indeed, published a model of calcium silicate hydrate distinguishing between low-density (LD) and high-density (HD) C-S-H, which corresponds to outer and inner hydration products, respectively. Figure 3.8 reports a SEM image of C₃S grain after 96 hours of hydration, where it is possible to distinguish the two types of C-S-H. The first one (at left) is formed during early hydration. It is away from the cement particle surface, filling water-filled space and characterized by high porosity. The second one (at right) is formed during later hydration and is characterized by lower porosity. It has been reported to be the inner C-S-H more abundant as w/c decreases [154].

A noticeable hydration of C₂S gets also under way. Portlandite precipitates from the liquid phase and its concentration in the liquid phase decreases, together with that of Ca²⁺. The calcium sulphate, interground to the cement, becomes completely dissolved and the concentration of SO₄⁻ in the liquid phase starts to decline, because of the formation of AFt phase together with its adsorption of SO₄⁻ on the surface of the formed C-S-H phase.

Post acceleration period

After having reached a maximum of hydration rate, the latter slows down gradually in what is called “post accelerated – period”. During this, “inner” C-S-H is formed from C₃S and C₂S. About the post acceleration period, one time more, several theories have been proposed to give reason of the change in kinetic. However, explanation for the presence of a deceleration have changed during time. One of the oldest theories was proposed by *De Jong, Stein* and *Stevels* in [156] is sustained by Breugel et al. [157], who provided a numerical simulation of hydration and microstructural development in hardening cement-based materials proposing a computer based - numerical model HYMOSTRUC. According to the authors, the variation of the hydration kinetic is related to the growth of a diffusion layer: as C-S-H precipitates on the surface of the cement grains, it forms a thickening layer that ultimately becomes thick enough to act as diffusion barrier. However, even if it remained valid for lots of time, thus theory has been refused during the last decade.

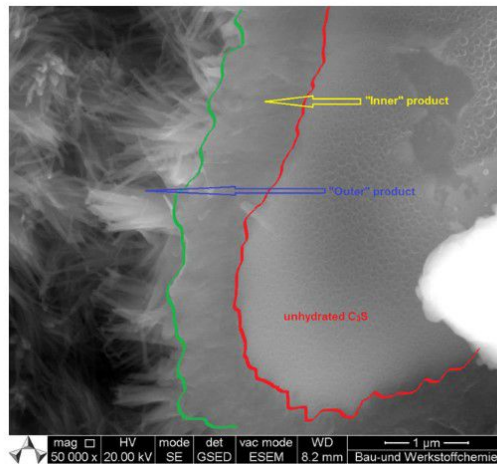


Figure 3.8: SEM image representing two types of C-S-H, the main product of Portland cement hydration. At left, *outer* is away from the cement particle surface, filling water-filled space and characterized by high porosity. At right, *inner* C-S-H is formed during later hydration and is characterized by lower porosity [155].

Argumentations contributing to the failure of the theory are deeply reported in [151] and left to the reader's interest. The main statement disproving this theory comes from the analysis of what happens to grains of different size. One would expect, indeed, to see similar hydrate layer thicknesses at the peak around alite grains of all sizes, even when these sizes are hydrated separately. This is not the case as shown by *Fernandez et al.* [158] (Figure 3.9). The thickness of the layer of products after hydration around small grains, indeed, is much greater than that around large grains. As explained in [159], the deceleration period for different grains fits with diffusion control only if changing parameter related to the diffusion coefficient of C-S-H by an order of magnitude across the range of particle sizes studies. However, C-S-H is the same independently on the size of particles above which it is formed so it cannot be presumed to have such a widely varying diffusion coefficient. Another qualitative evidence comes again from the fact that regions of very low density-product persist between the hydrating grain and the "shell" of hydrates hence a layer is not dense enough to largely hinder the diffusion of ions. Most recently, the work of *Bazzoni et al* [132] reports that during the acceleration period clusters of C-S-H nucleate on the cement grain surfaces and grow rapidly to a certain length. The deceleration period corresponds to a drastic slowing down of

the growth rate of the C-S-H, which at this point covers most of the surface of the grain. However, to understand the mechanisms behind the observed nucleation and growth rates is clearly one of the next challenges. The very last period of hydration is characterized by a low rate of hydration. The latter, indeed, seems to be limited by the less available space. Taking into account that hydrates can be formed only in water filled space, lack of space can be explained through two (non-exclusive) ways, the volume of water available for precipitation is depleted or the remaining water filled pores are smaller a critical pore size for precipitation (cit). In parallel with the formation of inner C-S-H, the supply of calcium sulfate continue to decrease till it becomes exhausted. At that point, the SO_4^- concentration in the liquid phase declines and the AFt phase that has been formed in the earlier stages of hydration starts to react in a through-solution reaction with additional C_3A and $\text{C}_2(\text{A},\text{F})$, yielding AFm. (cit)

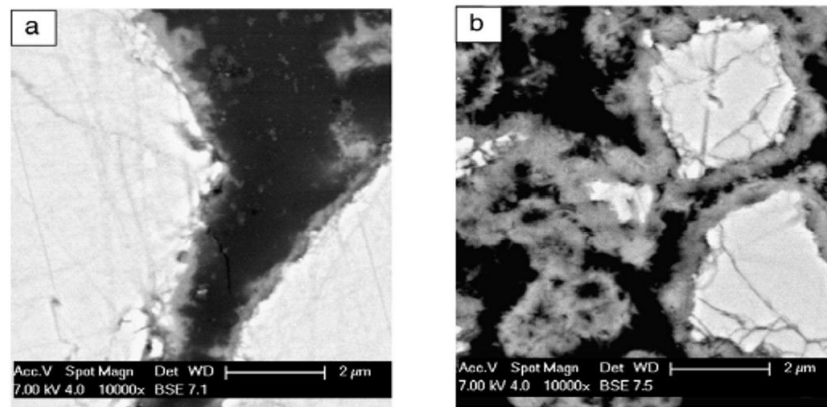


Figure 3.9: Images of two sizes of alite particles, hydrates separately, taken near the peak of reaction rate. a) original particle size is 38 micron, b) original particle size is 6 micron. It is possible to note that the thickness of the layer of products after hydration around small grains is much greater than that around large grains [160].

3.2.4 Heat of hydration

The mechanism of hydration is usually discussed in terms of the heat evolution curve. By looking at a typical curve of heat of hydration, reported in Figure 3.10, it is possible to recognize five different stages, schematized below:

1. Initial endothermic peak, immediately after mixing, due to the dissolution of potassium sulfate
2. Intense liberation of heat with a maximum within a few minutes, due to the rapid initial hydration of C_3S and C_3A , together with the hydration of calcium sulfate in the first period of hydration
3. Minimum, associated with the dormant period in which the overall rate of hydration is slowed down
4. Exothermic peak, due to the hydration of C_3S and the formation of C-S-H and Portlandite
5. Small peak at the descending branch of the main peak, due to the renewed AFt formation
6. Small peak due to the conversion from AFt to AFm

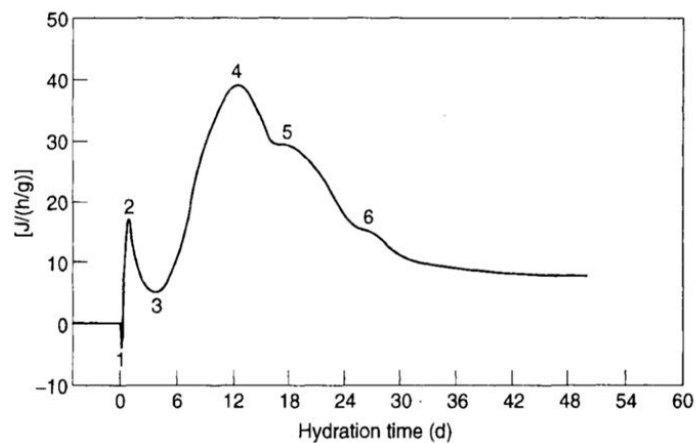


Figure 3.10: Plot of the hydration heat evolution of an ordinary Portland cement. 1: K_2SO_4 dissolution. 2: early stage reaction. 3: dormant period. 4: middle-stage reaction (C-S-H formation). 5: AFt formation. 6: AFt-AFm conversion [144].

3.3 Setting of Portland cement

ASTM C125 [161] defines "time of setting" as the elapsed time from the addition of mixing water to a cementitious mixture until the mixture reaches a specified degree of rigidity, which is measured by a specific procedure. In other words, setting is the process of transformation of a 'fresh' cement paste of plastic consistency into

a set material which is not more deformable. Therefore, conversion is gradual and continuous and the time required for the whole process is usually determined based on the penetration resistance using a Vicar beedle (ASTM c191 [161]). It is important to distinguish "setting" from "hardening", which follows the first one. Hardening, indeed, refers to the increase of hardness, strength and modulus of elasticity, until an ultimate value of these parameters is reached. Moreover, setting is preceded by a time of stiffening of the paste, during which the viscosity of the material increases, without losing its plastic behaviour.

3.3.1 Mechanism of setting

After entering in contact with water, Portland cement grains are distributed in the liquid phase. Within few minutes after mixing, cement particles undergo flocculation thus the viscosity of the paste increases. The flocculation structure of the cement paste was observed by *Uchikawa et al.* [162], through rapid freezing of the water with liquid nitrogen (Figure 3.11). Based on the results, few minutes after mixing with water only coarse particles (approximately 10 micron in diameter) with fin particles (3 micron or less) are dispersed in the free water. Besides, few single fine particles and further aggregated coarse particles can be observed. Thus, aggregates of cement particles entrap a fraction of the mixing water, thus making it unable to participate in the flow of the paste. During the dormant period the flocculation is reversible, hence aggregates can be destroyed by remixing the paste. As soon as the induction period of hydration of C_3S has finished (about three hours after mixing with water), C-S-H begins to precipitate besides AFt and the amount of hydrated material increases rapidly while the volume of the liquid phase declines. At this point, several particles agglomerate together through the fine particles existing between them. At six hours hydration, the hydrated compounds mainly consisting of C-S-H, are three-dimensionally connected to each other by locally deposited thick layers of hydrated compounds. Contacts between particles are now strong and can't be destroyed by mixing. As the hydration progresses, the amount of product continues increasing and the bonds between solid particles strengthen, resulting in a gradual increase of strength of the set paste. It is imperative that the hydration is stopped instantaneously at a predetermined time, hence a freeze-dry technique is used for that work. The freezing of the sample with liquid nitrogen ensures that all chemical processes are very much retarded, while

the subsequent water evaporation step at low temperature minimizes any thermally induced chemical transformations other than water removal while drying. However, the drying will surely affect a little the structures of some phases, modifying the morphology of the structure. Bound water, like in ettringite, could be partially removed, and morphological properties may change upon removal of water. The early hydration and setting of Portland cement was also monitored by *Ylmen et al.* [163] by Scanning Electron Microscopy, reported in Figure 3.12. While looking at that images, however, it must be noted that to study very early hydration using an ex situ technique,

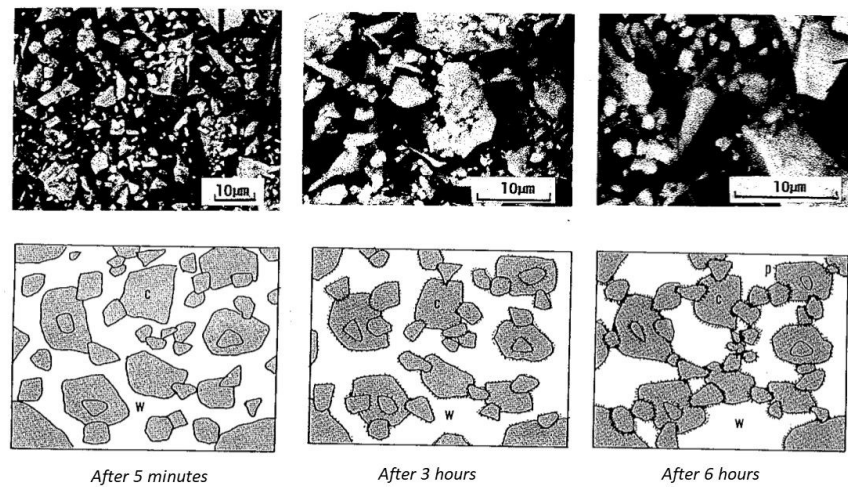


Figure 3.11: On top, back scattered electron images of fresh cement paste by SEM based on the sample freezing method after 5 minutes, 60 minutes and 6 hours. Below, schematic representation of the mechanism of flocculation in the same moments [162].

3.3.2 Flash setting and false setting

With the term “flash set” one refers to the rapidly loss of plasticity of the cement paste after mixing with water, strongly limiting the time of workability of the material. This fast transformation of the paste is due to the increase of early reaction of aluminat and ferrite phases, and the formation of plates of AFm throughout the paste, with high heat of hydration [164]. The meshwork of plates,

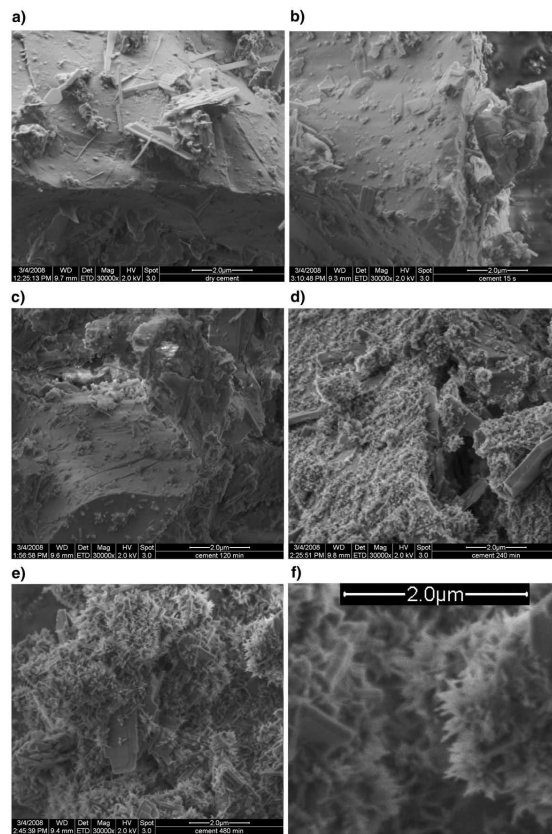


Figure 3.12: SEM pictures of surface of cement particle hydrated at a) 0 s, b) 15, c) 120 min, d) 240 min, e) 480 min, f) 480 min at higher magnification. At 0s, the surfaces are bare. After 15 s and 120 min of hydration, the surfaces of the particles are still found to be bare, but new lumps and platelets have formed. After 240 min of hydration, a carpet is covering the cement particles and is seen to consist of needle-like protruding structures. The latter can be attributed to the formation of C-S-H [163].

which is responsible for minimising the chances of remixing, can be contrasted with the much more compact coatings of gel and small needles of AFt phases that form in presence of gypsum. The latter, indeed, acts as a set regulator, which is added or interground with the clinker. It dissolves in the liquid phase, releasing a certain amount of Ca^{2+} and SO_4^{2-} . As described in Section 2.2.3, the amount of C_3A and C_4AF hydrated in the initial pre-induction period is reduced and AFt is formed during the hydration. The AFt phase precipitates at the cement grain surface in the form of a microcrystalline layer. Under these conditions the flowability

and plasticity of the paste is preserved until the formation of more hydrates, in particular C-S-H, causes 'normal set'. Similar, but not equal, to flash set is what is called "false set". It is due to the formation of calcium sulfate dehydrated (secondary gypsum) crystals, when in presence of low amount or no C_3A . The setting is due to the interlocking of gypsum crystals. In this case, unlike the case of "flash set", the plasticity of the mix may be restored by intensive mixing. The same effect can be observed in cements with high concentration of K_2O , because of the precipitation of $K_2Ca(SO_4)_2$ or in cements with high amount of C_3A , because of the excessive formation of AFt.

3.4 Pore structure

3.4.1 Type of pores

Gel pores Gel pores have size of approximately few nanometres and exist inside the hydration products that accumulate between the liquid phase and the anhydrous cement grains. Due to their small size, which is only an order of magnitude greater than the size of the water molecules, and due to the great affinity of water molecules on the gel surfaces, the movement of water in gel pores does not contribute to the cement paste permeability.

Capillary pores

Capillary pores arise from the initially water-filled spaces presented in the fresh paste. In the hardened phase, those spaces become interconnected channels or, if the cement paste is dense enough, cavities interconnected only by gel pores, and are called capillary pores. They have highly irregular shape and their size ranges from few nanometres to few micrometres. The presence of capillary pores is related to the amount of water that is involved in the process of hydration of the cement powder. It was found, indeed, that in order to reach the full hydration of 1 gram of cement, 0.42 g of water must be introduced. As a result, if the weight ratio water/cement is higher than 0.42, a part of the mixing water is still not combined and remains between cement particles, forming capillary pores. Hence, as showed in Figure 3.13, the higher the w/c ratio, the higher is the porosity of the hardened cement [165].

Hollow-shell pores

Hollow-shell pores can be considered as the third type of intrinsic pore of cement hydration. They are closed, very distinct pores and generally have the shape of the relicts of cement particles. Their formation is due to the fact that sometimes hydrates do not form within the original cement grain boundaries hence a void space (i.e. hollow shell) can develop within the boundary of the original cement grain as the cement grain recedes during hydration. This category of pores has size of around several micrometres. However, because of the so-strong “ink-bottle” nature, these pores may not easily be detected by many indirect methods for pore characterization, such as mercury intrusion porosimetry.

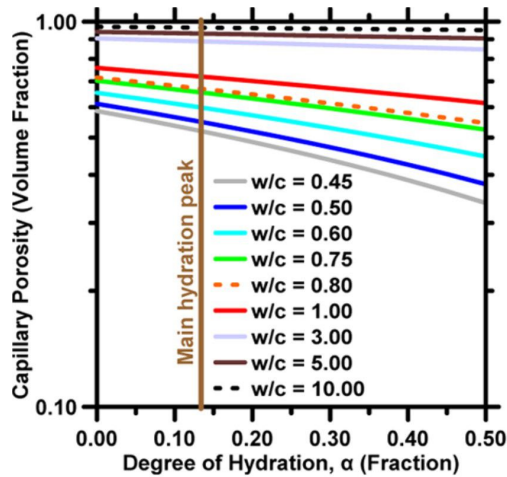


Figure 3.13: Correlation between capillary porosity and degree of hydration (α) in pastes prepared at different w/c . In these calculations, α is provided as an input, and the corresponding capillary porosity is calculated based on the phase assemblages predicted by the Powers model. The solid vertical line indicates the average value of α of all pastes, prepared using the coarse cement at the main hydration peak [166].

Air voids

Air voids can be “entrapped” or “entrained”. Entrapped air voids occur while mixing, because of the relevant viscosity of the cement paste. They could be of irregular shape and they are typically isolated from each other, hence they don’t contribute to the permeability of the material. They can be easily recognised under an optical microscope. Entrained air voids, instead, are introduced intentionally

during production of concrete by using an air-entraining chemical admixture, thus increasing the freeze-thaw resistant of cement-based materials. They present uniformly distributed through the cement paste and are usually not interconnected to each other hence they don't affect the permeability of the paste. They can be easily distinguished from the entrapped air voids because of their spherical shape and their average size similar to that of the cement grains [165].

3.4.2 Types of water

Water, essential for the reaction of cement, is introduced during the process of mixing the cement paste and leads the development of the hardened cement paste. According to its behaviour inside the cement paste, it is possible to distinguish three types of water: chemically bound water, gel water and evaporable or free water. Chemically bound water is a constituent of the solid material in the paste. Powers' model in 1960 [167] determined that the chemically bound water for a fully hydrated cement paste is equivalent to 0.23g over 1 gram of cement. *Prochoń et al.* in 2016 proposed the measurement of the chemically bound water as the relative mass loss between 105°C and 1050°C, finding values strictly similar to 0.23 for different types of cement pastes [168]. Gel water is defined as the water that is physically bound to C-S-H gel. In Power's model, it is considered to be 0.19 g over 1 gram of cement. If considering the previous value of chemically bound water, it results that 0.42 g is the minimal amount of water to completely hydrate 1 gram of cement, as previously mentioned. In the end, capillary water (or free water) is that contained in the capillary network of pores. At 105°C, gel water and free water are considered to be totally evaporated from the porous structure.

3.4.3 Bleeding of water in cement paste

The term "bleeding" refers to a form of sedimentation, in which a certain amount of mixing water tends to rise to the surface of the fresh cement paste. As a result, the interparticle distance is reduced and the final volume of the hardened paste results less than the volume immediately after placing. As a result, the actual amount of water inside the paste is minor than that originally introduced for mixing i.e. actual w/c is minor than initial w/c. The properties of bleeding of cement paste are usually described by the rate of sedimentation and the total amount



Figure 3.14: Picture representing the effect of bleeding.

of bleeding water, i.e. the difference between mixing water and the final content of water inside the cement. *Radocea et al.* (1992) [169], determined the settling velocity by measuring changes in pressure in the zone that, at the end of the sedimentation, consists of clear water. According to the author, cement paste is a suspension with a very high concentration of solid material hence cement particles hinder one another from falling freely. For most of the time, cement paste can be compared with a suspension of mono-size particles (Figure 3.15), whose rate of settling depends on to inter-particle attraction.

More recently, *Massoussy et al.* have clarified the mechanism of settling. As reported in [170] they recognized five stages. First, there exists an induction period displaying a low water extraction velocity. It is followed by an accelerating period, during which the apparent permeability of the paste increases due to the formation and percolation of the above water extraction channels. In the third stage the rate of water extraction is more or less constant. In the end, a consolidation decelerating regime leads to a condition in which gravity is not able to induce the settlement of particles anymore.

The effect of bleeding increases with increasing the amount of mixing water i.e. the w/c ratio. Therefore, in case of high w/c to be obtained, anti-settling agents are often added. Some examples of anti-settling agents are the following. Bentonite may be used to reduce slurry settling by absorbing large quantities of water so

that the slurry homogeneity is preserved (Figure 3.16). *Mesboua et al.* found that a bentonite content of 16% is considered to be an optimum dosage to produce a stable cement paste without sedimentation and bleeding [171]. Hydrosoluble polymers can act as viscosifying, increasing the viscosity of water. For this scope, one of the most commonly used class of materials is of cellulosic derivatives. By adding methyl cellulose to the cement paste, for example, *Nguyen et al.* reported a reduction of water settling in mortars (i.e. mixtures of cement, sand and water) as consequence of the increase in the cohesiveness between cement hydrates due to the presence of a film of methyl cellulose (Figure 3.17)[172]. In the end, metallic salts such as $MgCl_2$ create weak but extensive hydroxide structure through the slurry volume, hence water remains entrapped. However, their presence can cause a decrease in tensile and compression strength[173].

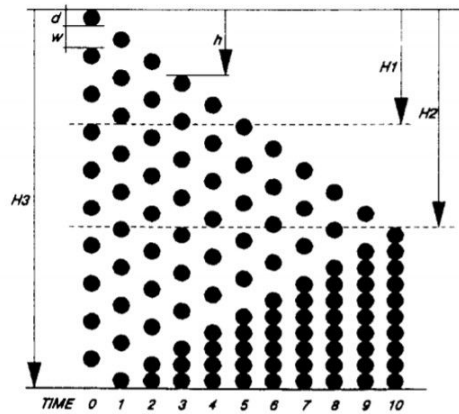


Figure 3.15: Schematic representation of mono-size particle sedimentation. For most of the time, cement paste can be compared with a suspension of mono-size particles, whose rate of settling depends on to inter-particle attraction [166].

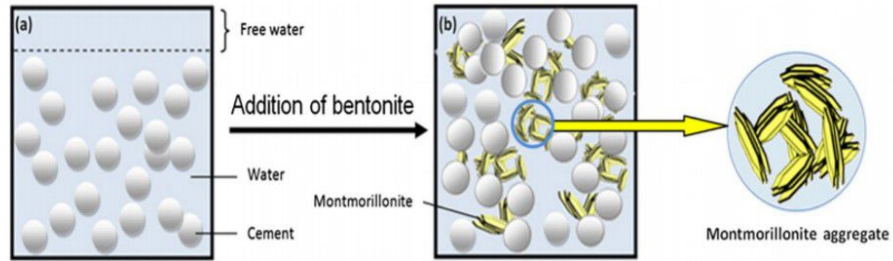


Figure 3.16: Schematic representation of bleeding of cement, in absence (a) or presence (b) of bentonite. Bentonite is showed to absorb large quantities of water so that the slurry homogeneity is preserved and settling is hindered [171].

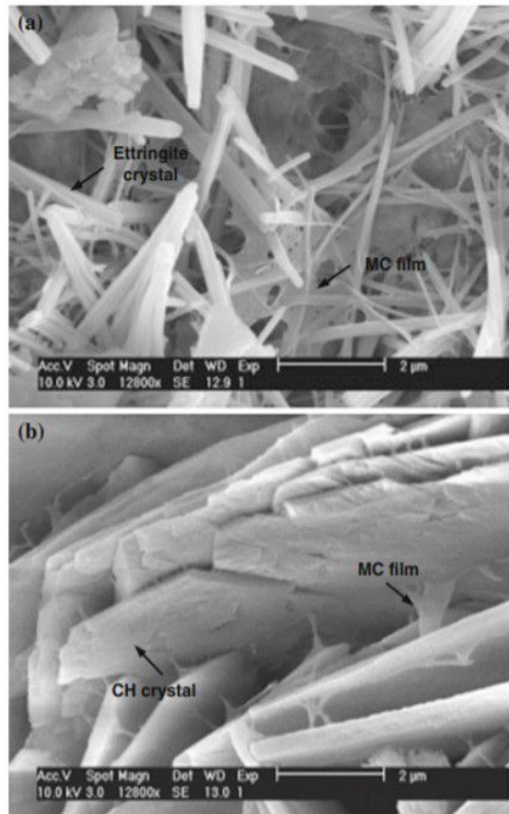


Figure 3.17: SEM image of mortar modified using 1% of methyl cellulose (MC). After wet storage, one can appreciate the presence of (a) bridges of MC film between ettringite crystals and (b) bridges of MC film between CH crystals [172].

Chapter 4

Experimental section

4.1 Preparation and morphological characterization

4.1.1 Materials and methods of characterization

Materials

Portland cement 52.5 (Ital Cementi s.p.a) is used as matrix for the composite material. The composition of the cement powder in terms of oxides weight percentage is reported in Table 4.1, while the weight percentage of the dehydrated and hydrated phases are reported in Table 4.2. MgSO_4 and CaCl_2 are provided from Merck.

Preparation of the cementitious matrix by impregnation

The method of preparation is schematically reported in Figure 4.1.

The first step involves the preparation of the fresh cement paste by adding a certain amount of cement dry powder (1), according to the desired w/c value, to 40 dm³ of clean water. The slurry is mechanically mixed for few minutes, until reaching homogeneity, (2) and then cast into a stainless-steel mould of size 20x20x80 mm³ (3). The second step consists on the heat treatment, to expedite the kinetic of hydration, thus reducing the hydration time of the cement fresh paste from 28 days to 24 hours. The material setting requires 100% of humidity hence, to keep the environment completely wet, the mould is leaning upon a ceramic support, into a plastic box. The latter is filled with water and sealed with aluminium. The

Oxide	%wt
SiO ₂	21.7
CaO	62.9
Al ₂ O ₃	3.2
Fe ₂ O ₃	3.7
MgO	4.3
SO ₃	2.2
Na ₂ O	
K ₂ O	
Na ₂ O	0.54
Loss on ignition	0.74
Insoluble residue	0.14

Table 4.1: Oxides weight percentage of Portland cement 52.5 .

Phase composition	%wt	Products of hydration	%wt
C ₃ S	66	C ₃ S ₂ H ₃	67,4
C ₂ S	18	CH	36
C ₃ A	7	C ₃ AH ₆	9,8
C ₄ AF	9	C ₄ AFH ₆	11

Table 4.2: Dehydrated phases (above) and hydrated products (below) weight percentage of Portland cement 52.5 .

whole system is put into the oven at 85 °C and kept for 24 hours (4). To limit the bleeding phenomenon, an anti-settling (AS) agent is added to the cement powder in different weight percentage, with respect to the cement weight. In Table 4.3 all prepared samples are reported.

Dry impregnation

For the preparation of the MgSO₄ -cement composite, the dry - impregnation method is chosen (6). First, the porous matrix is dried at 85 °C for 1 hour, such to

Name	AS agent [%]	theoretical w/c [g/g]
c04		0.4
c06		0.6
c08		0.8
c1		1
c1_05	0.5	1
c1_1	1	1
c1_1.5	1.5	1
c1_2	2	1
c1.5_05	0.5	1.5
c1.5_1	1	1.5
c1.5_1.5	1.5	1.5
c1.5_2	2	1.5
c2_1	1	2
c2_1.5	1.5	2
c2_2	2	2

Table 4.3: Lists of the prepared cement samples.

remove water from its surface and from the inner pore volume. Then, the material is impregnated with a saturated solution of heptahydrate MgSO_4 . The salt content inside the matrix must be controlled, thus to avoid the oversaturation of the matrix. During adsorption, indeed, the aqueous salt solution must not overcome in volume the available pore space, thus leaking out of the matrix. For this reason, the volume of solution is equal to the volume of accessible pores.

The result of both single and double impregnation (i.e. two consecutive impregnations of the sample, with a dehydration treatment after the first one) is evaluated. In the second case, the volume of solution is established by taking into account the volume of salt that has been introduced during the first impregnation, in the dehydration state.

The total amount of salt (in weight percentage) inside the cement sample is calculated according to 4.1:

$$x = \frac{Q_{sat} - Q_d}{Q_d} \cdot 100 \quad (4.1)$$

with Q_{sat} and Q_d the weight of the saturated and dehydrated cement sample,

respectively.

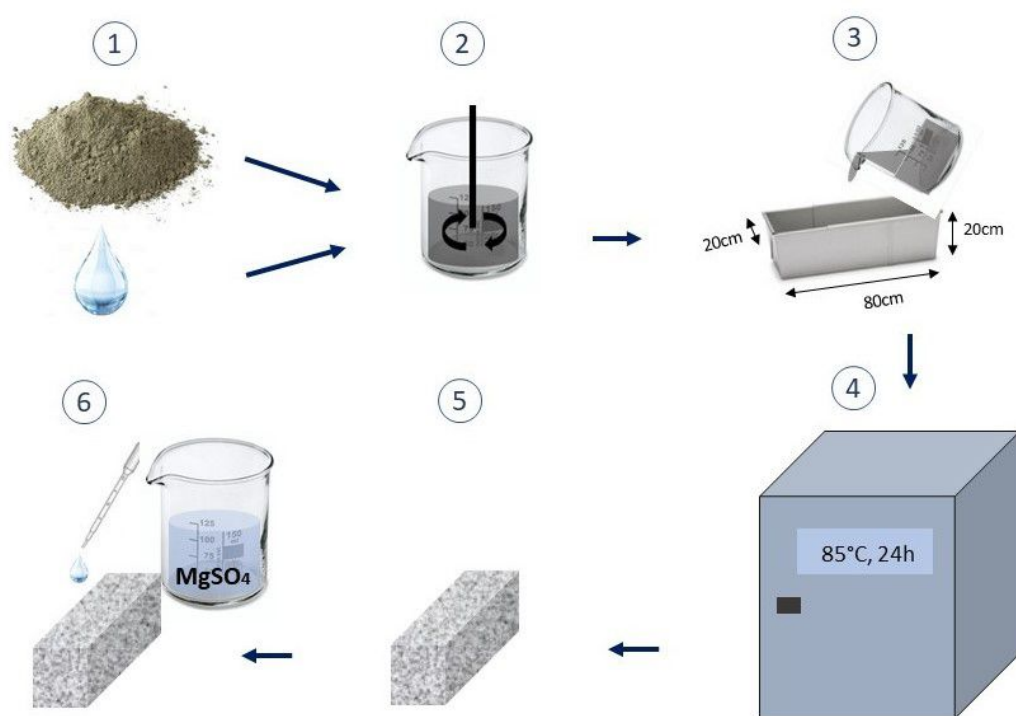


Figure 4.1: Schematic representation of the method of preparation of the composite cement-MgSO₄ sorbent material by *impregnation*.

Preparation of the cementitious composite in situ

The method of preparation is schematically reported in Figure 4.2. As first step, a volume of 40mL of saturated solution of MgSO₄·7H₂O is prepared, considering that the salt product of solubility is equal to 113 g/mL. The solution is mechanically stirred until complete dissolution of salt is reached. At that point, cement powder is added to the solution, according to the desired final w/c ratio. The cement paste is mixed for a while and then cast into the steel mould, which is put into the oven for the same thermal treatment used for the preparation of the cement matrix. In detail, S1, S1.5 and S2 (Table 4.4) are selected as best samples to be investigated for their energetic properties.

Sample	w/c ratio	Mass of salt [g]	Theoretical concentration of salt [%]
	[g]		
S1	1	45.5	53
S1.5	1.5	45.5	63
S2	2	45.5	70

Table 4.4: Composition of the *in situ* composite material.

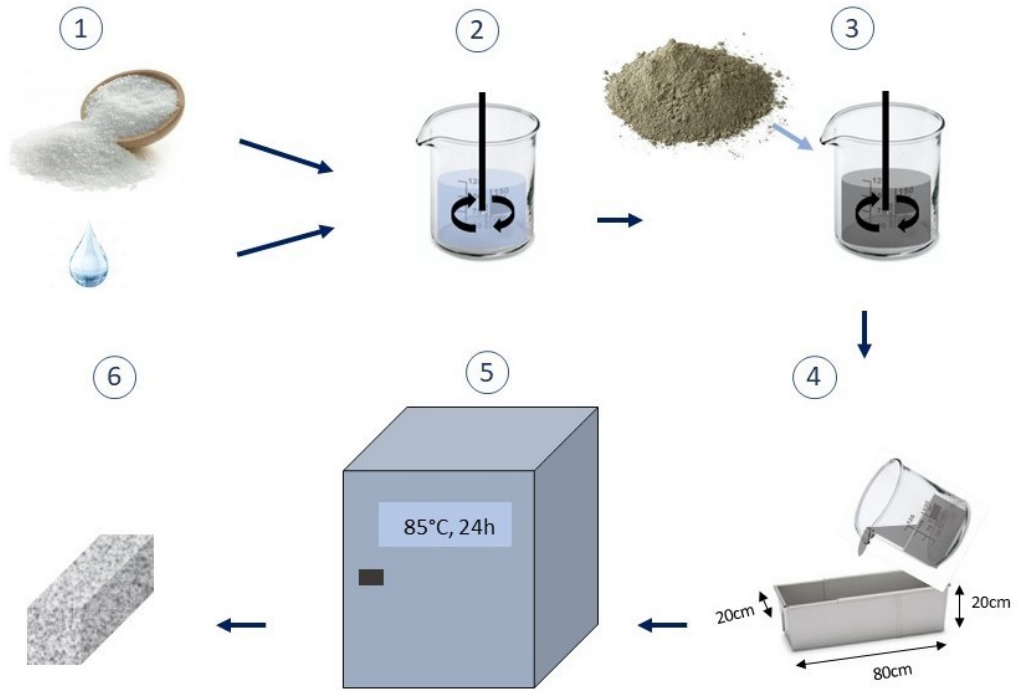


Figure 4.2: Schematic representation of the method of preparation of the composite cement-MgSO₄ sorbent material *in situ*.

Thermogravimetric analysis (TGA)

TGA is performed with Mettler Toledo 1600 for all samples thus to check the correct setting of the cementitious material. It reports the sample weight loss when heating it through a defined thermal ramp, with respect to the temperature. The result of a thermogravimetric analysis on a cement sample, indeed, is characterized by some peaks and each of them is associated to a specific phase composing the

cementitious material. By comparing the thermograms of samples having followed the traditional 28 days – curing process with that of samples thermally treated at 85 °C for 24 hours, the compatibility of the high temperature hydration can be checked. The analysis was performed with an heat rump of 1 °C/min, from 25 °C to 1000 °C , with the attempt to distinguish different peaks from each other as much clearly as possible.

Actual w/c ratio

For the calculation of the value of w/c characterizing the cement samples, the weight of the sample at saturation, Q_{sat} ,when pores are still filled with water, and the weight of the sample after dehydration, Q_d are measured. Moreover, two types of water are defined. In detail, w_h water of mixing, i.e. the amount of water mixed to the cement dry powder (c) while w_n refers to the chemically bonded water. As explained in Section 2.4.2, the w_n/c ratio shall be 0,23.

The value of w/c is calculated according to the following mathematical steps.

$$Q_{sat} = w_0 + c = \frac{w_0}{c} + c \quad (4.2)$$

$$Q_d = w_n + c = \frac{w_n}{c} + c \quad (4.3)$$

$$Q_{sat} - Q_d = w_0 + c - 0,23 - c = \frac{w_0}{c} \cdot c - 0,23 \quad (4.4)$$

Combining Eq. 4.2 and Eq. 4.4, with c and w_0/c as unknowns,

$$\frac{w_0}{c} = \frac{1,23Q_{sat} - Q_d}{Q_d} \quad (4.5)$$

Error bars are calculated by considering the uncertainty of the measurement of weight as $5 \cdot 10^{-2}$. As a result, the error value (ϵ) follows Eq. 4.6 :

$$\epsilon = \left(\frac{0,1}{1,23 \cdot Q_{sat} - Q_d} + \frac{0,05}{Q_d} \cdot \frac{w_0}{c} \right) \quad (4.6)$$

Geometrical density and porosity

The geometrical density of cement samples before impregnation is calculated according to Eq. 4.7:

$$\rho_g = \frac{Q_d}{V} \quad (4.7)$$

where ρ_g is the geometrical density and V is the volume. Error bars of the experimental values of density are calculated by taking into account the measurement uncertainty of the involved instruments. In particular, a measuring error of $5 \cdot 10^{-4}$ m for the geometrical dimensions and one of $5 \cdot 10^{-2}$ g for the weight of samples are considered. The whole accessible pore volume, P , is defined by Eq. 4.9:

$$P = \frac{Q_{sat} - Q_d \cdot \frac{1}{\rho_w}}{V} \quad (4.8)$$

where $Q_{sat} - Q_d$ represents the amount of free water filling the accessible pores, ρ_w the water density and V the volume of the sample. It must be pointed out that this method does not allow the calculation of the porosity as a whole but the accessible one, only. However, closed pores do not play a role in hosting the hygroscopic salt nor contribute to the formation of an internal path for water. Hence, closed pores can be ignored. In the end, the analysis of the pore structure through considerations of dimensions and weight do not return a pore size distribution. However, in this case it appears more feasible than other techniques, such as Hg-intrusion porosimetry, which can damage the pore structure of cementitious materials thus returning significantly altered results. ([174] [175]).

The experimental values of open porosity can be compared to the theoretical ones. The latter can be calculated through the following equations:

$$V_i = \frac{w}{c} + \frac{1}{\rho_c} \quad (4.9)$$

$$V_f = (1 - \alpha) \cdot \left(0,42 + \frac{1}{\rho_c}\right) + \alpha \cdot 2,14 + \left(\frac{w}{c} - 0,42\right) \quad (4.10)$$

$$v_{voids} = (v_i - v_f) + \left(\frac{w}{c} - 0,42\right) \quad (4.11)$$

$$P_{open} = \frac{V_{voids}}{V_{final}} \quad (4.12)$$

where V_i and V_f are the initial and final volume of the cement paste, respectively, 0,42 is the amount of water needed to complete the cement paste hydration and 2,14 is the volume of the products of hydration per unit of cement.

Optical microscopy and stereo microscopy

The cement samples are observed through the classic compound microscope (Leica CTR 4000 inverted microscope) and the stereo microscope (Leica EZ4 W). The first one is for viewing slides illuminated by light at high magnifications. It provides one optical path, which is then divided at the observation tube to convey the same image to both eyes. The second one, instead, is an optical microscope variant. It has two eyepieces and lower magnification than compound microscope. The dual eyepieces create two axes offset from one another, which creates depth perception for a three-dimensional view. Although the optical microscopy is widely used for visually analyse the morphology of materials, in the case of cementitious materials it could not work well. Its work mode, indeed, is based on the reflection of light from the surface of the specimens: since cement has a lot of fluctuation and its surface is not light-reflecting, seeing all details simultaneously could be hard. On the other side, in stereomicroscope, the light beam hits to the surface and the image is taken from the surface. Hence, clearer images can be produced fast and analysed microscopic with Image J, such to underline the visible pores. In detail, Auto-threshold plugin is exploited to clearly distinguish between black dots and the whiter background.

In this work, both types of analysis are performed, such to have a more complete morphological information of the materials.

4.1.2 Results and discussion

Thermogravimetric analysis

TGA is firstly performed on the pure cement sample. As an example, TGA of a cement sample with $w/c=0,4$ is reported in Figure 4.3. By reference to previous works in literature, it is possible to associated the different peaks of the weight loss derivate (DTG) to different cement phases. In detail, three main degradation steps are evident. CSH and AFt dehydrate at a temperature between 90 °C and 150 °C. In addition, around 100 °C, free water evaporates. Hence, two close narrow peaks are evident, confirming the coexistence of different multiple competitive phenomena.

CH shows a dehydration peak at a temperature around 500 °C. In the end, CaCO₃, which comes out from the process of carbonation (i.e. through the reaction of the cement sample with CO₂), has a peak of degradation at around 670 °C [176] [177]. Such to explore the effect of the high temperature treatment involved to reduce the cement curing time, the thermal degradation of a standard curing cement (i.e. 28 days in water) is compared to the thermal degradation of a cement sample obtained by the previously described thermal treatment (Figure 4.4). As can be seen, both curves present the same three peaks. The first one is more pronounced in the case of a 28 days-curing cement. However, this difference is not considered to be relevant in evaluating the similarities between the two cement compositions. As previously said, indeed, the first temperature range (50-150 °C) includes the evaporation of free water from the porous structure. It is reasonable to suppose that the sample which has been spent 28 days in water will present a higher water uptake inside hence the first weight loss will be hardly affected by the water evaporation. It must be noted, indeed, that a clearer comparison would have been done by starting from the same conditions (i.e. the same water uptake) for both samples. However, no thermal treatment of dehydration can be done before doing a thermal gravimetric analysis, such not to modify the morphological structure of the material nor induce the premature dehydration of CSH. The second step of degradation, which involves CH, has roughly the same extension in both curves, guaranteeing a good development of the cement hydration phases for both materials. It can be seen, also, that the DTG peaks of the 28 days – sample are little shifted towards lower temperatures than those of the one day – sample. This temperature shift is assumed to depend to morphological differences between the two materials. As general rule, low initial rates of hydration (i.e. the case of curing at room temperature) seem to favour the controlled precipitation of reaction products in interstitial space, raising the gel/space ratio and reducing the porosity [178], [179]. As a result, the thermal treated sample might show a slightly higher degree of porosity, thus inducing a temperature shift toward higher values because of its lower heat conductivity.

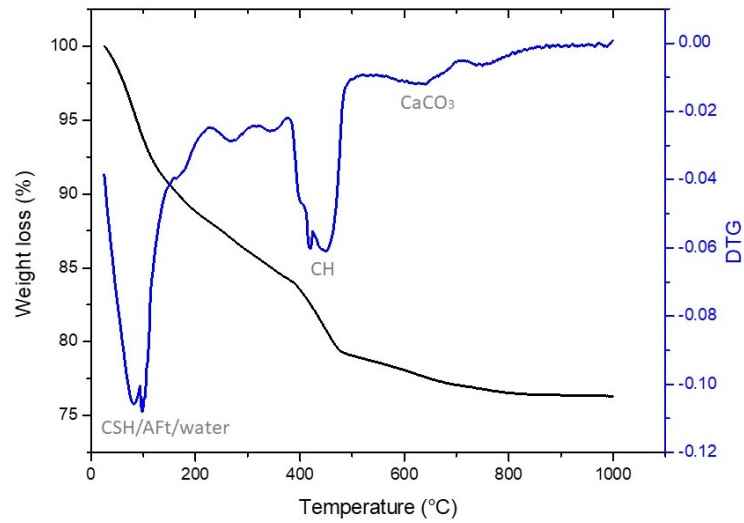


Figure 4.3: TGA and DTG curves of the pure Portland cement 52.5 sample cured in oven at 85 °C for 24 hours.

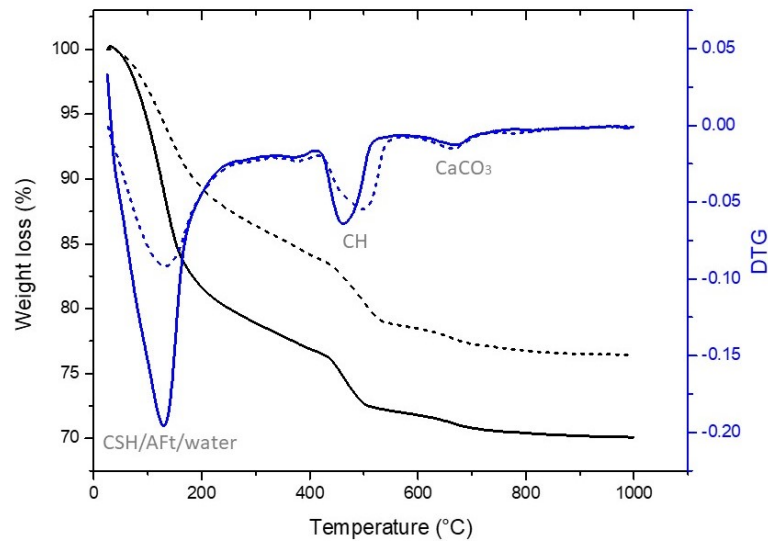


Figure 4.4: TGA and DTG curves of the pure Portland cement 52.5 sample cured in oven at 85 °C for 24 hours (dot line) and pure Portland cement 52.5 sample cured for 28 days at room temperature in water (continuous line).

TG analysis is also exploited to investigate the chemical structure of *in-situ*

samples. First of all, a thermogravimetric analysis of the selected salt is performed, thus to individuate the characteristic temperature of water desorption. As is possible to see from Figure 4.5, and with reference to previous works, different peaks of dehydration can be recognized. Firstly, around 40 °C, a weight loss by 7% is performed, which corresponds to the removal of a single water molecule. Hence, a transition from heptahydrate to hexahydrate salt occurs. Then, a second and more relevant peak of hydration appears at 97 °C, with a decisive weight loss corresponding to the removal of five water molecules. In the end, the last molecule leave the hygroscopic salt between 100 °C and 350 °C, above which the salt appears completely dehydrated. If the temperature increases above 800 °C, an additional weight loss is due to the evaporation of the salt itself, with the formation of SiO₂ [180].

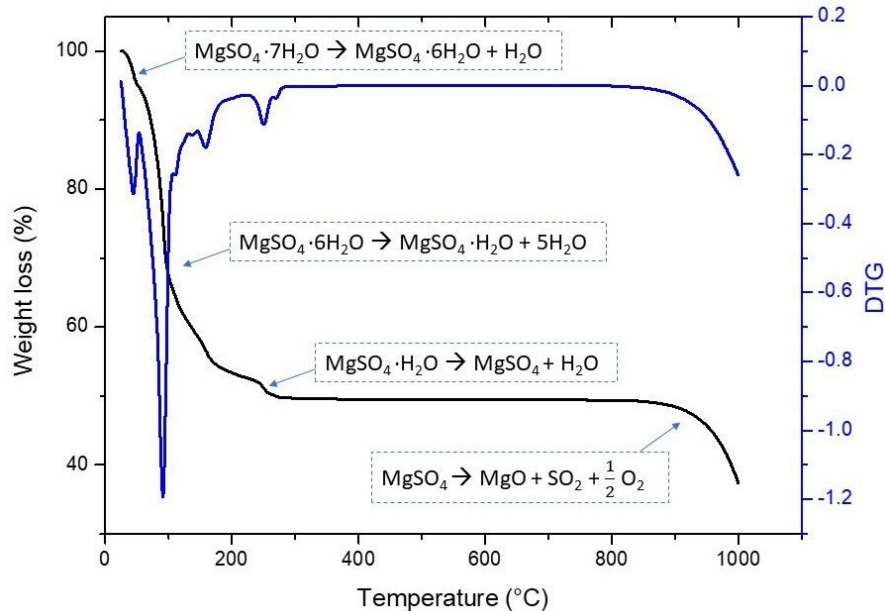


Figure 4.5: TGA and DTG curves of pure MgSO₄.

The same analysis is performed on the composite materials, thus to investigate the presence of salt inside the cement matrix. In Figure 4.6, the TGA curve of S1.5 is reported. The first small step of thermal degradation confirms the presence of the hygroscopic salt, since it corresponds to the loss of its first water molecule. The thermal footprint of CH (around 500 °C), one of the main components of the

cement matrix, is drastically smaller than what expected by observing the TGA curve of a pure cement material. To explain this result, a reaction between the cement material and the salt can be supposed. In particular, MgSO_4 can react with tricalcium silicate, thus forming dehydrated gypsum, brucite and silice.



However it is not the end of the reaction since the magnesium hydroxide and the silica gel can react very slowly to form a hydrated magnesium silicate (M-S-H) while gypsum can react with calcium aluminate, which is present in the cement powder, thus forming ettringite.



The reason why this reaction proceeds to completion is to be found in the low solubility of $\text{Mg}(\text{OH})_2$ and the resulting low pH value of its saturated solution. It is soluble only to the extent of 0.01 g/L and its saturated solution has a pH value of about 10.5, which is lower than the pH required to stabilise the hydrated calcium silicates. The silicates liberate lime to the solution to establish their equilibrium pH, but when magnesium sulfate is present the lime reacts with it, forming magnesium hydroxide and reducing the pH value to 10.5 again. The calcium sulfate accumulates in solution until it becomes saturated and crystals of gypsum precipitate [144]. Hence, the main peak, which takes place at a temperature around 100 °C, probably regroups different phenomena, including the evaporation of free water, the dehydration of C-S-H, M-S-H [181], AFt and the second step of dehydration of the hygroscopic salt, as observed in the previous chart. As a result, it is wider in shape than the main peak of salt decomposition. The second peak, instead, can mark the dehydration of brucite [182]. The latter peak, in the end, represents the decomposition of CaCO_3 . As a result, a certain amount of salt is reacted hence not all the introduced salt will be available for the cyclic water adsorption-desorption. However, by knowing the moles of salt and dicalcium silicate, and supposing the worst scenario in which the whole salt reacts with the cement hydration product, the amount of available salt after the composite synthesis can be calculated. [112].

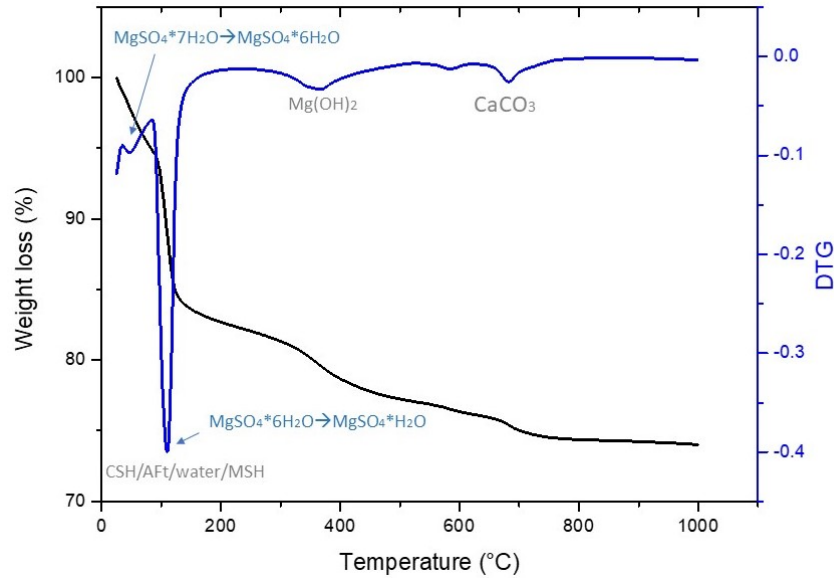


Figure 4.6: TGA and DTG curves of the cement+MgSO₄ material.

Actual w/c ratio

The value of the water to cement ratio of the cement samples after curing (which it is referred as actual w/c) is analysed with regards to the ratio between the amount of water and cement that has been mixed as first step of material preparation (which it is referred as ideal w/c). As explained in Section 2.4.3, indeed, cement is affected by the phenomenon of bleeding. In general terms, a certain amount of mixing water tends to rise to the surface of the fresh cement paste. In particular, the higher the amount of water, the lower is the ability of the cement paste to keep water. On the macroscale, this phenomenon is visible by a volume decrease of the sample. In Figure 4.7, the actual w/c ratio is calculated for samples with ideal w/c of 0.4, 0.6, 0.8, and 1. As expected, the actual amount of water slowly leaves the dotted curve representing the ideal w/c ratio. In particular, a plateau tendency can be observed when exceeding 0.8. For the latter, the calculated actual w/c is around 0.72 and that value does not change a lot when preparing a cement sample with ideal w/c of 1.

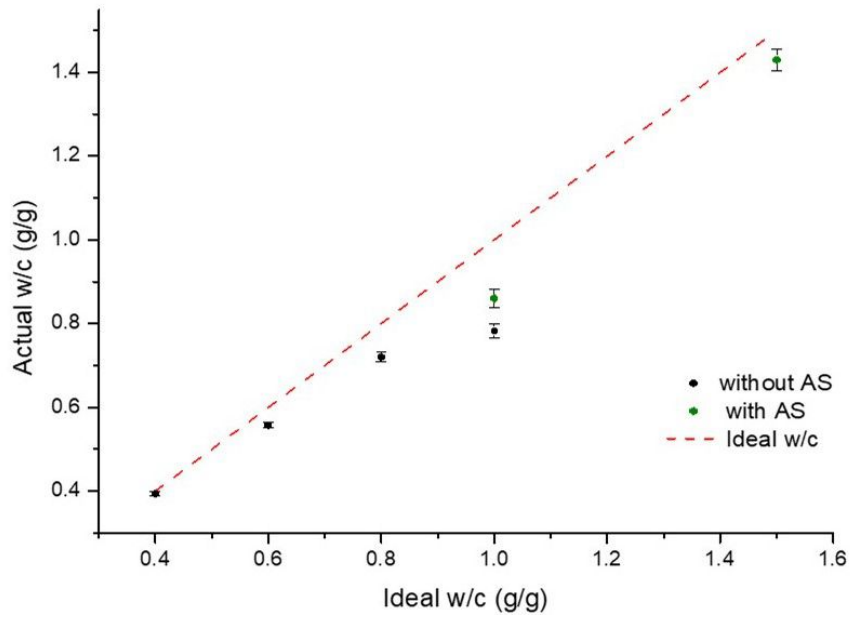


Figure 4.7: Chart of comparison between ideal w/c and actual w/c.

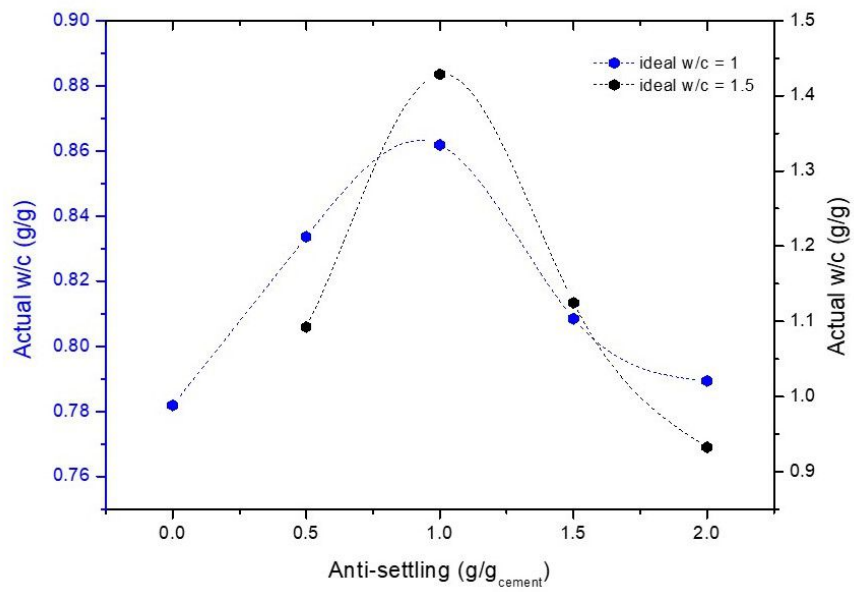


Figure 4.8: Chart of actual w/c with regards to the concentration of antisetling agent introduced into a cement sample with w/c equals to 1 (blue dots) or 1,5 (black dots).

In order to increase the real amount of water in the cement materials, an anti-settling agent in concentration of 1%wt is introduced when mixing the dry cement powder with water (green dots in Figure 4.7). The selected concentration of anti-settling agent (AS) is found to be the best in maximising the actual w/c value for both ideal w/c equals to 1 and 1.5 (Figure 4.8) . The decrease of actual w/c when exceeding 1%wt of AS suggests that there is a limit in weight beyond which it does not react anymore.

Geometrical density and porosity

The geometrical density of samples is reported in Table 4.5. In detail, the cement density is found to decrease with the increase of the w/c ratio, as expected. In particular, the trend of density of cement samples without AS (Figure 4.9) confirms the effect of bleeding. Only when plotting the values of density with regards to the actual w/c instead of the ideal w/c, indeed, a more regular decrease of density while increasing the amount of water is found. A density of 0,88 g/cm³ is reached when composing the cement sample with ideal w/c equals to 1. The presence of 1%wt AS with ideal w/c 1,5 leads to a cement with density of 0,052 g/cm³. At the same time, the cement porosity increases monotonically with increasing w/c, as expected (Figure 4.10). As is possible to see from the chart, the experimental values are in good agreement with the theoretical ones for water to cement ratios higher than 0.8. Before that value, however, the cement porosity seems to exceed the previsions. It can be due to the increase of viscosity when decreasing the w/c value. Low values of viscosity, indeed, favour the formation of air bubbles when casting the fresh cement paste into the mould, which in turn contribute to the whole value of porosity. The theoretical calculation does not taken into account macro bubbles hence their presence causes a discrepancy. With the higher value of w/c, the reached open porosity is equal to 58% , which is a good result in the view of hosting hygroscopic salt.

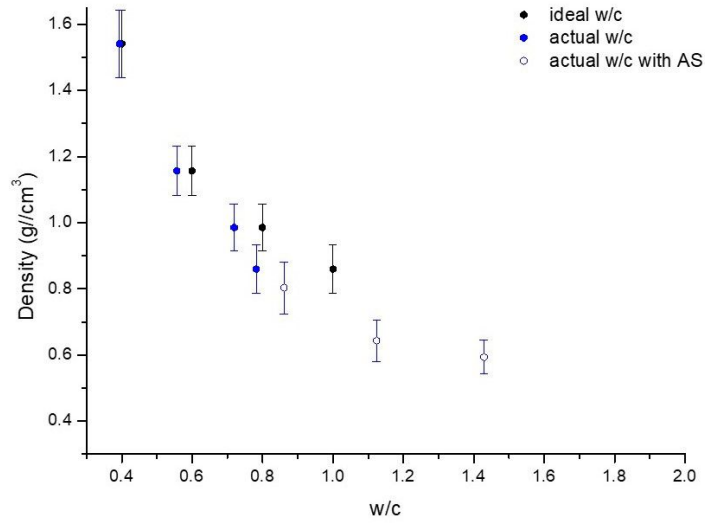


Figure 4.9: Chart representing the values of density of the pure cement samples, with respect to the ideal w/c (black dots) and actual w/c (blue dots); regarding the latter, empty dots represents cement samples with the anti-settling agent.

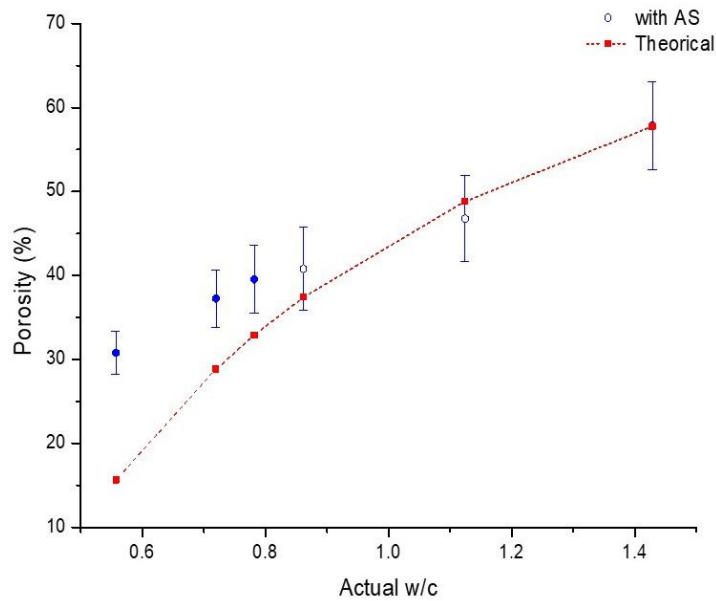


Figure 4.10: Chart representing the values of porosity of the pure cement samples, with respect to the ideal w/c (black dots) and actual w/c (blue dots); regarding the latter, empty dots represents cement samples with the anti-settling agent. The red line indicates the theoretical value of porosity.

Name	AS agent [%]	theoretical w/c [g/g]	Actual w/c [g/g]	Density [g/cm ³]	Porosity [%]
c04		0.4	0,39	1,54	0,21
c06		0.6	0,56	1,16	0,31
c08		0.8	0,72	0,99	0,39
c1		1	0,78	0,88	0,40
c1_05	0.5	1	0,83	0,86	0,42
c1_1	1	1	0,86	0,83	0,43
c1_1.5	1.5	1	0,81	0,89	0,42
c1_2	2	1	0,79	0,85	0,39
c1.5_05	0.5	1.5	1,09	0,61	0,42
c1.5_1	1	1.5	1,43	0,59	0,58
c1.5_1.5	1.5	1.5	1,12	0,64	0,47
c1.5_2	2	1.5	0,93	0,67	0,38
c2_1	1	2	1,33	0,56	0,50
c2_1.5	1.5	2	1,17	0,59	0,45
c2_2	2	2	0,89	0,60	0,32

Table 4.5: Main properties of the prepared cement samples.

Dry impregnation

C1.5as and C1as have been selected for both single and double impregnation. As is possible to see from Table 4.6, the first one shows the larger volume of porosity, hence it appears the best candidate in the scope of maximising the amount of hosted hygroscopic salt inside the porous matrix. The second one, instead, shows a more compact structure. However, in order to check the effect of the pore volume of the matrix when maximising the thermal energy performances, both types of cementitious materials might be explored.

As said before, the volume of solution involved to impregnate each sample is equal to its pore volume, which is calculated by knowing the its volume and percentage of porosity. During the second impregnation step, the available volume is calculated by taking into account also the volume of the amount of salt introduced during the first step of impregnation, which occupy part of the pores. As is possible to see from Table 4.6, the actual concentration of salt does not correspond to the theoretical concentration of salt. This discrepancy marks a certain inefficiency in the method of impregnation. It has been observed, indeed, that after a certain volume of the solution is introduced, the remaining solution has difficulty in entering

Material		Im1.5as1	Im1.5as1	Im1as1	Im1as1
N. of impregnation		1	2	1	2
Porosity	[%]	58	58	43	43
Density	[g/cm ³]	0,60	0,60	0,83	0,83
Mass of salt	[g]	0,76	0,61	0,65	0,25
Theoretical concentration of salt	[%]	37	53	24	37
Actual concentration of salt	[%]	27	36	15	22

Table 4.6: Composite samples after single or double impregnation.

the pores. Probably the outer pores saturate as first and it is not given enough time to the solution to penetrate the material. Hence, at a certain point, it is hard to continue the impregnation without losses of solution. This problem can be solved by automating the step of impregnation so that is programmed to proceed at very slow rate. Moreover, thinner samples can be prepared thus to increase the percentage of open pores hence ease the introduction of the solution.

A secondary reason for the low efficiency of the impregnation might be found into the provided carbonation of pure cement samples before the impregnation step. It is the result of chemical reactions between CO₂ and the hydration compounds (generally CH and C-S-H). It is known indeed that carbonation is generally responsible for a certain microstructural changes. For ordinary Portland cement, carbonation leads to a reduction in porosity of about 5% which is due to the positive difference of molar volume between CH and C-S-H and the precipitated carbonates [183] [184]. As a result, the development of carbonate products can cause the pore clogging of the outer pores thus making it difficult to fill the whole residue cement pore volume.

By repeating the process of impregnation twice, the salt amount is roughly increased by 70%. It is not doubled, as expected, because the available empty volume during the second step of impregnation is smaller than that of the first one.

Optical microscopy and stereo microscopy

As reported in Figure 4.11, optical micrographs of pure cement and cementitious composite, both obtained by in-situ synthesis or by impregnation, are provided. As expected, the porosity might increase with increasing the value of w/c. Black

dots are clearly visible in each image and they seem to grow in number and contemporary become smaller with increasing w/c. However, their background is not homogeneous in colour but a greyscale characterizes the whole image. Hence, detect all pores thus having an estimation of the difference in porosity between samples is tricky. As is possible to note from Figure 4.12, some spherical dots (red circles) are clearly detectable as pores, but some other dark spots (blue circles) are hard to recognise as big pores or the sum of small pores or even some light effects due to the surface roughness. It must be specified, indeed, that cement materials are characterized by a low hardness, hence the mechanical polishing must be not too invasive. As a result, the surface of material is not mirror polished and a certain degree of roughness remains, thus reducing the quality of the image.

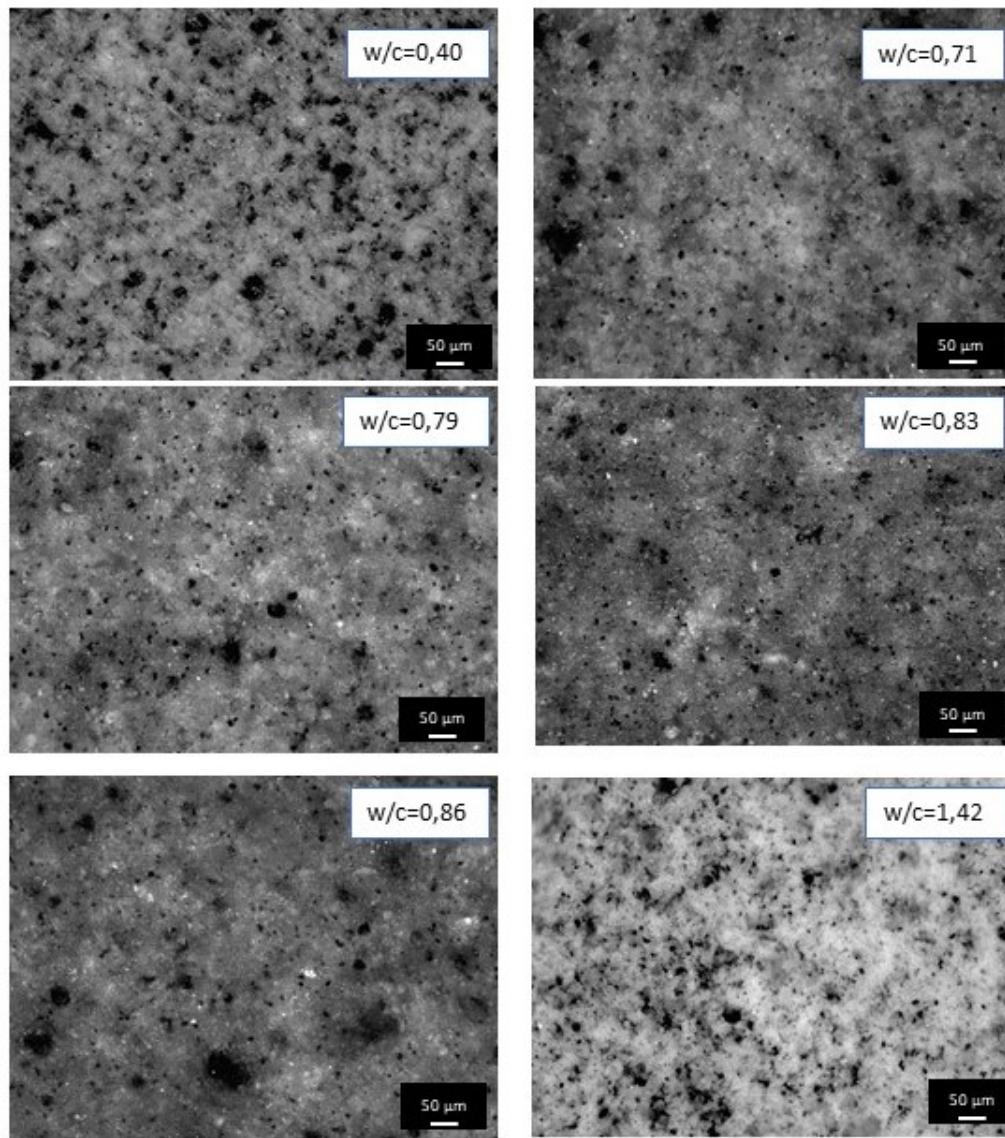


Figure 4.11: Optical microscopy images of pure cement samples with different w/c values.

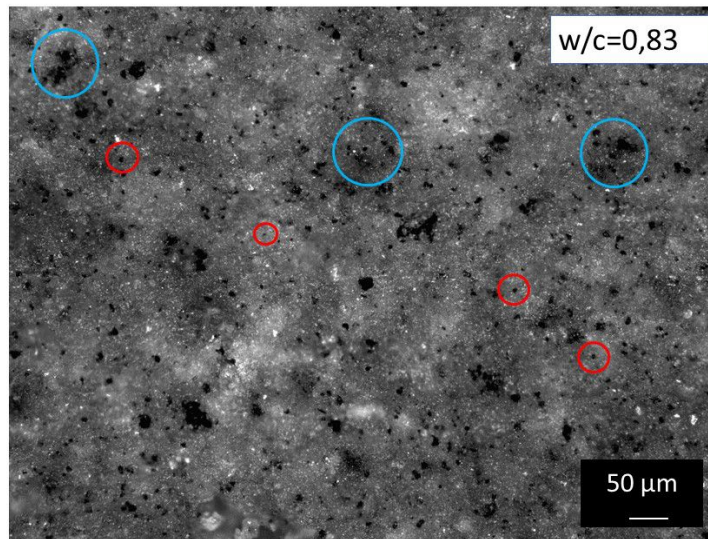


Figure 4.12: Optical microscopy image of a pure cement sample with w/c equals to 1: some spherical dots (red circles) are clearly detectable as pores, but some other dark spots (blue circles) are hard to recognise as big pores or the sum of small pores or even some light effects due to the surface roughness.

On the other side, stereo-images are provided for the different types of material. In detail, the images of pure cement samples with different values of water-to-cement ratio are reported in Figure 4.13 and 4.14, in which real images are reported to the left while elaborated black-white images are reported to the right. After the impregnation step, the presence of salt is visible in the form of small white dots (Figure 4.15), confirming that the porous matrix is able to host it. The stereo microscopic image confirm that most of the pores are filled with salt and, since after the step of dehydration the volume of pores is only partially filled by the dehydrated salt, some of them are still visible as black dots. For the cementitious composite *in-situ*, instead, the stereo-microscopy confirms that a chemical reaction between cement and hygroscopic salt, with the formation of gypsum, is happened. As can be seen from Figure 4.16, indeed, quite large dark shadows (orange circle) are supposed to correspond to gypsum precipitates. On the other side, small circular shadows (blue circle) are similar to the type of pores observed for pure cement samples, hence can be supposed to be the same.

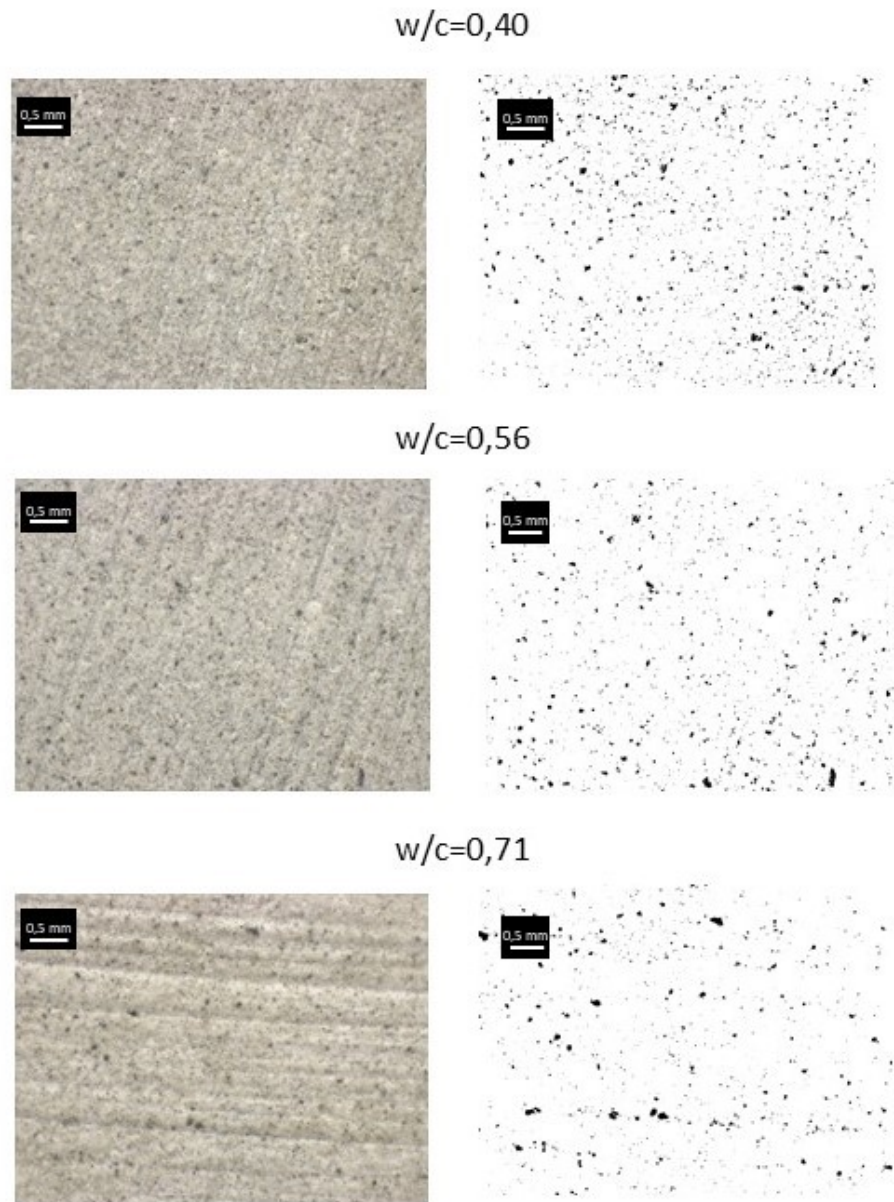


Figure 4.13: Stereomicroscopic images (left) and elaborated black-white images (right) of pure cement samples with w/c equals to 0.40, 0.56, 0.71 .

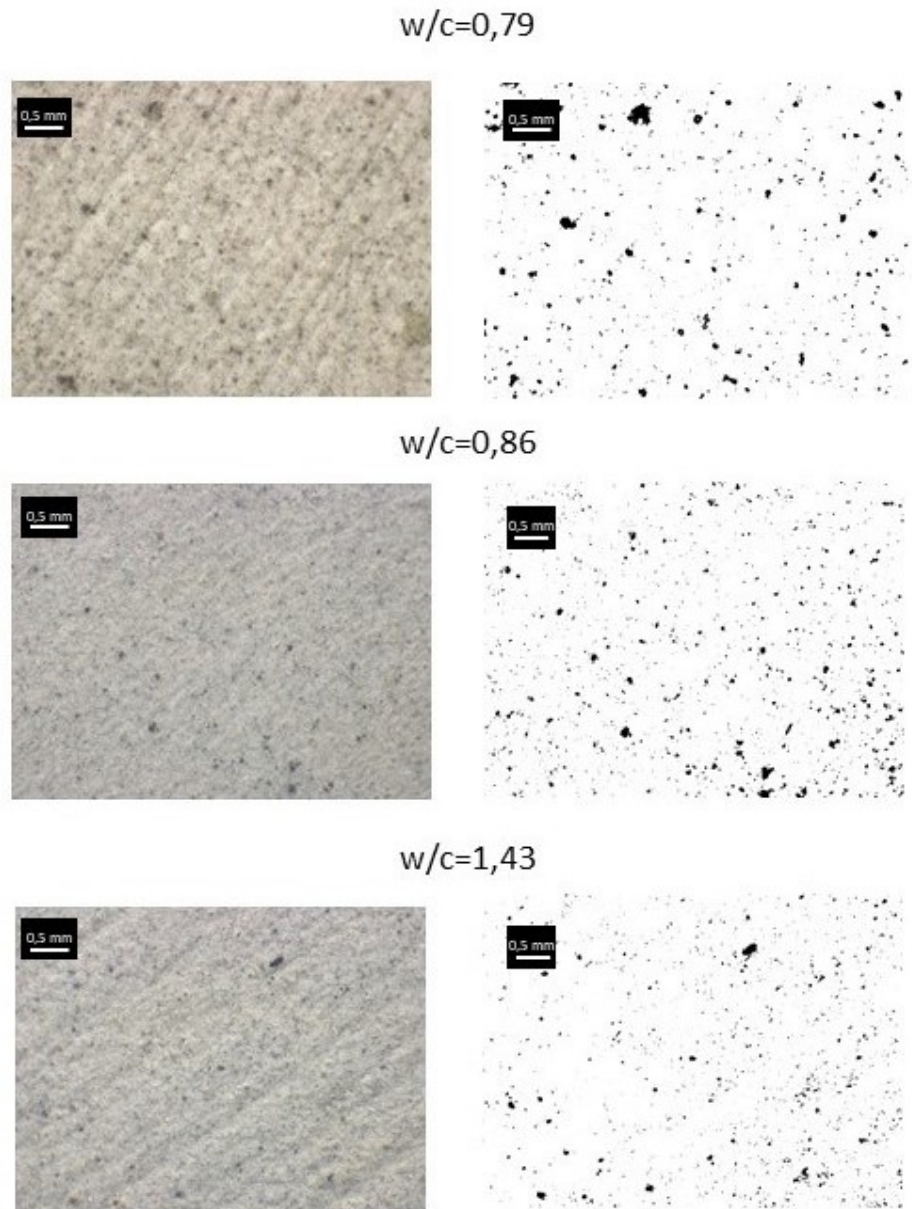


Figure 4.14: Stereomicroscopic images (left) and elaborated black-white images (right) of pure cement samples with w/c equals to 0.79, 0.86, 1.43 .

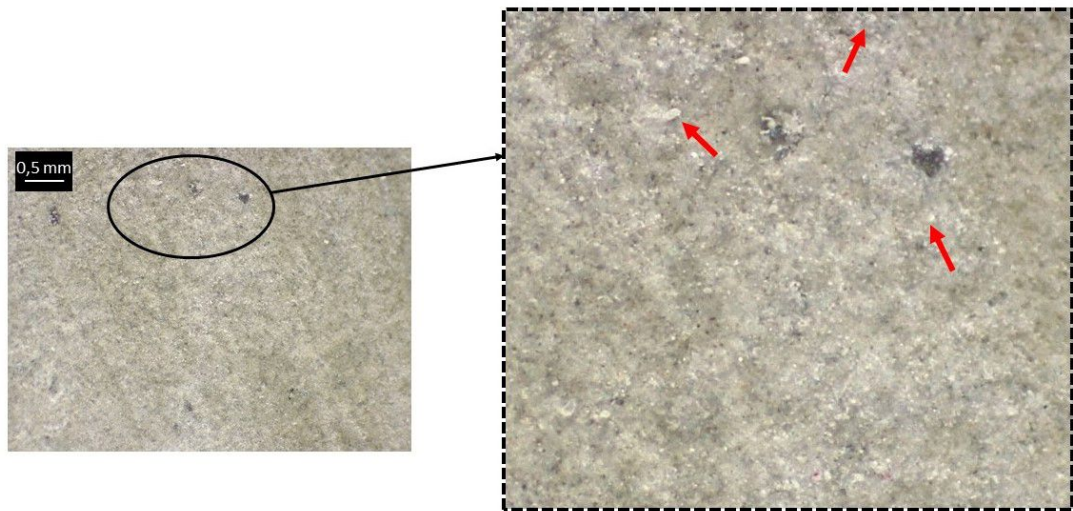


Figure 4.15: Stereomicroscopic image of a cementitious composite material after the impregnation step: small white dots confirm that the porous matrix is able to host the hygroscopic salt.

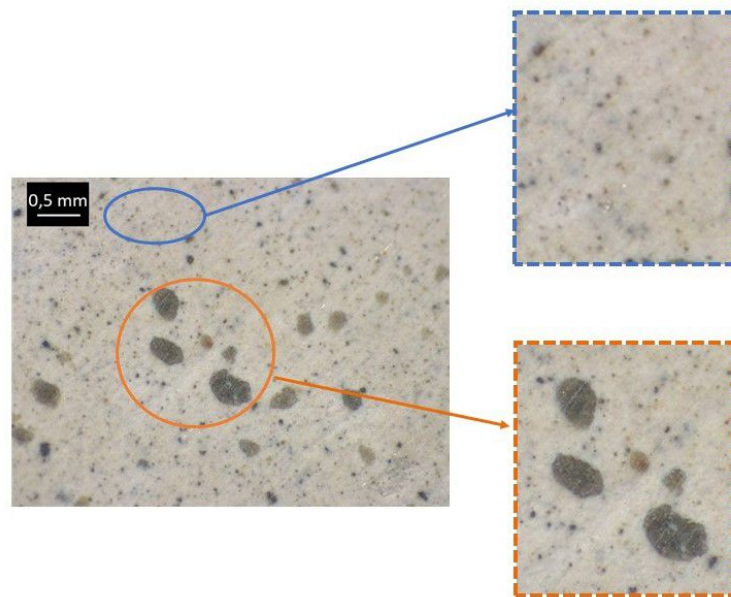


Figure 4.16: Stereomicroscopic image of an *in-situ* cementitious composite material: quite large dark shadows (orange circle) are supposed to correspond to gypsum precipitates while small circular shadows (blue circle) refers to pores.

4.2 Preliminary test analysis

4.2.1 Method

In order to first understand if the synthesised composites yield a certain adsorption heat or not, a preliminary experimental analysis is carried out. It consists on pouring liquid water on the samples and recording the temperature raise of hydrated samples. Water-composite system temperature is recorded continuously over time by a thermocouple, so as to acquire both the possible T produced and the time interval needed to reach the maximum temperature.

To perform this analysis, an ad-hoc experimental set-up was built in occasion of the preliminary work on the cementitious sorbent [112]. It is schematically represented in Figure 4.17, while Figure 4.18 shows the container design along with its actual dimensions in millimetres. In detail, the chamber is filled with 10 mL of water, whose temperature is recorded by the thermocouple. At $t=0$, the cementitious material (about 3 g) is introduced inside the water bath and the hydration occurs. The container volume is designed with height larger than diameter, in order to minimize the thermal losses. All the different parts composing the container were created using a 3D printer located in the SMaLL-Lab at the Department of Energy at Politecnico di Torino (DENERG). ABS (Acrylonitrile butadiene styrene) is used as printing material. While ABS presents good mechanical properties and acceptable thermal features (melting point 105°C), it is permeable to water. Therefore, a waterproof agent needs to be spread on the container external surface. The container was pierced on the external side to let the thermocouples be inserted within the chamber. K-type thermocouples (Chromel(NiCr)(+)/ Alumel (NiAl) (-)) were adopted, since suitable for the system investigated. The container was covered with polystyrene as insulation material both on the side and on the bottom. Temperature acquisition is performed using the datalogger D4I Thermometer. Using the T provided from the temperature acquisition, it is possible to estimate the composite energy density, by means of Equation 4.13:

$$\left(\sum_i^n M_i c_{p,i} \right) \cdot \Delta T = E - \frac{\Delta T}{R} \cdot \Delta t \quad (4.13)$$

where M_i is the mass of each component, $c_{p,i}$ is the specific heat , T is the temperature difference from water initial temperature ($T_0 = T_{\text{amb}} = 23^\circ\text{C}$) and the

maximum temperature reached by the water bath, measured by the thermocouple and t is the time interval, measured in seconds, needed to reach the maximum temperature. Hence, the right handside of Eq. 4.13 indicates the energy needed for the composite + water system to increase its temperature from T_0 to T_{\max} . In the end, R is the experimental set-up thermal resistance(container+polystyrene), and is equal to 95,81 K/W. From the value of E , and knowing the density of the samples, it is possible to evaluate the energy density expressed in GJ/m^3 (Equation 4.14).

$$ED = \frac{E}{m_{\text{comp}} \cdot \rho_{\text{comp}}} \quad (4.14)$$

It must be noted that ED does not correspond to the standard ESD value previously mentioned. The latter, indeed takes into account also the enthalpy of water vaporization (41 kJ/mol). However, by knowing ED and the water uptake, it is possible to obtain ESD according to Equation 4.15

$$ESD = \frac{41 \frac{\text{kJ}}{\text{mol}} \cdot \chi}{18} \cdot \rho + ED \quad (4.15)$$

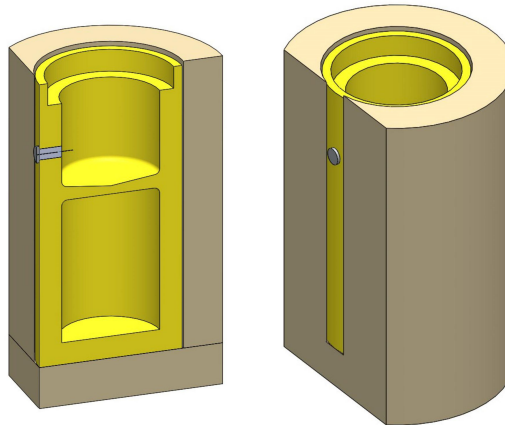


Figure 4.17: Schematic representation of the preliminary thermal test set up.

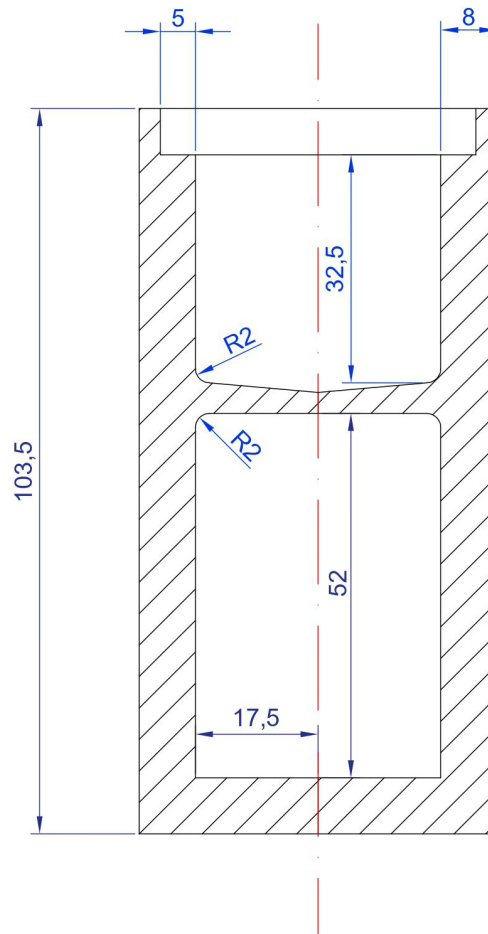


Figure 4.18: Schematic representation of the preliminary thermal test set up along with its actual dimension in millimeters.

4.2.2 Results

The most promising composite samples, both impregnated and synthesized *in-situ*, are analysed with this technique. Furthermore, also pure cement sample is tested, such to evaluate the thermal contribution of the cementitious matrix. In Figure 4.19 the typical temperature evolution of the water temperature is shown. All temperature evolution plots can be found in Appendix B.

This preliminary thermal test shows an energetic increment of about +54% for Im1.5-1 and +100% for Im1.5-2, thus confirming the positive improvement of thermal energetic performances by impregnating the porous cementitious matrix with a saturated solution of MgSO_4 . In the meantime, the innovative in-situ method of synthesis appears the best method such to provide the higher energy density. S1.5, for instance, shows an energetic increment of +194% with respect to the pure cement material, reaching +43% with respect to the pure cement material. It must be remembered that the experimental ED value does not correspond to the standard ESD which is usually considered when evaluating the energetic performances of a sorbent material. To make a comparison in terms of ESD, the enthalpic contribute of water vaporization must be added. As an example, if considering a water uptake of 0,1 g/g, the ED value of Im1.5 ($0,078 \text{ GJ/m}^3$) corresponds to ESD equals to $0,31 \text{ GJ/m}^3$.

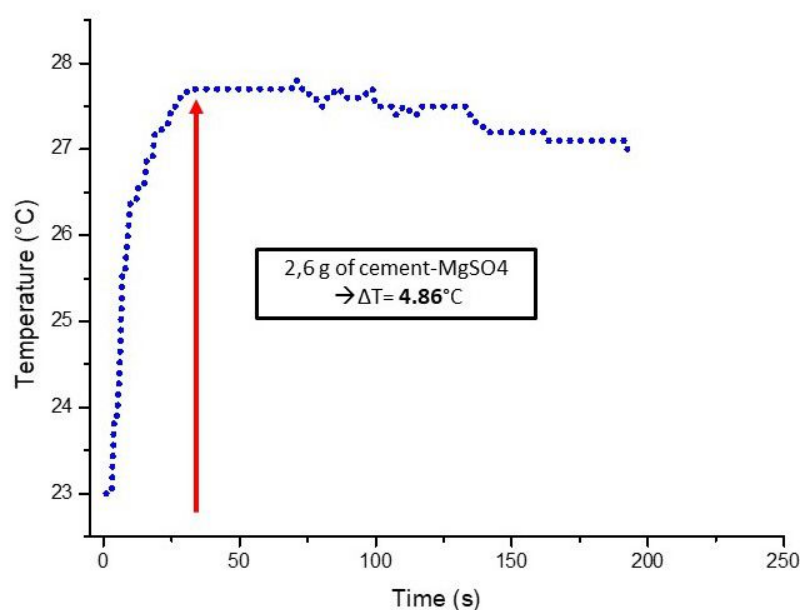


Figure 4.19: Plot reporting the water temperature evolution caused by the endothermic reaction of hydration of dried cement- MgSO_4 composite material introduced into the water bath.

The expected values of energy density can be theoretically calculated by knowing

both the cement and salt enthalpy of hydration, following Equation 4.16.

$$E = \Delta h_{cem}\chi_{cem} + \Delta h_{salt}\chi_{salt} \quad (4.16)$$

where δh_{cem} can be calculated from the experimental energy density of C1.5 while δh_{salt} is approximated to 300 J/g, which corresponds to the enthalpy of formation difference between $MgSO_4 \cdot 7H_2O$ and $MgSO_4$. As can be seen from Table 4.7, the expected values for the composite materials do not correspond to the theoretical ones, which are roughly double the experimental energy density.

Material	N. of impregnation	Density g/cm3	Theoretical salt %	Calculated Energy Density* GJ/m3	Experimental Energy Density** GJ/m3
C1.5		0,59		0,042	0,042
Im1.5	1	0,82	27	0,107	0,060
Im1.5	2	1,02	36	0,156	0,078
S1		1,46	7	0,126	0,104
S1.5		1,30	26	0,168	0,115
S2		1,20	39	0,190	0,137
Im1.5_CaCl2	1	0,81	26	0,100	0,110

Table 4.7: Results of the preliminary thermal analysis of *impregnated* and *in-situ* cementitious composites.

*Energy Density is calculated by considering an heat of hydration of 300J/g for $MgSO_4$ and 70J/g for pure cement, calculated from the experimental energy density of C1.5

**The Experimental Energy Density is a preliminary energetic parameter. To have the standard ESD value, the enthalpy of vaporization (41 kJ/mol) has to be added.

Regarding *in-situ* method of material preparation, the comparison between experimental and theoretical values gives confirm of the occurred reaction between $MgSO_4$ and dicalcium and/or tricalcium sulphate when mixing the cement powder with the saturated solution. As a result, only less salt is available for the hydration and the experimental energy departs from the theoretical value, in which the whole amount of salt is considered to play when the exothermic hydration occurs.

Regarding the *impregnated* composite materials, instead, the discrepancy between theoretical and experimental values is harder to understand. It suggests also in this case the development of a reaction between the salt solution and the cement sample, which can be favoured by the relative high temperature during the dehydration step before the preliminary thermal test. This hypothesis has been investigated by performing a thermo-gravimetric analysis of the impregnated cement sample after the dehydration step (Figure 4.20). The derivative thermogravimetric analysis

reports the typical peak of dehydration of brucite around 400 °C, as confirmed by TGA of $\text{Mg}(\text{OH})_2$ reported in Figure 4.21. It can be concluded that the cement structure is partially attacked by the salt solution, thus consuming CH to product gypsum and brucite. In addition, the third peak marks the decomposition of CaCO_3 and MgCO_3 , which have been formed from the exposure of the cement sample to air.

To double check the problem of reactivity between cement and MgSO_4 , the same cement sample with $w/c=1,5$ has been impregnated with the hygroscopic salt CaCl_2 . As can be seen, the theoretical value of energy match the experimental one, i.e. $0,11 \text{ GJ/m}^3$. Moreover, it overcomes the previous value of $0,07 \text{ GJ/m}^3$ of the same composite type reported in ([112]). It signs the first successful step towards the optimization of the sorbent material.

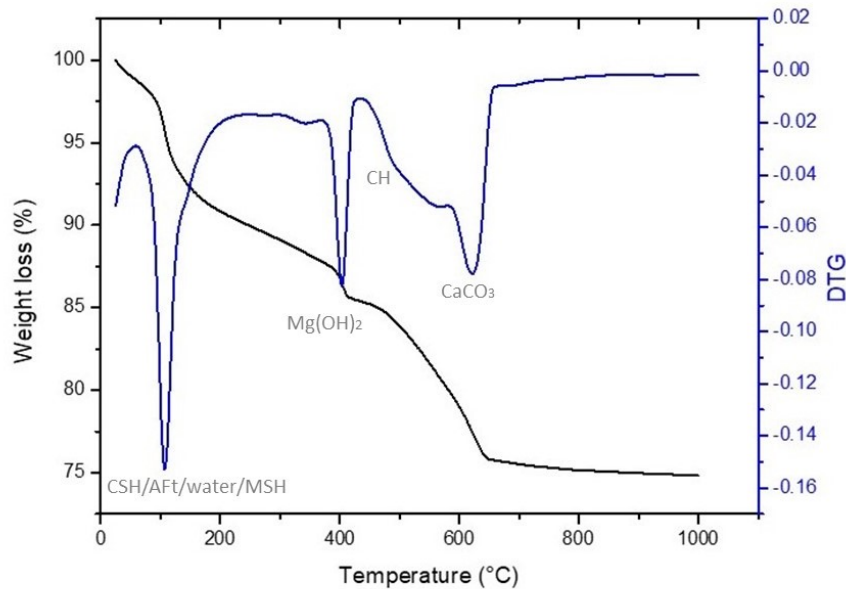


Figure 4.20: Plot reporting the TG analysis of Im1.5₁.

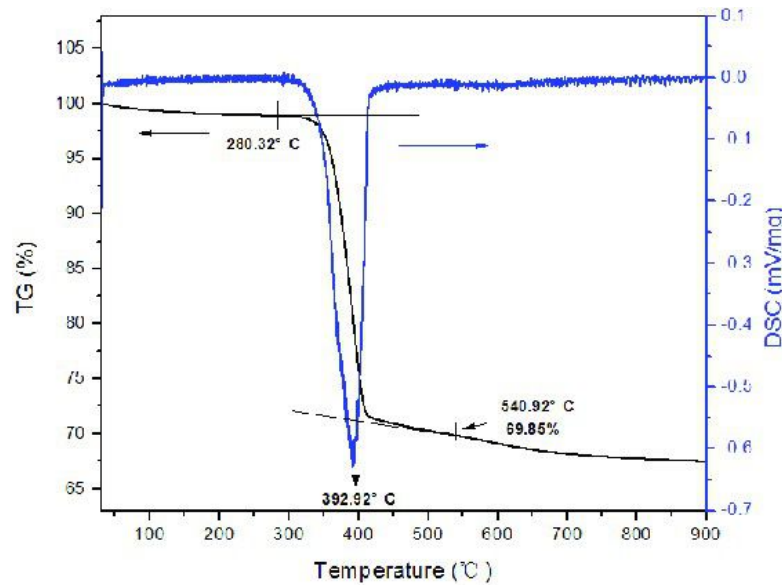


Figure 4.21: Plot reporting the TG analysis of $Mg(OH)_2$ [185].

4.2.3 Conclusion

The aim of this work was the investigation and optimization of the energetic performances of the cementitious composite for thermal energy storage. In order to choose the best way of synthesis, both impregnation and in-situ method have been explored. In the latter, salt is introduced when mixing cement powder with water so that hygroscopic salt molecules can be finely dispersed into the structure. Hence, it allows the increase in salt concentration and the decrease of the out of pores - salt deliquescence risk.

Super-porous cements have been prepared, reaching at maximum 58% of porosity. The latter has been reached by optimizing the use of an anti-settling agent, through which the viscosity of the material has been modulated. Thanks to the high level of porosity of the structure, the porous matrix has been impregnated with 36% of $MgSO_4$ thus overcoming the previous upper limit of 18%. The obtained salt load, however, is found to be roughly half the theoretically value of salt that can be introduced. This discrepancy could be due to an inefficiency of the impregnation method. The latter might be automated, such to control the very slow drip of salt solution over the cement surface and avoid any solution losses. Moreover, difficulties in introducing the salt solution in the porous matrix could be due to the

carbonation of the structure during the time interval between the step of cement preparation and the impregnation. This reaction, indeed, is demonstrated to cause a change of the porosity structure, thus reducing the whole pore volume. The stereo microscopic images has confirmed that most of the pores are filled with salt and some pores are still visible as black dots after the salt load. On the other side, the in-situ method of synthesis has been optimized thus reaching a concentration of MgSO_4 of 7%, 26% and 39% with w/c 1, 1.5, and 2 respectively.

In order to first understand if the synthesised composites yield a certain adsorption heat or not, a preliminary experimental analysis has been carried out. It consists on pouring liquid water on the samples and recording the temperature raise of hydrated samples. An energy storage density of 0.08 GJ/m^3 and 0.14 GJ/m^3 have been obtained for impregnated and in-situ cementitious sorbents respectively. It must be taken in mind that the experimental ED is a preliminary index of the energetic performances of the material. To have an energetic parameter in terms of the so-common ESD, the enthalpic contribute of water vaporization has to be added. The experimental values of ED have been found lower than what expected, thus underlining a certain reactivity between the cement and MgSO_4 which results in the decreasing of the amount of available hygroscopic salt. The hypothesis of reaction between the hygroscopic salt and our cement has been confirmed by the thermograms obtained by performing the TG analysis of the composite materials. In detail, MgSO_4 is supposed to react with C2S and C3S in powder, thus forming $\text{Mg}(\text{OH})_2$, gypsum and SiO_2 . Silica gel is also supposed to slowly react to form a hydrated magnesium silicate (M-S-H) while gypsum can react with calcium aluminate, which is present in the cement powder. The occurred reaction between matrix and salt has been visually check out by stereo-microscopic analysis, where new solid phases appear.

In order to investigate the effective optimization of the matrix structure, together with the control of whether the preliminary thermal energy approach works correctly, the cement matrix has been impregnated with CaCl_2 , which shows lower but still appreciable energetic performances than MgSO_4 . The theoretical value of energy of CaCl_2 -cement has been found to perfectly match the experimental one, which is equal to $0,11 \text{ GJ/m}^3$.

The obtained results sign the first successful step towards the optimization of an innovative type of cementitious material as sorbent for thermal storage. However, it

is well known that the preliminary Energy Density parameter alone is not sufficient to characterise a material for thermochemical heat storage purposes. Therefore, more standard water vapour physisorption analysis have to be performed on the cementitious materials, such to investigate their performances. It must be noted, moreover, that the reactivity between MgSO_4 and Portland Cement 52.5 critically limits the energetic performances, since a large part of loaded salt is not more available for the process of hydration. Future research works will investigate other types of cement, i.e. aluminous or magnesia cements, thus reducing the reactivity between the two phases. On the other side, other types of hygroscopic salts will be explored in the role of host into Portland Cement 52.5, thus looking for an almost inert loading phase.

Appendix A

Methods for evaluating the heat of adsorption

Experimentally, two methods are used to evaluate the heat of adsorption: calorimetric method (direct method) and isosteric method (indirect method) [186], [187].

The **calorimetric method** directly evaluates the heat released when the adsorbate is in contact with the adsorbent. It is the result of a combination of the methods of Thermo-Gravimetric Analysis (TGA) and Differential Scanning Calorimetry (DSC). A typical apparatus for the measurements is reported in the work of Gaeini et al [97], who well explained the principle of the analysis. The apparatus (Figure A.1, left) consists of a thermally controlled environment (furnace), which is subjected to a certain temperature program. Two aluminium crucibles, the first containing the sample and the second one empty, are positioned on a sample holder and subjected to identical conditions. A humidity generator provides an air flow with controlled conditions (temperature, humidity and flow rate). During an experiment, the TGA signal (Figure A.1 right, black line) shows the weight loss of the sample while two thermocouples allow to record the temperature difference between the two crucibles. The latter is directly related to the heat flux towards (dehydration) or from (hydration) the sample (DSC signal, Figure A.1 right, red line). In order to evaluate the performance of the sorbent-sorbate couple, TGA and DSC signals can be elaborated, such to obtain performance indication factors. The water sorption capacity (commonly named water uptake) is defined by Equation A.1:

$$w = \frac{m_h - m_d}{m_d} \quad (\text{A.1})$$

with m_d corresponding to the mass of the dehydrated sample and m_h corresponding to the final mass of the sample after hydration [70]. From DSC signal,

the heat flux experimentally measured is expressed by Equation A.2:

$$\Delta H_{exp} = \Delta H_{sorption} + c_p \Delta T + \Delta H_{crucible} \quad (\text{A.2})$$

with H_{cruc} the integration of the heat flow signal during a blank test (empty crucibles), m the anhydrous sample mass, c_p the heat capacity of the composite and ΔT the difference of temperature of the sample. ΔH_{exp} can be expressed in $\text{J mol}^{-1}_{\text{water}}$ or $\text{J g}_{\text{sample}}^{-1}$. Subtracting ΔH_{cruc} from H_{exp} , in J/g , ESC is obtained. By knowing the packing density of the material, also ESD can be calculated.

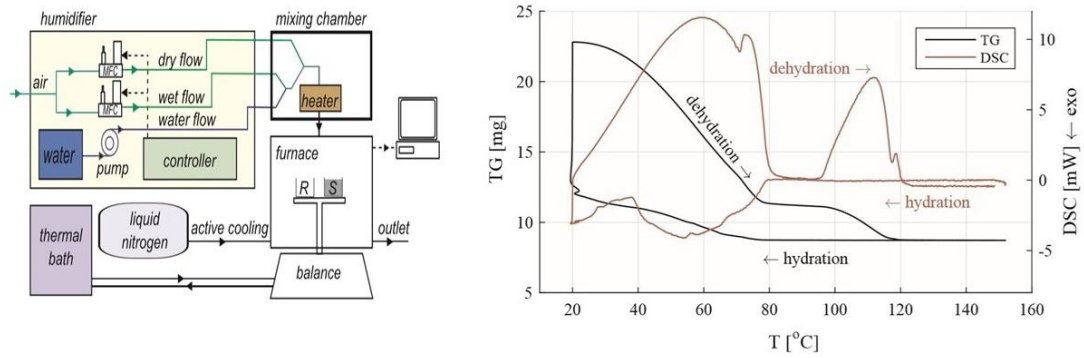


Figure A.1: Schematic view of TGA-DSC set-up (left) and typical result of de/re-hydration of a 7 mg encapsulated CaCl_2 sample subjected to 1.3kPa water vapour pressure (right)[97].

The **isosteric method** is based on a quantitative relationship between pressure and temperature, measured at a constant amount of the substance adsorbed by a certain amount of the adsorbent. Gibbs interpreted isosteric heat as the energy required to transfer an adsorbate molecule from the bulk to the adsorbate phase at some fixed thermodynamic conditions, such as temperature, pressure and amount of adsorbate. Through a rigorous thermodynamic framework for heat analysis, Tian et al. [188] pointed out that the differential heat of adsorption, i.e. the heat released from a sampling cell upon adding an infinitesimal amount of the adsorbate at constant temperature, volume and amount of adsorbate, is fully consistent with the differential heat of adsorption. Since the latter is evaluated in terms of the total amount of gas in the sampling cell, it is independent of any assumptions on the geometric measures or operating conditions. The isosteric heats of adsorption for a specific adsorbate can be calculated by applying the Clausius–Clapeyron (C-C)

equation (Eq. A.3) on the isothermal data.

$$\Delta_{ads}H_n = R \left(\frac{\delta \ln P}{\delta \frac{1}{T}} \right) \quad (\text{A.3})$$

where $\Delta_{ads}H_n$ is the enthalpy of adsorption and R is the gas constant. The isothermal data are generally reported by means a graphical representation of the pressure logarithm, $\ln(p)$, for a given amount adsorbed n_a as a function of the reciprocal temperature, $1/T$. In Figure A.2 an example of seasonal and daily cycles in the form of Clausius-Clapeyron graph type. It is reported that it is possible to measure two isotherms, thus relating the equilibrium pressures P_1 and P_2 to the corresponding temperatures T_1 and T_2 for a given amount adsorbed, according to Equation A.4:

$$\Delta_{ads}H_n = \frac{RT_1T_2}{T_2 - T_1} \ln \frac{P_2}{P_1} \quad (\text{A.4})$$

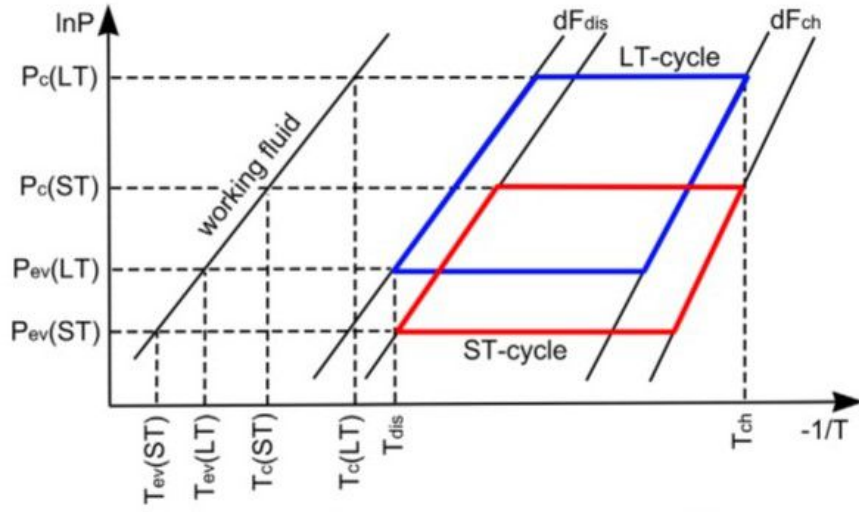


Figure A.2: Clausius-Clapeyron diagram representing two different adsorption cycles for Li/Ca halogenides inside Multi-wall Carbon Nano-tubes [102].

Moreover, a useful tool for the extrapolation of adsorption isobars or isotherms, thus obtaining the Clausius-Clapeyron graph, is the Dubinin-Astakhov model, with the Polanyi potential.

The Dubinin's theory [102], primary developed for microporous activated carbons, was found to be used for the adsorption processes in other microporous adsorbents.

In few words, Dubinin defines the specific volume W (cm^3) of the adsorption space as:

$$W = \frac{x}{\rho_s} \quad (\text{A.5})$$

with x the sorbate uptake (g/g) and the density of adsorbate. If the density of the sorbate is about 1, W results equal to the sorbate uptake. Assuming the adsorbate density constant with temperature and equal to the liquid-phase density, the water uptake is equal to W . On the other side, Dubinin defines the differential work of adsorption A as:

$$A = -\Delta F = RT \ln \frac{p_s}{p} \quad (\text{A.6})$$

with F the free energy and p_s the saturation pressure of the adsorptive in equilibrium with the liquid bulk phase at temperature T . The relation $W = f(A)$ is called “characteristic curve” and shows for many systems an invariance of temperatures (Figure A.3). That means, all measured point of adsorption isotherms are described by one single curve and $W=f(A)$ can be obtained by doing a single isotherm curve [79]. Among all the equations proposed to describe the relation between x and A , the Dubinin-Astakhov equation (Eq. A.7) is among the most popular ones:

$$x = e^{-\left(\frac{A}{\gamma E_0}\right)^n} \quad (\text{A.7})$$

where , E_0 and n are fitting parameters that describe the system. In particular, γ is the affinity constant and depends on the nature of the adsorbate, E_0 is the characteristic energy and depends on the adsorbent, n describes the pores heterogeneity [189]. Since the water uptake does not depend explicitly on T and P but only on the adsorption potential A , the relation between x and A is characteristic for a given couple and does not change when changing the experimental conditions. That means, from when the characteristic curve is obtained, all isotherms and isobars can be extrapolated. As a result, the isosteric heat can be calculated from different conditions, without the need of new experimental analysis.

In addition, it must be pointed out that isosteric heat can be also calculated by Dubinin’s theory, without calling in the Clausius Clapeyron’s equation. Stach et al. [79] and Wang et al. [76] reported in detail how the Dubinin’s theory can be used for the evaluation of the isosteric heat. The latter can be expressed as follow:

$$\Delta H_{is} = \Delta L + \Delta F - T\Delta S \quad (\text{A.8})$$

$$\Delta S = \alpha T \frac{\delta(\Delta F)}{\delta(\ln x)} \quad (\text{A.9})$$

where L is the latent heat of evaporation of water, S is the entropy change of sorption and α is the volume expansion coefficient for water [76]. The energy storage capacity of the sorbent results from:

$$ESC = \int_{T_{dis}}^{T_0} \Delta H_{is} \frac{dx}{dT} dT \quad (\text{A.10})$$

However, the latter method is less common and few works report it. By comparing isosteric heats measured directly using adsorption calorimetry with those obtained using the indirect adsorption isosteric method, according to Clausius–Clapeyron equation, a good agreement is found [186], [187]. Hence both methods lead to reliable results for isosteric heats. Usually, indirect measurements are used more than direct measurements, since the latter is often complicated and more costly, particularly in non-environmental conditions [188].

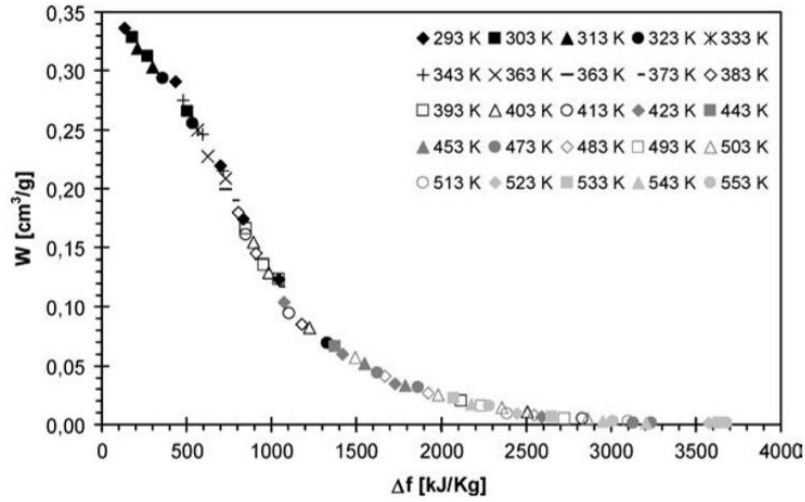


Figure A.3: Clausius-Clapeyron diagram representing two different adsorption cycles for Li/Ca halogenides inside Multi-wall Carbon Nano-tubes [102].

Appendix B

Thermal analysis

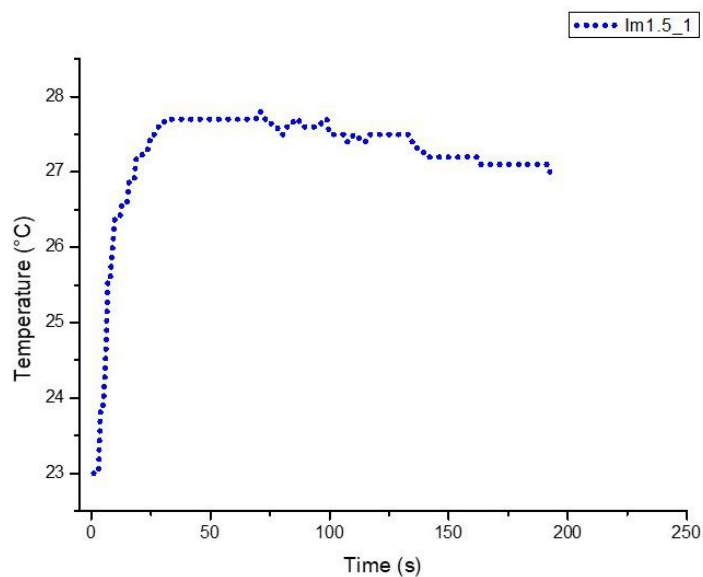


Figure B.1: Plot reporting the water temperature evolution caused by the endothermic reaction of hydration of Im1.5-1 introduced into the water bath.

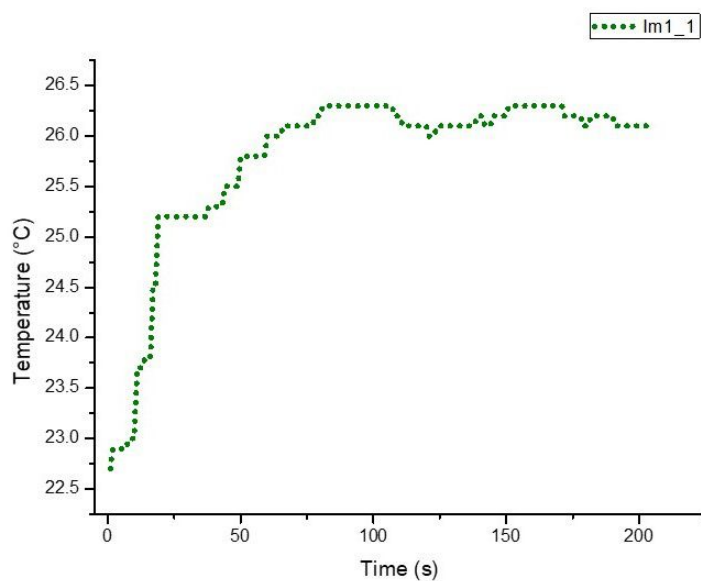


Figure B.2: Plot reporting the water temperature evolution caused by the endothermic reaction of hydration of Im1.1-1 introduced into the water bath.

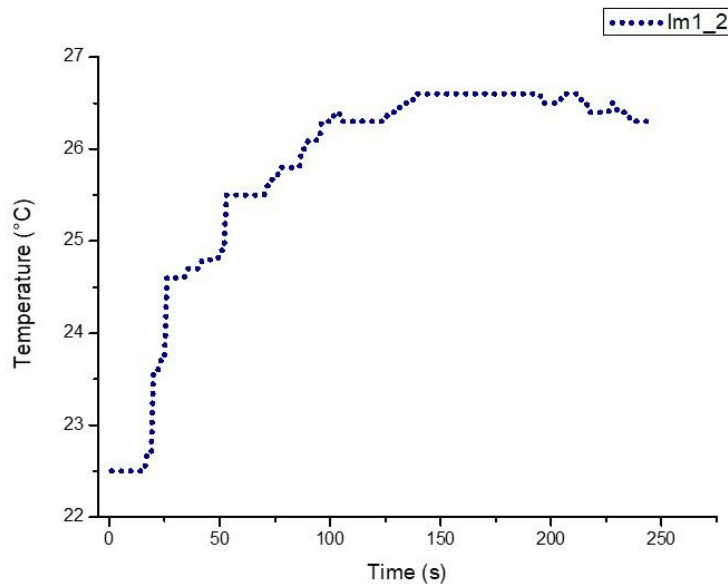


Figure B.3: Plot reporting the water temperature evolution caused by the endothermic reaction of hydration of Im1.1-2 introduced into the water bath.

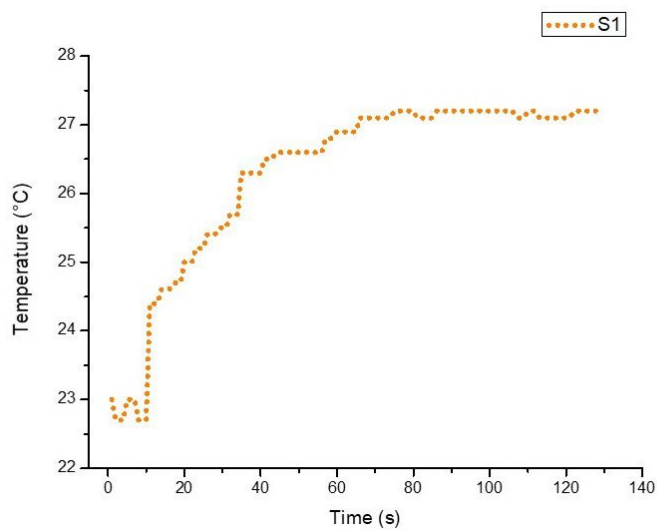


Figure B.4: Plot reporting the water temperature evolution caused by the endothermic reaction of hydration of S1 introduced into the water bath.

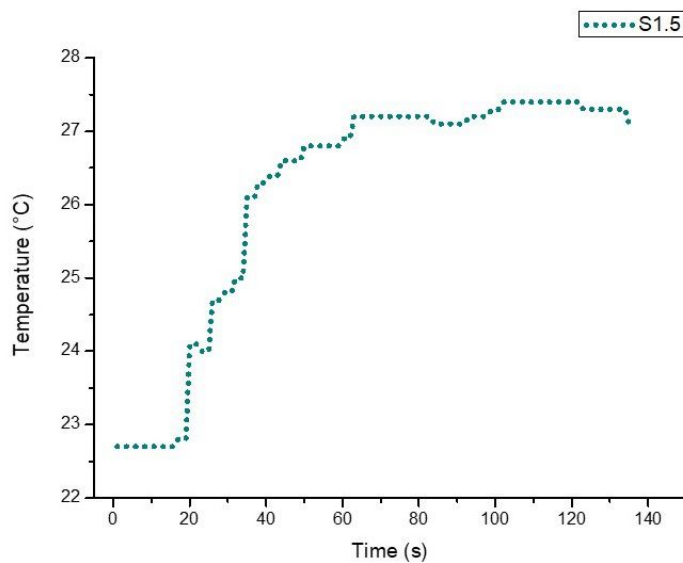


Figure B.5: Plot reporting the water temperature evolution caused by the endothermic reaction of hydration of S1.5 introduced into the water bath.

Bibliography

- [1] European commission directorate-general for energy. *Mapping and analyses of the current and future (2020-2030) heating/cooling fuel deployment (fossil/renewables)*. Tech. rep. 2016 (cit. on pp. 1, 2).
- [2] DG .E.N.E.R. *Communication from the commission to the european parliament, the council, the European economic and social committee and the committee of the regions*. Tech. rep. 2016 (cit. on p. 1).
- [3] Interseasonal heat transfer ICAX. *Heat Recycling / Seasonal Heat Storage / GSHC / Ground Source Heating and Cooling / Ground Energy / GSHP* (cit. on p. 2).
- [4] Yannan Zhang and Ruzhu Wang. «Sorption thermal energy storage: Concept, process, applications and perspectives». In: *Energy Storage Materials* 27 (2020), pp. 352–369. ISSN: 2405-8297. DOI: <https://doi.org/10.1016/j.ensm.2020.02.024> (cit. on pp. 3, 8).
- [5] Lavinia Socaciu. «Seasonal Sensible Thermal Energy Storage Solutions». In: *Leonardo Electronic Journal of Practices and Technologies* 10 (July 2011), pp. 49–68 (cit. on p. 3).
- [6] Hauer. *Thermal Energy Storage, IEA-ETSAP and IRENA Technology-Policy (January 2013)* (cit. on p. 3).
- [7] A. Felix Regin, S.C. Solanki, and J.S. Saini. «Heat transfer characteristics of thermal energy storage system using PCM capsules: A review». In: *Renewable and Sustainable Energy Reviews* 12.9 (2008), pp. 2438–2458. ISSN: 1364-0321. DOI: <https://doi.org/10.1016/j.rser.2007.06.009> (cit. on p. 3).
- [8] Yinping Zhang, Guobing Zhou, Kunping Lin, Qunli Zhang, and Hongfa Di. «Application of latent heat thermal energy storage in buildings: State-of-the-art and outlook». In: *Building and Environment* 42.6 (2007), pp. 2197–2209. ISSN: 0360-1323. DOI: <https://doi.org/10.1016/j.buildenv.2006.07.023> (cit. on p. 3).

- [9] B [Eanest Jebasingh] and A [Valan Arasu]. «A comprehensive review on latent heat and thermal conductivity of nanoparticle dispersed phase change material for low-temperature applications». In: *Energy Storage Materials* 24 (2020), pp. 52–74. ISSN: 2405-8297. DOI: <https://doi.org/10.1016/j.ensm.2019.07.031> (cit. on p. 3).
- [10] Harald Mehling and Luisa F. Cabeza. *Heat and cold storage with PCM*. Ed. by D. Mewes and F. Mayinger. Heat and Mass Transfer. Berlin, Heidelberg: Springer, 2008, pp. 1–308. ISBN: 978-3-540-68556-2. DOI: 10.1007/978-3-540-68557-9 (cit. on p. 3).
- [11] Liu Hui, Kokouvi N'Tsoukpoe, Le Nolwenn, and Luo Lingai. «Evaluation of a seasonal storage system of solar energy for house heating using different absorption couples». In: *Energy Conversion and Management* 52 (June 2011), pp. 2427–2436. DOI: 10.1016/j.enconman.2010.12.049 (cit. on p. 4).
- [12] Mina Rouhani. «Sorptions thermal energy storage for sustainable heating and cooling ». In: *School of Mechatronic Systems Engineering Faculty of Applied Science* (2019) (cit. on pp. 4, 47).
- [13] Ning Xie, Zhaowen Huang, Zigeng Luo, Xuenong Gao, Yutang Fang, and Zhengguo Zhang. «Inorganic salt hydrate for thermal energy storage». In: *Applied Sciences (Switzerland)* 7.12 (2017). ISSN: 20763417. DOI: 10.3390/app7121317 (cit. on p. 5).
- [14] K. Edem N'Tsoukpoe, Hui Liu, Nolwenn [Le Pierrès], and Lingai Luo. «A review on long-term sorptions solar energy storage». In: *Renewable and Sustainable Energy Reviews* 13.9 (2009), pp. 2385–2396. ISSN: 1364-0321. DOI: <https://doi.org/10.1016/j.rser.2009.05.008> (cit. on p. 6).
- [15] Gurdeep Raj. *Surface Chemistry* (cit. on p. 6).
- [16] Nabin Kharal. «Selection of Novel Technology for Wastewater Treatment». In: *Mathematical Sciences and Technology* May (2017), pp. 1–23. DOI: 10.13140/RG.2.2.32046.41286 (cit. on p. 7).
- [17] Luca Scapino, Herbert A. Zondag, Johan [Van Bael], Jan Diriken, and Camilo C.M. Rindt. «Energy density and storage capacity cost comparison of conceptual solid and liquid sorptions seasonal heat storage systems for low-temperature space heating». In: *Renewable and Sustainable Energy Reviews* 76 (2017), pp. 1314–1331. ISSN: 1364-0321. DOI: <https://doi.org/10.1016/j.rser.2017.03.101> (cit. on pp. 7, 11, 60, 72, 73).
- [18] Mina Rouhani. «Sorptions thermal energy storage for sustainable heating and cooling». In: (July 2019) (cit. on p. 8).

- [19] Andrea Frazzica and Angelo Freni. «Adsorbent working pairs for solar thermal energy storage in buildings». In: *Renewable Energy* 110 (2017). Increasing the renewable share for heating and cooling by the means of sorption heat pumps and chillers, pp. 87–94. ISSN: 0960-1481. DOI: <https://doi.org/10.1016/j.renene.2016.09.047> (cit. on p. 9).
- [20] Yaping Cui, Jingchao Xie, Jiaping Liu, and Song Pan. «Review of Phase Change Materials Integrated in Building Walls for Energy Saving». In: *Procedia Engineering* 121 (Dec. 2015), pp. 763–770. DOI: [10.1016/j.proeng.2015.09.027](https://doi.org/10.1016/j.proeng.2015.09.027) (cit. on p. 11).
- [21] S.Z. Xu, R.Z. Wang, L.W. Wang, and J. Zhu. «Performance characterizations and thermodynamic analysis of magnesium sulfate-impregnated zeolite 13X and activated alumina composite sorbents for thermal energy storage». In: *Energy* 167 (2019), pp. 889–901. ISSN: 0360-5442. DOI: <https://doi.org/10.1016/j.energy.2018.10.200> (cit. on p. 12).
- [22] Armand [Fopah Lele], Kokouvi Edem N'Tsoukpoe, Thomas Osterland, Frédéric Kuznik, and Wolfgang K.L. Ruck. «Thermal conductivity measurement of thermochemical storage materials». In: *Applied Thermal Engineering* 89 (2015), pp. 916–926. ISSN: 1359-4311. DOI: <https://doi.org/10.1016/j.applthermaleng.2015.06.077> (cit. on p. 12).
- [23] N. Yu, R.Z. Wang, and L.W. Wang. «Sorption thermal storage for solar energy». In: *Progress in Energy and Combustion Science* 39.5 (2013), pp. 489–514. ISSN: 0360-1285. DOI: <https://doi.org/10.1016/j.pecs.2013.05.004> (cit. on pp. 12, 35, 37).
- [24] Liu Hui, N'Tsoukpoe K. Edem, Le Pierres Nolwenn, and Luo Lingai. «Evaluation of a seasonal storage system of solar energy for house heating using different absorption couples». In: *Energy Conversion and Management* 52.6 (2011). 9th International Conference on Sustainable Energy Technologies (SET 2010), pp. 2427–2436. ISSN: 0196-8904. DOI: <https://doi.org/10.1016/j.enconman.2010.12.049> (cit. on pp. 12, 14, 15).
- [25] Vassilis Inglezakis and Antonis Zorpas. «Heat of adsorption, adsorption energy and activation energy in adsorption and ion exchange systems». In: *Desalination and Water Treatment - DESALIN WATER TREAT* 39 (Feb. 2012), pp. 149–157. DOI: [10.1080/19443994.2012.669169](https://doi.org/10.1080/19443994.2012.669169) (cit. on p. 17).
- [26] Antonio Lucciulli. *Corso di scienza e tecnologia dei materiali ceramici. Densità, porosità, superficie specifica e applicazioni* (cit. on p. 18).
- [27] Qing Chang. «Chapter 10 - Surface of Solids». In: *Colloid and Interface Chemistry for Water Quality Control*. Ed. by Qing Chang. Academic Press, 2016, pp. 175–225. ISBN: 978-0-12-809315-3. DOI: <https://doi.org/10.1016/B978-0-12-809315-3.00010-4> (cit. on p. 18).

- [28] Hui Liu, Li Long, Xin Weng, Shourong Zheng, and Zhaoyi Xu. «Efficient removal of tetrabromobisphenol A using microporous and mesoporous carbons: The role of pore structure». In: *Microporous and Mesoporous Materials* 298 (2020), p. 110052. ISSN: 1387-1811. DOI: <https://doi.org/10.1016/j.micromeso.2020.110052> (cit. on p. 19).
- [29] M.R. Usman, M. Saleem, and R. Aslam. *Chemical Engineering Terminology*. Lulu.com, 2015. ISBN: 9781329090583. URL: <https://books.google.it/books?id=EgfECQAAQBAJ> (cit. on pp. 19, 20).
- [30] Filip Ambroz, Thomas J. Macdonald, Vladimir Martis, and Ivan P. Parkin. «Evaluation of the BET Theory for the Characterization of Meso and Microporous MOFs». In: *Small Methods* 2.11 (Nov. 2018), p. 1800173. ISSN: 23669608. DOI: 10.1002/smt.201800173 (cit. on p. 19).
- [31] K. C. Ng, H. T. Chua, C. Y. Chung, C. H. Loke, T. Kashiwagi, A. Akisawa, and B. B. Saha. «Experimental investigation of the silica gel-water adsorption isotherm characteristics». In: *Applied Thermal Engineering* 21.16 (Nov. 2001), pp. 1631–1642. ISSN: 13594311. DOI: 10.1016/S1359-4311(01)00039-4 (cit. on p. 21).
- [32] G. D. Chukin and V. I. Malevich. «Structure of silica». In: *Journal of Structural Chemistry* 18.1 (Jan. 1977), pp. 76–83. ISSN: 00224766. DOI: 10.1007/BF00745434 (cit. on p. 21).
- [33] A. Feng, B.J. McCoy, Z.A. Munir, and D.E. Cagliostro. «Water Adsorption and Desorption Kinetics on Silica Insulation». In: *Journal of Colloid and Interface Science* 180.1 (1996), pp. 276–284. ISSN: 0021-9797. DOI: <https://doi.org/10.1006/jcis.1996.0300> (cit. on pp. 21, 22).
- [34] Kuei-Sen Chang, Hui-Chun Wang, and Tsair-Wang Chung. «Effect of regeneration conditions on the adsorption dehumidification process in packed silica gel beds». In: *Applied Thermal Engineering - APPL THERM ENG* 24 (Apr. 2004), pp. 735–742. DOI: 10.1016/j.applthermaleng.2003.11.003 (cit. on p. 22).
- [35] Motohide Matsuda. «Application 25 - Zeolite Membrane». In: *Nanoparticle Technology Handbook (Third Edition)*. Ed. by Makio Naito, Toyokazu Yokoyama, Kouhei Hosokawa, and Kiyoshi Nogi. Third Edition. Elsevier, 2018, pp. 539–542. ISBN: 978-0-444-64110-6. DOI: <https://doi.org/10.1016/B978-0-444-64110-6.00032-9> (cit. on p. 22).
- [36] Christèle Beauvais, Anne Boutin, and Alain H. Fuchs. «Adsorption of water in zeolite sodium-faujasite: A molecular simulation study». In: *Comptes Rendus Chimie* 8.3 (2005). Crystalline and organized porous solids, pp. 485–490. ISSN: 1631-0748. DOI: <https://doi.org/10.1016/j.crci.2004.11.011> (cit. on p. 23).

- [37] S. K. Henninger, F. P. Schmidt, and H. M. Henning. «Characterisation and improvement of sorption materials with molecular modeling for the use in heat transformation applications». In: *Adsorption*. Vol. 17. 5. Springer, Oct. 2011, pp. 833–843. DOI: 10.1007/s10450-011-9342-6 (cit. on pp. 23, 26).
- [38] W. Lutz, H. Toufar, D. Heidemann, Nesma Salman, Claus Rüscher, Thorsten Gesing, J.-Chr Buhl, and R. Bertram. «Siliceous extra-framework species in dealuminated Y zeolites generated by steaming». In: *Microporous and Mesoporous Materials* 104 (Aug. 2007), pp. 171–178. DOI: 10.1016/j.micromeso.2007.01.028 (cit. on p. 23).
- [39] B.L. Meyers, T.H. Fleisch, and C.L. Marshall. «Dealumination and aluminum ion migration in faujasites». In: *Applied Surface Science* 26.4 (1986), pp. 503–516. ISSN: 0169-4332. DOI: [https://doi.org/10.1016/0169-4332\(86\)90122-4](https://doi.org/10.1016/0169-4332(86)90122-4) (cit. on p. 23).
- [40] Andreas Jentys, Gerhard Warecka, Miroslaw Derewinski, and Johannes Lercher. «Adsorption of water on ZSM 5 zeolites». In: *The Journal of Physical Chemistry* 93 (June 1989). DOI: 10.1021/j100349a032 (cit. on pp. 23, 25).
- [41] J. Jänchen, D. Ackermann, H. Stach, and W. Brösicke. «Studies of the water adsorption on Zeolites and modified mesoporous materials for seasonal storage of solar heat». In: *Solar Energy* 76.1 (2004). Solar World Congress 2001, pp. 339–344. ISSN: 0038-092X. DOI: <https://doi.org/10.1016/j.solener.2003.07.036> (cit. on pp. 24, 35).
- [42] Hauer. «Thermal energy storage with zeolite for heating and cooling application». In: *Proceedings of the International Sorption Heat Pump Conference* (Sept. 2002) (cit. on p. 24).
- [43] Henner Kerskes, Sebastian Asenbeck, Barbara Mette, F. Bertsch, and Hans Müller-Steinhagen. «Experimental and Numerical Investigations on Thermo Chemical Heat Storage». In: Jan. 2010. DOI: 10.18086/eurosun.2010.16.14 (cit. on pp. 24, 35, 47, 62, 64).
- [44] Hao Wu, Philippe Trens, Bernard Fraise, Fabrice Salles, and Jerzy Zajac. «Hydration mechanism in Ce-exchanged zeolites and heat release performances upon adsorption of water vapour in support of their potential use in thermochemical storage of energy under mild conditions of adsorbent regeneration and saturation». In: *Microporous and Mesoporous Materials* 296 (2020), p. 109999. ISSN: 1387-1811. DOI: <https://doi.org/10.1016/j.micromeso.2020.109999> (cit. on pp. 24, 35).

- [45] Stephen T. Wilson, Brent M. Lok, Celeste A. Messina, Thomas R. Cannan, and Edith M. Flanigen. «Aluminophosphate molecular sieves: a new class of microporous crystalline inorganic solids». In: *Journal of the American Chemical Society* 104.4 (1982), pp. 1146–1147. DOI: 10.1021/ja00368a062 (cit. on p. 26).
- [46] Xiaona Liu, Nana Yan, Lei Wang, Chao Ma, Peng Guo, Peng Tian, Guang Cao, and Zhongmin Liu. «Landscape of AlPO-based structures and compositions in the database of zeolite structures». In: *Microporous and Mesoporous Materials* 280 (May 2019). DOI: 10.1016/j.micromeso.2019.01.047 (cit. on p. 26).
- [47] *Database of Zeolite Structures*. URL: <http://www.iza-structure.org/databases/> (visited on 06/06/2020) (cit. on p. 26).
- [48] Christoph Buttersack. «Modeling of type IV and V sigmoidal adsorption isotherms». In: *Phys. Chem. Chem. Phys.* 21 (10 2019), pp. 5614–5626. DOI: 10.1039/C8CP07751G (cit. on p. 26).
- [49] Guillaume Poulet, Philippe Sautet, and Alain Tuel. «Structure of Hydrated Microporous Aluminophosphates: Static and Molecular Dynamics Approaches of AlPO 4-34 from First Principles Calculations». In: (2002). DOI: 10.1021/jp020533p (cit. on p. 26).
- [50] Alenka Ristić, Nataša Zabukovec Logar, Stefan K. Henninger, and Venčeslav Kaučič. «The Performance of Small-Pore Microporous Aluminophosphates in Low-Temperature Solar Energy Storage: The Structure-Property Relationship». In: *Advanced Functional Materials* 22.9 (May 2012), pp. 1952–1957. ISSN: 1616301X. DOI: 10.1002/adfm.201102734 (cit. on p. 27).
- [51] J. Bauer, T. Selvam, J. Ofili, E. Che, R. Herrmann, and W. Schwieger. «Stability of AlPO and SAPO molecular sieves during adsorption-desorption cycles of water vapor investigated by in-situ XRD measurements». In: *From Zeolites to Porous MOF Materials - The 40th Anniversary of International Zeolite Conference*. Ed. by Ruren Xu, Zi Gao, Jiesheng Chen, and Wenfu Yan. Vol. 170. Studies in Surface Science and Catalysis. Elsevier, 2007, pp. 837–844. DOI: [https://doi.org/10.1016/S0167-2991\(07\)80930-X](https://doi.org/10.1016/S0167-2991(07)80930-X) (cit. on p. 27).
- [52] S.K. Henninger, G. Munz, K.-F. Ratzsch, and P. Schossig. «Cycle stability of sorption materials and composites for the use in heat pumps and cooling machines». In: *Renewable Energy* 36.11 (2011), pp. 3043–3049. ISSN: 0960-1481. DOI: <https://doi.org/10.1016/j.renene.2011.03.032> (cit. on p. 27).

- [53] Minchev, Ya Neinska, V. Valtchev, V. Minkov, T. Tsoncheva, V. Penchev, H. Lechert, and M. Hess. «Effect of the rehydration on the acidity and catalytic activity of SAPO molecular sieves». In: *Catalysis Letters* 18.1-2 (Mar. 1993), pp. 125–135. ISSN: 1011372X. DOI: 10.1007/BF00769505 (cit. on p. 28).
- [54] M. Briend, R. Vomscheid, M. J. Peltre, P. P. Man, and D. Barthomeuf. «Influence of the choice of the template on the short- and long-term stability of SAPO-34 zeolite». In: *Journal of Physical Chemistry* 99.20 (1995), pp. 8270–8276. ISSN: 00223654. DOI: 10.1021/j100020a060 (cit. on p. 28).
- [55] Michael Fischer. «Interaction of water with (silico)aluminophosphate zeotypes: A comparative investigation using dispersion-corrected DFT». In: *Physical Chemistry Chemical Physics* 18.23 (June 2016), pp. 15738–15750. ISSN: 14639076. DOI: 10.1039/c6cp02289h (cit. on p. 28).
- [56] Vincenza Brancato and Andrea Frazzica. «Characterisation and comparative analysis of zeotype water adsorbents for heat transformation applications». In: *Solar Energy Materials and Solar Cells* 180 (2018), pp. 91–102. ISSN: 0927-0248. DOI: <https://doi.org/10.1016/j.solmat.2018.02.035> (cit. on pp. 28, 35).
- [57] S.K. Henninger, F.P. Schmidt, and H.-M. Henning. «Water adsorption characteristics of novel materials for heat transformation applications». In: *Applied Thermal Engineering* 30.13 (2010), pp. 1692–1702. ISSN: 1359-4311. DOI: <https://doi.org/10.1016/j.applthermaleng.2010.03.028> (cit. on pp. 29, 35).
- [58] Mohadeseh Safaei, Mohammad Mehdi Foroughi, Nasser Ebrahimpoor, Shohreh Jahani, Ali Omidi, and Mehrdad Khatami. «A review on metal-organic frameworks: Synthesis and applications». In: *TrAC Trends in Analytical Chemistry* 118 (2019), pp. 401–425. ISSN: 0165-9936. DOI: <https://doi.org/10.1016/j.trac.2019.06.007> (cit. on p. 29).
- [59] *MOF Metal Organic Framework - Ê×Ò³-Í-ÀÖ³Ç¹ÙÍø|TLCBET¹Ù · ½ÍøÖ¾*. URL: <http://www.4006500671.com/mof-metal-organic-framework.php> (visited on 06/06/2020) (cit. on pp. 29, 30).
- [60] Pia Kuesgens, Marcus Rose, Irena Senkovska, Heidrun Froede, Antje Heerwig, Sven Siegle, and Stefan Kaskel. «Characterization of Metal-Organic Frameworks by Water Adsorption». In: *Microporous and Mesoporous Materials* 120 (Apr. 2009), pp. 325–330. DOI: 10.1016/j.micromeso.2008.11.020 (cit. on pp. 30, 31).
- [61] Nicholas Burtch, Himanshu Jasuja, and Krista Walton. «Water Stability and Adsorption in MetalOrganic Frameworks». In: *Chemical Reviews* 114 (Sept. 2014). DOI: 10.1021/cr5002589 (cit. on p. 30).

- [62] Chenghong Wang, Xinlei Liu, Nilay Keser Demir, J. Paul Chen, and Kang Li. «Applications of water stable metal–organic frameworks». In: *Chem. Soc. Rev.* 45 (18 2016), pp. 5107–5134. DOI: [10.1039/C6CS00362A](https://doi.org/10.1039/C6CS00362A) (cit. on p. 30).
- [63] Meili Ding, Xuechao Cai, and Hai-Long Jiang. «Improving MOF stability: approaches and applications». In: *Chem. Sci.* 10 (44 2019), pp. 10209–10230. DOI: [10.1039/C9SC03916C](https://doi.org/10.1039/C9SC03916C) (cit. on p. 30).
- [64] J.D Carruthers, D.A Payne, K.S.W Sing, and L.J Stryker. «Specific and nonspecific interactions in the adsorption of argon, nitrogen, and water vapor on oxides». In: *Journal of Colloid and Interface Science* 36.2 (1971), pp. 205–216. ISSN: 0021-9797. DOI: [https://doi.org/10.1016/0021-9797\(71\)90165-2](https://doi.org/10.1016/0021-9797(71)90165-2) (cit. on p. 31).
- [65] Brice F. Ngouana W. and Andrey G. Kalinichev. «Structural Arrangements of Isomorphic Substitutions in Smectites: Molecular Simulation of the Swelling Properties, Interlayer Structure, and Dynamics of Hydrated Cs–Montmorillonite Revisited with New Clay Models». In: *The Journal of Physical Chemistry C* 118.24 (2014), pp. 12758–12773. DOI: [10.1021/jp500538z](https://doi.org/10.1021/jp500538z) (cit. on p. 32).
- [66] Xiao Wen Liu, Min Hu, and Yue Hua Hu. «Chemical composition and surface charge properties of montmorillonite». In: *Journal of Central South University of Technology (English Edition)* 15.2 (Apr. 2008), pp. 193–197. ISSN: 10059784. DOI: [10.1007/s11771-008-0037-4](https://doi.org/10.1007/s11771-008-0037-4) (cit. on p. 32).
- [67] Olfat M Sadek and Wafaa K Mekhamer. «Ca-montmorillonite clay as thermal energy storage material». In: *Thermochimica Acta* 363.1 (2000), pp. 47–54. ISSN: 0040-6031. DOI: [https://doi.org/10.1016/S0040-6031\(00\)00598-0](https://doi.org/10.1016/S0040-6031(00)00598-0) (cit. on p. 32).
- [68] Emiel J. M. Hensen and Berend Smit. «Why Clays Swell». In: *The Journal of Physical Chemistry B* 106.49 (2002), pp. 12664–12667. DOI: [10.1021/jp0264883](https://doi.org/10.1021/jp0264883) (cit. on p. 32).
- [69] Fabrice Salles, Jean-Marc Douillard, Olivier Bildstein, Cedric Gaudin, Benedicte Prelot, Jerzy Zajac, and Henri [Van Damme]. «Driving force for the hydration of the swelling clays: Case of montmorillonites saturated with alkaline-earth cations». In: *Journal of Colloid and Interface Science* 395 (2013), pp. 269–276. ISSN: 0021-9797. DOI: <https://doi.org/10.1016/j.jcis.2012.12.050> (cit. on p. 32).
- [70] Amira Jabbari-Hichri, Simona Bennici, and Aline Auroux. «CaCl₂-containing composites as thermochemical heat storage materials». In: *Solar Energy Materials and Solar Cells* 172 (2017), pp. 177–185. ISSN: 0927-0248. DOI: <https://doi.org/10.1016/j.solmat.2017.07.037> (cit. on pp. 32, 35, 47, 147).

- [71] H [van Olphen]. «Thermodynamics of interlayer adsorption of water in clays. I.—Sodium vermiculite». In: *Journal of Colloid Science* 20.8 (1965), pp. 822–837. ISSN: 0095-8522. DOI: [https://doi.org/10.1016/0095-8522\(65\)90055-3](https://doi.org/10.1016/0095-8522(65)90055-3) (cit. on p. 32).
- [72] Ye Hua, Burcu Ugur, and F. [Handan Tezel]. «Adsorbent screening for thermal energy storage application». In: *Solar Energy Materials and Solar Cells* 196 (2019), pp. 119–123. ISSN: 0927-0248. DOI: <https://doi.org/10.1016/j.solmat.2019.01.052> (cit. on p. 35).
- [73] Valeria Palomba, Salvatore Vasta, and Angelo Freni. «Experimental testing of AQSOA FAM Z02/water adsorption system for heat and cold storage». In: *Applied Thermal Engineering* 124 (2017), pp. 967–974. ISSN: 1359-4311. DOI: <https://doi.org/10.1016/j.applthermaleng.2017.06.085> (cit. on p. 35).
- [74] Anastasia Permyakova et al. «Design of salt-metal organic framework composites for seasonal heat storage applications». In: *Journal of Materials Chemistry A* 5.25 (June 2017), pp. 12889–12898. ISSN: 20507496. DOI: 10.1039/c7ta03069j (cit. on p. 35).
- [75] Raya AL-Dadah, Saad Mahmoud, Eman Elsayed, Peter Youssef, and Fadhel Al-Mousawi. «Metal-organic framework materials for adsorption heat pumps». In: *Energy* 190 (2020), p. 116356. ISSN: 0360-5442. DOI: <https://doi.org/10.1016/j.energy.2019.116356> (cit. on p. 35).
- [76] N. Yu, R.Z. Wang, Z.S. Lu, and L.W. Wang. «Development and characterization of silica gel–LiCl composite sorbents for thermal energy storage». In: *Chemical Engineering Science* 111 (2014), pp. 73–84. ISSN: 0009-2509. DOI: <https://doi.org/10.1016/j.ces.2014.02.012> (cit. on pp. 35, 44, 47, 150, 151).
- [77] Yannan Zhang, Ruzhu Wang, Tingxian Li, and Yanjie Zhao. «Thermochemical Characterizations of Novel Vermiculite-LiCl Composite Sorbents for Low-Temperature Heat Storage». In: *Energies* 9.10 (Oct. 2016), p. 854. ISSN: 1996-1073. DOI: 10.3390/en9100854 (cit. on p. 35).
- [78] A.Hauer. «Thermal energy storage with zeolite for heating and cooling applications». In: *ZAE Bayern, center for Applied Energy Research, Domagkstr.11* () (cit. on p. 35).
- [79] H. Stach, J. Mugele, Jochen Jänchen, and E. Weiler. «Influence of Cycle Temperatures on the Thermochemical Heat Storage Densities in the Systems Water/Microporous and Water/Mesoporous Adsorbents». In: *Adsorption* 11 (July 2005), pp. 393–404. DOI: 10.1007/s10450-005-5405-x (cit. on pp. 35, 61, 150).

- [80] Chris P Bales, Paul Dr.rer.nat. Gantenbein, Andreas Hauer, H. K. Henning, Dagmar Jaenig, Henner Kerskes, Thomas Nuñez, and Klaas Visscher. *Thermal Properties of Materials for Thermo-chemical Storage of Solar Heat : Report B2 of Subtask B*. 2005 (cit. on p. 35).
- [81] Hyunho Kim et al. «Characterization of Adsorption Enthalpy of Novel Water-Stable Zeolites and Metal-Organic Frameworks». In: *Scientific Reports* 6.1 (Jan. 2016), pp. 1–8. ISSN: 20452322. DOI: 10.1038/srep19097 (cit. on p. 35).
- [82] Larisa G. Gordeeva, Marina V. Solovyeva, and Yuri I. Aristov. «NH₂-MIL-125 as a promising material for adsorptive heat transformation and storage». In: *Energy* 100 (Apr. 2016), pp. 18–24. ISSN: 03605442. DOI: 10.1016/j.energy.2016.01.034 (cit. on p. 35).
- [83] P.A.J. Donkers, L.C. Sögütoglu, H.P. Huinink, H.R. Fischer, and O.C.G. Adan. «A review of salt hydrates for seasonal heat storage in domestic applications». In: *Applied Energy* 199 (2017), pp. 45–68. ISSN: 0306-2619. DOI: <https://doi.org/10.1016/j.apenergy.2017.04.080> (cit. on pp. 36, 37, 39).
- [84] Tingxian Li, Ruzhu Wang, and Jeremiah K. Kiplagat. «A target-oriented solid-gas thermochemical sorption heat transformer for integrated energy storage and energy upgrade». In: *AIChE Journal* 59.4 (Apr. 2013), pp. 1334–1347. ISSN: 00011541. DOI: 10.1002/aic.13899. URL: <http://doi.wiley.com/10.1002/aic.13899> (cit. on p. 39).
- [85] Yu.I Aristov, G Restuccia, G Cacciola, and V.N Parmon. «A family of new working materials for solid sorption air conditioning systems». In: *Applied Thermal Engineering* 22.2 (2002), pp. 191–204. ISSN: 1359-4311. DOI: [https://doi.org/10.1016/S1359-4311\(01\)00072-2](https://doi.org/10.1016/S1359-4311(01)00072-2) (cit. on p. 40).
- [86] Larisa Gordeeva, Angelo Freni, Tamara Krieger, Giovanni Restuccia, and Yuri Aristov. «Composites “lithium halides in silica gel pores”: Methanol sorption equilibrium». In: *Microporous and Mesoporous Materials* 112 (July 2008), pp. 254–261. DOI: 10.1016/j.micromeso.2007.09.040 (cit. on pp. 40, 43, 47, 61).
- [87] Irina Simonova, Angelo Freni, Giovanni Restuccia, and Yuri Aristov. «Water sorption on composite “silica modified by calcium nitrate”». In: *Microporous and Mesoporous Materials - MICROPOROUS MESOPOROUS MAT* 122 (June 2009), pp. 223–228. DOI: 10.1016/j.micromeso.2009.02.034 (cit. on pp. 40, 43).

- [88] J.X. Xu, T.X. Li, J.W. Chao, T.S. Yan, and R.Z. Wang. «High energy-density multi-form thermochemical energy storage based on multi-step sorption processes». In: *Energy* 185 (2019), pp. 1131–1142. ISSN: 0360-5442. DOI: <https://doi.org/10.1016/j.energy.2019.07.076> (cit. on p. 42).
- [89] Alexandra D. Grekova, Larisa G. Gordeeva, and Yuri I. Aristov. «Composite “LiCl/vermiculite” as advanced water sorbent for thermal energy storage». In: *Applied Thermal Engineering* 124 (2017), pp. 1401–1408. ISSN: 1359-4311. DOI: <https://doi.org/10.1016/j.applthermaleng.2017.06.122> (cit. on p. 42).
- [90] Eman Elsayed, Raya AL-Dadah, Saad Mahmoud, Paul Anderson, and Ahmed Elsayed. «Adsorption cooling system employing novel MIL-101(Cr)/CaCl₂ composites: Numerical study». In: *International Journal of Refrigeration* 107 (2019), pp. 246–261. ISSN: 0140-7007. DOI: <https://doi.org/10.1016/j.ijrefrig.2019.08.004> (cit. on p. 42).
- [91] Y.N. Zhang, R.Z. Wang, Y.J. Zhao, T.X. Li, S.B. Riffat, and N.M. Wajid. «Development and thermochemical characterizations of vermiculite/SrBr₂ composite sorbents for low-temperature heat storage». In: *Energy* 115 (2016), pp. 120–128. ISSN: 0360-5442. DOI: <https://doi.org/10.1016/j.energy.2016.08.108> (cit. on pp. 43, 47).
- [92] V. Brancato, Larisa Gordeeva, Alessio Sapienza, Valeria Palomba, Salvatore Vasta, Alexandra Grekova, Andrea Frazzica, and Yuri Aristov. «Experimental characterization of the LiCl/Vermiculite composite for sorption heat storage applications». In: *International Journal of Refrigeration* (Aug. 2018). DOI: [10.1016/j.ijrefrig.2018.08.006](https://doi.org/10.1016/j.ijrefrig.2018.08.006) (cit. on p. 43).
- [93] Luigi Calabrese, Vincenza Brancato, Valeria Palomba, Andrea Frazzica, and Luisa F. Cabeza. «Innovative composite sorbent for thermal energy storage based on a SrBr₂ · 6H₂O filled silicone composite foam». In: *Journal of Energy Storage* 26 (2019), p. 100954. ISSN: 2352-152X. DOI: <https://doi.org/10.1016/j.est.2019.100954> (cit. on p. 43).
- [94] Armand Fopah Lele, Kathrin Korhammer, Nina Wegscheider, Holger Urs Rammelberg, Thomas Osterland, and Wolfgang Ruck. «Thermal conductivity measurement of salt hydrate as porous material using calorimetric (DSC) method». In: June 2013. DOI: [10.13140/RG.2.1.3034.9927](https://doi.org/10.13140/RG.2.1.3034.9927) (cit. on p. 44).
- [95] Lawrence Shere, Siddharth Trivedi, Samuel Roberts, Adriano Sciacovelli, and Yulong Ding. «Synthesis and Characterization of Thermochemical Storage Material Combining Porous Zeolite and Inorganic Salts». In: *Heat Transfer Engineering* 40.13-14 (Aug. 2019), pp. 1176–1181. ISSN: 15210537. DOI: [10.1080/01457632.2018.1457266](https://doi.org/10.1080/01457632.2018.1457266) (cit. on p. 44).

- [96] Sergio Salviati, Federico Carosio, Guido Saracco, and Alberto Fina. «Hydrated Salt/Graphite/Polyelectrolyte Organic-Inorganic Hybrids for Efficient Thermochemical Storage». In: *Nanomaterials* 9.3 (Mar. 2019), p. 420. ISSN: 2079-4991. DOI: 10.3390/nano9030420 (cit. on p. 44).
- [97] M. Gaeini, A.L. Rouws, J.W.O. Salari, H.A. Zondag, and C.C.M. Rindt. «Characterization of microencapsulated and impregnated porous host materials based on calcium chloride for thermochemical energy storage». In: *Applied Energy* 212 (2018), pp. 1165–1177. ISSN: 0306-2619. DOI: <https://doi.org/10.1016/j.apenergy.2017.12.131> (cit. on pp. 47, 147, 148).
- [98] Kathrin Korhammer, Mona-Maria Druske, Armand Fopah-Lele, Holger Urs Rammelberg, Nina Wegscheider, Oliver Opel, Thomas Osterland, and Wolfgang Ruck. «Sorptions and thermal characterization of composite materials based on chlorides for thermal energy storage». In: *Applied Energy* 162 (2016), pp. 1462–1472. ISSN: 0306-2619. DOI: <https://doi.org/10.1016/j.apenergy.2015.08.037> (cit. on p. 47).
- [99] A. Cammarata, V. Verda, A. Sciacovelli, and Y. Ding. «Hybrid strontium bromide-natural graphite composites for low to medium temperature thermochemical energy storage: Formulation, fabrication and performance investigation». In: *Energy Conversion and Management* 166 (2018), pp. 233–240. ISSN: 0196-8904. DOI: <https://doi.org/10.1016/j.enconman.2018.04.031> (cit. on p. 47).
- [100] Abbas Mehrabadi and Mohammed Farid. «New salt hydrate composite for low-grade thermal energy storage». In: *Energy* 164 (2018), pp. 194–203. ISSN: 0360-5442. DOI: <https://doi.org/10.1016/j.energy.2018.08.192> (cit. on p. 47).
- [101] Anastasia Permyakova et al. «Design of salt–metal organic framework composites for seasonal heat storage applications». In: *J. Mater. Chem. A* 5 (25 2017), pp. 12889–12898. DOI: 10.1039/C7TA03069J (cit. on pp. 47, 61).
- [102] Alexandra Grekova, Larisa Gordeeva, and Yuri Aristov. «Composite sorbents “Li/Ca halogenides inside Multi-wall Carbon Nano-tubes” for Thermal Energy Storage». In: *Solar Energy Materials and Solar Cells* 155 (2016), pp. 176–183. ISSN: 0927-0248. DOI: <https://doi.org/10.1016/j.solmat.2016.06.006> (cit. on pp. 47, 81, 149, 151).
- [103] Alenka Ristić and Nataša Zabukovec Logar. «New composite water sorbents CaCl₂-PHTS for low-temperature sorption heat storage: Determination of structural properties». In: *Nanomaterials* 9.1 (Jan. 2019). ISSN: 20794991. DOI: 10.3390/nano9010027 (cit. on p. 47).

- [104] Emilie Courbon, Pierre D'Ans, Anastasia Permyakova, Oleksandr Skrylnyk, Nathalie Steunou, Marc Degrez, and Marc Frère. «A new composite sorbent based on SrBr₂ and silica gel for solar energy storage application with high energy storage density and stability». In: *Applied Energy* 190 (2017), pp. 1184–1194. ISSN: 0306-2619. DOI: <https://doi.org/10.1016/j.apenergy.2017.01.041> (cit. on p. 47).
- [105] Emilie Courbon, Pierre D'Ans, Anastasia Permyakova, Oleksandr Skrylnyk, Nathalie Steunou, Marc Degrez, and Marc Frère. «Further improvement of the synthesis of silica gel and CaCl₂ composites: Enhancement of energy storage density and stability over cycles for solar heat storage coupled with space heating applications». In: *Solar Energy* 157 (2017), pp. 532–541. ISSN: 0038-092X. DOI: <https://doi.org/10.1016/j.solener.2017.08.034> (cit. on p. 47).
- [106] Elpida Piperopoulos et al. «Morphological and Structural Evaluation of Hydration/Dehydration Stages of MgSO₄ Filled Composite Silicone Foam for Thermal Energy Storage Applications». In: *Applied Sciences* 10.2 (Jan. 2020), p. 453. ISSN: 2076-3417. DOI: [10.3390/app10020453](https://doi.org/10.3390/app10020453) (cit. on p. 47).
- [107] Alessio Sapienza, Ivan S. Glaznev, Salvatore Santamaria, Angelo Freni, and Yuriy I. Aristov. «Adsorption chilling driven by low temperature heat: New adsorbent and cycle optimization». In: *Applied Thermal Engineering* 32 (2012), pp. 141–146. ISSN: 1359-4311. DOI: <https://doi.org/10.1016/j.applthermaleng.2011.09.014> (cit. on p. 47).
- [108] Lawrence Shere, Siddharth Trivedi, Samuel Roberts, Adriano Sciacovelli, and Yulong Ding. «Synthesis and Characterization of Thermochemical Storage Material Combining Porous Zeolite and Inorganic Salts». In: *Heat Transfer Engineering* 40.13-14 (2019), pp. 1176–1181. DOI: [10.1080/01457632.2018.1457266](https://doi.org/10.1080/01457632.2018.1457266). eprint: <https://doi.org/10.1080/01457632.2018.1457266>. URL: <https://doi.org/10.1080/01457632.2018.1457266> (cit. on p. 47).
- [109] Stéphanie Hongois, Frédéric Kuznik, Philippe Stevens, and Jean-Jacques Roux. «Development and characterisation of a new MgSO₄zeolite composite for long-term thermal energy storage». In: *Solar Energy Materials and Solar Cells* 95.7 (2011), pp. 1831–1837. ISSN: 0927-0248. DOI: <https://doi.org/10.1016/j.solmat.2011.01.050> (cit. on p. 47).
- [110] T.S. Yan, T.X. Li, J.X. Xu, and R.Z. Wang. «Water sorption properties, diffusion and kinetics of zeolite NaX modified by ion-exchange and salt impregnation». In: *International Journal of Heat and Mass Transfer* 139 (2019), pp. 990–999. ISSN: 0017-9310. DOI: <https://doi.org/10.1016/j.ijheatmasstransfer.2019.05.080> (cit. on p. 47).

- [111] Valeria Palomba and Andrea Frazzica. «Recent advancements in sorption technology for solar thermal energy storage applications». In: *Solar Energy* 192 (2019). Thermal Energy Storage for Solar Applications, pp. 69–105. ISSN: 0038-092X. DOI: <https://doi.org/10.1016/j.solener.2018.06.102> (cit. on p. 49).
- [112] Lavagna, Burlon, Nisticò, Brancato, Frazzicà, Pavese, and Chiavazzo. «Cementitious composite materials for thermal energy storage applications: A preliminary characterization and theoretical analysis». In: *Scientific Reports*, *In press* (2020) (cit. on pp. 54, 55, 61, 125, 138, 143).
- [113] *Competitiveness of the European cement and lime sectors / Internal Market, Industry, Entrepreneurship and SMEs*. URL: https://ec.europa.eu/growth/content/competitiveness-european-cement-and-lime-sectors%7B%5C_%7Den (visited on 06/23/2020) (cit. on p. 55).
- [114] Y.J. Zhao, R.Z. Wang, T.X. Li, and Y. Nomura. «Investigation of a 10 kWh sorption heat storage device for effective utilization of low-grade thermal energy». In: *Energy* 113 (2016), pp. 739–747. ISSN: 0360-5442. DOI: <https://doi.org/10.1016/j.energy.2016.07.100> (cit. on pp. 62, 64).
- [115] R. Köll, W. [van Helden], G. Engel, W. Wagner, B. Dang, J. Jänchen, H. Kerskes, T. Badenhop, and T. Herzog. «An experimental investigation of a realistic-scale seasonal solar adsorption storage system for buildings». In: *Solar Energy* 155 (2017), pp. 388–397. ISSN: 0038-092X. DOI: <https://doi.org/10.1016/j.solener.2017.06.043> (cit. on pp. 62, 64).
- [116] Barbara Mette, Henner Kerskes, and Harald Drück. «Experimental and Numerical Investigations of Different Reactor Concepts for Thermochemical Energy Storage». In: *Energy Procedia* 57 (2014). 2013 ISES Solar World Congress, pp. 2380–2389. ISSN: 1876-6102. DOI: <https://doi.org/10.1016/j.egypro.2014.10.246> (cit. on p. 62).
- [117] M. Gaeini, M.R. Javed, H. Ouwerkerk, H.A. Zondag, and C.C.M. Rindt. «Realization of a 4kW thermochemical segmented reactor in household scale for seasonal heat storage». In: *Energy Procedia* 135 (2017). 11th International Renewable Energy Storage Conference, IRES 2017, 14-16 March 2017, Düsseldorf, Germany, pp. 105–114. ISSN: 1876-6102. DOI: <https://doi.org/10.1016/j.egypro.2017.09.491> (cit. on pp. 72, 73).
- [118] Rebecca Weber, Sebastian Asenbeck, Henner Kerskes, and Harald Drück. «SolSpaces – Testing and Performance Analysis of a Segmented Sorption Store for Solar Thermal Space Heating». In: *Energy Procedia* 91 (2016). Proceedings of the 4th International Conference on Solar Heating and Cooling for Buildings and Industry (SHC 2015), pp. 250–258. ISSN: 1876-6102. DOI: <https://doi.org/10.1016/j.egypro.2016.06.214> (cit. on pp. 72, 73).

- [119] *World Average Yearly Annual Temperatures*. (Visited on 06/10/2020) (cit. on p. 82).
- [120] P. Hewlett. *Lea's Chemistry of Cement and Concrete*. Elsevier Science, 2003. ISBN: 9780080535418 (cit. on p. 88).
- [121] *Cambridge Dictionary - cement definition*. URL: <https://dictionary.cambridge.org/it/dizionario/inglese/cement> (visited on 03/14/2020) (cit. on p. 88).
- [122] P.K. Mehta and Paulo J. M. Monteiro. *Concrete: Microstructure, Properties, and Materials*. Third. New York: McGraw-Hill, 2005. ISBN: 0071462899 (cit. on p. 89).
- [123] Wissenschaftliche Berichte Fzka, M Achternbosch, K.-R Bräutigam, N Hartlieb, C Kupsch, U Richers, P Stemmermann, and M Gleis Umweltbundesamt. *Forschungszentrum Karlsruhe in der Helmholtz-Gemeinschaft Heavy Metals in Cement and Concrete Resulting from the Co-incineration of Wastes in Cement Kilns with Regard to the Legitimacy of Waste Utilisation*. Tech. rep. 2003 (cit. on p. 89).
- [124] Rajeb Salem Hwidi, Tengku Nuraiti Tengku Izhar, Farah Naemah Mohd Saad, Rajeb Salem Hwidi, Tengku Nuraiti Tengku Izhar, and Farah Naemah Mohd Saad. «Characterization of Limestone as Raw Material to Hydrated Lime». In: *E3SWC* 34 (2018), p. 02042. DOI: 10.1051/E3SCONF/20183402042 (cit. on p. 90).
- [125] G. Schumacher and L. Juniper. «Coal utilisation in the cement and concrete industries». In: *The Coal Handbook: Towards Cleaner Production*. Vol. 2. Elsevier Inc., Oct. 2013, pp. 387–426. ISBN: 9781782421177. DOI: 10.1533/9781782421177.3.387 (cit. on p. 90).
- [126] Frederick M. Lea and Thomas O. Mason. *Cement - Extraction and processing*. July 2019 (cit. on p. 91).
- [127] Whittaker. *The Effects of Prehydration on Cement Performance*. (Visited on 03/14/2020) (cit. on p. 91).
- [128] Mark Whittaker, E Dubina, J Plank, and Leon Black. «The Effects of Prehydration on Cement Performance». In: Jan. 2010 (cit. on p. 92).
- [129] T. C. Powers and T. L. Brownyard. «Studies of the Physical Properties of Hardened Portland Cement Paste». In: *ACI Journal Proceedings* 43.9 (Nov. 1946), pp. 249–336. ISSN: 0002-8061. DOI: 10.14359/15301 (cit. on p. 92).

- [130] Marcella Alesiani, I. Pirazzoli, and B. Maraviglia. «Factors affecting early-age hydration of ordinary Portland cement studied by NMR: Fineness, water-to-cement ratio and curing temperature». In: *Applied Magnetic Resonance* 32.3 (2007), pp. 385–394. ISSN: 09379347. DOI: 10.1007/s00723-007-0019-y (cit. on p. 93).
- [131] Jessica Crees. «Implementing Change in an SME». In: *The Role of Enterprise Systems - IS Practices for SME Success*. Ed. by Jessica Crees and Richard Self. Vol. 26. 1-2. 2013. Chap. 2, pp. 9–12. DOI: n/a (cit. on p. 93).
- [132] Andrew Chiu Supervisor and Ian Robinson. *Hydration of Tricalcium Silicate*. Tech. rep. 2016 (cit. on pp. 94, 102).
- [133] Ana Cuesta, Jesus D. Zea-Garcia, Diana Londono-Zuluaga, Angeles G. De La Torre, Isabel Santacruz, Oriol Vallcorba, Monica Dapiaggi, Susana G. Sanf elix, and Miguel A.G. Aranda. «Multiscale understanding of tricalcium silicate hydration reactions». In: *Scientific Reports* 8.1 (Dec. 2018), pp. 1–11. ISSN: 20452322. DOI: 10.1038/s41598-018-26943-y (cit. on p. 94).
- [134] Jeffrey J. Thomas, Sam Ghazizadeh, and Enrico Masoero. «Kinetic mechanisms and activation energies for hydration of standard and highly reactive forms of β -dicalcium silicate (C2S)». In: *Cement and Concrete Research* 100 (Oct. 2017), pp. 322–328. ISSN: 00088846. DOI: 10.1016/j.cemconres.2017.06.001 (cit. on pp. 94, 97).
- [135] S. M. Park, J. G. Jang, H. M. Son, and H. K. Lee. «Stable conversion of metastable hydrates in calcium aluminate cement by early carbonation curing». In: *Journal of CO2 Utilization* 21 (Oct. 2017), pp. 224–226. ISSN: 22129820. DOI: 10.1016/j.jcou.2017.07.002 (cit. on p. 95).
- [136] H.F.W Taylor, C Famy, and K.L Scrivener. «Delayed ettringite formation». In: *Cement and Concrete Research* 31.5 (May 2001), pp. 683–693. ISSN: 00088846. DOI: 10.1016/S0008-8846(01)00466-5 (cit. on p. 95).
- [137] D. Marchon and Robert J. Flatt. «Mechanisms of cement hydration». In: *Science and Technology of Concrete Admixtures*. Elsevier Inc., Jan. 2016, pp. 129–145. ISBN: 9780081006962. DOI: 10.1016/B978-0-08-100693-1.00008-4 (cit. on p. 95).
- [138] N. Meller, C. Hall, and J. Crawshaw. «ESEM evidence for through-solution transport during brownmillerite hydration». In: *Journal of Materials Science* 39.21 (Nov. 2004), pp. 6611–6614. ISSN: 00222461. DOI: 10.1023/B:JMSC.0000044904.51813.74 (cit. on p. 95).
- [139] J. Rose, A. B enard, S. El Mrabet, A. Masion, I. Moulin, V. Briois, L. Olivi, and J. Y. Bottero. «Evolution of iron speciation during hydration of C4AF». In: *Waste Management* 26.7 (2006), pp. 720–724. ISSN: 0956053X. DOI: 10.1016/j.wasman.2006.01.021 (cit. on p. 96).

- [140] Ernest W. Flick. *Handbook of Adhesive Raw Materials - Ernest W. Flick - Google Libri* (cit. on p. 96).
- [141] Josep M. Soler. «Thermodynamic Description of the Solubility of C-S-H Gels in Hydrated Portland Cement Literature Review». In: (2007) (cit. on p. 96).
- [142] L. Nicoleau, E. Schreiner, and A. Nonat. «Ion-specific effects influencing the dissolution of tricalcium silicate». In: *Cement and Concrete Research* 59 (May 2014), pp. 118–138. ISSN: 00088846. DOI: 10.1016/j.cemconres.2014.02.006 (cit. on p. 96).
- [143] George W. Scherer, Jie Zhang, and Jeffrey J. Thomas. «Nucleation and growth models for hydration of cement». In: *Cement and Concrete Research* 42.7 (July 2012), pp. 982–993. ISSN: 00088846. DOI: 10.1016/j.cemconres.2012.03.019 (cit. on p. 97).
- [144] Frederick Measham Lea, P. C. Hewlett, and Martin Liska. *Lea's chemistry of cement and concrete*. ISBN: 9780081007952 (cit. on pp. 97, 98, 104, 125).
- [145] P. Meredith, A. M. Donald, and K. Luke. «Pre-induction and induction hydration of tricalcium silicate: an environmental scanning electron microscopy study». In: *Journal of Materials Science* 30.8 (Jan. 1995), pp. 1921–1930. ISSN: 00222461. DOI: 10.1007/BF00353014 (cit. on p. 97).
- [146] N. L. Thomas and D. D. Double. «Calcium and silicon concentrations in solution during the early hydration of portland cement and tricalcium silicate». In: *Cement and Concrete Research* 11.5-6 (Sept. 1981), pp. 675–687. ISSN: 00088846. DOI: 10.1016/0008-8846(81)90026-0 (cit. on pp. 98, 99).
- [147] Jiahui Peng, Jianxin Zhang, and Jindong Qu. «Mechanism of the formation and transformation of ettringite». In: *Journal Wuhan University of Technology, Materials Science Edition* 21.3 (Sept. 2006), pp. 158–161. ISSN: 10002413. DOI: 10.1007/BF02840908 (cit. on p. 98).
- [148] H. El-Didamony, A. M. Sharara, I. M. Helmy, and S. Abd El-Aleem. «Hydration characteristics of β -C2S in the presence of some accelerators». In: *Cement and Concrete Research* 26.8 (1996), pp. 1179–1187. ISSN: 00088846. DOI: 10.1016/0008-8846(96)00103-2 (cit. on p. 99).
- [149] Karen L. Scrivener, Patrick Juilland, and Paulo J.M. Monteiro. *Advances in understanding hydration of Portland cement*. Dec. 2015. DOI: 10.1016/j.cemconres.2015.05.025 (cit. on p. 99).
- [150] H. M. Jennings and P. L. Pratt. «An experimental argument for the existence of a protective membrane surrounding portland cement during the induction period». In: *Cement and Concrete Research* 9.4 (July 1979), pp. 501–506. ISSN: 00088846. DOI: 10.1016/0008-8846(79)90048-6 (cit. on p. 99).

- [151] Alexandre Reda Constantin William Caleb Ouzia. «Modeling the kinetics of the main peak and later age of alite hydration». In: (2019), p. 288. DOI: 10.5075/epfl-thesis-9499 (cit. on pp. 100, 102).
- [152] Patrick Juilland, Luc Nicoleau, Rolf S Arvidson, and Emmanuel Gallucci. «Advances in dissolution understanding and their implications for cement hydration». In: *RILEM Technical Letters* 2 (Dec. 2017), pp. 90–98. ISSN: 2518-0231. DOI: 10.21809/rilemtechlett.2017.47 (cit. on p. 100).
- [153] Paul D. Tennis and Hamlin M. Jennings. «Model for two types of calcium silicate hydrate in the microstructure of Portland cement pastes». In: *Cement and Concrete Research* 30.6 (2000), pp. 855–863. ISSN: 00088846. DOI: 10.1016/S0008-8846(00)00257-X (cit. on p. 101).
- [154] Semion Zhutovsky. *Chemical shrinkage of high-strength / high-performance cementitious materials* (cit. on p. 101).
- [155] Y. Sakalli and R. Trettin. «Investigation of C3S hydration by environmental scanning electron microscope». In: *Journal of Microscopy* 259.1 (July 2015), pp. 53–58. ISSN: 13652818. DOI: 10.1111/jmi.12247 (cit. on p. 102).
- [156] J. G. M. de Jong, H. N. Stein, and J. M. Stevels. «Hydration of tricalcium silicate». In: *Journal of Applied Chemistry* 17.9 (May 2007), pp. 246–250. DOI: 10.1002/jctb.5010170902 (cit. on p. 101).
- [157] K. van Breugel. «Numerical simulation of hydration and microstructural development in hardening cement-based materials (I) theory». In: *Cement and Concrete Research* 25.2 (Feb. 1995), pp. 319–331. ISSN: 00088846. DOI: 10.1016/0008-8846(95)00017-8 (cit. on p. 101).
- [158] Maria Mercedes Costoya Fernandez. «Effect of Particle Size on the Hydration Kinetics and Microstructural Development of Tricalcium Silicate». In: *Techniques* 4102.7 (2008), pp. 99–114. DOI: 10.5075/epfl-thesis-4102 (cit. on p. 102).
- [159] Karen L. Scrivener and André Nonat. *Hydration of cementitious materials, present and future*. July 2011. DOI: 10.1016/j.cemconres.2011.03.026 (cit. on p. 102).
- [160] GRONAU and J. «A new method for determining the degree of hydration of Portland cement brick». In: *Silikattechnik* 18 (1967), pp. 143–146 (cit. on p. 103).
- [161] *ASTM C125 - 20 Standard Terminology Relating to Concrete and Concrete Aggregates*. URL: <https://www.astm.org/Standards/C125.htm> (visited on 03/16/2020) (cit. on pp. 104, 105).

- [162] H. Uchikawa, S. Uchida, and Shunsuke Hanehara. «Flocculation structure of fresh cement paste determined by sample freezing». In: *Il Cimento* 84 (Jan. 1987), pp. 3–22 (cit. on pp. 105, 106).
- [163] Rikard Ylmén, Ulf Jäglid, Britt Marie Steenari, and Itai Panas. «Early hydration and setting of Portland cement monitored by IR, SEM and Vicat techniques». In: *Cement and Concrete Research* 39.5 (May 2009), pp. 433–439. ISSN: 00088846. DOI: 10.1016/j.cemconres.2009.01.017 (cit. on pp. 106, 107).
- [164] H.F.W. Taylor. *Cement Chemistry*. 1990 (cit. on p. 106).
- [165] Pierre-Claude Aïtcin and Jean-Martin Lessard. «The composition and design of high-strength concrete and ultrahigh-strength concrete». In: *Developments in the Formulation and Reinforcement of Concrete*. Elsevier, Jan. 2019, pp. 171–192. ISBN: 9780081026168. DOI: 10.1016/b978-0-08-102616-8.00008-3 (cit. on pp. 108, 110).
- [166] Aida Margarita Ley-Hernandez, Jonathan Lapeyre, Rachel Cook, Aditya Kumar, and Dimitri Feys. «Elucidating the Effect of Water-To-Cement Ratio on the Hydration Mechanisms of Cement». In: *ACS Omega* 3.5 (May 2018), pp. 5092–5105. ISSN: 24701343. DOI: 10.1021/acsomega.8b00097 (cit. on pp. 109, 112).
- [167] TC Powers. «Properties of cement paste and concrete». In: *Chemistry of Cement: Fourth International Symposium*. 1960 (cit. on p. 110).
- [168] Piotr Prochoń and Tomasz Piotrowski. «Bound water content measurement in cement pastes by stoichiometric and gravimetric analyses». In: *J. Build. Chem* 1 (2016), pp. 18–25. DOI: 10.17461/j.buildchem.2016.103 (cit. on p. 110).
- [169] Adrian Radocea. «A new method for studying bleeding of cement paste». In: *Cement and Concrete Research* 22.5 (Sept. 1992), pp. 855–868. ISSN: 00088846. DOI: 10.1016/0008-8846(92)90110-H (cit. on p. 111).
- [170] Nadia Massoussi, Emmanuel Keita, and Nicolas Roussel. «The heterogeneous nature of bleeding in cement pastes». In: *Cement and Concrete Research* 95 (May 2017), pp. 108–116. ISSN: 00088846. DOI: 10.1016/j.cemconres.2017.02.012 (cit. on p. 111).
- [171] Nouredine Mesboua, Khaled Benyounes, and Abdelbaki Benmounah. «Study of the impact of bentonite on the physico-mechanical and flow properties of cement grout». In: *Cogent Engineering* 5 (2018), p. 1446252. DOI: 10.1080/23311916.2018.1446252 (cit. on pp. 112, 113).

- [172] D. D. Nguyen, L. P. Devlin, P. Koshy, and C. C. Sorrell. *Impact of water-soluble cellulose ethers on polymer-modified mortars*. Feb. 2014. DOI: 10.1007/s10853-013-7732-8 (cit. on pp. 112, 113).
- [173] V Venkateswara Reddy, N V Ramana, K Gnaneswar, and C Sashidhar. «Effect of magnesium chloride (MgCl_2) on ordinary Portland cement concrete». In: *Indian Journal of Science and Technology* 4.6 (2011). ISSN: 0974-6846 (cit. on p. 112).
- [174] Xiaohu Wang, Yu Peng, Jiyang Wang, and Qiang Zeng. «Pore Structure Damages in Cement-Based Materials by Mercury Intrusion: A Non-Destructive Assessment by X-Ray Computed Tomography». In: *Materials* 12 (July 2019), p. 2220. DOI: 10.3390/ma12142220 (cit. on p. 120).
- [175] Sidney Diamond. «Mercury Porosimetry—An Inappropriate Method for the Measurement of Pore Size Distributions in Cement-Based Materials». In: *Cement and Concrete Research* 30 (Oct. 2000), pp. 1517–1525. DOI: 10.1016/S0008-8846(00)00370-7 (cit. on p. 120).
- [176] Okiemute Ogirigbo. «Influence of Slag Composition and Temperature on the Hydration and Performance of Slag Blends in Chloride Environments». PhD thesis. June 2016. DOI: 10.13140/RG.2.1.2611.6083 (cit. on p. 122).
- [177] Izabela Hager. «Colour Change in Heated Concrete». In: *Fire Technology* 49 (July 2013). DOI: 10.1007/s10694-012-0320-7 (cit. on p. 122).
- [178] Imad Elkhadiri, M. Elkhadiri, and F. Puertas. «Effect of curing temperature on cement hydration». In: *Ceramics - Silikaty* 53 (Jan. 2009), pp. 65–75 (cit. on p. 122).
- [179] Paul Klieger. «Effect of Mixing and Curing Temperature on Concrete Strength». In: *ACI Journal Proceedings* 54.6 (June 1958), pp. 1063–1081. ISSN: 0002-8061. DOI: 10.14359/11495 (cit. on p. 122).
- [180] Madeleine N. Scheidema and Pekka Taskinen. «Decomposition thermodynamics of magnesium sulfate». In: *Industrial and Engineering Chemistry Research* 50.16 (Aug. 2011), pp. 9550–9556. ISSN: 08885885. DOI: 10.1021/ie102554f (cit. on p. 124).
- [181] Tingting Zhang, Jing Zou, Baomin, Zhenlin Wu, Yuan Jia, and C.R. Cheeseman. «Characterization of Magnesium Silicate Hydrate (MSH) Gel Formed by Reacting MgO and Silica Fume». In: *Materials* 11 (May 2018), p. 909. DOI: 10.3390/ma11060909 (cit. on p. 125).

- [182] J.A Wang, O Novaro, X Bokhimi, T López, R Gómez, J Navarrete, M.E Llanos, and E López-Salinas. «Characterizations of the thermal decomposition of brucite prepared by sol–gel technique for synthesis of nanocrystalline MgO». In: *Materials Letters* 35.5 (1998), pp. 317–323. ISSN: 0167-577X. DOI: [https://doi.org/10.1016/S0167-577X\(97\)00273-5](https://doi.org/10.1016/S0167-577X(97)00273-5) (cit. on p. 125).
- [183] Thiery et al. Morandean Antoine. «Effect of Carbonation on the Microstructure and Moisture Properties of Cement-Based Materials». In: vol. 3. Apr. 2011 (cit. on p. 131).
- [184] T. [Van Gerven], G. Cornelis, E. Vandoren, and C. Vandecasteele. «Effects of carbonation and leaching on porosity in cement-bound waste». In: *Waste Management* 27.7 (2007), pp. 977–985. ISSN: 0956-053X. DOI: <https://doi.org/10.1016/j.wasman.2006.05.008> (cit. on p. 131).
- [185] Yongbin Chen, Tao Zhou, and Fang et al. «A Novel Preparation of Nano-sized Hexagonal Mg(OH)₂». In: *Procedia Engineering* 102 (Dec. 2015), pp. 388–394. DOI: 10.1016/j.proeng.2015.01.169 (cit. on p. 144).
- [186] Dongmin Shen, Martin Bülow, Flor Siperstein, Maximilian Engelhard, and Alan L. Myers. «Comparison of experimental techniques for measuring isosteric heat of adsorption». In: *Adsorption* 6.4 (2000), pp. 275–286. ISSN: 09295607. DOI: 10.1023/A:1026551213604 (cit. on pp. 147, 151).
- [187] Liliana Giraldo, Paola Rodriguez-Estupiñán, and Juan Carlos Moreno-Piraján. «Isosteric Heat: Comparative Study between Clausius–Clapeyron, CSK and Adsorption Calorimetry Methods». In: *Processes* 7.4 (Apr. 2019), p. 203. ISSN: 2227-9717. DOI: 10.3390/pr7040203 (cit. on pp. 147, 151).
- [188] Yun Tian and Jianzhong Wu. «Differential heat of adsorption and isosteres». In: *Langmuir* 33.4 (Jan. 2017), pp. 996–1003. ISSN: 15205827. DOI: 10.1021/acs.langmuir.7b00004 (cit. on pp. 148, 151).
- [189] Ranjan Ghosal and Douglas M. Smith. «Micropore characterization using the Dubinin-Astakhov equation to analyze high pressure CO₂ (273 K) adsorption data». In: *Journal of Porous Materials* 3.4 (1996), pp. 247–255. ISSN: 13802224. DOI: 10.1007/BF01137914 (cit. on p. 150).